DESIGN AND MANUFACTURING OF ZnO NANOWIRE AND NANOWALL STRUCTURES FOR ENERGY HARVESTING VIA FLEXIBLE PIEZOELECTRIC AND HYBRID NANOGENERATORS IN WEARABLE TEXTILES

PhD Dissertation

Gamze YÜKSEL

Eskişehir 2025

DESIGN AND MANUFACTURING OF ZnO NANOWIRE AND NANOWALL STRUCTURES FOR ENERGY HARVESTING VIA FLEXIBLE PIEZOELECTRIC AND HYBRID NANOGENERATORS IN WEARABLE TEXTILES

Gamze YÜKSEL

PhD DISSERTATION

Department of Materials Science and Engineering

Supervisor: Prof. Dr. Ender SUVACI

Eskişehir

Eskişehir Technical University

Institute of Graduate Programs

August 2025

This thesis has been supported by the project 20AG029 which is approved by the TÜBİTAK and 23DRP015 which is approved by the SRP Committee.

FINAL APPROVAL FOR THESIS

This thesis titled DESIGN AND MANUFACTURING OF ZnO NANOWIRE AND NANOWALL STRUCTURES FOR ENERGY HARVESTING VIA FLEXIBLE PIEZOELECTRIC AND HYBRID NANOGENERATORS IN WEARABLE TEXTILES has been prepared and submitted by Gamze YÜKSEL in partial fulfillment of the requirements in "Eskişehir Technical University Directive on Graduate Education and Examination" for the Degree of PhD in Materials Science and Engineering Department has been examined and approved on 25/08/2025.

Committee Members		**Title, Name and Surname**	**Signature**
Member	:	Prof. Dr. Ender SUVACI	
Member	:	Prof. Dr. Mustafa Erdem ÜREYEN	
Member	:	Prof. Dr. Kemal ÖZKAN	
Member	:	Asst. Prof. Dr. Seval KINDEN	
Member	:	Asst. Prof. Dr. Yeliz KÖSE	

Prof. Dr. Harun BÖCÜK
Director of the Institute of Graduate Programs

25/08/2025

SUPERVISOR APPROVAL

PhD student Gamze YÜKSEL, whom I supervise, has completed this thesis titled DESIGN AND MANUFACTURING OF ZnO NANOWIRE AND NANOWALL STRUCTURES FOR ENERGY HARVESTING VIA FLEXIBLE PIEZOELECTRIC AND HYBRID NANOGENERATORS IN WEARABLE TEXTILES. According to my inspections, the work is scientifically and ethically appropriate for the student to the thesis defense exam.

Supervisor
Prof. Dr. Ender SUVACI

ABSTRACT

DESIGN AND MANUFACTURING OF ZnO NANOWIRE AND NANOWALL STRUCTURES FOR ENERGY HARVESTING VIA FLEXIBLE PIEZOELECTRIC AND HYBRID NANOGENERATORS IN WEARABLE TEXTILES

Gamze YÜKSEL

Department of Materials Science and Engineering

Eskişehir Technical University, Institute of Graduate Programs, August 2025

Supervisor: Prof. Dr. Ender SUVACI

The increasing demand for wearable technologies has highlighted the need for portable and sustainable energy sources. In this context, piezoelectric and triboelectric nanogenerators stand out due to their ability to convert ambient mechanical energy into electrical energy. Their potential to harvest energy from human body movements enables these devices to serve as sustainable power sources within the ecosystem of wearables. However, the performance of nanogenerators is influenced by factors such as module design, the structure of the active layer, and the electrode-active layer interface. In this thesis, ZnO nanowires and nanowalls synthesized via hydrothermal methods, were systematically investigated within the framework of the synthesis–structure relationship. ZnO nanowall structures providing homogeneous growth, reproducibility, and high electrical output were identified as the main focus of the study. The effects of 0.5–2 at. % doping on the ZnO nanowall structure and, consequently, on piezoelectric performance were evaluated according to structure–property–performance relationships. Furthermore, the crucial roles of module architecture, electrode-active layer interface, and contact type (Schottky/Ohmic) on electrical performance were demonstrated through different module designs. In hybrid nanogenerator designs, the contribution of the triboelectric effect enabled high power generation under low forces, successfully powering an LCD screen. The developed modules were also integrated into a glove, confirming their ability to harvest energy from hand movements. Overall, this study, covering the entire process from synthesis to application, demonstrates the feasibility of ZnO nanowall-based flexible nanogenerators in wearable electronics and presents significant potential for commercialization in the field of energy harvesting.

Keywords: ZnO, Piezoelectric, Nanogenerator, Flexible, Energy.

ÖZET

GİYİLEBİLİR TEKSTİLLERDE ESNEK PİEZOELEKTRİK VE HİBRİT NANOJENERATÖRLER İLE ENERJİ HASATI İÇİN ZnO NANOTEL VE NANODUVAR YAPILARIN TASARIMI VE ÜRETİMİ

Gamze YÜKSEL

Malzeme Bilimi ve Mühendisliği Anabilim Dalı

Eskişehir Teknik Üniversitesi, Lisansüstü Eğitim Enstitüsü, Ağustos 2025

Danışman: Prof. Dr. Ender SUVACI

Giyilebilir teknolojilere olan talebin artışı, taşınabilir ve sürdürülebilir enerji kaynakları ihtiyacını da beraberinde getirmiştir. Bu bağlamda piezoelektrik ve triboelektrik nanojeneratörler, çevredeki mekanik enerjiyi elektrik enerjisine dönüştürme yetenekleri sayesinde öne çıkmaktadır. İnsan vücudu hareketlerinden enerji üretebilme potansiyelleri, bu cihazların giyilebilir elektroniklerde kendi ekosistemlerinde sürdürülebilir enerji kaynağı olarak kullanılabilmesini mümkün kılmaktadır. Ancak nanojeneratörlerin performansı modül tasarımı, aktif tabaka yapısı, elektrot-aktif tabaka arayüz etkileşimi gibi faktörlerden etkilenmektedir. Bu tez çalışmasında, nanojeneratör tasarımlarında aktif tabaka olarak kullanılan, hidrotermal yöntemle sentezlenen ZnO nanotel ve nanoduvar morfolojileri, sentez-yapı ilişkisi çerçevesinde sistematik olarak incelenmiştir. Özellikle, homojen büyüme, tekrarlanabilirlik ve yüksek elektriksel çıktı sağlayan ZnO nanoduvar yapıları, çalışmanın temel odak noktasını oluşturmuştur. %0,5-%2 at. aralığında farklı element katkılarının ZnO nanoduvar yapısı ve dolayısıyla piezoelektrik performans üzerindeki etkileri, yapı-özellik-performans ilişkisi doğrultusunda değerlendirilmiştir. Ayrıca, nanojeneratör tasarımlarında, modül mimarisi, elektrot-aktif tabaka arayüzü ve kontak tipinin (Schottky/Ohmik) elektriksel performans üzerindeki belirleyici rolü, üretilen farklı modül tasarımlarıyla ortaya konmuştur. Hibrit nanojeneratör tasarımlarında, triboelektrik etkinin katkısıyla düşük kuvvetler altında yüksek güç üretimi sağlanmış ve bir LCD ekran başarıyla çalıştırılmıştır. Geliştirilen modüller, aynı zamanda eldiven üzerine entegre edilmiş ve modüllerin el hareketleriyle enerji üretme yeteneği kanıtlanmıştır. Sonuç olarak, sentez aşamasından uygulamaya kadar tüm süreçleri kapsayan bu çalışma, ZnO nanoduvar temelli esnek nanojeneratörlerin giyilebilir elektroniklerde kullanılabilirliğini göstermekte ve enerji hasadı alanında ticarileşmeye yönelik önemli bir potansiyel sunmaktadır.

Anahtar Sözcükler: ZnO, Piezoelektrik, Nanojeneratör, Esnek, Enerji.

ACKNOWLEDGEMENTS

I would like to begin by expressing my sincere appreciation to the advisors who have guided me throughout this work with unwavering support and encouragement. My gratitude first goes to Prof. Dr. Mustafa Erdem ÜREYEN, my initial doctoral advisor, whose early guidance was invaluable; although health reasons prevented us from continuing our collaboration, I deeply appreciate the foundation he helped me build. I am especially indebted to my principal advisor, Prof. Dr. Ender SUVACI, whose mentorship has been crucial not only in advancing my academic pursuits but also in shaping my personal and professional development.

I am also sincerely grateful to the members of my dissertation defense committee, Prof. Dr. Kemal ÖZKAN, Asst. Prof. Dr. Yeliz KÖSE and Asst. Dr. Seval KINDEN, for their invaluable feedback, constructive critiques, and thoughtful guidance, all of which have played a significant role in enhancing the quality and rigor of this research.

I am deeply thankful to Buse Muslu KOP, Sakhavat DADASHOV, and Beytullah GÖL, members of TÜBİTAK 1004 PieNo project team, for their dedication, hard work, and invaluable contributions. I would also like to extend my thanks to Aydın Süleyman GÜZEL and Dr. Yusuf ÖZTÜRK from the TÜBİTAK MAM team for their continuous guidance and support.

I am equally thankful to my colleagues in the SRG research team - Dilek UÇAR, Nisa ERGİN, Hakan KAYA, Nesli YÜRÜK, and Gökçe YILDIRIM ÖZARSLAN - for the daily collaboration, knowledge sharing, and both moral and practical support they provided. Their companionship and encouragement made this challenging journey significantly more manageable and enjoyable.

I would like to extend my sincere gratitude to all the faculty, technical staff, and administrative staff of the Department of Materials Science and Engineering at Eskişehir Technical University. I am especially grateful to those who keep laboratory facilities available to students 24/7 and whose dedicated work ensures the uninterrupted operation of all systems.

I am deeply thankful to YÖK for supporting me throughout my doctoral studies through the 100/2000 YÖK Doctoral Scholarship. Similarly, I sincerely appreciate TÜBİTAK for funding my research via the 2211 - Domestic Doctoral Fellowship Program.

I would like to thank Dr. Awais QADIR for encouraging me to participate in international conferences and for instilling in me the confidence to see myself as a global researcher and scientist. Thanks to his support, my journey that began in Europe extended to Asia and the Americas. I am also especially grateful to Véronique HUART and Aurore BELOT, whom I fondly regard as the “angels without wings” of the European Ceramic Society (ECerS), for their unwavering support and patience throughout my experiences abroad. I would also like to express my sincere gratitude to Assistant Professor Anna STAERZ, who mentored me through the mentor - mentee program organized by the American Ceramic Society (ACerS), for her guidance and valuable insights. I sincerely appreciate the travel grants and support provided by TÜBİTAK, JECS Trust, and the Engineering Ceramics Division of ACerS, which made these opportunities possible.

I am deeply grateful to my friends Selin DURSUN and Çağlar SUBAŞI for their unwavering support throughout this long journey.

I would like to express my special thanks to Azmi Mert ÇELİK, who demonstrated remarkable patience and provided immense encouragement from afar during the final stages of my doctoral studies.

Finally, I owe infinite thanks to my first teachers in life - my mother Nezahat YÜKSEL, my father Hüseyin YÜKSEL, and my sister Esra YÜKSEL - for their unconditional support, love, and belief in me. Without their guidance and encouragement, this thesis would not have been possible. I would also like to express my heartfelt gratitude to my grandfather İbrahim SAY, with whom I shared some of the most precious moments of my life, who always with me in my childhood, and who passed away only two months before my defense. His love, wisdom, and strength will always remain with me.

Gamze YÜKSEL

25/08/2025

STATEMENT OF COMPLIANCE WITH ETHICAL PRINCIPLES AND RULES

I hereby truthfully declare that this thesis is an original work prepared by me; that I have behaved in accordance with the scientific ethical principles and rules throughout the stages of preparation, data collection, analysis and presentation of my work; that I have cited the sources of all the data and information that could be obtained within the scope of this study, and included these sources in the references section; and that this study has been scanned for plagiarism with "scientific plagiarism detection program" used by Eskişehir Technical University, and that "it does not have any plagiarism" whatsoever. I also declare that, if a case contrary to my declaration is detected in my work at any time, I hereby express my consent to all the ethical and legal consequences that are involved.

Gamze YÜKSEL

CONTENTS

LIST OF TABLES

Page

LIST OF FIGURES

Page

GLOSSARY OF SYMBOLS AND ABBREVIATIONS

1-D	:	1 Dimensional
2-D	:	2 Dimensional
ΔT	:	Temperature Difference
dT/dt	:	Time-dependent Temperature Change
AC	:	Alternative Current
AFM	:	Atomic Force Microscopy
AR	:	Augmented Reality
BT	:	Barium Titanate
CVD	:	Chemical Vapor Deposition
DC	:	Direct Current
EDX	:	Energy Dispersive X-ray Spectroscopy
FE-SEM	:	Field Emission Scanning Electron Microscopy
HMTA	:	Hexamethylenetetramine
HT	:	Hydrothermal Synthesis
ITO	:	Indium Tin Oxide
Kgf	:	Kilogram-force
KNN	:	Potassium Sodium Niobate
LDH	:	Layered Double Hydroxide
µA	:	Micro Amper
mM	:	Mili Molar
µW	:	Micro Watt
mW	:	Mili Watt
µV	:	Micro Volt
mV	:	Mili Volt
nA	:	Nano Amper
NBT	:	Sodium Niobate
NW	:	Nanowire
NWl	:	Nanowall
PDMS	:	Polydimethylsiloxane
PENG	:	Piezoelectric Nanogenerators
PES	:	Polyether Sulfone

PET	:	Polyethylene Terephthalate
Pd-Au	:	Palladium - Gold
PLD	:	Pulsed Laser Deposition
PVC	:	Polyvinyl Chloride
PVD	:	Physical Vapor Deposition
PVDF	:	Polyvinylidene fluoride
[P(VDF-TrFE)]:	:	Polyvinylidene fluoride-trifluoroethylene
PyENG	:	Pyroelectric Nanogenerators
PZT	:	Lead Zirconate Titanate
RoHS	:	Restriction of Hazardous Substances
SEM	:	Scanning Electron Microscopy
TEG	:	Thermoelectric Generators
TENG	:	Triboelectric Nanogenerators
VLS	:	Vapor-Liquid-Solid
VR	:	Virtual Reality
XRD	:	X-Ray Diffraction
ZnO	:	Zinc Oxide

1. INTRODUCTION

The continuous advancement of technology from the past to present has enabled computer systems to become smaller and more wearable; this transformation has increased the interest of consumers and led to the rapid growth of the wearable technology market. According to the 2015–2025 Wearable Technology Report published by IDTechEx, the market volume, which was $0.75 billion in 2012, reached $14 billion in 2014 and $70 billion by 2024. The global market is expected to grow at a compound annual rate of 6% compared to 2023 and reach $161 billion by 2033 (Skyrme, 2022). Even, the wearable sensor market alone is expected to reach $7.2 billion by 2035 (Skyrme and Howley, 2024). Figure 1.1 shows the market share distributions between 2013 and 2033 of a total of forty different wearable technologies in five main categories: wrist-worn devices (smart watches), hearing aids, augmented reality (AR) and virtual reality (VR) headsets, electronic skin patches, and smart textiles. In this distribution, it is seen that basic smart watches, cochlear implants, wireless headphones, and glucose monitoring devices stand out. The widespread use of wearable technologies in areas such as communication and health monitoring has led leading major technology companies such as Samsung, Sony, Apple, Google, Weartech, and Fitbit, as well as sportswear giants such as Nike and Adidas, to rapidly adapt to this growing trend.

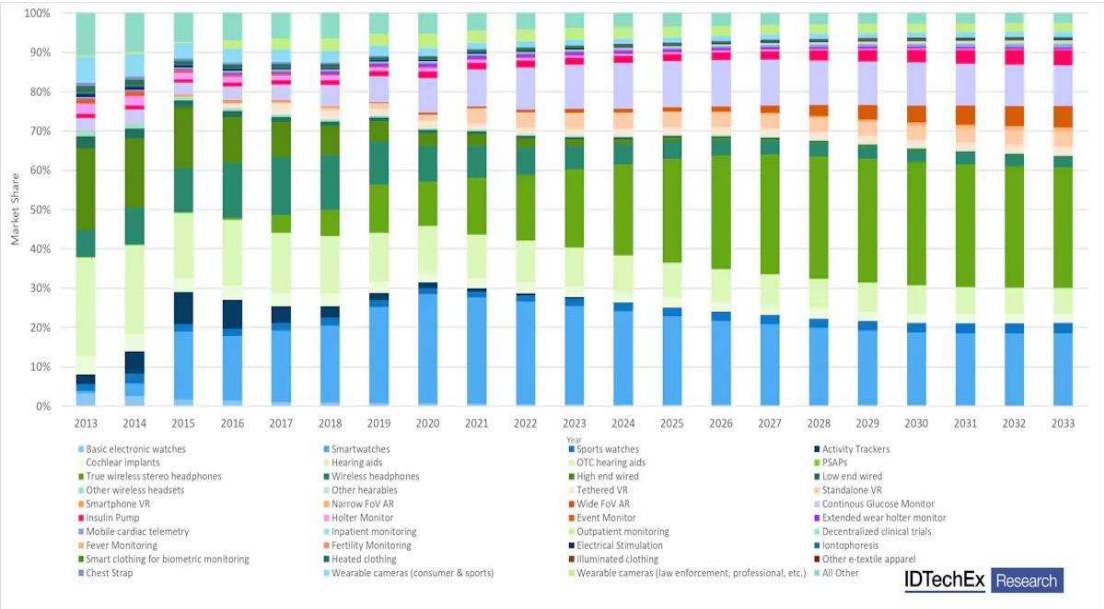

Figure 1.1. *Market share of wearable electronics over the years (Skyrme, T., 2022)*

It is known that wearable electronics presented schematically in Figure 1.2 (b) need low operating energy at the level of microwatts (μW) and milliwatts (mW) thanks to the developing electronic systems (Annapureddy et al., 2017). The energy consumption amounts of various wearable devices are given in Figure 1.2 (a). For example, the energy consumption amounts are 3 μW for glucose sensor, 300 μW for heartbeat sensor, 0.5 mW – 5 mW for hearing aid and 7 mW – 300 mW for smart watch. Although the energy required by wearable electronic devices today is generally very low, this energy is still mostly provided by conventional batteries. However, the large volumes of these batteries cause an increase in weight in wearable devices, prevent their size from being reduced, limit the flexibility of the devices and negatively affect their ergonomic features. In addition, the limited lifespan of batteries necessitates their replacement or charging at certain intervals. This situation makes it difficult for users to use their devices without interruption; it restricts freedom of movement by making the user dependent on a certain place during the charging process. On the other hand, these limited-life energy sources also cause environmental problems in terms of waste management and recycling in the long term. For all these reasons, research into the development of alternative renewable and sustainable power sources that can meet the energy needs of wearable electronic systems operating at nano and micro scales and that will not compromise their comfort of use has accelerated significantly in recent years.

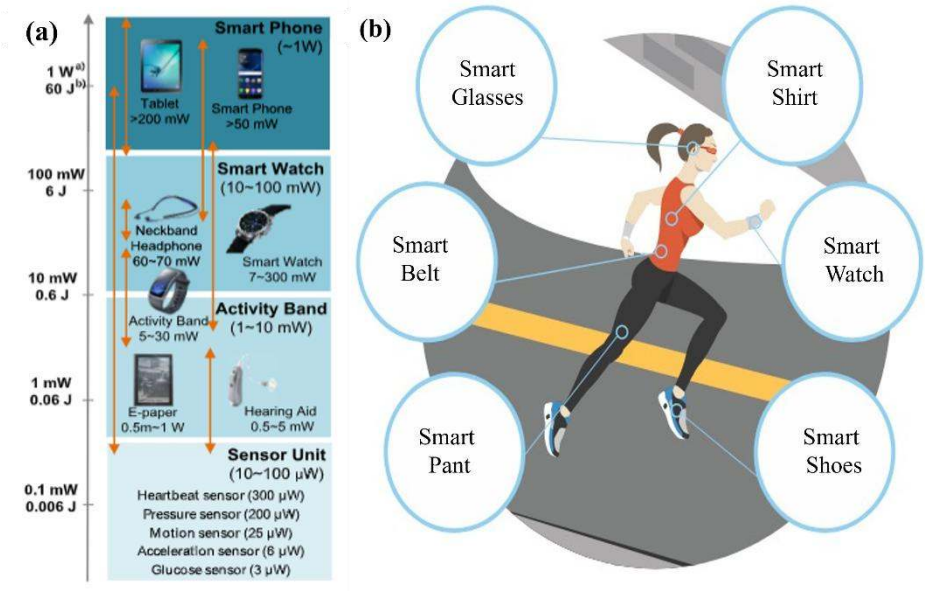

Figure 1.2. *(a) Power consumption amounts of various electronic devices (Byun et al., 2017), (b) Schematical presentation of wearable electronics*

Renewable energy is defined as a type of energy obtained from sources that are self-renewing and have no risk of depletion in nature. Solar, wind, water (hydroelectric and wave), geothermal and biomass energy are among the most widely known renewable energy sources. The basic features expected from alternative energy systems that can replace traditional batteries used in wearable technologies are; obtaining electrical energy from environmental sources without the need for an additional power source, being long-lasting and durable, and also being environmentally friendly, i.e. in line with the 'green energy' approach (Jung et al., 2015). The development of such energy systems directly contributes to the 7th 'Accessible and Clean Energy', 9th 'Industry, Innovation and Infrastructure' and 13th 'Climate Action' targets of the United Nations Sustainable Development Goals (SDGs) (in Figure 1.3) (http-1, 2025).

Figure 1.3. *United Nations sustainable development goals (http-1, 2025)*

However, the systems currently used to harvest solar, wind and wave energy do not always offer the most suitable solution for portable and constantly moving wearable electronics, as they operate depending on geographical conditions and environmental factors. Therefore, there is a need for new generation energy harvesting technologies that can effectively harvest environmental energy even under lower density conditions and that can be integrated with flexible, lightweight, and miniature structures. Therefore, nanogenerators that can convert low-energy inputs - continuously obtained from the environment - into electrical energy come to the fore. Nanogenerator systems can be classified under four main headings: piezoelectric, triboelectric, thermoelectric, and

pyroelectric. These technologies have the capacity to harvest energy using environmental or biomechanical stimuli such as movement, friction, pressure, or temperature differences (Prauzek et al., 2018). In this respect, they provide continuous and sustainable energy production without the need for an external energy source, offering ideal solutions especially for wearable electronics.

Pyroelectric and thermoelectric nanogenerators given in Figure 1.4 basically have mechanisms that can directly convert low-energy inputs due to heat into electrical energy. However, the working principles and usage conditions of these two systems are different from each other. Pyroelectric nanogenerators (PyENG) work based on the pyroelectric effect. This effect occurs when certain crystalline materials show changes in their polarization levels in response to temperature changes. This change causes charge separation on the surface of the material, creating an instantaneous electric current (Mondal et al., 2023). Therefore, in order for PyENG systems to produce energy, a time-dependent temperature change (dT/dt) on the material is required; a constant temperature difference is not sufficient. PyENG systems are particularly suitable for short-term energy production in environments with intense day and night temperature transitions or by taking advantage of periodic changes in body temperature (Zhang et al. 2021). PyENG systems generally use crystals that exhibit pyroelectric properties such as zinc oxide (ZnO), lead zirconate titanate (PZT) and barium titanate (BT, $BaTiO_3$) (Yang et al., 2012; Xue et al., 2017). On the other hand, thermoelectric generators (TEGs) are based on the “Seebeck effect” and create a continuous electrical potential with the movement of carriers (electrons or holes) as a result of a fixed temperature difference (ΔT) between two different points (Bell, 2008). In thermoelectric systems, a constant temperature gradient is required, not a change in temperature. Therefore, TEG systems are advantageous in terms of being able to provide continuous energy production. They are frequently preferred for wearable systems that operate by taking advantage of the temperature difference between the human skin and the ambient air (Leonov and Vullers, 2009). Semiconductor thermoelectric materials such as bismuth telluride (Bi_2Te_3) and antimony (III) telluride (Sb_2Te_3) are used in TEG systems (He et al., 2015). As a result, while TEGs generally have the potential to provide continuous energy; PyENGs allow for instantaneous energy output, but the efficiency of both systems is relatively low.

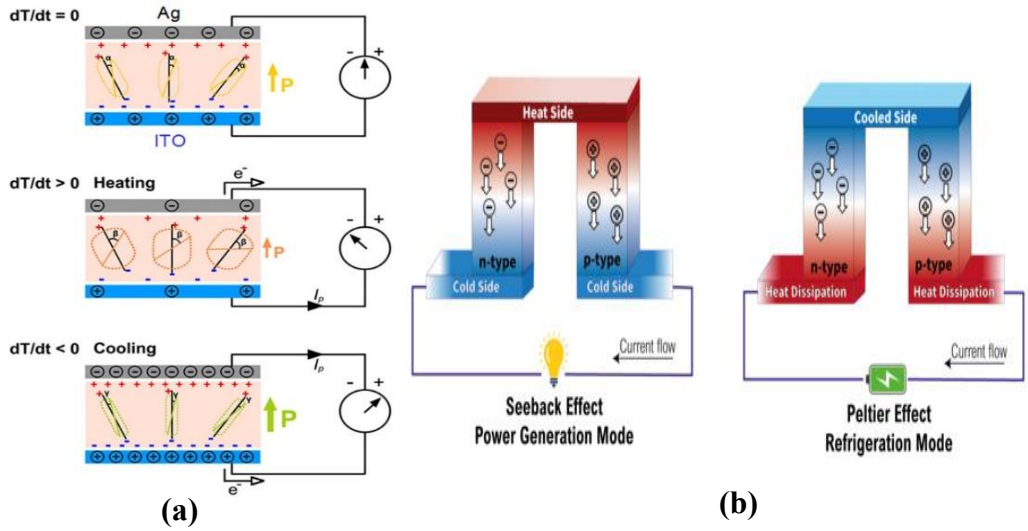

Figure 1.4. *Schematic illustrations of (a) Pyroelectric nanogenerators (PyENG) (Yang et al., 2012), (b) Thermoelectric generators (TEGs) (Ibn Shamsah, 2024)*

Triboelectric and piezoelectric nanogenerators have unique working mechanisms that can directly convert mechanical energy into electrical energy. Mechanical energy is one of the most available and sustainable energy sources in nature; generated continuously from environmental stimuli such as wind, water waves, acoustic and ultrasonic vibrations, and everyday human activities, including walking, running, breathing, and even the heartbeat. In Figure 1.5, Byun et al. have reported the amount of energy that can be generated (in joules) from various body movements performed by an average person over a one-minute duration (Byun et al., 2017). It has been indicated that approximately 24.5 mW can be produced from finger tapping, around 600 mW from arm swinging, and nearly 13.5 W from footfall within one minute. However, unless this large mechanical energy is effectively harvested, it remains a largely wasted and unused potential. In this context, triboelectric nanogenerators (TENGs) and piezoelectric nanogenerators (PENGs) which can convert this free mechanical energy, which is constantly present in the environment, into electrical energy, have become highly significant technologies for renewable, sustainable, and environmentally friendly energy harvesting systems.

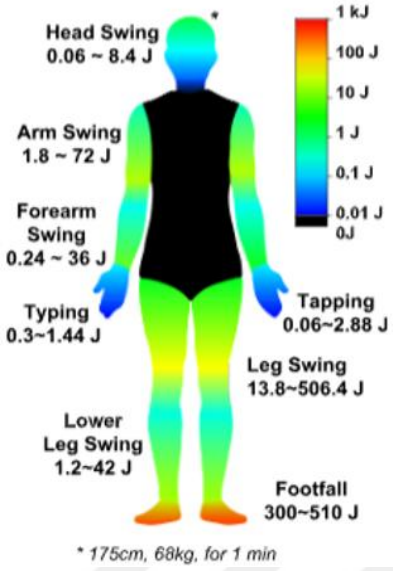

Figure 1.5. *Amount of energy produced by various human body motion (Byun et al., 2017)*

Triboelectric nanogenerators were first reported by Wang and his team in 2012 by sandwiching two different polymer layers between the electrodes, and 3.3 V output voltage, 0.6 μA output current and ~10.4 mW/cm^3 power density were achieved (Fan, Tian and Wang, 2012). TENGs systems work on the principles of triboelectric effect and electrostatic induction. They provide energy conversion by surface charge transfer that occurs during the contact and separation of two different materials. The efficiency of this charge transfer varies depending on the position of the two different materials used in TENGs systems in the triboelectric series (electronegative side or electropositive side) given in Figure 1.6 (Chen and Wang, 2017), surface charge density, and the effective contact area of the materials (Wu, Zheng and Li, 2021).

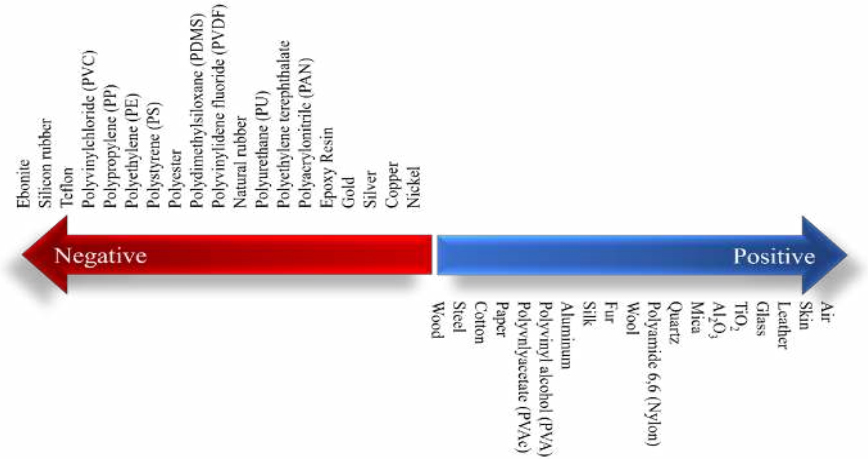

Figure 1.6. *Triboelectric series (Chen and Wang, 2017)*

TENG systems convert mechanical energy in four different modes: contact-separation, lateral sliding, single-electrode and freestanding triboelectric layer configurations. In the contact-separation mode given in Figure 1.7 (a), when two different triboelectric materials meet each other, electric charges of opposite signs are formed on their surfaces. When these surfaces are separated from each other, an electric field is created in the circuit due to the potential difference between them and a charge flow occurs. When the materials come into contact again, the accumulated charges are neutralized, and the cycle is repeated. In lateral sliding mode given in Figure 1.7 (b), when the upper surface is laterally slid to the side, the charge transfer occurs along the friction surfaces. As the sliding motion increases, an imbalance occurs in the charge distribution, which creates a potential difference. Due to this potential difference, electrons flow in the external circuit. In the freestanding triboelectric layer mode given in Figure 1.7 (c), there is a triboelectric material layer that can move freely between two fixed electrodes. When this layer approaches one electrode, a potential difference occurs between the two electrodes and electron flow begins in the circuit. When the layer approaches the other electrode, the current changes direction. Thus, two-way current can be generated. In the single-electrode mode shown in Figure 1.7 (d), include one electrode which is grounded or connected to a reference electrode. Only one surface is connected to the electrode; the other surface has a reference potential directly to the ground or the environment. When the triboelectric material moves closer to or farther from the single electrode, the resulting charge imbalance induces a current. (Wu, Zheng and Li, 2021). Important advantages of TENGs include flexibility, light weight, low cost, compatibility with various surface materials, and easy integration with microscale systems. However, TENG systems also have technical limitations, such as low current levels despite their high output voltage and sensitivity to environmental factors such as moisture and abrasion.

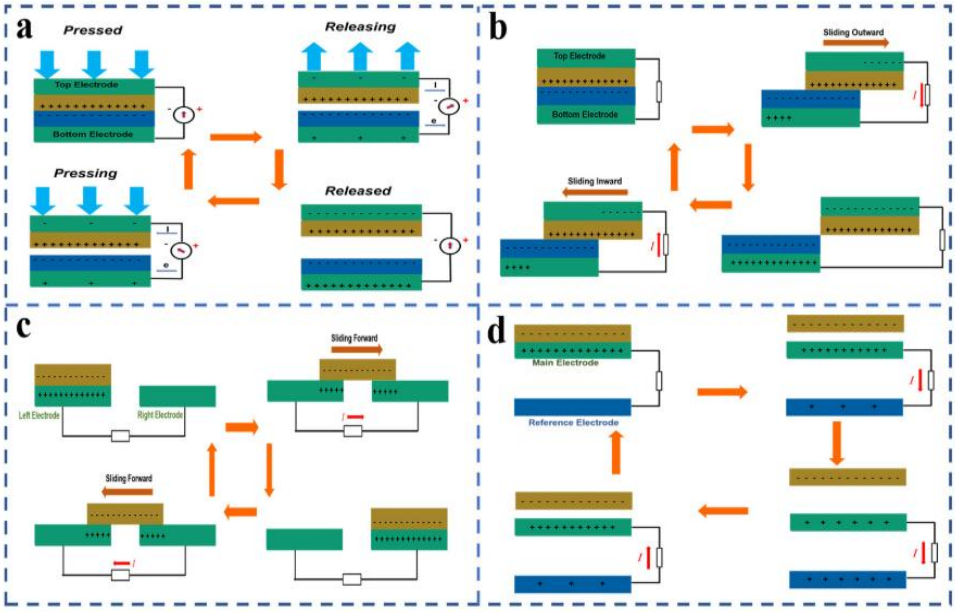

Figure 1.7. *TENGs energy conversion modes (a) contact-separation, (b) lateral sliding, (c) freestanding triboelectric layer, and (d) single-electrode (Wu, Zheng and Li, 2021)*

Piezoelectric nanogenerators have a mechanism that converts mechanical energy into electrical energy using the piezoelectric effect principle. The piezoelectric effect was first discovered in 1880 by Jacques and Pierre Curie brothers because of their work on quartz crystals (Curie and Curie, 1880). In these studies, it was observed that when mechanical stress is applied to materials with certain crystal structures, an electric charge can be produced as in Figure 1.8. This is called the direct piezoelectric effect. In the opposite case, when an electric field is applied to materials with certain crystal structures, it is observed that the crystal structure undergoes shape changes such as elongation or shortening. This situation is called the reverse piezoelectric effect. The direct and inverse piezoelectric effect is expressed mathematically as follows.

$$D(P) = dT + \varepsilon^T E \tag{1.1}$$

$$S = s^E T + d^T E \tag{1.2}$$

In the direct piezoelectric effect, a stress T (N/m²) applied to the material will produce a polarization P or a displacement D *(C/m²)* in the material that is linear in the stress as in Equation 1.1. On the other hand, the application of electric field E *(V/m)* produces a strain S that is linear in the field as in Equation 1.2. In Equations 1.1 and Equation 1.2, ε^T *(F/m)* is the permittivity at constant stress, s^E *(m²/N)* is the compliance

at constant field (if the surface area does not change with stress), and *d (C/N)* is called the piezoelectric coefficient (Pointon, 1982). The equations defining the piezoelectric effect can be expressed as follows with tensor components (in Equation 1.3 and Equation 1.4). In this context, tensors are multidimensional quantities that mathematically represent both material properties and physical effects and reactions. Polarization is a vectorial quantity and is a first-order tensor since it is defined with only one direction (i). In contrast, stress is a second-order tensor since it involves a two-way interaction, both the direction of application and the direction of effect. The piezoelectric constant or piezoelectric coefficient, which connects these two quantities, is defined as a third-order tensor since it includes both two components (j, k) coming from stress and one component (i) coming from polarization. Since the stress and strain tensors are symmetric, the piezoelectric tensor also reflects this symmetry and generally satisfies the $d_{ijk} = d_{ikj}$ condition. Using this symmetry and Einstein notation, the piezoelectric coefficient can be expressed by simplifying it with two subscripts (d_{ij}) in most cases (Newnham, 2004). For example, from piezoelectric constants d_{31} is the coefficient that defines the magnitude of the electrical polarization in the 3rd direction (along the z axis) because of the mechanical stress applied in the 1st direction (along the x axis) of the material. d_{33} is the coefficient that defines the magnitude of the electrical polarization in the 3rd direction (along the z axis) because of the mechanical stress applied in the 3rd direction (along the x axis) of the material.

$$D_i = d_{ijk}T_{JK} + \varepsilon_{ij}^{T}E_j \tag{1.3}$$

$$S_{ij} = s_{ijkl}^{E}T_{kl} + d_{kij}E_k \tag{1.4}$$

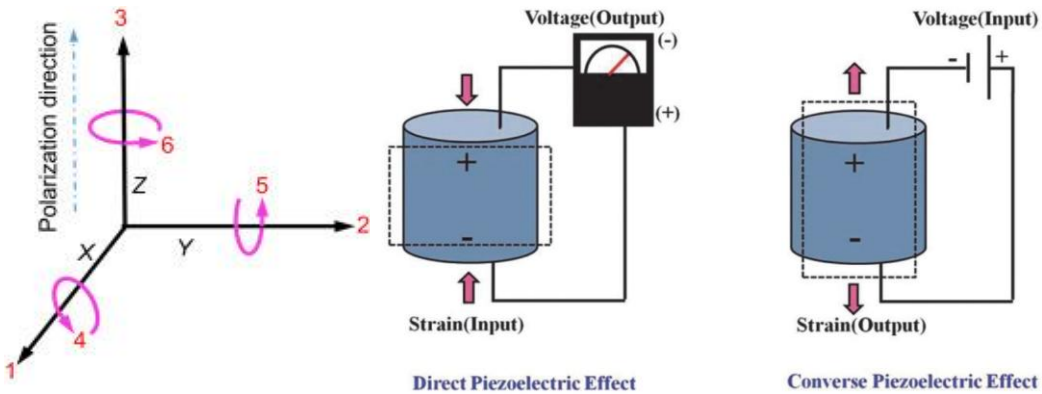

Figure 1.8. *Schematic illustration of direct and inverse piezoelectric effect (Chandra Sekhar et al., 2021)*

Piezoelectric effect is not a property seen in every material. It is found in anisotropic crystal structures that do not show central symmetry. Crystal structures are formed by the regular three-dimensional repetition of the unit cells, and are divided into seven basic classes as triclinic, monoclinic, orthorhombic, tetragonal, trigonal, hexagonal and cubic according to the size and symmetry properties of the cells. However, not only the unit cell geometry but also the atomic arrangements in these cells are determinant on the physical properties of the crystal. As a result of these combinations, a total of 230 different regular structures of crystals in space, namely space groups, have been defined. Point group symmetries are generally used for the analysis of the physical properties of crystals. Point groups contain symmetry elements such as pure rotation axes, planes of reflection symmetry and axes of rotatory inversion. These groups directly influence the mathematical representation of physical quantities such as elasticity, dielectricity, and piezoelectricity, and there are 32 in total. Each point group defines the symmetry rules that determine the directional distribution of the physical properties of the crystal. The piezoelectric effect can only occur in point groups without a center of symmetry (Figure 1.9 and Figure 1.10), as it arises from the generation of electric polarization. In centrosymmetric structures, this polarization is neutralized through symmetrical cancellation. Therefore, only 20 of the 32-point groups allow piezoelectric effect and are called "piezo classes". These classes are distributed in the crystal systems triclinic (1), monoclinic (2 and m), orthorhombic (222 and mm2), tetragonal (4, 422, 4 mm), trigonal (3, 32, 3 m), hexagonal (6, 622, 6 mm) and cubic (23). The 11-point groups that have centroid symmetry do not exhibit piezoelectric properties and are called Laue groups (Ballato, 1995).

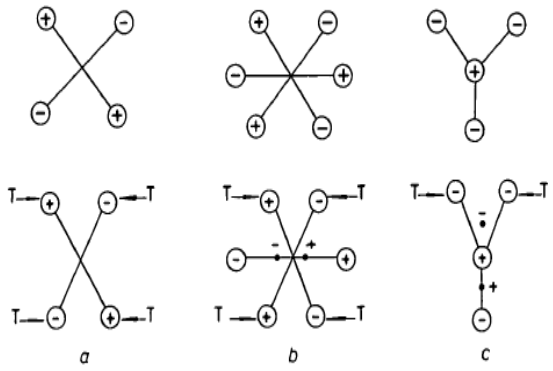

Figure 1.9. *Effect of stress on different molecules a) Centrosymmetric, stress produces no polarization b) Polarization parallel to stress c) Polarization perpendicular to stress (Pointon, 1982)*

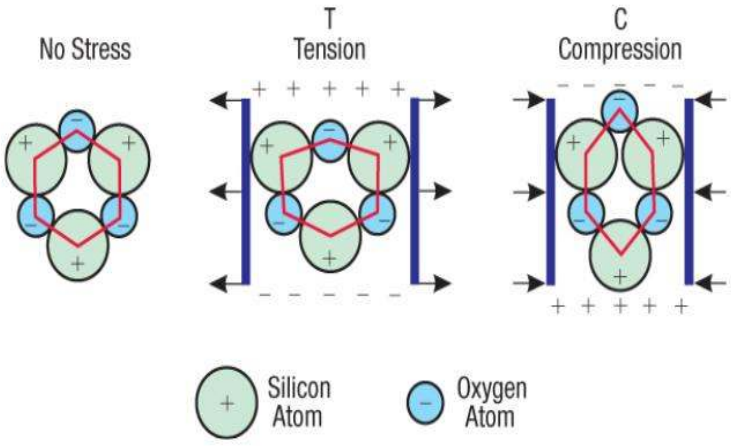

Figure 1.10. *Schematic representation of the piezoelectric effect of a quartz crystal (Govind et al., 2012)*

Following the piezoelectric effect discovery, piezoelectric materials began to be used in areas such as sensors, actuators, and ultrasonic devices. Fist piezoelectric device developed by Langevin and called as "'Langevin's sandwich" during First World War (1914-1918). This device generated high frequency sound waves in water to detach the submerged objects as a submarine detection system (sonar). During World War II (1939–1945), interest in piezoelectric materials increased significantly and these materials began to be used in military radar systems, and frequency stabilizers in communication technologies (Pointon, 1982). The first study on the use of piezoelectric effect for energy generation at the nanoscale was carried out by Zhong Lin Wang and his colleagues in 2006 (Wang and Song, 2006). Wang and his colleagues developed the first piezoelectric nanogenerator that can generate electrical signals through externally applied mechanical forces using hydrothermal-grown ZnO nanowire structures. This pioneering work proved that the piezoelectric effect is also functional at the nanoscale and opened a new area of research in the field of energy harvesting technologies. Since PENGs can be produced in very small sizes, they offer the potential to be easily integrated into areas of the human body where there are movable joints. It is thought that nanogenerators placed in these regions can meet the energy needs of wearable electronics by converting the mechanical energy released by joint movements into electrical energy. Thus, the energy needs of wearable electronics will be met within the body's own ecosystem without the need for additional power sources.

PENG designs consist of a piezoelectric layer placed between two electrodes connected by a conductive wire, as shown in Figure 1.11. Nanogenerator performances are highly dependent on the electrodes used in their design and the type and morphology

of the selected piezoelectric materials. In nanogenerator designs, ceramic, polymer, or composite structures with a combination of both materials are used in the active piezoelectric layer (Figure 1.12). As presented in Table 1.1, the energy harvesting capabilities of ceramic-based piezoelectric materials are considerably higher compared to other structures. Such ceramic-based systems typically include lead-containing materials, such as lead zirconate titanate (PZT), as well as lead-free alternatives, including barium titanate (BT, $BaTiO_3$) and zinc oxide (ZnO). Lead-containing structures in piezoelectric ceramics have a remarkably high energy harvesting capacity. However, due to the use of lead-based materials in daily life has negative effects on human and environmental health, their use is restricted within the scope of the Restriction of Hazardous Substances Directive 2002/95/EC, adopted by the European Council in 2003 (Directive, 2013). Therefore, as an alternative to these lead-containing materials, there has been an increased trend towards lead-free metal oxides that are friendly to human and environmental health.

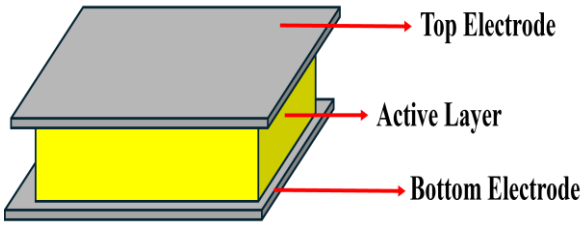

Figure 1.11. *Schematic illustration of the PENG design*

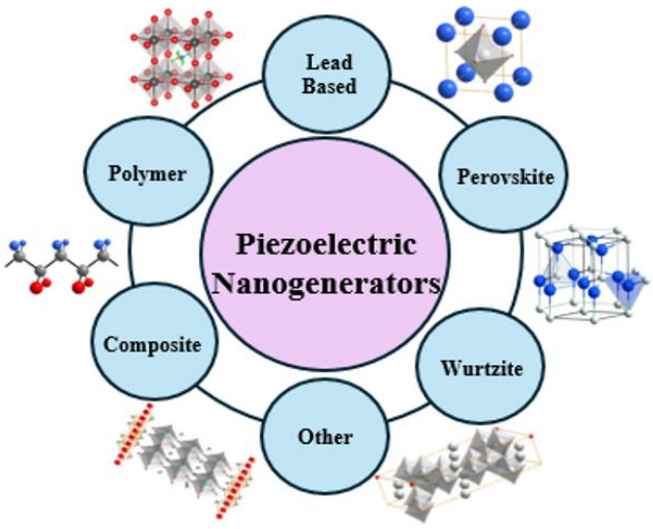

Figure 1.12. *Piezoelectric material classes used in PENG design* (Zhao et al. 2021)

Table 1.1 *Comparison of piezoelectric coefficients for different materials (Zaszczyńska, Gradys and Sajkiewicz, 2020)*

	Materials	Type	Piezoelectric Coefficient	
			d_{33} (pC/N)	d_{31} (pC/N)
Inorganic	PMN-PT	Single Crystal	2000-3000	-
	Quartz		2.3	-0.67
	ZnO	Crystal	6-13	-5
	GaN		2-4	-1.5
	AlN		3-6	-2
	PZT-5H	Ceramic	593	-274
	$BaTiO_3$		190	-78
	$LiNbO_3$		16	-1
Organic	PVDF	Polymer	-33	23
	PLLA		6-12	-

One of the most widely preferred lead-free materials in PENGs is ZnO. ZnO is a white inorganic compound with a direct band gap of 3.37 eV and a large exciton binding energy of 60 meV at room temperature. Also, it has high light emissions, mechanical and chemical stability (Look, 2001; Klingshirn, 2007). Therefore, it is preferred as a highly effective functional inorganic semiconductor material in optoelectronic and electronic applications. ZnO has three different crystal structures. These are hexagonal wurtzite, cubic zinc mixture, and rock salt, as shown in Figure 1.13 (Han et al., 2023). The wurtzite structure is thermodynamically quite stable at room temperature.

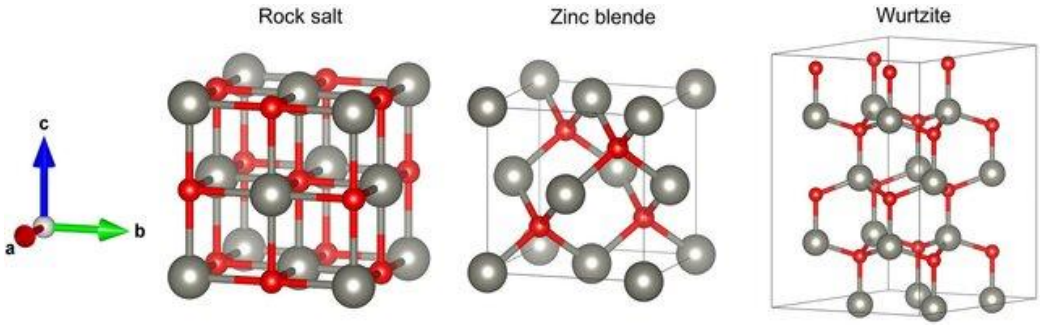

Figure 1.13. *Crystal structures of ZnO: rock salt (cubic symmetry), zinc blende (cubic symmetry) and wurtzite (hexagonal symmetry) (Han et al., 2023)*

ZnO, with its hexagonal wurtzite crystal structure, also exhibits favorable piezoelectric properties due to the inherent polarization along its c-axis. The wurtzite structure belongs to the C_{6V}^4 Schoenflies notation and the $P6_{3mc}$ Hermann-Mauguin

notation space group. Crystal structures in this group do not exhibit centrosymmetric properties, so negative and positive charges do not overlap. In a ZnO crystal with wurtzite structure given in Figure 1.14, oppositely charged ion planes with positive (0001)-Zn and negative (000$\bar{1}$)-O spontaneously form a polarization on the c axis. This polarization gives the ZnO piezoelectric property (Wang, 2004; Özgür et al., 2005; Bagga, Akhtar and Mishra, 2018; Pandey et al., 2021).

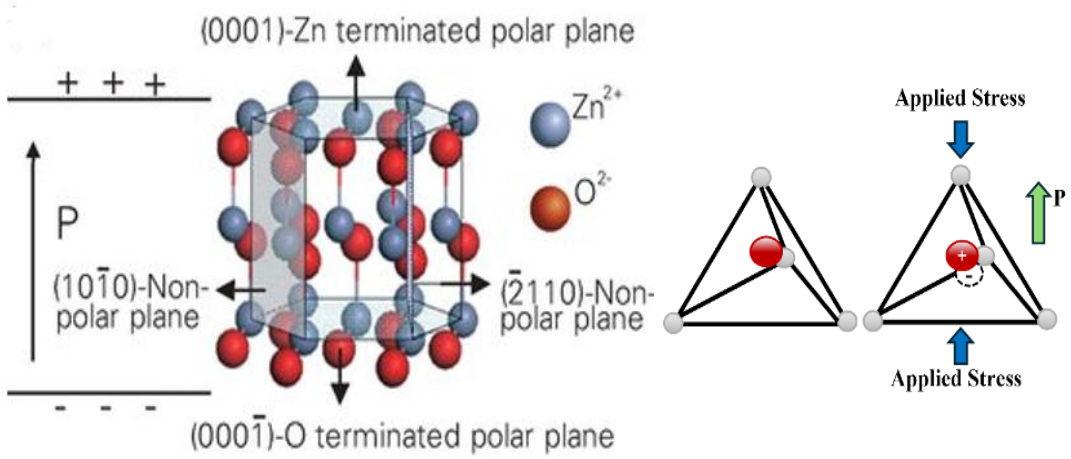

Figure 1.14. *Schematic representation of hexagonal wurtzite ZnO crystal structure and polarization mechanism (Wang, 2012)*

ZnO used in the piezoelectric layer are preferred in different morphologies such as plate, film, nanowire. In the first experiments, piezoelectric thin films were used in nanogenerator designs, mechanical vibrations were transmitted to the film with a carrier and converted into electrical energy. Since the electrical energy produced in these systems is realized in a narrow band gap, it can only be used in environments where the resonance frequency and source frequency are remarkably close. However, since the frequencies of sources such as human movements and environmental vibrations vary in a wide range over time, the first trials with thin films could not find potential for use in this area. On the other hand, with the developments in nano-manufacturing methods, piezoelectric materials can be produced in nanowire (1-Dimensional) and nanowall (2-Dimensional) morphologies. This problem has been overcome, thanks to the nanogenerators developed with these structures, which can operate outside the resonance frequency with the principle of reversing mechanical tension into electrical energy. In the study by Wang and Song (2006), ZnO nanowires were grown on a rigid substrate, and these nanowire arrays were scanned with the tip of a contact mode atomic

force microscope (AFM). During scanning, voltage output was observed at each contact of the tip with the nanowires. In this developed system, energy conversion efficiency was between 17-30% (Wang and Song, 2006). These results revealed the potential of PENG developed with ZnO nanowires to be used in energy harvesting devices.

In the literature, it was determined that 1-D and 2-D ZnO nanostructures were obtained by methods such as vapor-liquid-solid (VLS), chemical vapor deposition (CVD), physical vapor deposition (PVD), pulsed laser deposition (PLD), electrochemical deposition and hydrothermal (HT)/solvothermal synthesis. The growth of ZnO nanostructures with CVD is based on the principle of depositing the steam obtained by chemical reduction and evaporation of the starting materials in a tube furnace reactor on a low temperature substrate with a gas flow (Law, Goldberger and Yang, 2004; Schmidt-Mende and MacManus-Driscoll, 2007). In CVD, PVD and PLD production methods, ZnO nanostructures are generally obtained with high purity starting material and elevated temperatures such as 700-1400°C (Jie et al., 2005; Li et al., 2006), as seen in Table 1.2. Although very well aligned, highly crystalline ZnO nanowires can be produced by these methods, a limited number of substrate materials such as silicon, quartz and sapphire are used because they operate at elevated temperatures. It is not suitable for the fabrication of ZnO nanostructures on substrates containing flexible polymer materials with low temperature resistance.

The hydrothermal method is another method used to grow ZnO nanostructures. ZnO nanowire growth process by hydrothermal synthesis method usually takes place in two steps. In the first step, a ZnO layer, which acts as a seed layer, is formed on the substrate. Magnetron sputtering, dipping, dripping or spin coating methods are used to form the seed layer. In the magnetron sputtering method, ZnO particles can be deposited directly on the substrate in the desired thickness in a vacuum environment. In dipping, dripping or spin coating methods, firstly, the seed solution obtained with zinc acetate dihydrate and alcohol is prepared, and then this prepared solution is transferred onto the substrate. Finally, a heat treatment is applied to convert the zinc acetate to ZnO. In the second step followed the seed layer is obtained, an aqueous precursor solution is prepared with certain proportions (0.01-0.1M) of zinc salt ($Zn(NO_3)_2$, $ZnCl_4$) and alkaline agent (hexamethylenetetramine, HMTA). The prepared precursor solution and the substrate coated with the seed layer are transferred to the hydrothermal reactor and nanowire growth is performed at the specified temperature (<100°C) and time (2-48

hours) (Leprince-Wang, 2015). This method for producing ZnO nanostructures with an aspect ratio of 10-20 was developed by Vayssieres (Vayssieres, 2003).

Table 1.2. Comparative table of 1-D and 2-D ZnO nanostructure synthesis methods

Method	Substrate	ZnO Source	Temperature	Time	Morphology	Reference
VLS	Si (001)	ZnO + graphite powder	850-900°C	1-30 min	Single crystal wurtzite NW	(Lee et al., 2003)
VLS	Si	ZnO powder	700-800°C		Single crystal wurtzite NW	(Chu et al., 2012)
PVD	Alumina	ZnO powder	1400°C	2 h	Single crystal wurtzite NW	(Pan and Wang, 2001)
PVD	Sapphire	ZnO powder	750°C	90 min	Single crystal wurtzite NW	(Wang et al., 2005)
PVD	Si	ZnO + graphite powder	990°C	30 min	Single crystal wurtzite NW	(Fang et al., 2007)
PVD	Si	ZnO powder	500°C	1 h	Single crystal wurtzite NW	(Zhang et al., 2009)
CVD	Si (001)	Metallic Zn + O_2/Ar mix	670°C	30 min	Single crystal wurtzite NW	(Lupan et al., 2010)
PLD	Sapphire, Si	ZnO Target	900°C		Single crystal wurtzite NW	(Zhang at al., 2005)
PLD	Si	ZnO Target	600°C		Single crystal wurtzite NW	(Sun, Fuge and Ashfold, 2006)
HT	Si, glass	$Zn(NO_3)_2$ + HMTA	95°C	1-10 h	Single crystal wurtzite NW	(Vayssieres et al., 2001)
HT	Si (001) wafer	$Zn(NO_3)_2$ + HMTA	90°C	0.5-6 h	Single crystal wurtzite NW	(Greene et al., 2003)
HT	Al-foil	$Zn(NO_3)_2$ + HMTA	95°C	3 h	Single crystal wurtzite NWl	(Kim et al., 2013)

Materials to be used in piezoelectric nanogenerator applications must have certain morphological properties. For example, it was determined that ZnO with 1-D nanowire morphology should have a length of 3-4 μm and a diameter of >50 nm to produce

acceptable output power (Wang, 2012). These morphologies and morphology properties of the materials are mostly determined by the production method and the parameters that are effective in this production method. In the literature, it was concluded that the dimensions and morphology of ZnO nanowires synthesized by the hydrothermal method were significantly affected by process parameters such as the thickness of the seed layer deposited on the substrate, growth solution concentration, solution pH value, hydrothermal synthesis temperature, and synthesis time. In general, nanowire density depends on seed layer thickness and growth solution concentration (Kenanakis et al., 2009; Ji et al., 2009), nanowires aspect ratios depend on growth solution concentration (Ghayour et al., 2010), synthesis time and temperature (Leprince-Wang, 2015); the morphology changes depending on the pH value of the growth solution (Vernardou et al., 2007). By changing these parameters, nanostructures of different sizes and morphologies can be obtained.

ZnO based nanogenerators can be produced in rigid or flexible structures depending on the preferred substrate. In the first studies using the hydrothermal synthesis method, rigid substrates were used (Lu et al., 2009; Zhu et al., 2012). Recently, when flexible and wearable systems are considered, the use of flexible substrates for flexible nanogenerator production has become widespread. In nanogenerators designed using rigid substrates, energy harvesting can only be done under compression or vibration, while in nanogenerators designed using flexible substrates, energy harvesting can be accomplished by bending the device as well as by compression or vibration effects. The first flexible energy harvesting system was developed by Gao et al in 2007 (Gao et al., 2007). It was produced by hydrothermal growth of ZnO nanowires on a 50 μm thick Kapton polyimide film. The substrates, which were coated with a 100 nm thick layer of gold by thermal evaporation, then covered with a seed layer. Finally, the substrates covered with the seed layer were kept in an equimolar solution of zinc nitrate hexahydrate and HMTA at a concentration of 0.01 - 0.04 M. It was stated that as a result of stretching the nanowires with the AFM tip, an output voltage of 45 mV was produced. In later years, flexible nanogenerators were also fabricated by growing ZnO nanowires on indium tin oxide (ITO)-coated polyether sulfone (PES) substrates (Figure 1.15) using a low-temperature solution of zinc nitrate and HMT by Choi and his group (Choi et al., 2009). Two different devices were fabricated by directly joining the upper and lower electrodes on which the nanowire was grown and applying a Pd-Au coating between the

substrates and the nanowires. It was stated that the coated devices reached 10 μA.cm^{-2} current density values when compressed with a load of 0.9 kgf, and this value was higher than the uncoated device.

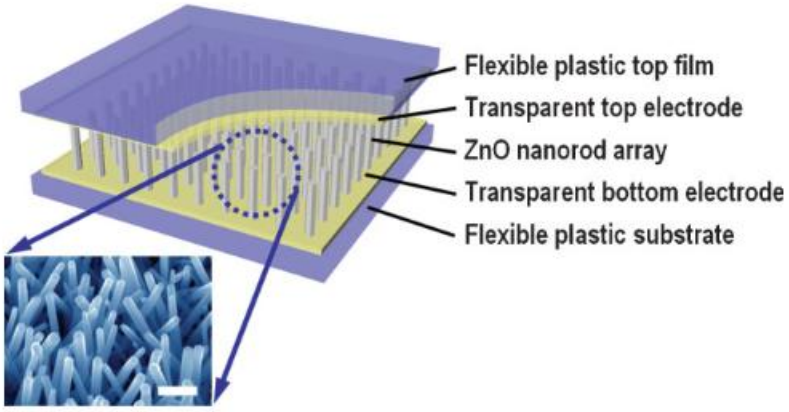

Figure 1.15. *Piezoelectric nanogenerator obtained by growing ZnO nanowire on ITO coated PES substrates (Choi et al., 2009)*

In another study by Hu and his colleagues ZnO nanowires were grown on a Kapton substrate by hydrothermal method and the grown nanowires were filled with polymethyl methacrylate (PMMA). When the device was subjected to periodic bending, approximately 350 mV open circuit voltage, and 125 nAcm^{-2} short circuit current density were produced (Hu et al., 2011).

In addition to polymer-based flexible plates, different flexible substrates such as paper, fiber and fabric have been used in the design of flexible piezoelectric nanogenerators containing ZnO nanowire arrays. Studies on ZnO nanowires grown on fibers were first performed by Qin and colleagues (Qin, Wang and Wang, 2008). ZnO nanowires were grown on Kevlar fibers via hydrothermal synthesis method. One of the ZnO nanowire coated fiber was coated with gold to act as an electrode. Then, these two fibers were wrapped on each other and subjected to a stretching process. When the stretching process applied to the fibers, an open circuit voltage of around 1 mV and a short circuit current of 5 pA were produced. On the other hand, Khan and colleagues' growth ZnO nanowires on the silver (Ag) coated fabric surface via hydrothermal method. Within the scope of the study, the piezoelectric output produced as a result of bending the nanowires with the AFM tip was measured as 10 mV, but the current density could not be determined. ZnO nanowire arrays were grown on the paper substrate with similar hydrothermal synthesis methods and 15 mV output voltage and 10 nA output

current could be produced by bending the structure (Khan et al., 2012). These studies show that ZnO nanowires can be successfully grown on different surfaces such as fiber and fabric.

Most of the 1-D ZnO nanowire-based PENG developed using different substrates and different fabrication methods produce alternating current (AC) output. However, the devices that are planned to use the developed nanogenerators need direct current (DC). Therefore, an extra converter unit is needed to convert the alternating current obtained in 1-D ZnO nanowire-based nanogenerator systems into DC that can be used in devices. A unit to be added to the energy harvesting system enlarges the system volume and adversely affects the comfort properties, especially in wearable systems. At the same time, significant reductions in the power obtained during the conversion process occur (Kim et al., 2013). For this reason, nanogenerator designs that can produce DC have gained importance in recent years and new studies have focused on piezoelectric structures that can provide this feature. It has been tried to develop nanogenerators that can produce DC by using electrodes with different morphologies (Wang et al., 2007) or by producing sparse ZnO nanowires that are not exactly parallel to the c-axis (Park et al., 2011). However, there are not many studies in this area.

In the literature review, it has been seen that DC in ZnO-based PENG systems can be obtained by using structures called 2-D ZnO nanowalls instead of 1-D ZnO nanowires as a piezoelectric layer (Kumar et al., 2011). It has been stated that 2-D ZnO nanowall structures have higher structural stability and power generation performance and better mechanical strength compared to 1-D ZnO nanowire structures, as well as their potential to generate DC. At the same time, it was determined that the electrical output obtained by using 2-D ZnO nanowalls in PENG designs is higher than 1-D ZnO nanowire based nanogenerators (Kim et al., 2013). Kaur and Singh compared the piezoelectric performances of 0-D, 1-D, and 2-D ZnO nanostructures produced by hydrothermal synthesis method, both experimentally and through simulation. While the highest voltage (226 mV) and power density (2.4 $\mu W/cm^2$) values were obtained in 2-D ZnO nanostructures in experimental studies, the highest voltage value was obtained in 1-D ZnO nanostructures in simulation results. They explained the reason for this difference as follows: While measuring the output voltage values in the simulation program, isolated single 1-D ZnO nanostructure and single 2-D ZnO nanostructure were considered. Therefore, when the mechanical deformation of these two structures was

compared against the applied force, the 1-D ZnO nanostructure deforms more and creates a higher piezoelectric potential. However, experimental studies were performed on an array that was not performed with a single isolated nanostructure. Therefore, when the 1-D ZnO nanostructure arrays were densely packed, the bending and compression capacities of the nanowires decreased due to the reduced area, and thus low piezoelectric outputs could be produced. However, higher piezoelectric outputs can be obtained in 2-D ZnO nanostructures due to the presence of sufficient intrastructure voids and the strengthening of the structures interacting with each other during mechanical deformation (Kaur and Singh, 2020).

Aluminum (Al) substrates are widely used in the hydrothermal synthesis of 2-D ZnO nanowalls. During the synthesis, the formation of a Zn:Al layered double hydroxide (LDH) layer is observed between the ZnO nanowalls and the Al substrate (Figure 1.16). It was stated that this LDH layer formed acts as anionic clay, anion scavenger and exchanger, and a capacitor with poor conductivity. Therefore, it is thought that the LDH layer formed in the synthesis stage has an important role in the generation of DC. Kim et al. tried to obtain direct current by synthesizing 2-D ZnO nanowall structures on Al-substrates. As with 1-D ZnO nanowire synthesis, they did not apply any seed layer formation process. Hydrothermal synthesis was carried out in one step. When the field emission scanning electron microscope (FE-SEM) images of the synthesized ZnO nanowall structure were examined, the width of the nanowalls was measured as 80 nm and the height as 3 μm. In the nanogenerator design step, a PES electrode covered with a 100 nm thick gold (Au) layer was used as the top electrode. In electrical measurements, 0.44 V output voltage, 6.5 $\mu A/cm^2$ DC output current and 2.86 $\mu W/cm^2$ DC power density were produced under 1 kgf force (Kim et al., 2013).

In another study, Saravanakumar and Kim grew 2-D ZnO nanowall structures on a flexible substrate by hydrothermal synthesis method and measured the electrical output of this structure. In the nanogenerator design, the obtained structure was coated with PMMA using the spin coating method. The bottom and top electrode structure was provided by coating with 100 nm thick Au. Bottom and top electrode connections were made with copper (Cu) cables. The device was finally encapsulated with Poly(dimethyl siloxane) (PDMS). When the produced device was bent with finger movements, the maximum output voltage was measured as 2.5 V, the output current was 80 nA and the power density was 0.2 $\mu W/cm^2$ (Saravanakumar and Kim, 2014). In the following years,

Manjula et al. designed nanogenerator modules by synthesizing ZnO nanowalls on an Al substrate by hydrothermal synthesis method and using ITO-coated Poly (ethylene terephthalate) (PET) as the top electrode. Then, they examined the piezoelectric outputs produced by connecting these nanogenerator modules in series. They were able to obtain an output voltage in the range of 100 - 150 mV from a single module in the measurements they made with finger tapping movements on the nanogenerator modules. On the other hand, when 2, 3 and 4 nanogenerator modules are connected in series, they can obtain ~200 mV, ~300 mV and ~400 mV output voltages, respectively (Manjula et al., 2020).

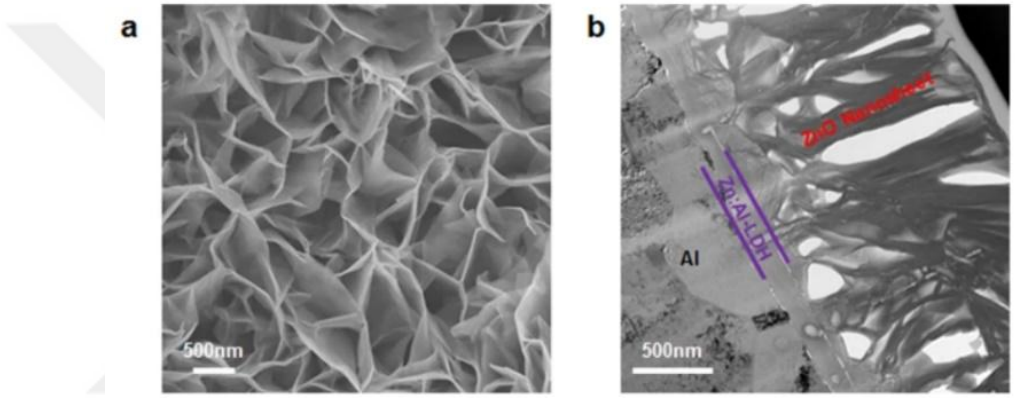

Figure 1.16. *a) Front view of the ZnO nanowall network grown on Al substrate (FE-SEM image), b) cross section TEM image of the ZnO nanowall network (Kim et al., 2013)*

Although different morphologies are used to increase the energy efficiency of ZnO-based nanogenerator modules, pure ZnO-based nanogenerators have low current density and power density. For bulk ZnO, the piezo response is ~9.9 pC/N (Zhao, Wang and Mao, 2004) and for an oriented ZnO film, the piezo response is only ~12.4 pC/N (Desai and Haque, 2007). The undoped ZnO nanostructures are intrinsically n-type semiconductors with large oxygen deficiencies. Oxygen deficiencies in the structure cause the formation of free charge carriers. In ZnO structures, unlike in ideal insulating piezoelectric materials, free charge carriers partially screen the immobile charges generated by the piezoelectric effect. When a mechanical force is applied to a ZnO structure, free electrons in the conduction band migrate into the piezoelectric potential regions to balance the potential, resulting in depleted ionized donors in the negative potential region and accumulated electrons in the positive potential region. Consequently, to enhance the piezoelectric response of ZnO, the concentration of free

charge carriers must be minimized. This reduction can be achieved through processes such as doping, annealing, or plasma treatment. (Indumathi, Venkatesan and Manikandan, 2023). In the literature, studies have been carried out with different dopants such as silver (Ag) (Zhang et al., 2021), vanadium (V) (Gupta et al., 2013), lithium (Li) (Shin et al., 2014), aluminum (Al) (Chang, Fang and Tsai, 2015), chromium (Cr) (Sinha et al., 2014), gallium (Ga) (Zhao et al., 2015), and Neodymium (Nd) (Batra et al., 2018) to improve the piezoelectric property of ZnO. Rajagopalan et al. have used various dopants (tin, copper, and lanthanum) with ZnO material that enhanced the piezo response (Rajagopalan, Singh and Palani, 2018; Rajagopalan et al., 2020; Manikandan et al., 2020).

Although numerous studies have been conducted to enhance the piezoelectric performance of ZnO nanostructures and improve the efficiency of ZnO-based PENGs, to the best of our knowledge, no commercial design has yet been realized. This indicates that research on ZnO nanowires grown on flexible substrates via hydrothermal synthesis still faces significant challenges in terms of optimization. Furthermore, ZnO nanowall-based nanogenerator applications are relatively recent and have not yet been thoroughly explored. Therefore, this field remains highly open to research and development. The research objective of this study is to develop flexible nanogenerator modules for wearable systems by growing ZnO nanowire and ZnO nanowall arrays on flexible substrates through hydrothermal synthesis and integrating them into textiles. To achieve this goal, the study has been structured into five sections, as described below.

1- Hydrothermal synthesis of 1-D ZnO nanowire arrays on flexible ITO/PET substrates: Effect of the hydrothermal synthesis parameters such as seed solution solvent and concentration, growth solution concentration, and synthesis time on ZnO nanowire arrays were investigated in Chapter 2.
2- Hydrothermal synthesis of 2-D nanowall arrays on Al-foil substrates: Effect of the hydrothermal synthesis parameters such as growth solution concentration, synthesis time, and synthesis temperature on ZnO nanowall structures were investigated in Chapter 3.
3- Doping of 2-D ZnO nanowalls: Effect of different dopants on the piezoelectric potentials of ZnO nanowall structures were investigated in Chapter 4.

4- Module design and integration: Design of various piezoelectric, triboelectric, and hybrid nanogenerator modules, their integration onto textiles, and their electrical performance were systematically investigated in Chapter 5.
5- Design of Piezoelectric Nanogenerator on Textile Surface: To enable direct module design on textiles, the fabrication of ZnO nanowall structures on textile surfaces via hydrothermal synthesis was investigated in Chapter 6.

In Chapter 7, the overall outcomes of the conducted experimental studies were systematically summarized, highlighting the key findings obtained throughout the research. Subsequently, in Chapter 8, these findings were critically discussed in the context of the broader literature, and potential directions for future work were outlined, thereby providing a comprehensive conclusion to the thesis.

2. HYDROTHERMAL SYNTHESIS OF 1-D ZnO NANOWIRE ARRAYS

2.1 Introduction

In recent years, developments in electronic devices have not been limited to increased performance, but have also come to the fore with flexibility, portability, biocompatibility, and sustainability. With the rapid evolution in nanotechnology, flexible electronic systems have begun to replace traditional rigid systems, paving the way for body-compatible wearable technologies. Wearable devices such as smart watches, biosensors, biomedical implants, and smart textiles, which have become a part of our lives, especially in the fields of communication, entertainment, and health, constitute the most active research areas of this transformation. One of the key factors in the research area is the development of flexible, lightweight, sustainable, and self-charging power systems to meet the energy needs of wearable technologies.

Today, traditional battery systems that can be charged from an external source are still used for wearable devices. Although studies are being conducted to extend battery life, these batteries need to be removed and charged at certain intervals or replaced with new ones due to their limited lifespan. This issue not only hinders continuous device usage and negatively impacts user comfort but also poses challenges for environmental recycling. Emerging solutions are being developed in the form of next-generation alternative energy harvesting systems, such as flexible solar cells. However, the performance of these systems is highly dependent on environmental conditions, which limits their attractiveness as a preferred energy solution. Therefore, interest in flexible, wearable nanogenerator systems that are not dependent on environmental conditions has increased. Piezoelectric nanogenerators, which can convert mechanical energy into electrical energy, have suggested the idea that waste mechanical energy released from daily human movements can be converted into electrical energy for wearable technologies.

The idea of flexible nanogenerator was first put forward by Prof. Wang and his team in 2006 (Wang and Song, 2006). They developed a nanogenerator module by producing ZnO nanowire arrays on a flexible substrate and suggested that an energy conversion efficiency of 17-30 % could be achieved. In flexible nanogenerator applications, different ceramic materials with piezoelectric properties such as PZT, BT, sodium niobate (NBT), potassium sodium niobate (KNN) with perovskite structure, ZnO with wurtzite structure, polymer materials such as Polyvinylidene fluoride

(PVDF), Poly(vinylidene fluoride–trifluoro ethylene) (P(VDF-TrFE)), polyamides or composite materials using these together can be used. Although the material with the highest piezoelectric properties is PZT, it was restricted within the scope of the Restriction of Hazardous Substances Directive 2002/95/EC, adopted by the European Council in 2003, due to its adverse effects on human and environmental health (Directive, 2013). Therefore, lead-free systems have become the focus of attention. Considering that bulk ceramics are brittle, polymer materials are the first materials that come to mind in flexible nanogenerator systems, but ceramic materials with 1-D morphology such as nanowire, nanobelt (Wang, 2009), nanotube (Xi et al., 2009), nanorod (Banna and Park, 2017), needle-like (Fu et al., 2022) can also be used in flexible nanogenerator systems. Although the synthesis of 1-D perovskite-structured materials on flexible substrates is challenging, the fabrication of 1-D ZnO nanostructures with a wurtzite structure is comparatively easier. This advantage makes ZnO a preferred material for flexible piezoelectric nanogenerator applications.

ZnO is a semiconductor material of group II-VI, composed of zinc and oxygen. It has a wide band gap (3.37eV) and high exciton binding energy (60meV) (Özgür et al., 2005; Look, 2001). The oppositely charged ion planes with positive (0001)-Zn and negative (000$\bar{1}$)-O in the C_{6V}^4 Schoenflies notation and the P63mc Hermann-Mauguin notation space group of hexagonal wurtzite structure of ZnO spontaneously form a polarization on the c axis. Its inherent polarization provides ZnO with piezoelectric properties (Wang, 2004; Özgür et al., 2005; Bagga, Akhtar and Mishra, 2018; Pandeyet al., 2021). ZnO in the hexagonal wurtzite structure is also both mechanically and chemically stable. Thanks to these properties, ZnO are widely preferred in different application areas such as sensors (Wei et al., 2009; Zhou et al., 2009), light emitted diodes (Park and Yi, 2004), varistors (Pearton et al., 2004) as well as energy harvesting systems such as photovoltaic solar cells (Baxter et al., 2006).

1-D ZnO nanowires can be synthesized on substrates with production methods such as CVD (Lupan et al., 2010), PVD (Wang et al., 2005), PLD (Sun, Fuge and Ashfold, 2006). However, these synthesis methods are quite costly processes due to the requirement of specific equipment and the expensive high purity raw materials and are not suitable for high volume production. Moreover, these methods are typically carried out at elevated temperatures. Since flexible substrates are commonly polymer-based, such high-temperature synthesis processes are generally incompatible with flexible

substrates (Lee et al., 2003; Zhang, Russo and Mao, 2005; Lupan et al., 2010). On the other hand, production by hydrothermal method is an alternative production technique that does not require complex system requirements, offers low cost, production at low temperatures, and allows high volume production (Leprince-Wang, 2015).

Hydrothermal synthesis of 1-D ZnO nanowire arrays on flexible substrates occurs by reacting to zinc precursors (zinc nitrate, zinc acetate, zinc chloride, etc.) with a suitable base (hexamethylenetetramine, HMTA or NaOH, etc.) in an aqueous solution (Chevalier-César, Capochichi-Gnambodoe and Leprince-Wang, 2014; Zhang et al., 2015). In general, the reactions of hydrothermal synthesis using zinc nitrate and HMTA can be expressed as follows (Wang, 2009):

$$Zn(NO_3)_2{\cdot}6H_2O \rightarrow Zn^{2+} + 2NO_3^- + 6H_2O \quad (2.1)$$

$$C_6H_{12}N_4 + 6H_2O \rightarrow 4NH_3 + 6HCHO \quad (2.2)$$

$$NH_3 + H_2O \rightleftharpoons NH_4^+ + OH^- \quad (2.3)$$

$$Zn^{2+} + 2OH^- \rightarrow Zn(OH)_2 \quad (2.4)$$

$$Zn(OH)_2 \rightarrow ZnO + H_2O \quad (2.5)$$

Zinc nitrate hexahydrate dissolves in water and dissociates into zinc ions (Zn^{2+}) and nitrate ions (Equation 2.1). T > 70°C HMTA slowly hydrolyzes in water and produces ammonia (NH_3) and formaldehyde (HCHO) (Equation 2.2). The resulting ammonia provides hydroxide ion (OH^-) in water through the following equilibrium reaction (Equation 2.3). OH^- ions formed in the solution react with Zn^{2+} ions to form insoluble zinc hydroxide ($Zn(OH)_2$) (Equation 2.4). Finally, under hydrothermal conditions, $Zn(OH)_2$ decomposes to form ZnO crystals and water (Equation 2.5).

For effective performance in flexible PENG applications, the ZnO nanowire arrays grown on flexible substrates must be well oriented to the c-axis. As seen in Figure 2.1, when force is applied to the module for energy generation in ZnO nanowire-based nanogenerators, the ZnO nanowires are compressed. The compressed surface of the nanowires becomes negatively charged, while the stretched surface becomes positively charged, creating a voltage difference. When the applied force is removed, the system neutralizes itself and returns to its original state. In this mechanism, it is crucial that the nanowires do not touch each other and that each nanowire contacts the upper electrode to achieve high efficiency. Proper c-axis orientation of the nanowires increase the number of nanowires in contact with the upper electrode, thereby enhancing the

nanogenerator's performance. Consequently, ensuring well-aligned ZnO nanowires on the substrate during hydrothermal synthesis is essential.

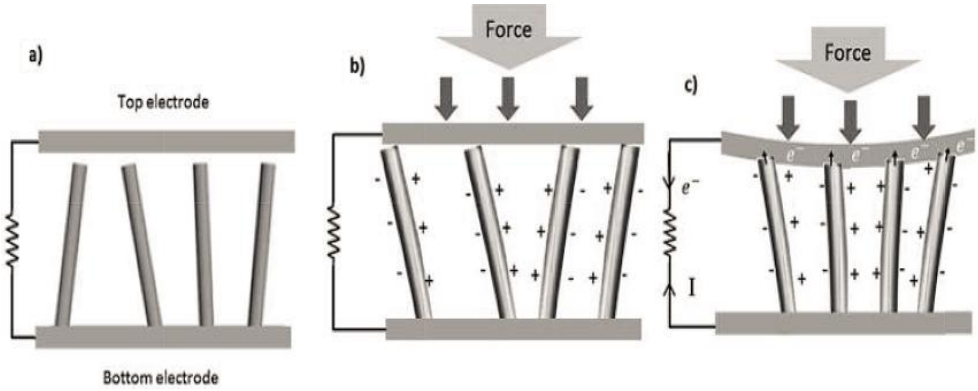

Figure 2.1. *Schematic diagrams of ZnO nanowires charge generation mechanism (Leprince-Wang, 2015)*

To obtain well oriented ZnO nanowires on the substrate, hydrothermal synthesis is conducted in two stages. The first stage is deposition the ZnO seed layer on the flexible substrate. This seed layer acts like heterogeneous nucleation point - the precipitation address of ZnO - at the second stage which is the growth of nanowires (Verde et al., 2013). The seed layer coating step can be performed with different methods such as sputtering, electrodeposition, dip coating, or spin coating. Sputtering (RF or DC magnetron) provides dense and uniform ZnO seed layer films with high crystal quality. Film thickness and crystal orientation can be controlled with high precision (Szyszka, 2008). However, it is costly due to vacuum systems. In the commonly used dip coating and spin coating, the process is conducted with a prepared solution. Dip coating is based on the principle of dipping the surface into the ZnO solution and withdrawing it at a certain speed (Guillemin et al., 2015). In the spin coating method, the ZnO solution is spread by rotating it on the substrate and then annealed at a certain temperature to obtain a homogeneous ZnO seed layer on the surface (Wang et al., 2006). In the spin coating method, parameters such as the type of solvent in the seed solution, solution concentration and coating number affect the seed layer quality and thickness. Therefore, it also affects the diameters and orientation of the nanowires grown on the substrate and the nanowire density per unit area (Basinova et al., 2019).

Inorganic zinc salts (such as nitrate, chloride) or organic zinc salts (such as acetate) are used when preparing seed solutions. However, when it is difficult to

completely remove the anionic by-product found in inorganic salts, the most preferred precursor is zinc acetate. Because unwanted organic by-products can be easily removed during heat treatment (Znaidi, 2010). A suitable solvent is required to ensure the dissolution of zinc salts. In addition, the solvent should support the formation of alkoxide or alkoxy complexes in the medium. Therefore, the most commonly preferred solvents are low carbon alcohols, such as methanol, ethanol, 1-propanol and 2-methoxyethanol (Znaidi et al., 2003; Guillemin et al., 2015).

After the substrate surfaces are coated with the prepared seed solution, they should be subjected to a heat treatment. Heat treatment removes the solvent in the solution from the medium while also allowing the formation of ZnO crystals. The heat treatment temperature should be above the boiling point of the solvents and by-products. Excessively elevated temperatures may cause cracks in the seed layer due to rapid crystallization and rapid evaporation of the solvent and organics. When it is too low, the seed layer may cause randomly oriented nanowire growth because of its low texture. In the literature, processes have been applied at temperatures ranging from 200°C to 800°C (Ohyama, Kouzuka and Yoko, 1997; Guillemin et al., 2012; Demes et al., 2016; Syrrokostas and Govatsi, 2016).

In the literature, studies have compared the properties of ZnO structures synthesized using solutions prepared with several types of alcohol. Hosono et al. tried to obtain ZnO particles at low temperatures by adding zinc acetate to methanol, ethanol and 2-methoxyethanol, they concluded that the most suitable solvent was methanol. They also gave the solubility order of zinc acetate dihydrate from highest to lowest as follows: methanol, ethanol and 2-methoxyethanol (Hosono et al., 2004). Foo et al. reported that when seed solutions were prepared using 2-methoxyethanol, ethanol and isopropyl alcohol, the smallest grain size was obtained from the solution prepared with 2-methoxyethanol, and the largest grain size was obtained from the solution prepared with ethanol. It was reported that the strongest diffraction peak corresponding to the (002) plane was observed in thin films prepared with 2-methoxyethanol and ethanol solutions, whereas the most intense peak appeared corresponding to the (101) plane in thin films prepared with an isopropyl alcohol solution. (Foo et al., 2014). However, in these studies, either ZnO particles or only ZnO film formations were investigated. Nanowire structures were not grown on film structures obtained with different solutions. Consequently, the effect of the seed layer solvent on nanowire structures and, indirectly,

on their piezoelectric properties has not been thoroughly investigated. One of the objectives of this study is to examine how seed layers prepared with different solvents influence nanowire growth and, in turn, their piezoelectric performance.

After the formation of the seed layer, the second step is the growth of ZnO nanostructures on the seed layer by hydrothermal synthesis. At this stage, hydrothermal synthesis parameters such as solution concentration, synthesis time, and synthesis temperature are important on the grown nanostructures. In general, nanowire density depends on seed layer thickness and growth solution concentration (Kenanakis et al., 2009; Ji et al., 2009), nanowires aspect ratios depend on growth solution concentration (Ghayour et al., 2010), synthesis time and temperature (Leprince-Wang, 2015); the morphology changes depending on the pH value of the growth solution (Vernardou et al., 2007). By changing these parameters, nanostructures of varied sizes and morphologies can be obtained.

In the reviewed studies, $Zn(NO_3)_2$ salt and HMTA were commonly used as precursors during the growth of ZnO nanowires via hydrothermal synthesis. Precursor solutions were obtained by dissolving equimolar $Zn(NO_3)_2$ and HMTA in deionized water. Ghayour et al. investigated the effects of precursor solution concentration on the size and morphology of the grown nanowires in their study (Ghayour et al., 2010). In this context, they prepared precursor solutions at different concentrations (0.001 M - 0.1 M) and grew ZnO nanowires by hydrothermal method. XRD analyses revealed nanowires grown vertically and in the (002) direction from all solutions. However, it was observed that the obtained nanowire diameters decreased with decreasing solution concentration. In another study, the effects of precursor solutions prepared with $Zn(NO_3)_2$ and HMTA at different ratios (1:2, 1:1, and 2:1) on nanowires were investigated. It was concluded that nanowires grown in solution with high $Zn(NO_3)_2$ concentration were obtained in more disordered structures (Ruhaizat and Ainuddin, 2021). Furthermore, when growing ZnO nanowires via hydrothermal synthesis, the synthesis temperature must be at least 60 °C, as hexamethylenetetramine (HMTA) in the solution becomes active above this temperature. Studies have demonstrated that at temperatures between 60 °C and 80 °C, nanowires grow both laterally and axially, whereas at temperatures above 80 °C, growth occurs predominantly along the axial direction. (Leprince-Wang, 2015).

Varying pH values in hydrothermal synthesis is one of the parameters that affect the resulting nanostructures. Vernardou and colleagues investigated the effect of varying pH values on ZnO nanostructures grown by hydrothermal synthesis. They used equimolar zinc nitrate hexahydrate and HMTA to synthesize ZnO nanostructures and conducted the synthesis process at 95°C. They obtained growth solutions at different pH values by adding different amounts of NaOH to the prepared solutions. In their study, they observed that at pH = 7, ZnO nanostructures formed as nanorods, and with increasing pH values, ZnO nanostructures began to form prismatic and flower-like shapes given in Figure 2.2 (Vernardou et al., 2007).

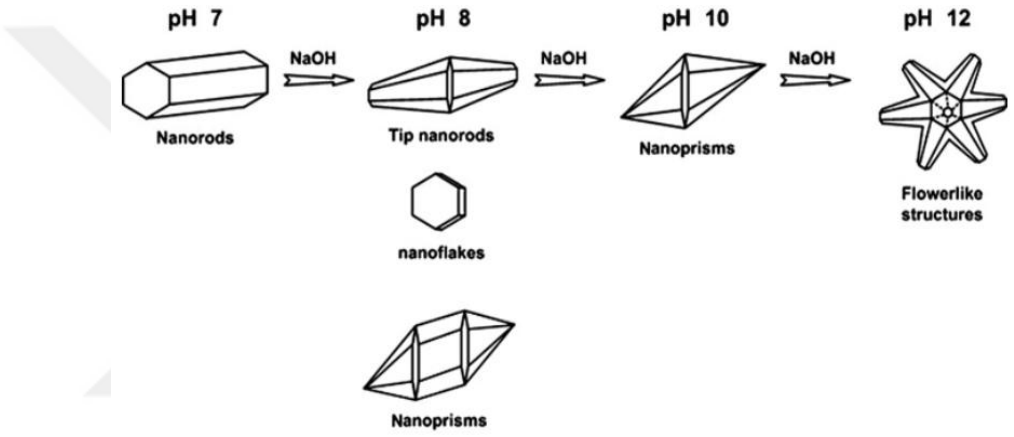

Figure 2.2. *Schematic representations of ZnO nanostructures obtained depending on the changing pH value (Vernardou et al., 2007)*

Another parameter affecting the morphology and size of ZnO nanowires obtained by hydrothermal synthesis is the reaction time. In his study, Laprince-Wang conducted hydrothermal synthesis at 90 °C and pH 7 for different times to investigate the effects of synthesis time. He observed that the growth of nanowires occurred in two stages. The first stage occurred in the first hour, and the growth rate of the nanowires was calculated to be approximately 13 nm/min. The second stage continued until the 6 hours, and a decrease in the growth rate of the nanowires occurred (2.5 nm/min). However, there was no significant increase in the nanowire diameters with time. The reason for this is that the axial growth rate in the c-axis is greater than the lateral growth rate (Leprince-Wang, 2015). The same situation has also been stated by Guo and Postel in the literature (Guo, Diao and Cai, 2005; Postels et al., 2007).

The hydrothermal synthesis method is widely preferred to produce ZnO nanowires because it allows for low-temperature crystal growth and the achievement of controlled

morphologies. Literature studies indicate that the size and orientation of ZnO nanowires are directly dependent on parameters such as the type and thickness of the seed layer, the concentration of the growth solution, the synthesis temperature, and the time. Furthermore, the pH of the solution plays a critical role in determining the morphological properties of the nanostructures (e.g., the formation of wire, rod, or flower-like structures). Therefore, systematic optimization of these parameters is crucial for improving the piezoelectric performance of the resulting ZnO nanostructures. However, despite all current research and development efforts, to the best of our knowledge, it has not yet been possible to design a mass-produced, stable, and highly efficient piezoelectric nanogenerator on a commercial scale. This suggests that the parameters related to the synthesis of ZnO nanostructures need to be further investigated and optimized for practical application.

The research objective of this study is to systematically investigate how the morphological properties of ZnO nanowires, synthesized via hydrothermal methods on flexible substrates, vary with synthesis parameters, and to evaluate the piezoelectric properties of the resulting nanostructures in order to assess their suitability for energy harvesting applications.

2.2. Experimental

ZnO nanowires growth on the ITO coated PET substrates by two-step hydrothermal synthesis method. According to the literature, the ZnO seed layer on substrates is obtained through the oxidation of a zinc acetate coating applied to the substrates. Sreekanth et all. reported that zinc acetate dihydrate decomposition to zinc oxide occur between the 187°C and 310°C (Sreekanth et al., 2017). After the 310°C decomposition is completed. So, generally the oxidation process is applied at 350°C for 30 minutes. But this oxidation temperature is too high for PET substrates. To understand the proper condition for ITO coated PET substrates, the oxidation temperature of zinc acetate dihydrate (Sigma Aldrich, MW: 219.49 g/mol) was determined with thermogravimetric analysis (TGA).

Before the hydrothermal synthesis, ITO coated PET substrates were cleaned in ultrasonic bath for 30 min with acetone, isopropyl alcohol, and ethanol, respectively. Then the cleaned substrates were left to dry in room condition. After that, cleaned substrates coated with the seed solution prepared under the conditions specified in Table

2.1, then heat treatment was applied. Finally, the seed layer-coated substrates were placed in the growth solutions prepared under the conditions specified in Table 2.1, and hydrothermal synthesis was carried out at 90°C for the specified times. Throughout the text, the P-XM-Y-Z designation system where XM, Y and Z refer to seed solution solvent and seed solution concentration in (mM), Zn^{2+} concentration in the hydrothermal growth solution in (mM) and synthesis time in (h), respectively, is used for describing the samples, developed in this study.

Table 2.1. *Hydrothermal synthesis conditions of ZnO nanowires on ITO/PET substrates*

Sample Code	Seed Layer		Hydrothermal Growth	
	Solvent	***Concentration (mM)***	***Concentration (mM)***	***Growth Time* (h)**
P-M20	Methanol	20.0	-	-
P-E20	Ethanol	20.0	-	-
P-I20	IPA	20.0	-	-
P-M20-25.0-6	Methanol	20.0	25.0	6
P-E20-25.0-6	Ethanol	20.0	25.0	6
P-I20-25.0-6	IPA	20.0	25.0	6
P-M80-25.0-6	Methanol	80.0	25.0	6
P-M100-25.0-6	Methanol	100.0	25.0	6
P-M300-25.0-6	Methanol	300.0	25.0	6
P-M500-25.0-6	Methanol	500.0	25.0	6
P-M100-6.25-6	Methanol	100.0	6.25	6
P-M100-12.5-6	Methanol	100.0	12.5	6
P-M100-25.0-6	Methanol	100.0	25.0	6
P-M100-50.0-6	Methanol	100.0	50.0	6
P-M100-25.0-3	Methanol	100.0	25.0	3
P-M100-25.0-9	Methanol	100.0	25.0	9
P-M100-25.0-12	Methanol	100.0	25.0	12
P-M100-25.0-15	Methanol	100.0	25.0	15

2.2.1. Seed layer coating on the substrates

First of all, to determine the effect of seed solution solvent on the ZnO nanowire arrays, 20 mM seed solution prepared with zinc acetate dihydrate ($Zn(CH_3COO)_2$) (Sigma Aldrich, MW: 219.49 g/mol) and 3 different solvents as methanol, ethanol, and isopropyl alcohol. Proper amount of zinc acetate dihydrate was added to methanol,

ethanol, and isopropyl alcohol separately and mixed with magnetic stirrer at room temperature until to get clear solution. After that cleaned substrates were coated with different seed solutions with spin coating method at 1500 rpm for 60 seconds given in Figure 2.3. Then soft baking applied for coated substrates at 100°C for 2 min. This coating and baking process were applied 5 times to obtain full coverage on the substrates. Finally, all the coated substrates were oxidized at 200°C for 3 hours given in Figure 2.4.

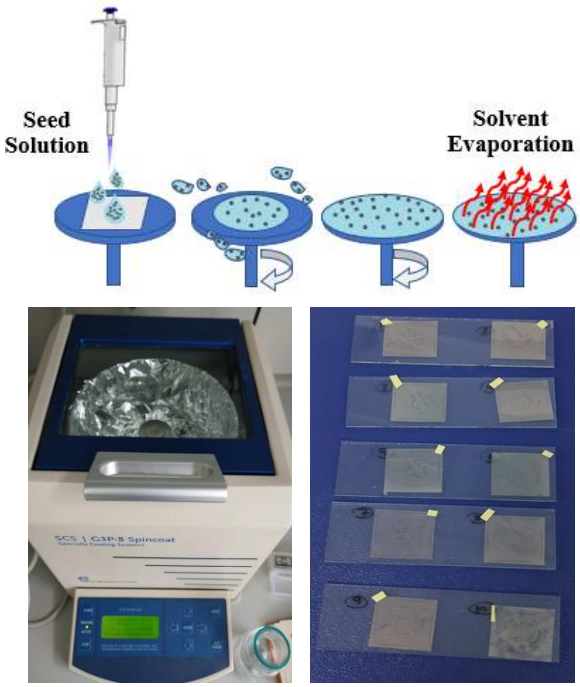

Figure 2.3. *Illustration of spin coating process, photographs of spin coater, and seed layer coated ITO/PET substrates*

Figure 2.4. *Oxidation process applied to seed layer deposited ITO/PET substrates at 200°C for 3 h*

2.2.2. Hydrothermal synthesis of ZnO nanowire on the substrates

Hydrothermal synthesis was performed as described in the literature (Chevalier-César, Capochichi-Gnambodoe and Leprince-Wang, 2014). Equal molar (1:1) zinc nitrate hexahydrate ($Zn(NO_3)_2$) (Sigma Aldrich, MW: 297.49 g/mol) and HMTA ($C_6H_{12}N_4$) (MERCK, MW: 140.19 g/mol) aqueous solutions at different concentrations (6.25mM to 50mM) were prepared. The proper amount of zinc nitrate hexahydrate and HMTA were added to 100 ml of distilled water separately and mixed with magnetic stirrer at room temperature for 20 minutes. Then two clear solutions mixed with each other with magnetic stirrer at room temperature for 20 minutes as given in the Figure 2.5. The seed layer coated substrates were placed in the growth solution. Then the covered beakers were placed in a hot water bath previously set at 90°C and kept for various times (3 hours to 15 hours). At the end of the synthesis, they were removed from the hot water bath and allowed to cool to room temperature. After cooling the samples were removed from the beakers and washed several times with distilled (DI) water then left to dry at room conditions.

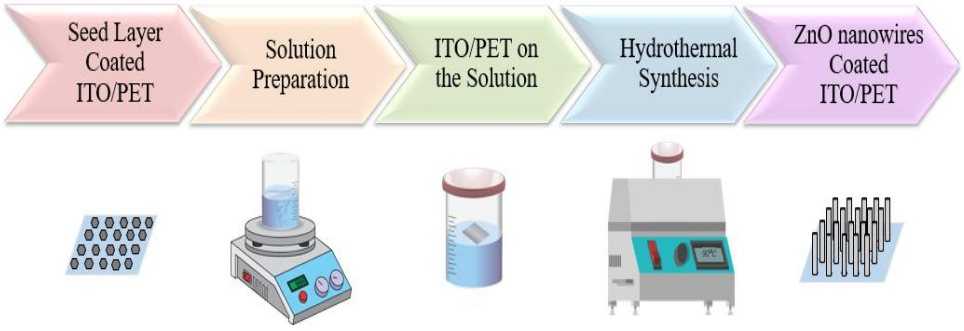

Figure 2.5. *Schematic illustration of hydrothermal synthesis of ZnO nanowire array on the ITO/PET*

2.2.3. Characterization

To determine the appropriate oxidation temperature of zinc acetate on the ITO coated PET substrates stepwise thermogravimetric (TG) analysis (TA, SDT Q600) was performed for zinc acetate dihydrate under air atmosphere and 10°C/min heating rate up to 600°C. X-ray diffraction (XRD, Bruker D2 Phaser, Cu anode kα1 = 1.54Å) analysis was performed to examine the crystal structure of ZnO nanowire arrays grown on the ITO coated PET substrates and to determine the planes in which the crystals are oriented. Scanning electron microscopy (SEM, Zeiss Supra, secondary electron mode

and 15kV acceleration voltage) analysis was performed for morphological examinations. In addition, Image J program (http-2, 2024) was used to measure diameter and length of the ZnO nanowire arrays grown on the ITO coated PET substrates. Time-dependent electrical voltage measurements were analyzed with the B2902B Precision Source / Measurement Unit (2 ch, 100 fA) system integrated into the Ambios/Quesant Q-Scope Atomic Force Microscope AFM device. Measurements on AFM system were implemented that scanning type/angle; Z type/90˚, scanning rate; 0.25 Hz; setpoint: 0 V and 40 µm x 40 µm scanning area. In the system interface created by B2902B Precision Source, voltage compliance was optimized as 5 V and current compliance was optimized as 0.1 A. In this integrated system, 50 measurements of 50 ms (milliseconds) were taken every 60 ms in the x direction (laterally) over the piezoelectric ZnO nanowire structures on the sample surface with a platinum-coated AFM probe/tip (Type Radius < 30 nm). The AFM probe cantilever structure has a constant force of 2 N m^{-1}. 50 measurements were enforced at least 5 times from various parts of the sample surface and graphed, and the amplitude formations were calculated from the maximum/minimum piezoelectric potential voltage difference. Bending of the ZnO nanowire created positive potential on the tensile side and negative potential on the compression side. Experimentally, when the AFM probe was scanned over aligned nanowire arrays, the corresponding output voltage along the resulting force was simultaneously recorded.

2.3. Results and Discussions

The appropriate temperature required for the oxidation of zinc acetate on the ITO coated PET substrate is critical for the formation of the seed layer. Therefore, stepwise TG analysis was performed for zinc acetate dihydrate to obtain appropriate oxidation temperature for ITO coated PET substrate. The weight loss vs. temperature graph of zinc acetate dihydrate given in Figure 2.6. Two moles of water (16.8% wt.) move away from the structure up to 100°C. Then the decomposition of the zinc acetate to zinc oxide begins at 187°C. Approximately 3 hours later decomposition was completed with 48% weight loss at 200°C. These decomposition steps are consistent with Sreekanth's study (Sreekanth et al., 2017), and it has also been proven that zinc oxide layer can be obtained at 200°C if oxidation process is applied for 3 hours.

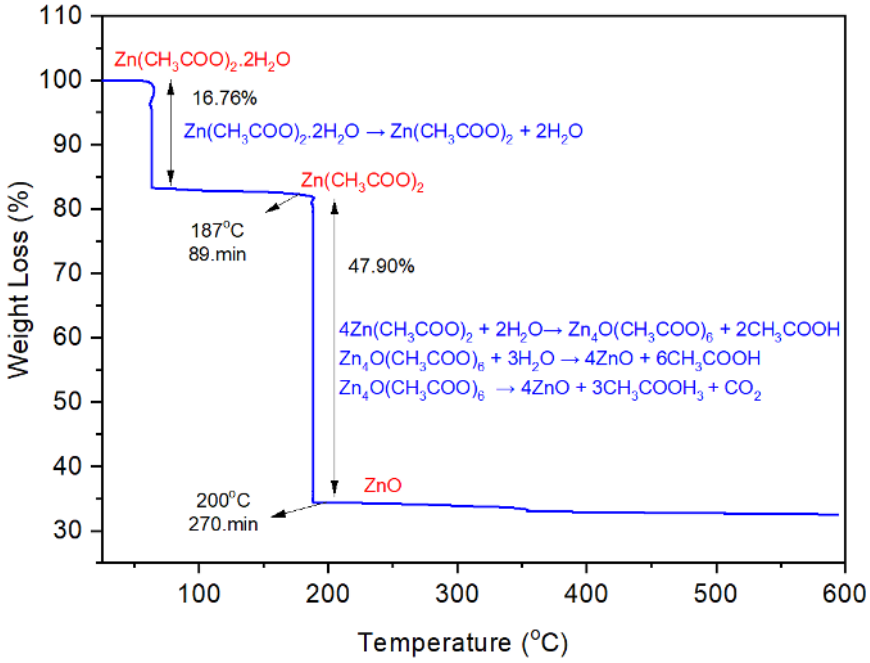

Figure 2.6. *Stepwise-TG analysis of zinc acetate dihydrate*

XRD, SEM, and EDX analyses were performed on the powder sample obtained from TGA. Examination of the XRD pattern shown in Figure 2.7 reveals diffraction peaks at 2θ values of 31.9°, 34.5°, and 36.4°, corresponding to the (100), (002), and (101) planes of the hexagonal ZnO structure, respectively. EDX analyses confirmed that the resulting powder contained 80.34% Zn-19.66% O by weight, and 50% Zn-50% O by atomic, confirming the formation of the ZnO structure. Based on the TGA data, it was concluded that the oxidation process applied during the seed layer coating step can be effectively conducted at 200 °C for 3 hours, resulting in the formation of a ZnO layer on the substrate surface.

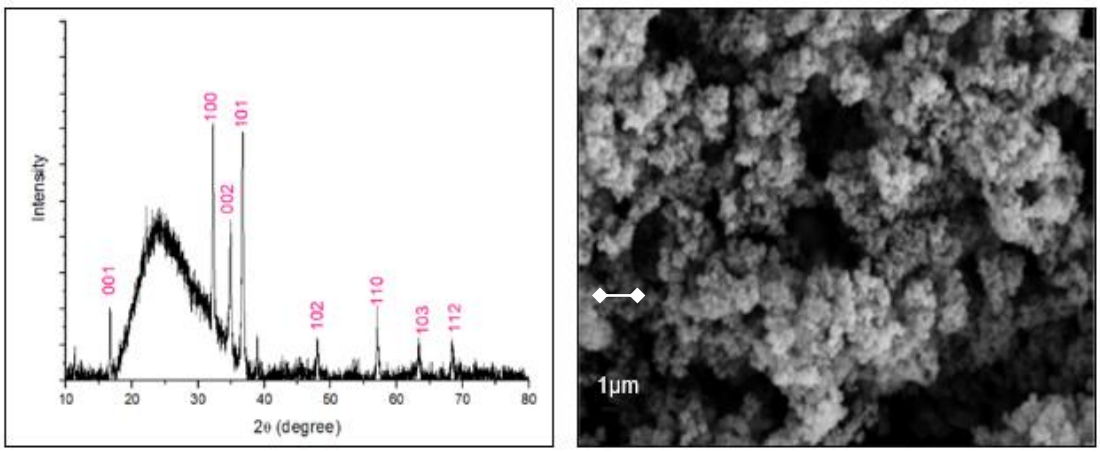

Figure 2.7. *XRD graph and SEM image of the ZnO powder obtained from Stepwise-TGA*

2.3.1. Effect of solvent type and solution concentration on the seed layer

After determining the appropriate oxidation temperature and time of ZnO, the surfaces of the ITO coated PET substrates were spin-coated with zinc acetate dihydrate seed solutions prepared with different alcohols. Heat treatment was applied to the coated substrates at 200°C for 3 hours to allow the formation of a ZnO seed layer on the surface. XRD plots of untreated ITO coated PET substrates and ITO coated PET substrates coated with seed solutions prepared with different alcohols are shown in Figure 2.8. The diffraction peak for the PET substrate was obtained at 2θ = 26° for all samples. A closer examination of the 30°–40° range in the inset graphs (b–d) shows diffraction peaks corresponding to the (100), (002), and (101) planes of ZnO with a hexagonal wurtzite structure in the seed layer coated substrates. However, in Figure 2.8 (b), the diffraction peak corresponding to the (002) plane appears more intense for the substrate coated with the seed solution prepared using methanol (P-M20). This suggests that the c-axis orientation is more pronounced in the substrate coated with the methanol-based seed solution compared to the others.

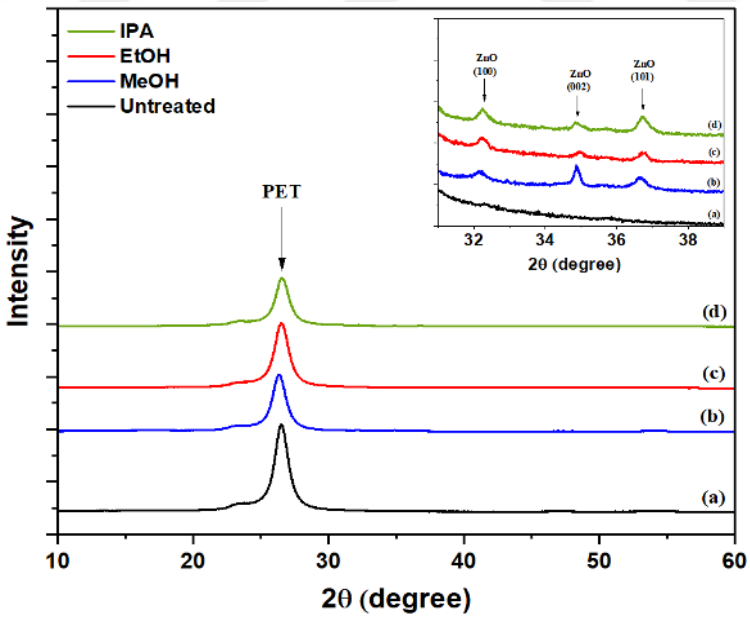

Figure 2.8. *XRD graphs of a) untreated ITO/PET substrate, b) P-M20 c) P-E20, d) P-I20*

Substrates coated with seed layers were placed in aqueous solutions prepared with equimolar (25 mM) zinc nitrate hexahydrate and HMTA and hydrothermal synthesis applied at 90°C for 6 hours. XRD graphs of the ZnO structures grown on the substrates at the end of the hydrothermal synthesis are given in Figure 2.9. As shown in the graphs,

ZnO structures were grown on the surfaces of all substrates. However, the diffraction pattern of the substrate without a seed layer (Figure 2.9 a) indicates that the ZnO structures lack a specific orientation and grow randomly. In these graphs, diffraction peaks belonging to all planes of ZnO with hexagonal wurtzite structure were obtained. In contrast, in the cases of P-M20-25.0-6 and P-E20-25.0-6 (Figure 2.9 b and Figure 2.9 c), only the diffraction peak corresponding to the (002) plane is present, suggesting that the ZnO structures are oriented along the c-axis. Moreover, the (002) peak of the ZnO structures grown on the substrate coated with the methanol-based seed solution (P-M20-25.0-6) appears more intense, confirming that c-axis orientation is more effectively achieved. This result is consistent with the graph presented in Figure 2.8 (b) and also study of Hosono et. al (Hosono et al., 2004). On the other hand, a diffraction pattern similar to that of the untreated substrate was observed for the sample coated with the IPA-based seed solution (P-I20-25.0-6, Figure 2.9 d), indicating that the ZnO structures again grew randomly on the surface.

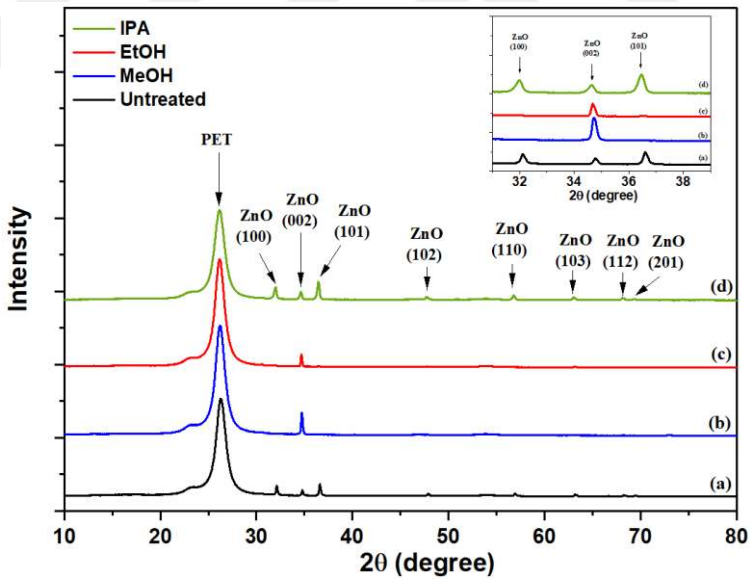

Figure 2.9. *XRD graphs of ZnO nanowires synthesized via hydrothermal method on a) untreated ITO/PET substrate, b) P-M20-25.0-6, c) P-E20-25.0-6, and d) P-I20-25.0-6*

Top view SEM micrographs of ZnO nanowires grown on substrates coated with seed solutions prepared with different solvents are given in Figure 2.10. On the untreated ITO coated PET substrate (Figure 2.10 a), the ZnO nanowires are not oriented along the c-axis on the substrate surface. Instead, a random orientation occurs. The diameters of the nanowires were measured using the Image J software, yielding an average value of

340 ± 90 nm. In the P-M20-25.0-6 and P-E20-25.0-6 samples (Figure 2.10 b and Figure 2.10 c), the ZnO nanowires were observed to exhibit good c-axis orientation. The diameters of the P-M20-25.0-6 and P-E20-25.0-6 samples were measured 91 ± 19 nm and 96 ± 21 nm, respectively. In the P-I20-25.0-6 sample, inhomogeneous ZnO nanowire structures with random orientation were observed. The diameters of the P-I20-25.0-6 sample were measured 65 ± 41 nm. These morphologies observed in the SEM micrographs are quite consistent with the diffraction patterns obtained in the XRD graphs presented in Figure 2.9. A homogeneous and consistent seed layer was obtained on substrate surfaces coated with seed solutions prepared with ethanol and methanol, which enabled the growth of well-oriented ZnO nanowires along the c-axis. However, the seed solutions prepared with IPA resulted in a nonhomogeneous seed layer on the substrate surface, leading to the growth of ZnO nanowires without the desired orientation. These results demonstrate the critical importance of the seed layer for the formation of a homogeneous c-axis-oriented ZnO nanowire array on the substrate surface.

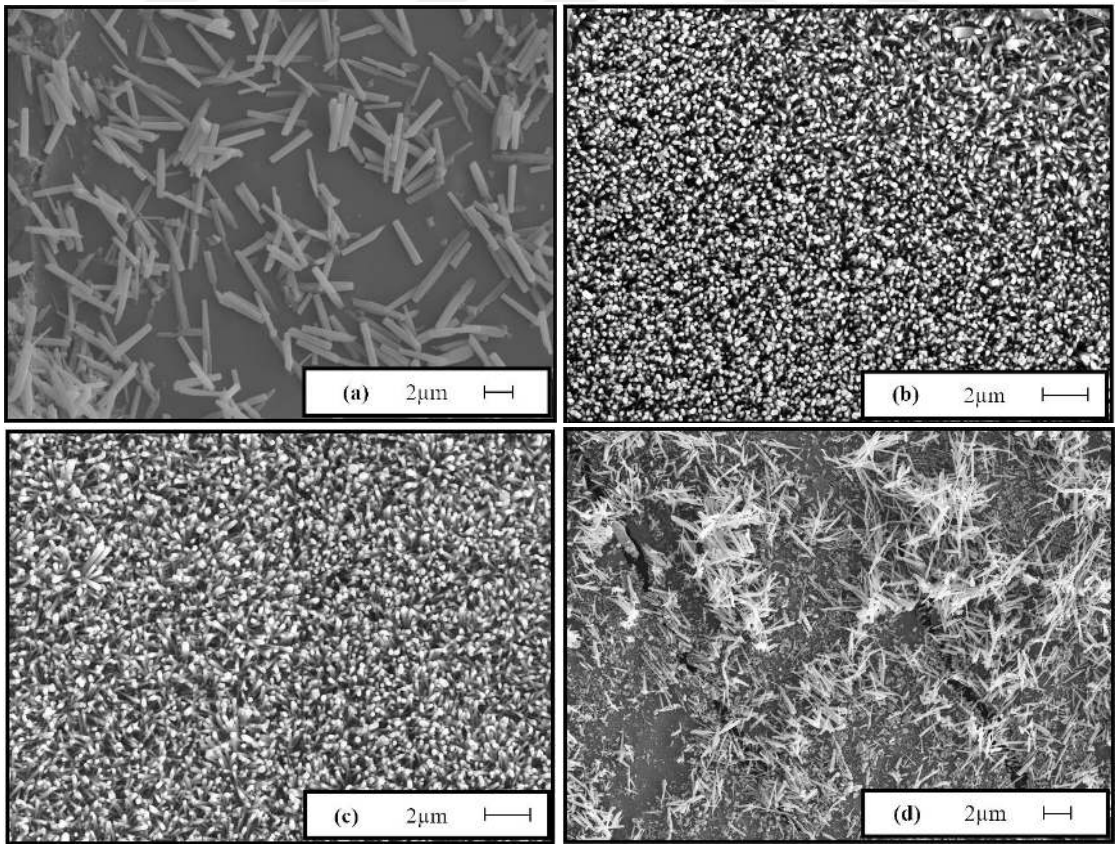

Figure 2.10. *Top view* SEM micrographs of *a) untreated ITO/PET substrate, b) P-M20-25.0-6, c) P-E20-25.0-6, and d) P-I20-25.0-6*

Since well-oriented ZnO structures along the c-axis were obtained on substrate surfaces coated with methanol-based seed solutions, it was decided to proceed with methanol-prepared seed solutions in the subsequent studies. In the second step, the effect of seed solution concentration on ZnO nanowires was investigated, and zinc acetate dihydrate/methanol seed solutions were obtained at different concentrations (80 mM - 500 mM). The substrate surfaces were coated with prepared seed solutions by spin coating, and the coated substrates were then heat treated. Figure 2.11 shows the XRD graphs of the substrates coated with seed solutions at different concentrations. Diffraction peaks corresponding to the (100), (002), and (101) planes of hexagonal wurtzite ZnO were observed on all substrate surfaces. On the substrate coated with the 80 mM seed solution (P-M80), these peaks appeared with relatively low intensity. At a concentration of 100 mM (P-M100), only the diffraction peak corresponding to the (002) plane was observed with higher intensity, while the (100) and (101) peaks disappeared, indicating the formation of a c-axis oriented ZnO seed layer. However, when the concentration increased beyond 100 mM (P-M300 and P-M500), the (002) peak intensity decreased, the peak width broadened, and additional diffraction peaks corresponding to the (100) and (101) planes reappeared. This behavior can be attributed to the higher Zn^{2+} ion concentration at high solution concentrations, which promotes the formation of multiple seed crystals on the substrate surface. At the same time, at higher concentrations, the seed layer becomes thicker and rougher. This causes multidirectional nucleation of ZnO on the surface, disrupting its orientation along the c-axis and promoting multidirectional growth.

After the seed layer coating process, ZnO structures were synthesized on the substrates via hydrothermal growth at 90 °C for 6 hours. The corresponding XRD patterns are shown in Figure 2.12. For the ZnO structures grown on substrates coated with 80 mM and 100 mM seed solutions (P-M80-25.0-6 and P-M100-25.0-6), only the diffraction peak corresponding to the (002) plane was observed, confirming the formation of well-oriented ZnO nanowires along the c-axis. In contrast, the samples coated with 300 mM and 500 mM seed solutions (P-M300-25.0-6 and P-M500-25.0-6) exhibited additional diffraction peaks corresponding to the (100) and (101) planes, indicating random growth of ZnO nanowires. As also shown in Figure 2.11, the weaker orientation of the seed layer formed at higher concentrations resulted in the random orientation of ZnO nanowires during hydrothermal growth.

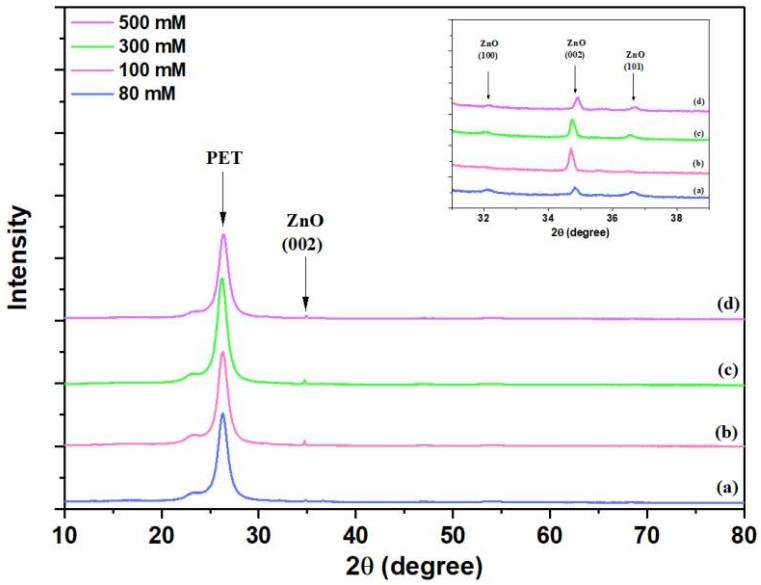

Figure 2.11. *XRD graphs of a) P-M80, b) P-M100, c) P-M300 and d) P-M500*

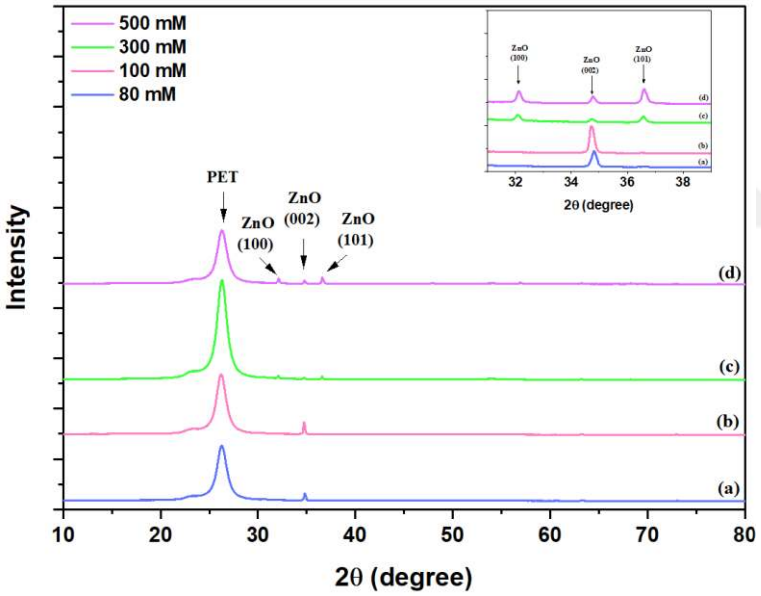

Figure 2.12. *XRD graphs of a) P-M80-25.0-6, b) P-M100-25.0-6, c) P-M300-25.0-6 and d) P-M500-25.0-6*

Top view SEM micrographs of ZnO nanowires grown on substrates coated with seed solutions prepared with different concentrations are given in Figure 2.13. The best orientation was observed in samples P-M80-25.0-6 and P-M100-25.0-6 (Figure 2.13 a and Figure 2.13 b). The diameters of the P-M80-25.0-6 and P-M100-25.0-6 samples were measured 66 ± 15 nm and 82 ± 19 nm, respectively. In P-M300-25.0-6 and P-M500-25.0-6 samples, irregularities occurred in the formation of the nanowires, and the homogeneity in the diameter distribution of the ZnO nanowires was disrupted. The

diameters of the P-M300-25.0-6 and P-M500-25.0-6 samples were measured 92 ± 39 nm and 98 ± 17 nm, respectively. This was caused by the increased concentration of seed solutions. The increase in seed solution concentration enhanced the nucleation density on the substrate surface, leading to the formation of ZnO nanowires with a denser yet more random orientation. Simultaneously, the higher nucleation density promoted interconnection or agglomeration among the nanowires.

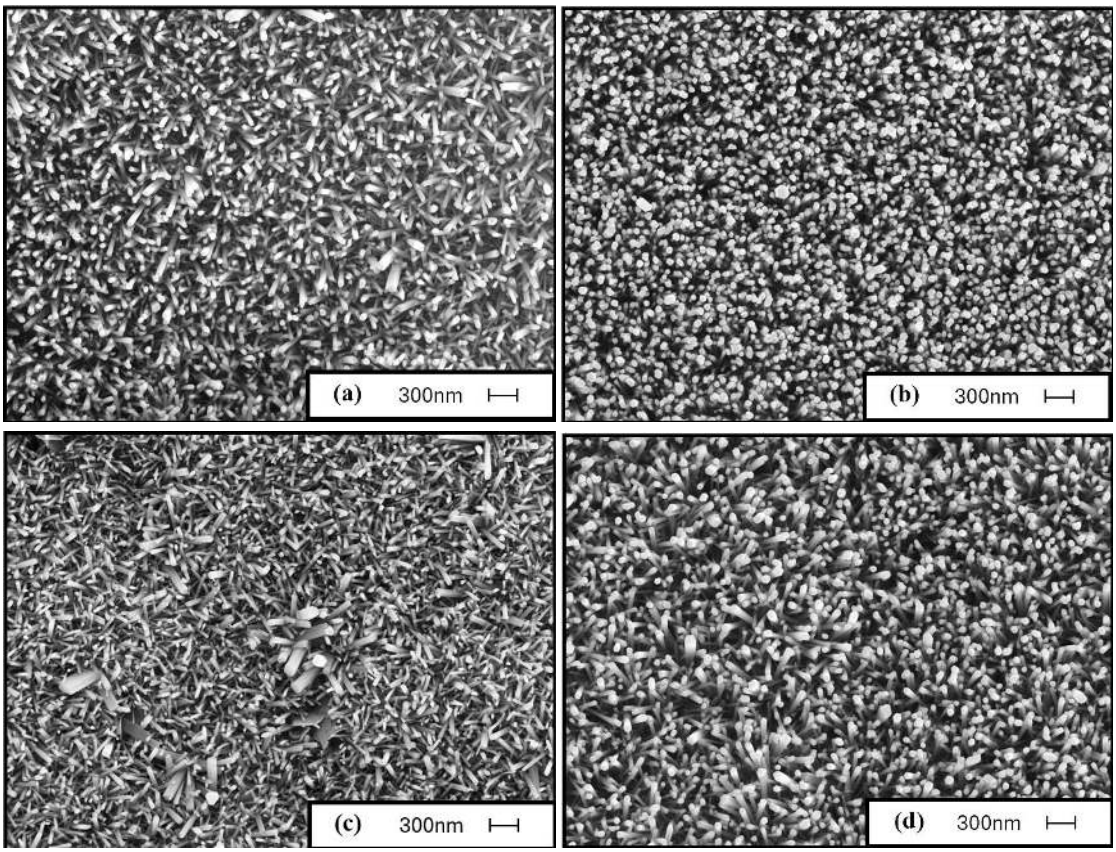

Figure 2.13. *Top view* SEM micrographs of *a) P-M80-25.0-6, b) P-M100-25.0-6, c) P-M300-25.0-6 and d) P-M500-25.0-6*

2.3.2. Effect of Zn^{2+} ion concentration on ZnO nanowire arrays

To determine the effect of Zn^{2+} ion concentration on ZnO nanowire arrays, the concentration was varied from 6.25 to 50 mM while keeping synthesis time and temperature constant as 6 h and 90°C, respectively. Figure 2.14 shows the XRD graphs of the samples obtained with different Zn^{2+} ion concentration. Examination of the XRD patterns revealed that the ZnO nanowires with the best orientation along the (002) plane was obtained in the P-M100-12.5-6 and P-M100-25.0-6 samples. Based on the

intensities of the (002) diffraction peaks, the P-M100-25.0-6 sample exhibited the highest degree of c-axis alignment. In contrast, the P-M100-6.25-6 and P-M100-50.0-6 samples showed diffraction peaks corresponding to the (100) and (101) planes in addition to the (002) plane, indicating less preferential orientation. These results demonstrate that ZnO nanowires grown at very low or very high solution concentrations do not achieve good c-axis alignment and instead exhibit random orientation.

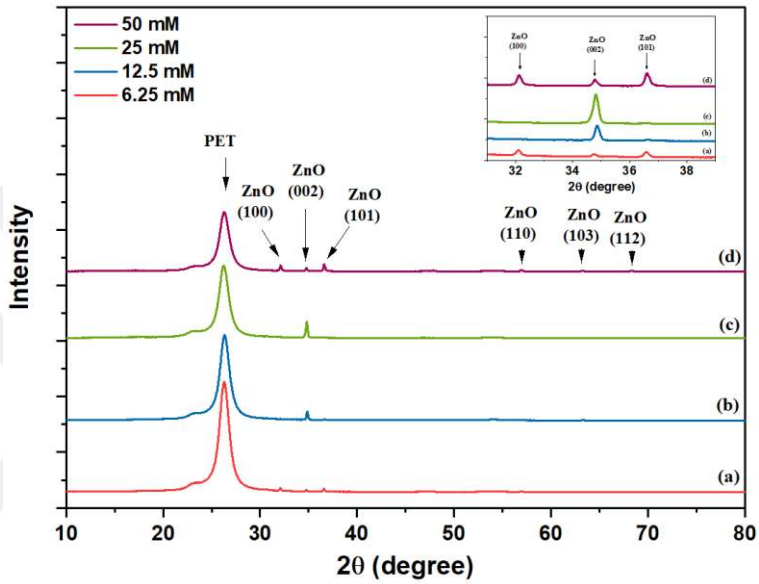

Figure 2.14. *XRD graphs of a) P-M100-6.25-6, b) P-M100-12.5-6, c) P-M100-25.0-6 and d) P-M100-50.0-6*

Top view SEM micrographs of ZnO nanowires grown in solutions of varying concentrations are shown in Figure 2.15. In the P-M100-6.25-6 sample with the lowest concentration, randomly oriented and thin nanowires were observed (Figure 2.15 a). As the concentration increased to 12.5 mM (P-M100-12.5-6), ZnO nanowires exhibited relatively improved orientation (Figure 2.15 b). The highest degree of c-axis alignment was achieved in the P-M100-25.0-6 sample prepared at 25 mM (Figure 2.15 c). Conversely, in the P-M100-50.0-6 sample with the highest concentration, disordered ZnO nanowire structures and the formation of star-like ZnO structures were observed (Figure 2.15 d). The diameters of the P-M100-6.25-6, P-M100-12.5-6, P-M100-25.0-6, and P-M100-50.0-6 samples were measured 57 ± 11 nm, 62 ± 15 nm, 82 ± 19 nm, and 172 ± 85 nm, respectively. Consistent with results reported in the literature (Ghayour et al., 2010), an increase in solution concentration was found to result in a corresponding increase in nanowire diameters.

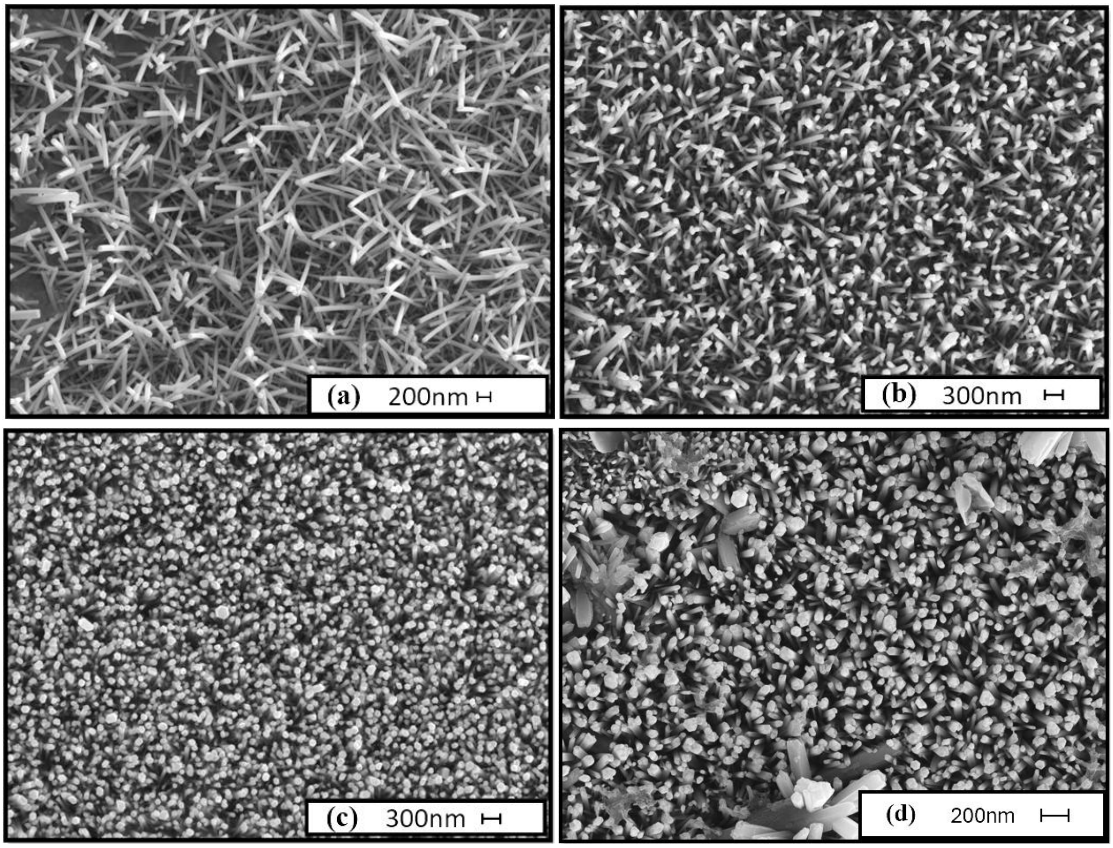

Figure 2.15. *Top view SEM micrographs of a) P-M100-6.25-6, b) P-M100-12.5-6, c) P-M100-25.0-6, and d) P-M100-50.0-6*

2.3.3. Effect of hydrothermal synthesis time on ZnO nanowire arrays

The hydrothermal synthesis time directly determines the morphology, and crystalline orientation of ZnO nanowires. This time parameter affects not only the growth rate but also the crystallinity and structural alignment, making it a critical factor in piezoelectric performance. Figure 2.16 shows the XRD patterns of ZnO nanowires grown on ITO-coated PET substrates as a function of hydrothermal synthesis time, with the solution concentration (25.0 mM) and synthesis temperature (90 °C) kept constant. In all samples, only the diffraction peak corresponding to the (002) plane was observed. A low-intensity peak appeared after 3 hours of synthesis. For short-term hydrothermal treatments (< 3 hours), the diffusion of Zn^{2+} and OH^- ions to nucleation sites on the substrate surface is limited (Leprince-Wang, 2015). Under these conditions, nucleation dominates, leaving insufficient time for nanowire growth. Consequently, ZnO structures tend to be short, low-density, and poorly crystalline. This is reflected in the XRD patterns by the low intensity of the characteristic (002) peak and the occasional presence of (100) and (101) peaks corresponding to other orientations. The intensity of the

diffraction peak corresponding to the (002) plane increased with longer synthesis times. When the hydrothermal synthesis exceeds 3 hours, conditions become favorable for the directional growth of ZnO nanowires. During this period, Zn^{2+} and OH^- ions are incorporated into the ZnO crystals in a controlled manner, promoting c-axis-oriented crystal growth. As shown in the XRD patterns in Figure 2.16 (b-d), the (002) peak becomes dominant, while diffraction peaks corresponding to other planes weaken or disappear. However, prolonging the synthesis time beyond 12 hours can induce morphological instabilities and deterioration of crystal orientation. Over extended periods, the ion concentration in the growth solution decreases, slowing the growth rate and initiating recrystallization processes such as Ostwald ripening. Consequently, some ZnO nanowires may thicken, bend, or merge, which is also reflected in the XRD patterns: the (002) peak intensity may decrease or broaden, and peaks corresponding to the (100) and (101) planes may reappear.

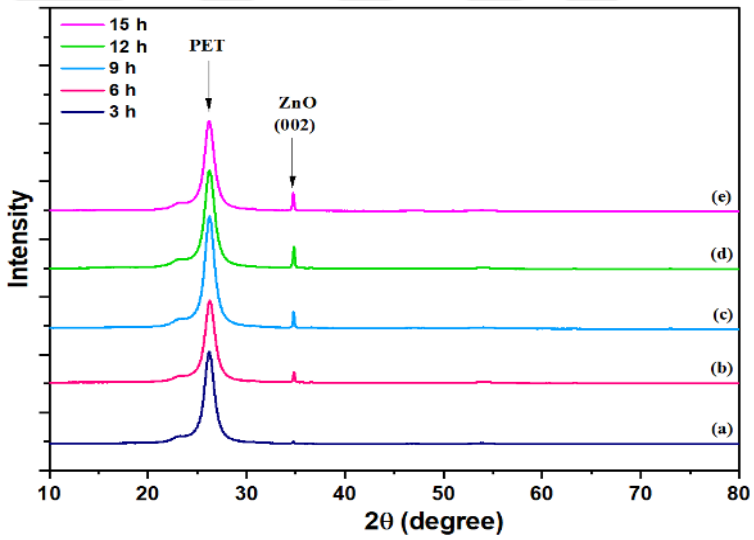

Figure 2.16. *XRD graphs of a) P-M100-25.0-3, b) P-M100-25.0-6, c) P-M100-25.0-9, d) P-M100-25.0-12 and e) P-M100-25.0-15*

Cross-sectional SEM micrographs of ZnO nanowires grown at different hydrothermal synthesis times are presented in Figure 2.17. The diameters of the P-M100-25.0-3, P-M100-25.0-6, P-M100-25.0-9, P-M100-25.0-12, and P-M100-25.0-15 samples were measured 245 ± 45 nm, 83 ± 22 nm, 84 ± 25 nm, 71 ± 17 nm, and 74 ± 23 nm respectively. The lengths of the P-M100-25.0-3, P-M100-25.0-6, P-M100-25.0-9, P-M100-25.0-12, and P-M100-25.0-15 samples were measured 0.405 ± 0.115 µm, 0.703 ± 0.181 µm, 0.892 ± 0.150 µm, 1.221 ± 0.370 µm, and 1.267 ± 0.248 µm

respectively. The length of the nanowires increased rapidly with synthesis time, up to 12 hours. However, no significant increase in length was observed for samples synthesized for more than 12 hours. This behavior may be attributed to the depletion of Zn^{2+} ions in the growth solution during prolonged hydrothermal synthesis.

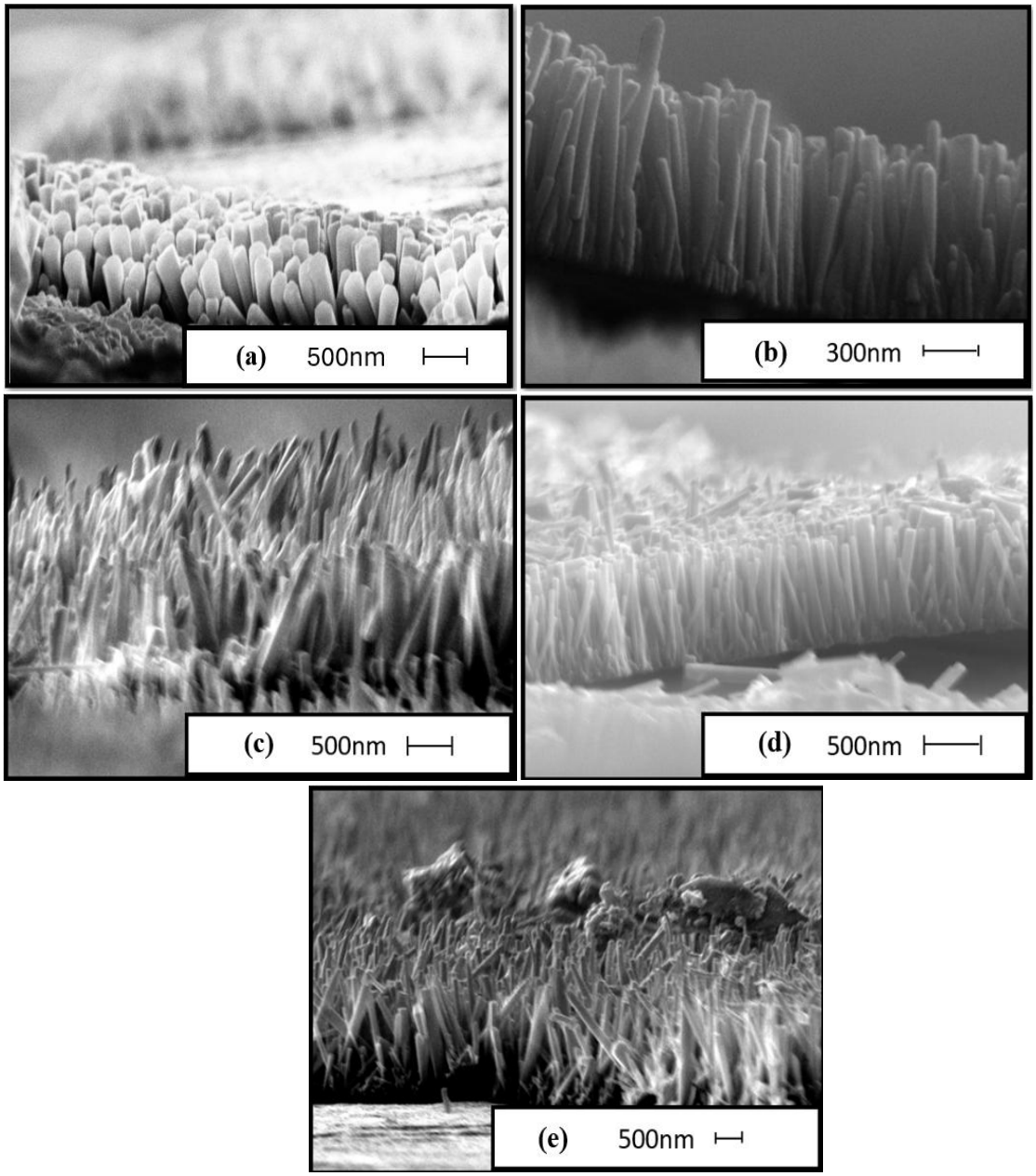

Figure 2.17. *C*ross-section SEM micrographs of *a) P-M100-25.0-3, b) P-M100-25.0-6, c) P-M100-25.0-9, d) P-M100-25.0-12 and e) P-M100-25.0-15*

2.3.4. Electrical output voltage generation capability of ZnO nanowire arrays

Time-dependent electrical voltage measurements of ZnO nanowires grown on ITO coated PET substrates under varying hydrothermal synthesis conditions were analyzed with the B2902B Precision Source / Measurement Unit (2 ch, 100 fA) system integrated into the Ambios/Quesant Q-Scope Atomic Force Microscope AFM device. Measurements were repeated five times for each sample. Figures 2.18 a and Figure 2.18 b show the measurement graphs for P-M100-12.5-6 and P-M100-25.0-6 samples, respectively. Table 2.2 presents the output voltage values of ZnO nanowires synthesized under different hydrothermal conditions. It can be seen that the output voltages measured after bending individual nanowires with an AFM tip were relatively low and showed no significant differences among the samples. For instance, the output voltage was 0.21 mV for P-M100-6.25-6, 0.26 mV for P-M100-25.0-6, and 0.31 mV for P-M100-25.0-9.

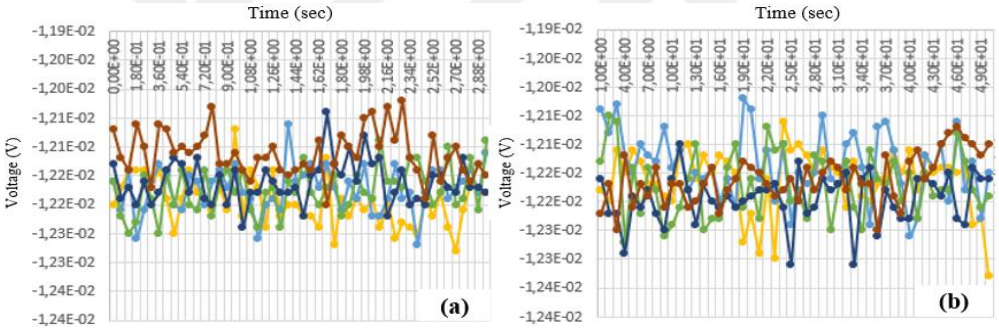

Figure 2.18. *Output voltage graphs of ZnO nanowires with AFM/semiconductor parameter analyzer (a) P-M100-12.5-6, (b) P-M100-25.0-6*

Table 2.2. *Output voltage values of ZnO nanowires according to hydrothermal synthesis conditions*

Sample Code	Seed Layer	Hydrothermal Growth		Output Voltage
	Concentration (mM)	*Concentration (mM)*	*Growth Time* (h)	(mV)
P-M100-6.25-6	100.0	6.25	6	0.21
P-M100-12.5-6	100.0	12.5	6	0.24
P-M100-25.0-6	100.0	25.0	6	0.26
P-M100-50.0-6	100.0	50.0	6	0.21
P-M100-25.0-3	100.0	25.0	3	0.19
P-M100-25.0-9	100.0	25.0	9	0.31
P-M100-25.0-12	100.0	25.0	12	0.27
P-M100-25.0-15	100.0	25.0	15	0.23

The relatively low output voltage values were attributed to two main factors. First, the heat treatment applied during seed layer formation may have adversely affected the electrical conductivity of the ITO-coated substrates. To examine this, SEM analyses were performed on ITO-coated substrates with and without heat treatment. The top-view SEM micrographs shown in Figure 2.19 reveal that heat treatment at 200 °C for 3 h induced cracks in the ITO layer. These cracks increased the internal resistance of the conductive layer and reduced its conductivity, leading to decreased output voltage from the nanowires. Second, some of the ZnO nanowires grown via hydrothermal synthesis were observed to detach from the substrate surface. Top-view SEM micrographs at lower magnifications (Figure 2.20) indicate that the ZnO nanowires did not grow uniformly across the substrate surface, with localized detachment occurring. Consequently, nanowires that grew non-uniformly and exhibited a tendency to detach physically from the surface inevitably produced lower voltage outputs.

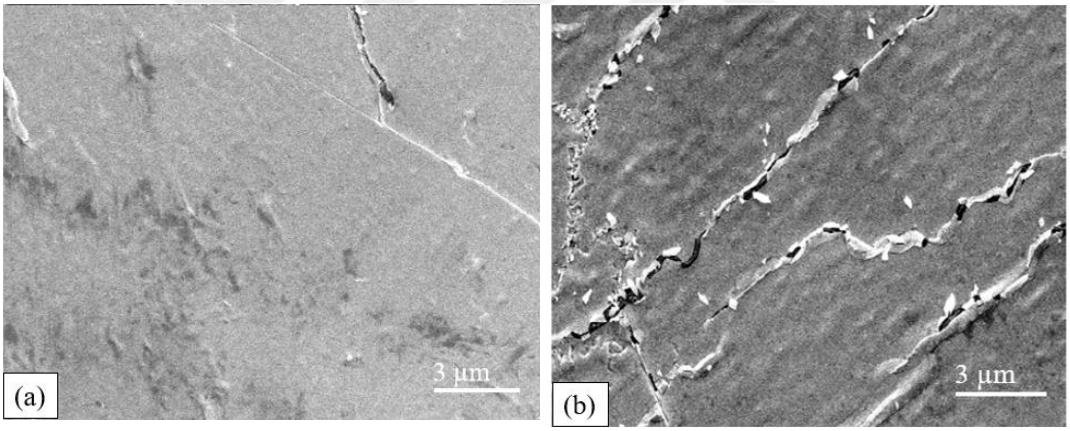

Figure 2.19. *Top view SEM micrographs of a) ITO/PET before heat treatment, and b) ITO/PET after heat treatment at 200°C for 3 h*

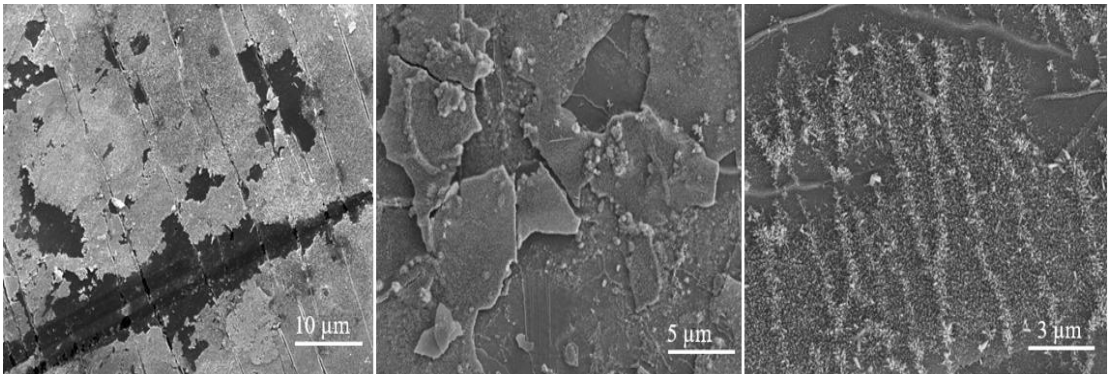

Figure 2.20. *Top view SEM micrographs of the samples at low magnifications after hydrothermal synthesis*

2.4. Conclusions

In this study, the effects of hydrothermal synthesis parameters on ZnO nanowire arrays grown on flexible ITO coated PET substrates were systematically investigated. It was found that a 3-hour heat treatment at 200 °C can be applied to produce a solution-based seed layer on polymer-based substrates such as PET. Furthermore, the seed layer was identified as crucial for obtaining c-axis oriented ZnO nanowire arrays on the substrate. Among the tested options, a seed solution prepared with methanol provided the most continuous and homogeneous seed layer. The concentration of the seed solution was also found to significantly influence the density and orientation of the ZnO nanowire arrays. High-concentration seed solutions disrupted the orientation of the ZnO nanowires and promoted agglomeration due to contact between adjacent nanowires. Therefore, to achieve well-oriented and uniform nanowire arrays, the seed solution concentration should not exceed 100 mM.

Another parameter influencing the ZnO nanowire arrays was the Zn^{2+} ion concentration in the growth solution. It was observed that nanowire arrays grown at very low or very high concentrations exhibited random orientation, whereas ZnO nanowire arrays grown at 12.5 mM and 25.0 mM showed well-aligned structures. Low concentrations, in particular, led to low-density nanowire arrays, causing individual nanowires to tilt in various directions and thus reducing overall alignment. Conversely, higher concentrations resulted in denser nanowires, but agglomeration occurred, contributing to deterioration in orientation. Hydrothermal synthesis duration was also found to significantly affect nanowire dimensions. Rapid crystal growth occurred during the first 12 hours, after which the growth rate decreased significantly due to depletion of Zn^{2+} ions in the precursor solution. However, it is believed that it may be possible to obtain longer and denser nanowire arrays over longer synthesis times if the growth solution is refreshed at regular intervals.

Although ZnO nanowire arrays grown on ITO coated PET substrates under varying hydrothermal synthesis conditions exhibited different morphological characteristics, no significant differences were observed in the output voltage values measured using an AFM semiconductor parameter analyzer, and the measured voltages were relatively low. This is attributed to several factors. First, the low quality of the ITO coating on the PET substrate may have caused cracks to form during heat treatment at oxidation stage, increasing the internal resistance of the conductive layer. Second, the

nanowire arrays may not have established proper contact with the conductive substrate, or they may have been broken or fractured during AFM scanning.

Considering the literature and experimental data, it is evident that significant challenges remain in achieving homogeneous, high-density, and continuous growth of ZnO nanowire arrays on conductive substrates, while maintaining structural and mechanical compatibility with the substrate material. In low-cost and scalable techniques, particularly hydrothermal methods, the lack of comprehensive optimization of synthesis parameters complicates reproducibility and standardization of the growth process. These limitations directly affect the morphological and electrical integrity of the resulting nanostructures, thereby reducing the overall efficiency of the system.

Consequently, the mass production of high-efficiency and stable ZnO nanowire based piezoelectric nanogenerator modules at an industrial scale is not yet feasible with current techniques. To make ZnO nanowire-based systems suitable for commercial applications, comprehensive optimization of parameters such as substrate selection, surface modification, and solution chemistry is essential, particularly during the growth process.

3. HYDROTHERMAL SYNTHESIS OF 2-D ZnO NANOWALL ARRAYS

3.1. Introduction

Wearable electronics, developed with the rapid evolution of technology, have penetrated our lives, and become an integral part of our daily lives. Increasing use of such devices has also revealed a growing need for energy. Currently this energy demand is predominantly met by traditional batteries. However, traditional batteries pose certain limitations, particularly in terms of sustainability and comfort when it comes to wearable electronics. Despite efforts to develop flexible batteries with innovative technologies, the need to periodically recharge these batteries and their limited-service life have directed researchers toward other alternative renewable solutions. Renewable energy systems are described by their potential to convert diverse forms of ambient energy into electrical energy. Piezoelectric nanogenerators (PENGs), which can convert readily accessible mechanical energy in the environment into electrical energy, have attracted attention as novel devices that can be utilized in wearable systems.

The most efficient energy conversion in piezoelectric systems is achieved with lead-containing structures. However, lead is among the most harmful elements whose use is restricted within the scope of the Restriction of Hazardous Substances Directive 2002/95/EC, adopted by the European Council in 2003 (Directive, 2013). As a result, research on piezoelectric structures has shifted towards lead-free systems (Coban Tetik et al., 2023). Among lead-free systems, ceramic structures such as $BaTiO_3$, KNN, bismuth titanate, and ZnO are included. The biggest disadvantage of the ceramics in wearable systems is that they are brittle and rigid. Considering these factors, flexible nanogenerator designs tend to prefer 1-D nanorod, nanotube, nanobelt, needle-like structure, or 2-D nanowall, nanosheet structures rather than bulk and film structures. These structures exhibit the potential to generate electrical output by bending without breaking under applied mechanical force.

In this context, ZnO is a widely preferred material for development of novel PENG designs in the alternative energy resource industry. ZnO is an inorganic compound with properties such as a wide direct band gap (3.37 eV), high exciton binding energy (60 meV), (Look, 2001; Klingshirn, 2007) high light emission, mechanical and chemical stability. ZnO, with its hexagonal wurtzite crystal structure, also exhibits favorable piezoelectric properties due to the inherent polarization along its c-axis. The wurtzite structure belongs to the C_{6V}^4 Schoenflies notation and the $P6_{3mc}$

Hermann-Mauguin notation space group. Crystal structures in this group do not exhibit centrosymmetric properties, so negative and positive charges do not overlap. In a ZnO crystal with wurtzite structure, oppositely charged ion planes with positive (0001)-Zn and negative (000$\bar{1}$)-O spontaneously form a polarization on the c axis. This polarization gives the ZnO piezoelectric property (Wang, 2004; Özgür et al., 2005; Bagga, Akhtar and Mishra, 2018; Pandey et al., 2021). Thanks to all these unique properties, it finds a wide range of applications such as varistors (Pearton et al., 2004), solar cells (Baxter et al., 2006), gas sensors (Hsueh et al., 2007), light-emitting diodes (Chen et al., 2010), and nanogenerators (Wang et al., 2007; Gullapalli et al., 2010; Sun et al., 2013).

From past to present, ZnO structures with different morphologies have been used in lead-free piezoelectric nanogenerator designs. These structures include bulk, thin films, nanorods, nanobelts, nanowires and nanowalls (Kaur and Singh, 2019). These ZnO nanostructures have been synthesized using methods such as chemical vapor deposition (CVD) (Lupan et al., 2010), physical vapor deposition (PVD) (Wang et al., 2005), pulsed laser deposition (PLD) (Sun, Fuge and Ashfold, 2006), electrochemical deposition, and hydrothermal or solvothermal synthesis (Vayssieres et al., 2001; Greene et al., 2003). In CVD, PVD, and PLD production methods, specialized equipment is required for nanostructure fabrication, and these methods are relatively costly due to the need for high-purity raw materials. Additionally, nanostructure production takes place at elevated temperatures (> 900 °C). Although very well aligned, highly crystalline ZnO nanostructures can be produced by these methods, a limited number of substrate materials such as silicon, quartz and sapphire can be used because they operate at elevated temperatures. It is not suitable for the fabrication of ZnO nanostructures on flexible, polymer-based substrates (Pan and Wang, 2001; Lee et al., 2003; Zhang, Russo and Mao, 2005; Lupan et al., 2010). Considering all these, it can be concluded that the most suitable method to grow ZnO nanostructure on flexible substrates is the hydrothermal method. Because the hydrothermal synthesis method can be applied at lower temperatures (< 100 °C), is low-cost, suitable for large area coverage and has environmentally friendly features (Leprince-Wang, 2015).

In recent years, nanowire structures have gained importance in wearable and flexible piezoelectric nanogenerator applications due to their high flexibility and ability to deform under low forces. However, it has been observed that there are issues of homogenization and repeatability in the production of ZnO nanowires, especially

through the hydrothermal synthesis method, which has hindered commercialization. On the other hand, studies have indicated that ZnO nanowall structures exhibit higher structural stability and power generation performance compared to ZnO nanowire structures, with better mechanical durability. ZnO nanowall structures, mostly used in sensor applications due to their high surface area-to-volume ratio, have also been used in piezoelectric nanogenerator applications in limited studies. These studies report that the use of ZnO nanowalls in piezoelectric nanogenerator designs can provide higher electrical outputs compared to ZnO nanowire-based nanogenerators. Kaur and Singh (Kaur and Singh, 2020) compared the piezoelectric performances of ZnO nanowire and nanowall structures produced by hydrothermal synthesis method (0.1 M, 90 °C and 4 h), and the highest current (8 nA) and voltage (226 mV) values were obtained in nanowall structures. In nanowires, the current value was 5 nA, and the voltage value was 185 mV. The bending and compression capacities of ZnO nanowires decreased when the nanowires were densely packed, resulting in lower piezoelectric outputs. However, ZnO nanowall structures, with sufficient interstitial voids and interactions between deforming structures during mechanical deformation, yielded higher piezoelectric outputs. Furthermore, ZnO nanowall-based nanogenerators were found to have the potential to generate DC currents. In a study by Kim et al. (Kim et al., 2013) the hydrothermal synthesis stage (25 mM, 95 °C, and 3 h) led to the formation of a Zn:Al layered double hydroxide (LDH) layer between the ZnO nanowalls and an aluminum substrate. It was stated that this LDH layer acts as anionic clay, anion scavenger and exchanger, and a capacitor with poor conductivity. Therefore, it was believed that the LDH layer formed during the synthesis played an important role in generating direct current (6.5 $\mu A.cm^{-2}$).

ZnO nanowall structures can be produced in two simple methods on different substrates by hydrothermal synthesis method. The first method is to etch the ZnO nanorods synthesized on the ZnO seed layer with aqueous KOH solution. In this method, nanowall formations are based on selective dissolution of defects in plane (0001) and OH^- ions etch along the c-axis in chemical bath (Liu et al., 2006; Liang et al., 2013). The second technique involves direct nanowall synthesis via direct hydrothermal synthesis on aluminum or aluminum-coated surface (Huang et al., 2013; Iwu et al., 2015). Especially within the scope of the second method, different studies have been carried out for the direct synthesis of ZnO nanowalls via hydrothermal synthesis on

different substrates. In addition to aluminum and Al_2O_3 substrates, attempts have been made to synthesize ZnO nanowalls on substrates such as Cr, Si, Ag, SiC and SiO_2. However, it was concluded that the nanowall structure could only be obtained on aluminum and Al_2O_3 substrates. Based on this understanding, it has been proven that aluminum has a critical role on the formation of the nanowall structure (Nayak et al., 2012; Murillo et al., 2019). In ZnO crystal growth under ideal conditions, the growth rate of direction is expressed as $V_{<0001>} > V_{<01\text{-}10>} > V_{<000\text{-}1>}$ (Li et al., 1999). However, aluminum reacts chemically under alkaline conditions in the presence of amines (e.g., hexamethylene tetra amine, HMTA) to form AlO_2^-, and this ion affects the formation of the nanowall structure by preventing the growth of the ZnO structure in the [0001] direction (Nayak et al., 2012; Tang et al., 2015). In the literature, ZnO nanowall formation on aluminum substrate is explained as follows:

$$(CH_2)_6N_4 + 6H_2O \rightarrow 6HCHO + 4NH_3 \quad (3.1)$$

$$NH_3 + H_2O \rightarrow NH_4^+ + OH^- \quad (3.2)$$

$$Al^{3+} + OH^- \rightarrow Al(OH)_3 + OH^- \rightarrow AlO_2^- \quad (3.3)$$

As stated in Equation 3.1 and Equation 3.2, HMTA used in hydrothermal synthesis forms hydroxyl ions. In addition, aluminum is an amphoteric metal, it can be dissolved into the solution under alkaline conditions and form to Al^{3+} ions. Hydroxyl ions react with Al^{3+} ions formed by dissolution of aluminum, and form AlO_2^- ions as stated in Equation 3.3. AlO_2^- binds to Zn^{2+} terminated surfaces in the growing ZnO crystal. As a result of this bonding occurring in the polar plane (0001), AlO_2^- acts as surface-passivating agents. It causes changes in the growth rates of ZnO crystal planes by suppressing growth in the plane (0001) and promoting lateral growth (Cheng, Zhang and Luo, 2008; Nayak et al., 2012; Huang et al., 2013). At the same time, it was determined that an aluminum layer of at least 100 nm thickness was required for the formation of an effective ZnO nanowall structure. Because it has been suggested that the aluminum layer below 100 nm does not provide the AlO_2^- ion concentration required for the formation of the ZnO nanowall structure (Nayak et al., 2012).

Although the above-mentioned studies report that physical characteristics of the ZnO nanowall structures are controlled by the processing parameters during the hydrothermal synthesis, they do not present any quantitative correlation between processing parameters such as Zn^{2+} concentrations and synthesis time, and the nanowall

characteristics such as height, thickness, aspect ratio and void size. Moreover, as noted above there are limited number of studies regarding the use of the nanowall structured systems as PENGs in the literature and these studies do not present any quantitative relationship between the nanowall structure characteristics and electrical output production potentials of such systems. As it is known, the performance of materials varies depending on their properties. Moreover, the properties are dictated by the structure of the material. Therefore, it is critical to establish a fundamental understanding on the processing-structure-property-performance relationship for the ZnO nanowall-based nanogenerators to achieve advanced, high performance PENGs. Once it is established, then this understanding can enable one to tailor the structure via processing conditions and hence develop high performance ZnO nanowall-based nanogenerators. Accordingly, the research objective of this study was to develop a basic and quantitative understanding on relations between processing and nanowall structure and energy generation in the ZnO nanowall-based nanogenerators as a first time in the literature. To achieve this objective, ZnO nanowall structures were grown on aluminum foil by hydrothermal synthesis method at different Zn^{2+} concentrations and different synthesis temperature and synthesis time. In addition, both the effects of synthesis parameters on ZnO nanowall morphologies, and the effects of changes in the nanowall morphology on electrical outputs were quantitatively examined. Additionally, a simple flexible PENG module was fabricated using samples with optimized structural characteristics, to achieve the highest performance, and the maximum output voltage.

3.2. Experimental

3.2.1. Hydrothermal synthesis of ZnO nanowalls

An aluminum foil (5 cm × 5 cm) was used as the substrate, which acts as the bottom electrode. Before the hydrothermal synthesis, the substrates were cleaned with acetone for 10 minutes and then left to dry. Table 3.1 shows the experimental conditions used in this study. Throughout the text, the AlX-Y-Z-T designation system where X, Y, Z, and T refer to thickness of the foil in micrometer, Zn^{2+} concentration in (mM), synthesis time in (h), and synthesis temperature in (°C) respectively, is used for describing the samples, developed in this study.

Hydrothermal synthesis was performed as described in the literature (Kaur and Singh, 2020). Equal molar (1:1) zinc nitrate hexahydrate ($Zn(NO_3)_2$, Sigma Aldrich,

MW: 297.49 g.mol^{-1}) and hexamethylenetetramine (HMTA, $C_6H_{12}N_4$, MERCK, MW: 140.19 g.mol^{-1}) aqueous solutions at different concentrations were prepared. The hydrothermal synthesis steps are shown in Figure 3.1. The proper amount of zinc nitrate hexahydrate and HMTA were added to 100 ml of distilled water separately and mixed with magnetic stirrer at room temperature for 20 minutes. Then two clear solutions mixed with each other with magnetic stirrer at room temperature for 20 minutes. At the end of the process, a clear solution was obtained. The cleaned aluminum foil substrates were placed on the solution. Because of the surface tension, aluminum foil was floating over the solution meniscus. The beaker was covered then placed in a hot water bath previously set at determined temperature and kept for the times indicated in Table 3.1. At the end of the synthesis, the beakers were removed from the hot water bath and allowed to cool to room temperature. After cooling the samples were removed from the beakers and washed several times with distilled water then left to dry at room conditions.

Table 3.1. *Hydrothermal synthesis condition of ZnO nanowall arrays on Al-foil substrates*

Sample Code	*Concentration (mM)*	*Growth Time* (h)	*Temperature (°C)*
Al18-6.25-2-95	6.25	2	95.0
Al18-6.25-4-95	6.25	4	95.0
Al18-6.25-6-95	6.25	6	95.0
Al18-12.5-2-95	12.50	2	95.0
Al18-12.5-4-95	12.50	4	95.0
Al18-12.5-6-95	12.50	6	95.0
Al18-25-2-95	25.00	2	95.0
Al18-25-4-95	25.00	4	95.0
Al18-25-6-95	25.00	6	95.0
Al18-25-6-85	25.00	6	85.0
Al18-25-6-75	25.00	6	75.0
Al18-25-6-65	25.00	6	65.0
Al18-37.5-2-95	37.50	2	95.0
Al18-37.5-4-95	37.50	4	95.0
Al18-37.5-6-95	37.50	6	95.0
Al18-50-2-95	50.00	2	95.0
Al18-50-4-95	50.00	4	95.0
Al18-50-6-95	50.00	6	95.0

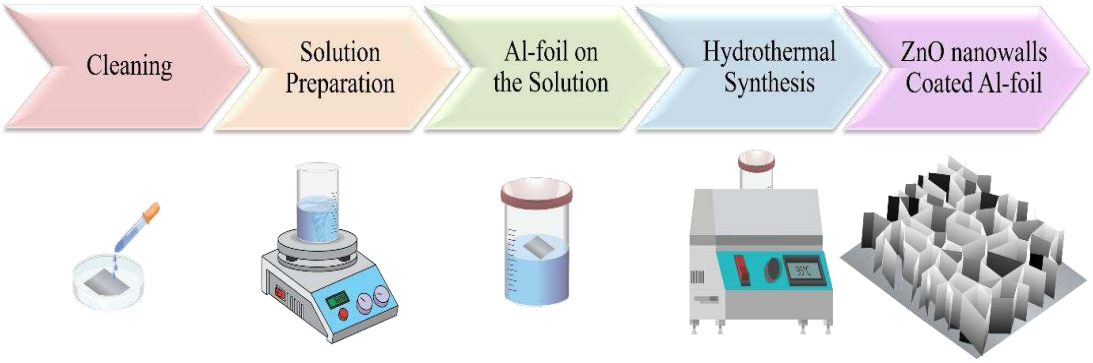

Figure 3.1. *Schematic illustration of hydrothermal synthesis of ZnO nanowall array on Al-foil*

3.2.2. Characterization

X-ray diffraction (XRD, Bruker D2 Phaser, Cu anode kα1 = 1.54 Å) analysis was performed to examine the crystal structure of ZnO nanowalls grown on the surface of aluminum foil and to determine the planes in which the crystals are oriented. Scanning electron microscopy (SEM, Zeiss Supra, secondary electron mode and 15 kV acceleration voltage) analysis was performed for morphological examinations. In addition, Image J program (http-2, 2024) was used to measure thickness and length of the ZnO nanowalls grown on the aluminum foil substrates as well as inter-nanowall void length. Time-dependent electrical voltage measurements were analyzed with the B2902B Precision Source / Measurement Unit (2 ch, 100 fA) system integrated into the Ambios/Quesant Q-Scope Atomic Force Microscope AFM device. The schematic representation of the system is shown in Figure 3.2. Measurements on AFM system were implemented that scanning type/angle; Z type/90˚, scanning rate; 0.25 Hz; setpoint: 0 V and 40 µm x 40 µm scanning area. In the system interface created by B2902B Precision Source, voltage compliance was optimized as 5 V and current compliance was optimized as 0.1 A. In this integrated system, 50 measurements of 50 ms (milliseconds) were taken every 60 ms in the x direction (laterally) over the piezoelectric ZnO nanowall structures on the sample surface with a platinum-coated AFM probe/tip (Type Radius <30 nm). The AFM probe cantilever structure has a constant force of 2 N m^{-1}. 50 measurements were enforced at least 10 times from various parts of the sample surface and graphed, and the amplitude formations were calculated from the maximum/minimum piezoelectric potential voltage difference. Bending of the ZnO nanowall created a positive potential on the tensile side and a negative potential on the compression side. Experimentally, when the AFM probe was scanned over aligned

nanowall arrays, the corresponding output voltage along the resulting force was simultaneously recorded. The voltage generated by the flexible piezoelectric modules from finger tapping was measured using an oscilloscope.

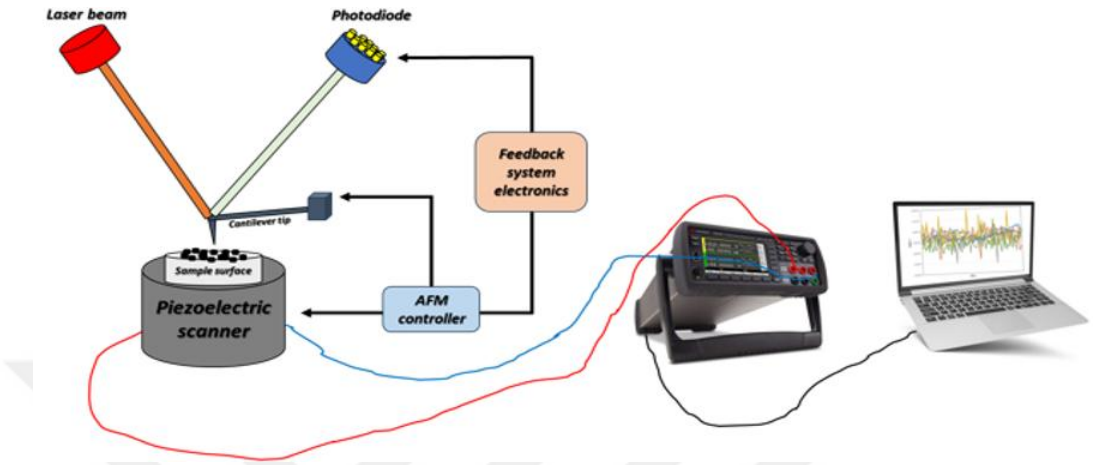

Figure 3.2. *Schematic illustration of the Ambios/Quesant Q-Scope AFM and B2902B Precision Source electrical measurement system*

3.3. Results and Discussions

3.3.1. Effect of synthesis temperature on nanowall structure development

In the first step of the study, a 6-hour hydrothermal synthesis was performed on an 18 µm aluminum foil substrate at various temperatures (65 °C to 95 °C) using an equimolar (25 mM) zinc nitrate hexahydrate/HMTA aqueous solution. Figure 3.3 presents the XRD patterns of the samples obtained under these conditions. In the graphs, the diffraction peaks at 2θ= 44.8°, 65.2° and 78.3° belong to the (200), (220) and (311) planes of aluminum in the cubic crystal structure, respectively. In addition to the diffraction peaks of cubic aluminum, the diffraction peaks of the (006), (012) and (110) planes belong to ZnAl:LDH layer were obtained at angles of 2θ = 21.3°, 34.0° and 60.4°. The XRD pattern obtained for the Al18-25-6-95 sample is consistent with the studies of Kim et al (Kim et al., 2013). They observed three peaks at 22.7°, 33.6° and 60.1° corresponding to ZnAl:LDH planes in their study, which was confirmed from standard powder diffraction peaks of ZnAl:LDH (JCPDS card No. 85-1327). It was observed that the only diffraction peak belongs to the ZnO structure obtained at 2θ = 34.6° indicate the plane (0002). Since only the diffraction peak belonging to the plane (0002) was obtained, it is possible to say that the ZnO structures grown on the substrate have a

preferred growth orientation along the c-axis. However, it was determined that the intensity of the diffraction peak corresponding to the (0002) plane decreased in the samples obtained from syntheses conducted at temperatures below 95 °C.

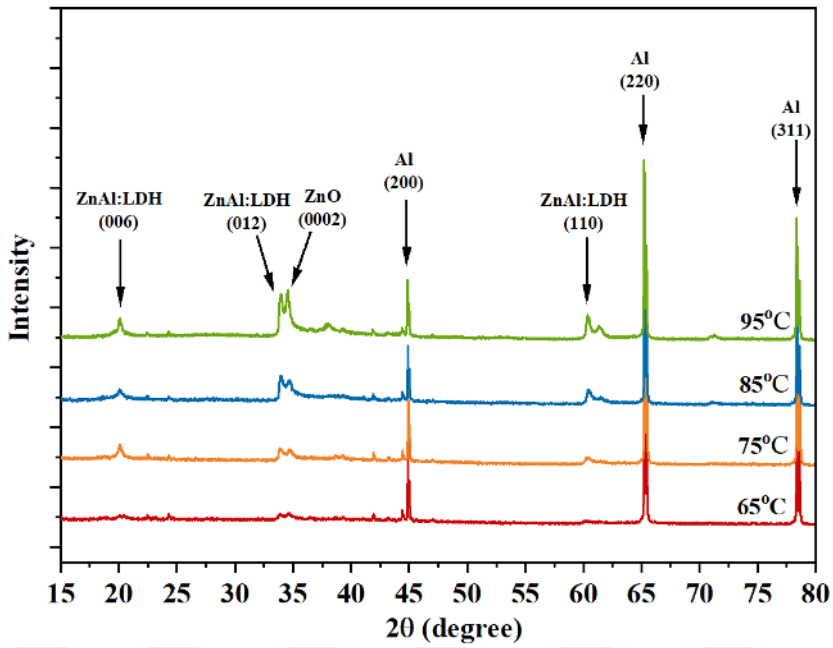

Figure 3.3. *XRD graph of (a) Al18-25-6-65, (b) Al18-25-6-75, (c) Al18-25-6-85 and (d) Al18-25-6-95*

Figure 3.4 shows top-view SEM micrographs of samples obtained at different temperatures. In Figure 3.4 (d) shows that a homogeneous and continuous ZnO nanowall structure with an interconnected network structure was formed on the aluminum foil surface at 95°C. The obtained ZnO nanowall morphology looks remarkably similar to the microstructures, reported in previous studies in the literature (Kim et al., 2013; Kaur and Singh, 2020). However, it was determined that such a structure could not be obtained at lower temperatures. At 65 °C, the temperature was insufficient for the formation of nanowalls; nucleation had initiated, but the growth process could not be completed within 6 hours. At 75 °C, nanowall structures were obtained; however, the formation of regional agglomerations was observed. At 85 °C, a relatively more uniform nanowall network was formed, but the most well-defined and homogeneous network structure was achieved at 95 °C. Measurements made by Image J software, revealed that ZnO nanowall thicknesses as 81 ± 21 nm on average, and the inter-nanowall void length as 2.4 ± 1.1 µm on average for Al18-25-6-95 sample.

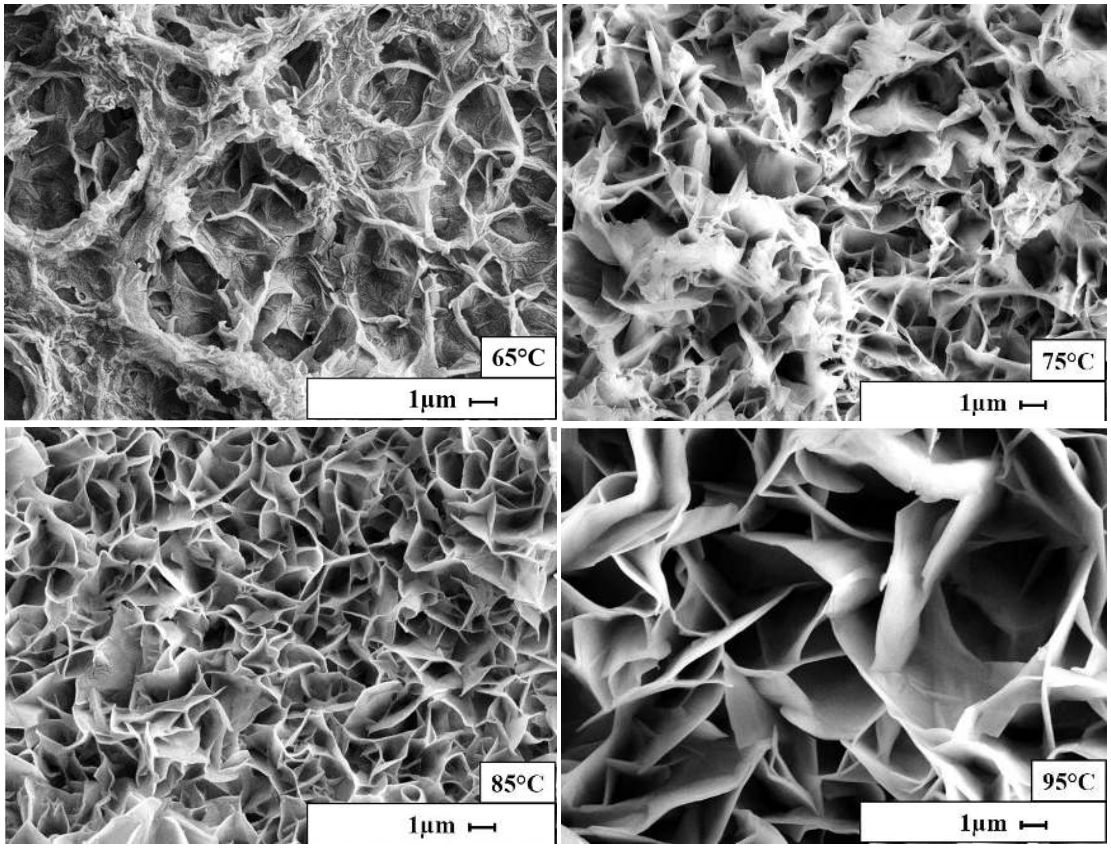

Figure 3.4. *Top-view SEM micrographs of (a) Al18-25-6-65, (b) Al18-25-6-75, (c) Al18-25-6-85, and (d) Al18-25-6-95*

As a result of the synthesis conducted at 95 °C, a distinct white layer was observed on the surface of the aluminum foil, as shown in Figure 3.5. This figure shows that a homogeneous and continuous ZnO nanowall structure with an interconnected network structure was formed on the aluminum foil surface.

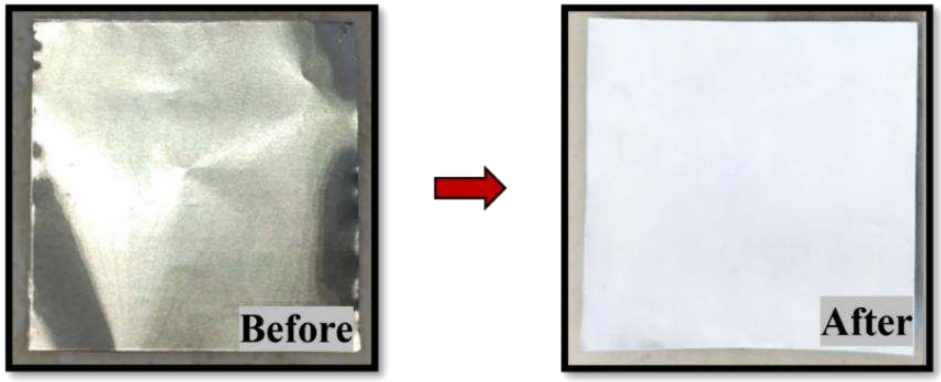

Figure 3.5. *Photograph of Al-foils before and after hydrothermal synthesis at 95°C*

3.3.2. Effect of Zn^{2+} concentration on nanowall structure development

To determine the effect of Zn^{2+} ion concentration on ZnO nanowall structure, the concentration varied from 6.25 to 50 mM while keeping synthesis time and temperature constant as 6 h and 95°C, respectively. The XRD graphs of sample present in Figure 3.6. In the bottom graph, the diffraction peaks at 2θ= 44.8°, 65.2° and 78.3° belong to the (200), (220) and (311) planes of aluminum in the cubic crystal structure, respectively. In the graph (b-f), it can be seen that in addition to the diffraction peaks of cubic aluminum, the diffraction peaks of the (006), (012) and (110) planes belong to ZnAl:LDH layer were obtained at angles of 2θ = 21.3°, 34.0° and 60.4°. It was observed that the only diffraction peak belongs to the ZnO structure obtained at 2θ = 34.6° indicate the plane (0002). Since only the diffraction peak belonging to the plane (0002) was obtained, it is possible to say that the ZnO structures grown on the substrate have a preferred growth orientation along the c-axis.

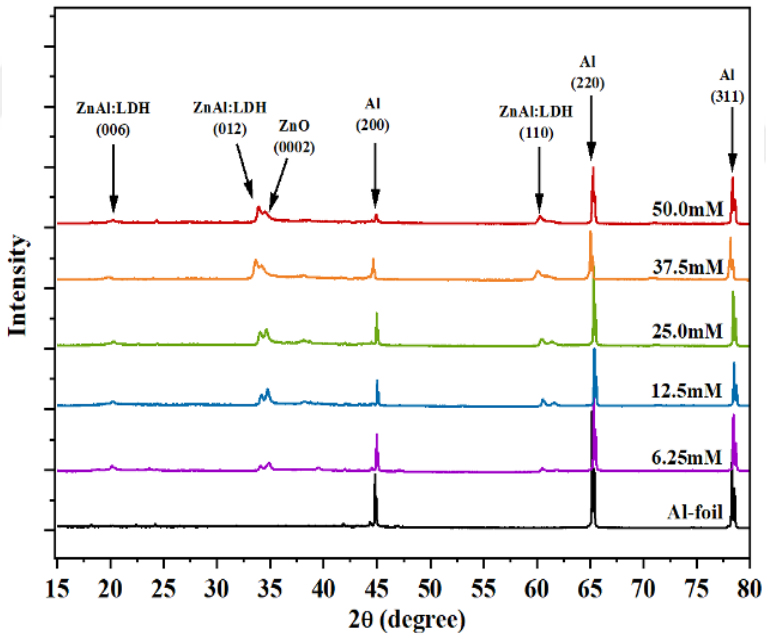

Figure 3.6. *XRD graph (a) untreated 18µm Al-foil, (b) Al18-6.25-6-95, (c) Al18-12.5-6-95, (d) Al18-25-6-95, (e) Al18-37.5-6-95 and (f) Al18-50-6-95*

Figure 3.7 shows top-view SEM micrographs of the samples. Top-view SEM micrographs show that homogeneous and continuous ZnO nanowall structures with an interconnected network structure were obtained at concentrations up to 25 mM. However, above 25 mM, the interconnected network structure began to deteriorate. In addition, due to the increasing concentration above 25 mM, the density of ZnO

nanowalls per unit area increased, ZnO nanowalls were wrinkled together and piled up from several thinner nanowalls. It has been reported in the literature that ZnO nanowall density depends on the Zn^{2+} concentration in the growth solution and the increase of the Zn^{2+} concentration increases the ZnO nanowall density, eventually. It is possible to explain this situation by the acceleration in the formation and increase in the number of ZnO nanowalls due to the increase in the nucleation frequency on the substrate when a critical concentration is reached (Ye et al., 2006; Chang et al., 2022).

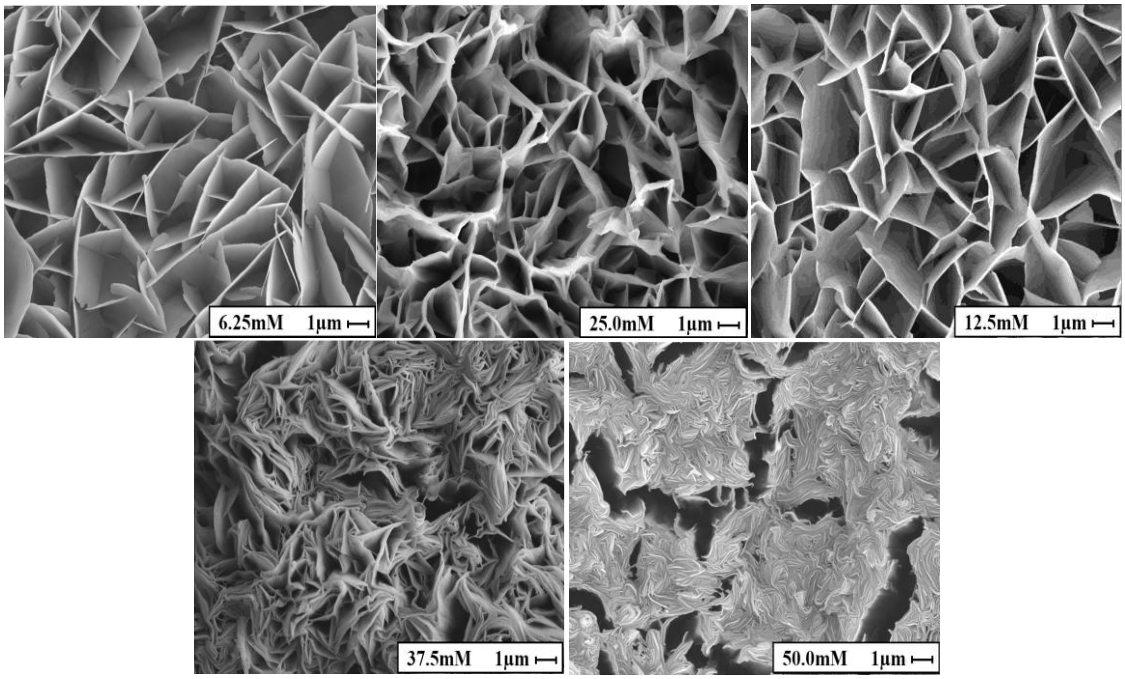

Figure 3.7. *Top-view SEM micrographs of (a) Al18-6.25-6-95, (b) Al18-12.5-6-95, (c) Al18-25-6-95, (d) Al18-37.5-6-95 and (e) Al18-50-6-95*

3.3.3. Effect of hydrothermal synthesis time on nanowall structure development

To understand the effect of hydrothermal synthesis time on ZnO nanowall structure development, hydrothermal synthesis was conducted at various times and at the Zn^{2+} ion concentration specified in Table 3.1. Top-view SEM micrographs of the samples given in Figure 3.8 to Figure 3.12, clearly show that ZnO nanowalls form even after 2 h in all samples. These results are consistent with the study by Jiang et al (Jiang and Yang, 2021) where they reported that ZnO nanowall structures were formed on aluminum foil substrates after 2 hours.

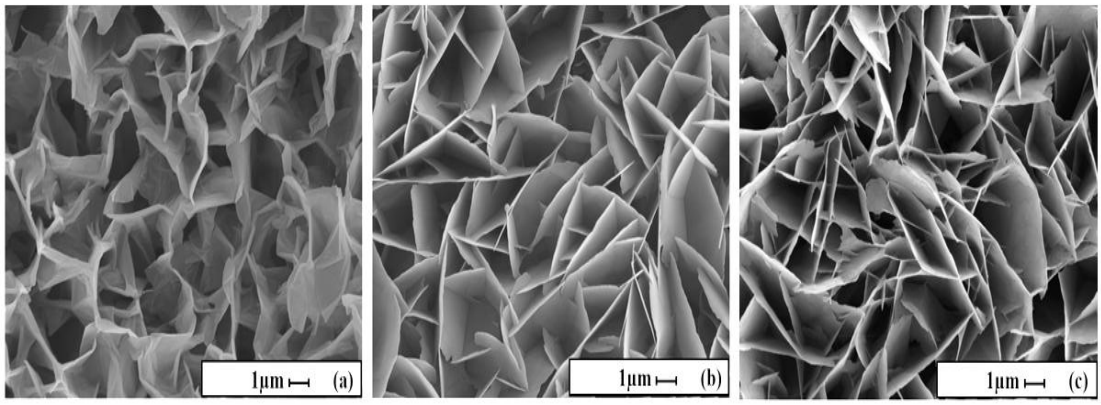

Figure 3.8. *Top-view SEM micrographs of Al18-6.25-95 sample depending on reaction time (a) 2 h, (b) 4 h and (c) 6 h*

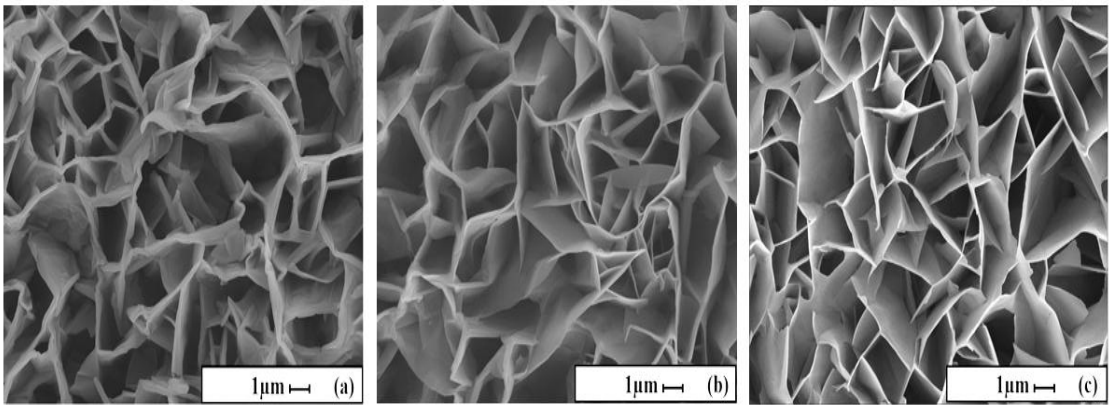

Figure 3.9. *Top-view SEM micrographs of Al18-12.5-95 sample depending on reaction time (a) 2 h, (b) 4 h and (c) 6 h*

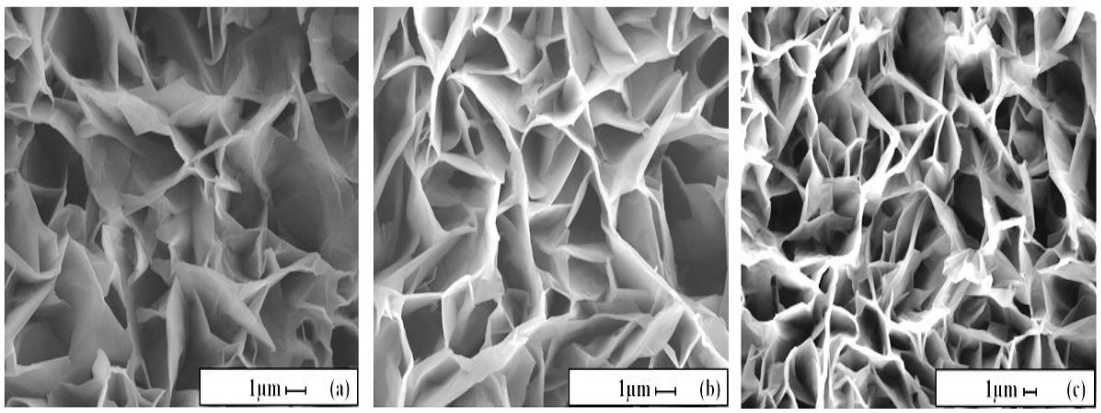

Figure 3.10. *Top-view SEM micrographs of Al18-25-95 sample depending on reaction time (a) 2 h, (b) 4 h and (c) 6 h*

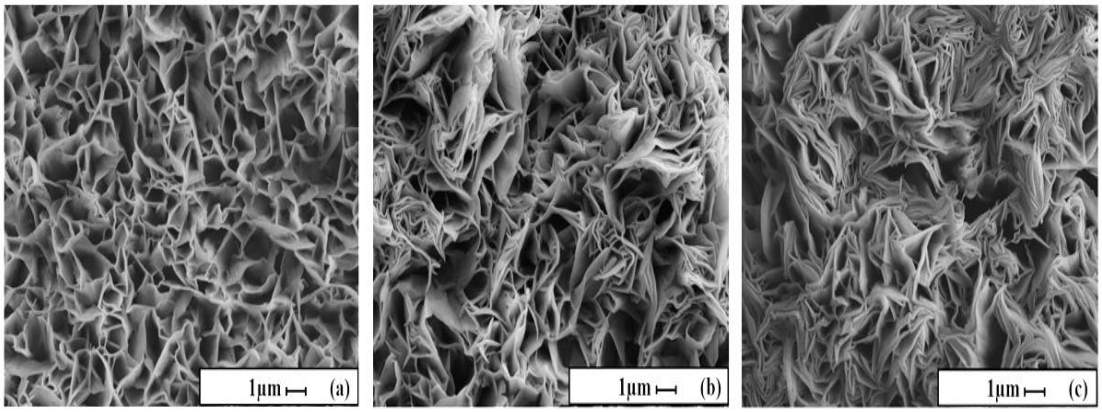

Figure 3.11. *Top-view SEM micrographs of Al18-37.5-95 sample depending on reaction time (a) 2 h, (b) 4 h and (c) 6 h*

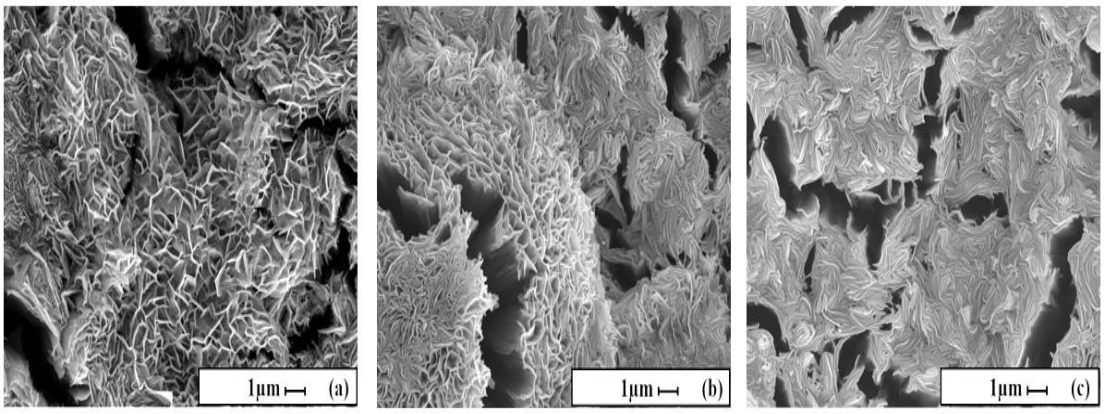

Figure 3.12. *Top-view SEM micrographs of Al18-50-95 sample depending on reaction time (a) 2 h, (b) 4 h and (c) 6 h*

To examine the effect of hydrothermal synthesis time on ZnO nanowalls in more detail, cross-sectional SEM micrographs given in Figure 3.13 to Figure 3.17 of these samples were taken. It has been observed that changes in ZnO nanowall lengths occur depending on the hydrothermal synthesis time. To express the changes quantitatively, the thickness and length of the nanowalls were measured by Image J software and the results are presented in Table 3.2.

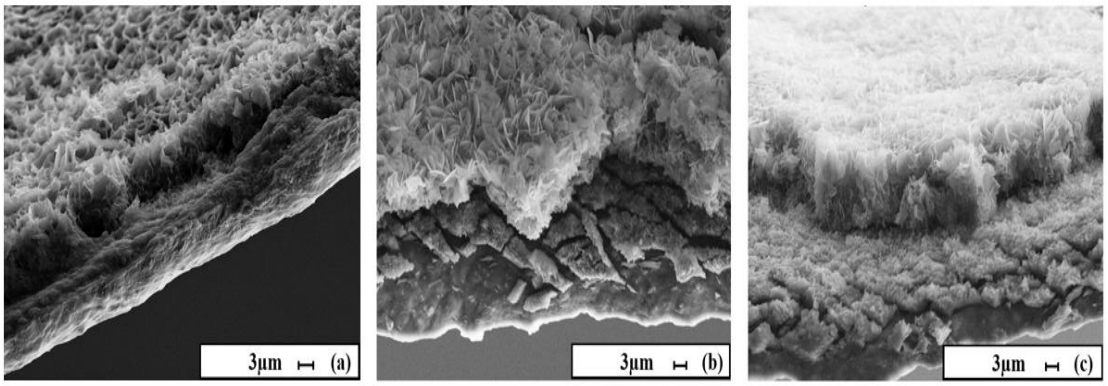

Figure 3.13. *Cross-section SEM micrographs of Al18-6.25-95 sample depending on reaction time (a) 2 h, (b) 4 h and (c) 6 h*

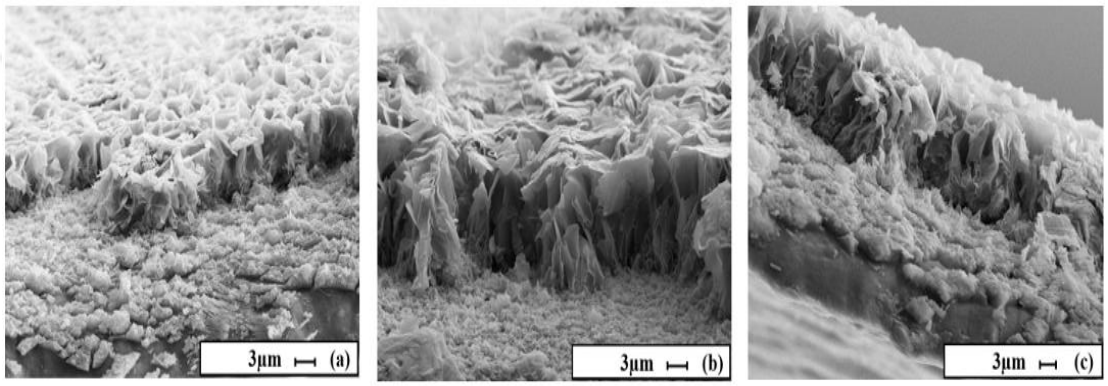

Figure 3.14. *Cross-section SEM micrographs of Al18-12.5-95 sample depending on reaction time (a) 2 h, (b) 4 h and (c) 6 h*

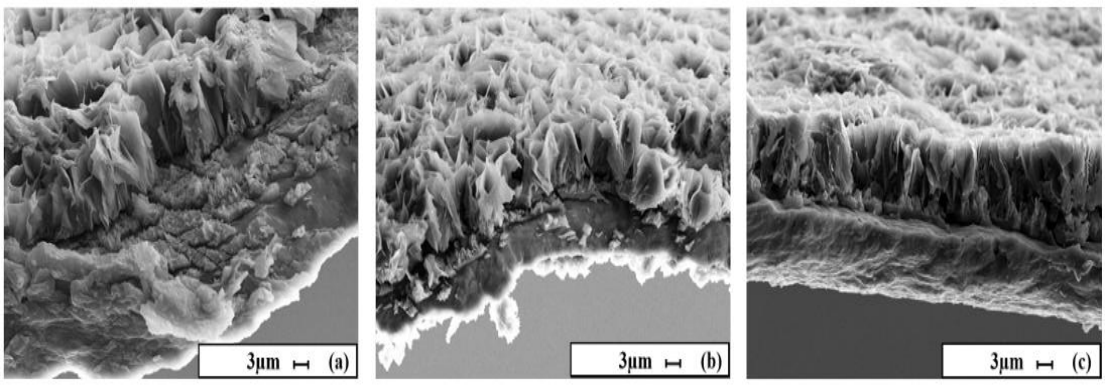

Figure 3.15. *Cross-section SEM micrographs of Al18-25-95 sample depending on reaction time (a) 2 h, (b) 4 h and (c) 6 h*

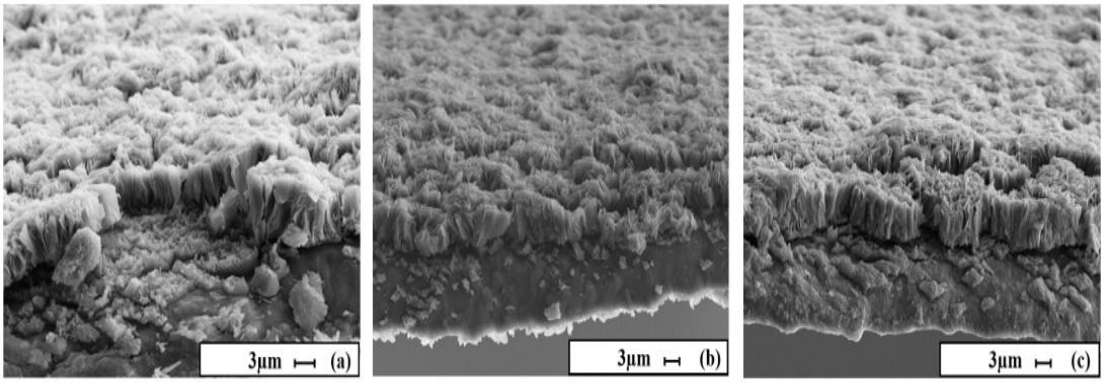

Figure 3.16. *Cross-section SEM micrographs of Al18-37.5-95 sample depending on reaction time (a) 2 h, (b) 4 h and (c) 6 h*

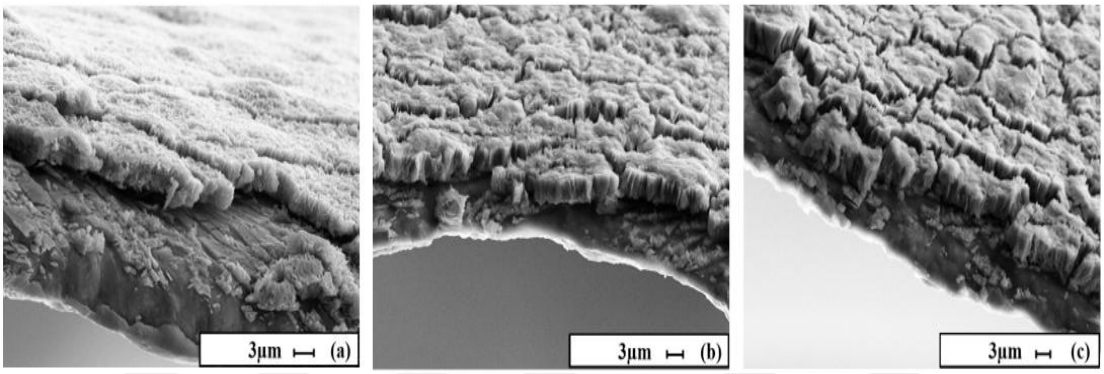

Figure 3.17. *Cross-section SEM micrographs of Al18-50-95 sample depending on reaction time (a) 2 h, (b) 4 h and (c) 6 h*

Table 3.2. *ZnO nanowall thickness, length and void length value according to Zn^{2+} ion concentration and synthesis time*

Sample Code	*Concentration* (mM)	*Growth Time* (h)	*Nanowall Thickness* (nm)	*Nanowall Length* (µm)	*Void Length* (µm)
Al18-6.25-2-95	6.25	2	82.1 ± 16.5	8.7 ± 1.1	1.4 ± 0.4
Al18-6.25-4-95	6.25	4	62.2 ± 13.6	11.6 ± 1.8	1.5 ± 0.4
Al18-6.25-6-95	6.25	6	56.0 ± 11.5	12.5 ± 2.1	1.7 ± 0.5
Al18-12.5-2-95	12.50	2	115.6 ± 22.8	5.8 ± 0.8	2.0 ± 0.4
Al18-12.5-4-95	12.50	4	113.4 ± 20.6	12.5 ± 1.9	2.2 ± 0.3
Al18-12.5-6-95	12.50	6	91.4 ± 17.7	10.2 ± 1.1	2.4 ± 0.3
Al18-25-2-95	25.00	2	92.4 ± 18.5	7.5 ± 1.2	2.1 ± 0.4
Al18-25-4-95	25.00	4	83.9 ± 15.8	8.9 ± 1.1	2.3 ± 0.4
Al18-25-6-95	25.00	6	81.2 ± 12.9	11.2 ± 1.3	2.4 ± 0.3
Al18-37.5-2-95	37.50	2	55.7 ± 12.6	4.0 ± 0.6	0.6 ± 0.2
Al18-37.5-4-95	37.50	4	54.2 ± 13.8	5.3 ± 0.8	0.6 ± 0.2
Al18-37.5-6-95	37.50	6	49.8 ± 10.6	6.8 ± 1.0	0.7 ± 0.2
Al18-50-2-95	50.00	2	28.2 ± 9.7	2.7 ± 0.6	0.2 ± 0.06
Al18-50-4-95	50.00	4	26.1 ± 7.9	3.8 ± 0.7	0.2 ± 0.06
Al18-50-6-95	50.00	6	25.7 ± 8.5	3.9 ± 0.7	0.1 ± 0.02

Figure 3.18 (a) shows the variation of nanowall thicknesses as a function of Zn^{2+} ion concentration and synthesis time. There is an increase in nanowall thickness up to 12.5 mM, and then the nanowall thickness decreases. For example, while the nanowall thickness was 82.1 nm for the Al18-6.25-2-95 sample, it was 115.6 nm for the Al18-12.5-2-95 sample. Additionally, it was determined that there was a decrease in nanowall thickness as the synthesis time increased. For instance, thicknesses of the nanowalls for the Al18-12.5-95 samples after 2, 4 and 6 h were 115.6, 113.4 and 91.4 nm, respectively. This change in thickness as a function of time suggests dissolution from the prismatic planes of the ZnO nanowalls during the hydrothermal synthesis.

Figure 3.18 (b) exhibits the changes in the inter-nanowall void length depending on the Zn^{2+} ion concentration and synthesis time. There is an increase in the inter-nanowall void length up to 25 mM and that void length decreases significantly at concentrations above 25 mM. For example, while the void length was 1.4 μm for the Al18-6.25-2-95 sample, it was 2.4 μm for the Al18-25-6-95 sample. But the void length was measured 0.1 μm for the Al18-50-2-95 sample. Depending on the synthesis time, it can be concluded that the inter-nanowall void length increases with increasing time. For instance, the inter-nanowall void lengths for the Al18-12.5-95 samples after 2, 4 and 6 h were 2.0, 2.2 and 2.4 μm, respectively. In addition, when the time-dependent graphs in Figure 3.18 (a) and Figure 3.18 (b) are evaluated together, it is concluded that there is an increase in the inter-nanowall void length as the nanowall thickness decreases. Although it is stated in the literature that there are no significant changes in nanowall lengths after 60 minutes in time-based studies (Pellegrino et al., 2019), in this study it was observed that the increase in synthesis time provided a significant increase in ZnO nanowall lengths, as shown in Figure 3.19 (a). Therefore, when all the graphs in Figure 18 and Figure 19 are evaluated together, it can be concluded that with increasing synthesis time during hydrothermal synthesis, Zn^{2+} ions, which dissolve on the nanowall surfaces and pass into the solution environment, provide elongation because of precipitation again at the top of the nanowalls which results in nanowall length increase as a function of time. On the other hand, the dramatic decrease in nanowall lengths due to the increase in solution concentration (37.5 mM and 50 mM) can be explained by the rapid depletion of Zn^{2+} ions in the medium due to the increased nucleation rate and increased ZnO nanowall density. Rapid depletion of Zn^{2+} ions prevented the resulting nanowall structures from elongating.

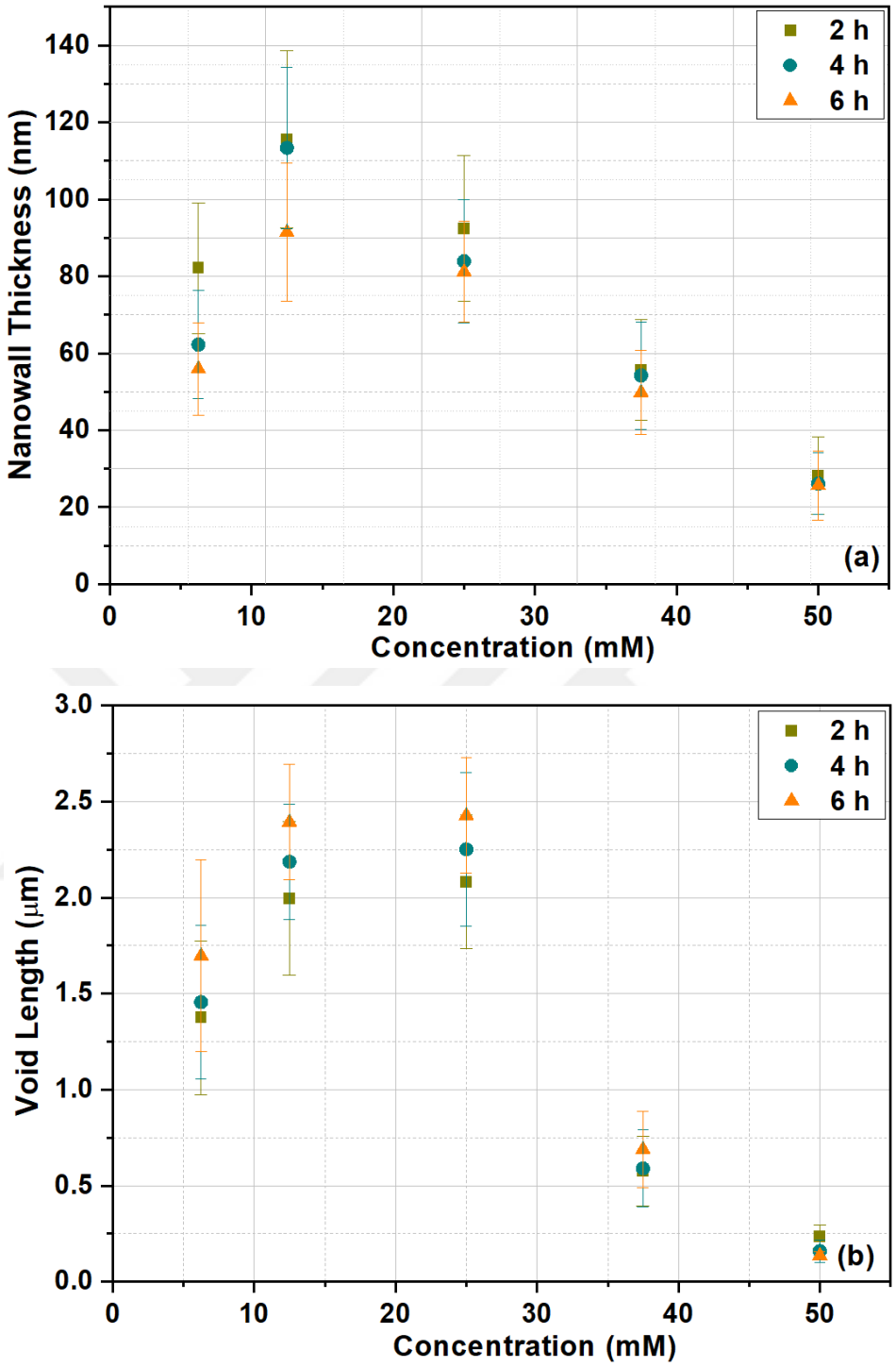

Figure 3.18. *Graphs of change in (a) nanowall thickness and (b) void length depending on Zn^{2+} ion concentration*

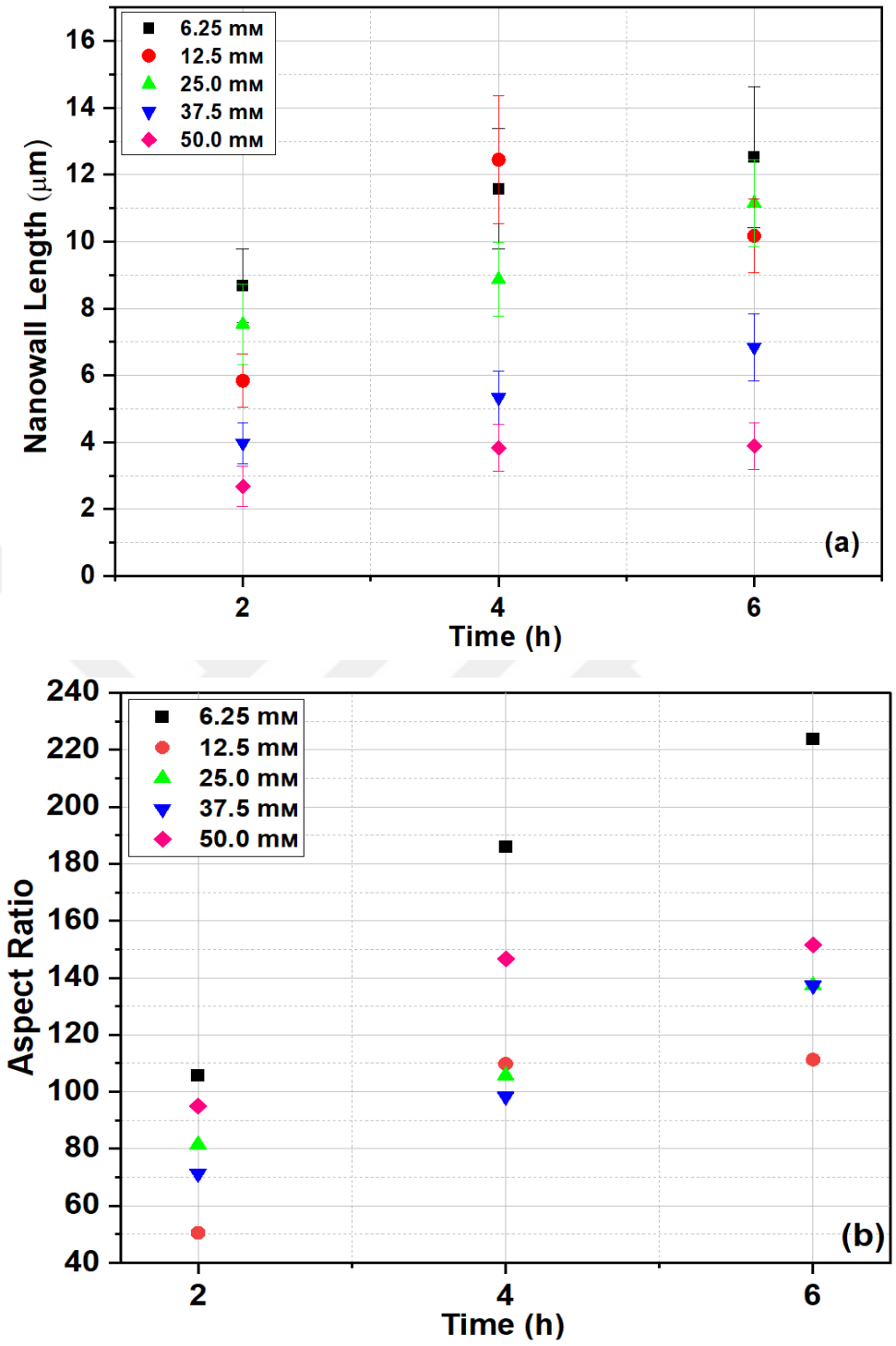

Figure 3.19. *Graphs of change in (a) nanowall length and (b) aspect ratio of nanowalls as a function of synthesis time*

3.3.4. Effect of nanowall structure on electrical output voltage generation capability

To determine the relationship between nanowall structure characteristics and electrical output voltage generation, electrical characterization of all samples was carried out with an AFM semiconductor parameter analyzer. As a result of the mechanical force applied to ZnO nanowalls by the AFM tip, the non-symmetrical lattice structure of zinc oxide was distorted, pushing some atoms closer or further apart, disturbing the balance of positive (Zn^{2+}) and negative (O^{2-}) ions. Negative potential (V^{-}) is created over the compressed areas and positive potential (V^{+}) over stretched parts. When the force is applied on the nanowalls, the empty space between nanowalls gives them enough space to bend due to which outer areas stretched, and inner parts are compressed. The strain produces V^{-} over the compressed areas and V^{+} over stretched ones owing to the piezoelectric effect (Kaur and Singh, 2019). This produces a net output voltage. Within the scope of the study, the electrical measurement results obtained by scanning the ZnO nanowalls along a line with the AFM type are given in Table 3.3. Although the obtained output voltage values are low compared to the literature (Kim et al., 2013; Kaur and Singh, 2020), it should be noted that while the output voltage values in the literature were obtained with ZnO nanowall-based nanogenerator modules (i.e., multiple nanowall contributed to output voltage generation), the output voltage values measured in this study were obtained by scanning the individual ZnO nanowalls along a line with AFM type.

When the output voltage values were compared, it was determined that the highest output voltage values in ZnO nanowall growth with different Zn^{2+} ion concentration were obtained as a result of 6 hours of hydrothermal synthesis. Figure 3.20 shows the output voltage values obtained depending on the nanowall thickness and inter-nanowall void lengths for the samples produced after 6-hour hydrothermal synthesis. Figure 3.20 (a) demonstrates that as the wall thickness increases initially output voltage increases and then it reaches a plateau. The results indicate a minimum critical thickness requirement for high voltage output from the nanowalls. Since in this study the maximum voltage values were achieved for the ZnO nanowalls with a thickness of 56 nm or greater, the critical thickness to achieve maximum output voltage was determined as 56 nm. It is also interesting to note that there was an 1.5-fold difference between the

output voltage values of the samples with similar nanowall thicknesses such as 56 and 50 nm.

Figure 3.20 (b) shows the effect of inter-nanowall void length on output voltage values. As observed in the thickness case, when the void length increases, the output voltage increases initially up to 1.7 mm and reaches 0.62 mV then the voltage remains constant. These results clearly show that there is a critical minimum void length requirement to achieve the maximum output voltage. In this study, this critical void length is demonstrated as above 1.7 mm. Furthermore, when the nanowall thickness and the void length effects on output voltage are compared, the void length is more effective than the nanowall thickness on the output voltage values. Because the maximum output voltage was observed in the sample whose thicknesses were similar, but their void lengths were significantly different. In other words, reducing the void length limits the ability of nanowalls to bend under applied force. It has been determined that nanowalls with limited bending ability cause a decrease in the potential to produce output voltage under applied force. This result is consistent with the Kaur and Singh study (Kaur and Singh, 2020). They stated that tightly packed structures have less space for deformation, therefore they will create less potential under applied force, thus producing less voltage and current.

Table 3.3. Output Voltage of ZnO nanowalls according to Zn^{2+} ion concentration and synthesis time

Sample Code	***Concentration* (mM)**	***Growth Time* (h)**	***Output Voltage* (mV)**
Al18-6.25-2-95	6.25	2	0.29
Al18-6.25-4-95	6.25	4	0.55
Al18-6.25-6-95	6.25	6	0.62
Al18-12.5-2-95	12.50	2	0.34
Al18-12.5-4-95	12.50	4	0.36
Al18-12.5-6-95	12.50	6	0.61
Al18-25-2-95	25.00	2	0.60
Al18-25-4-95	25.00	4	0.37
Al18-25-6-95	25.00	6	0.64
Al18-37.5-2-95	37.50	2	0.21
Al18-37.5-4-95	37.50	4	0.31
Al18-37.5-6-95	37.50	6	0.42
Al18-50-2-95	50.00	2	0.23
Al18-50-4-95	50.00	4	0.30
Al18-50-6-95	50.00	6	0.26

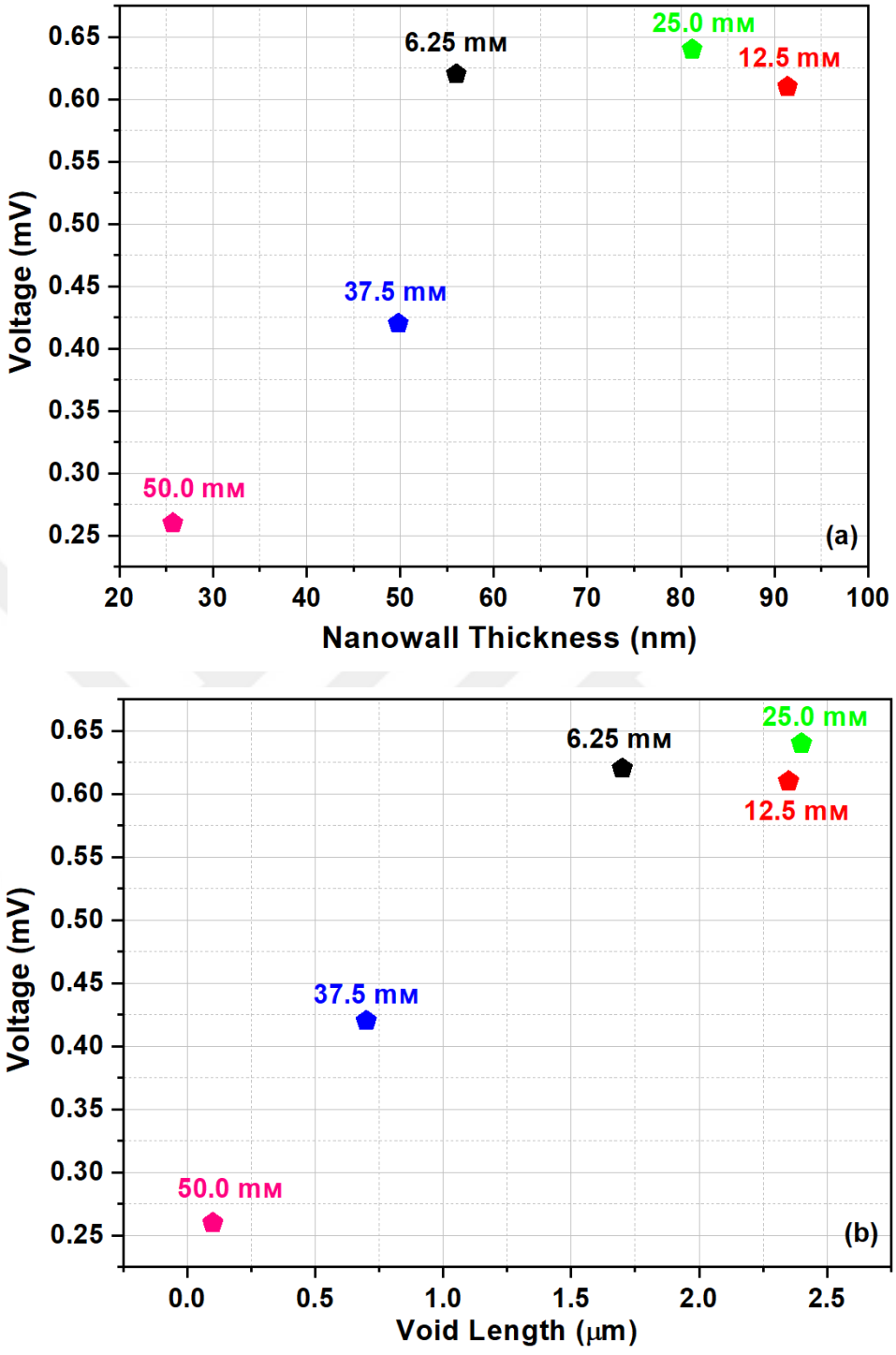

Figure 3.20. *Graphs of output voltage values changing depending on (a) nanowall thickness and (b) inter-nanowall void length*

The graph presented in Figure 3.21 was created with the critical values determined according to these results. Certain critical values must be met in order to create ZnO nanowall arrays with high output voltage values. In this study, critical wall thickness ($W.T_c$) and critical void length ($V.L_c$) were determined as 56 nm and 1.7 μm,

respectively. Therefore, to produce highly efficient piezoelectric nanogenerators, it is necessary to create arrays where the nanowalls with a thickness of greater than 56 nm and inter-wall void length more than 1.7 µm.

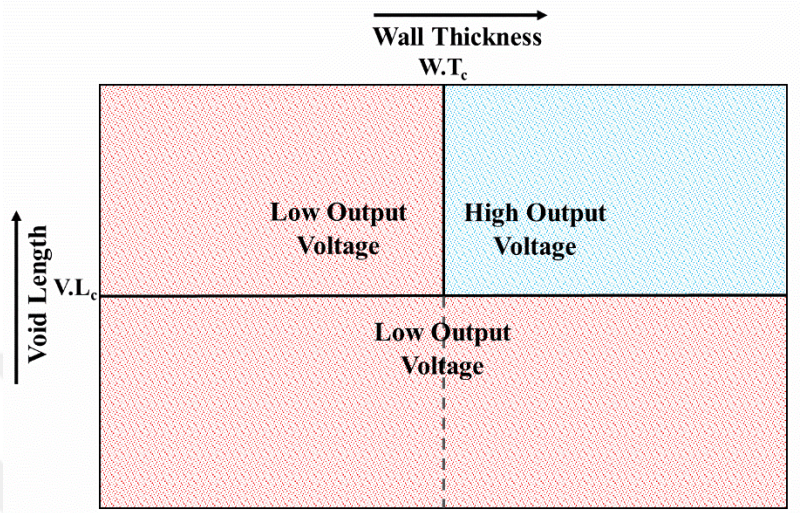

Figure 3.21. *Tailoring of ZnO nanowall arrays by critical void length and critical nanowall thickness for high efficiency nanogenerator applications*

3.4. Electrical Output Voltage Generation Capability of a ZnO Nanowall-Based Flexible Piezoelectric Nanogenerator

In measurements conducted with an AFM semiconductor parameter analyzer, the highest output voltage (0.64 mV) was obtained from individual ZnO nanowall in the Al18-25-6-95 sample. Subsequently, a flexible piezoelectric nanogenerator module with an active area of 1 cm² was fabricated using the Al18-25-6-95 sample, as shown in the inset photograph of Figure 3.22. Copper wires integrated into the module enabled a forward polarity connection to the oscilloscope, after which a finger tapping force was applied. The blue voltage graph in Figure 3.22 shows that the module generated approximately 400 mV rectified output voltage at positive side in response to the finger tapping force. Major and minor voltage peaks of opposite directions were observed. The major peaks occurred when the force was applied to the module, while the minor peaks in the contrary direction appeared when the applied force was released. To confirm that this output voltage originated from the piezoelectric module, the measurement was repeated with a reverse polarity connection. As shown in Figure 3.22 red graph, the piezoelectric module generated approximately 400 mV rectified output voltage at

negative side in response to the finger tapping force. This result confirmed that the output voltage was generated by the piezoelectric module under applying force.

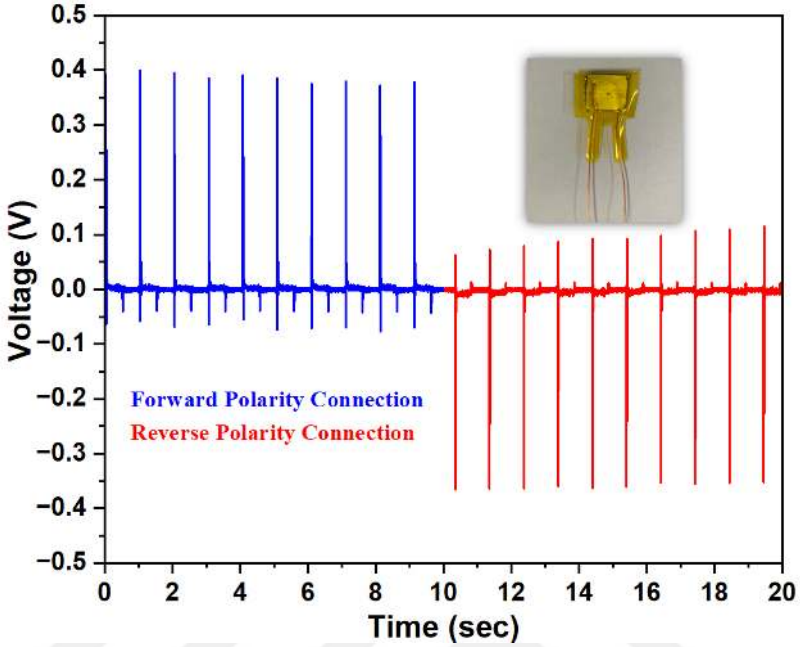

Figure 3.22. *Voltage response of a ZnO nanowall-based flexible PENG under forward and reverse polarity connections during finger tapping*

A review of the literature reveals that an output voltage of 228 mV was obtained under a 10 N force in similar module structures fabricated with different electrodes (Kaur and Singh, 2020). In contrast, the piezoelectric module developed in this study, with careful consideration of critical parameters demonstrates an output voltage approximately twice as high. This result highlights the crucial role of process-structure-property relationships in the design and fabrication of high-efficiency nanogenerators. Also, it should be noted that the nanogenerator module is estimated to contain approximately 3500 nanowalls per square centimeter. This calculation is based on the number of nanowalls intersecting a linear line drawn on SEM images. AFM analyses indicate that individual nanowalls generate 0.64 mV under open-circuit conditions. Therefore, theoretically, a 1 cm² nanogenerator module is expected to produce an open-circuit voltage of 2.2 V according to Equation 3.4. $N_{\text{nanowalls}}$ represents the number of nanowalls in the PENG module, V_{nanowall} represents the open circuit voltage value of an individual nanowall, and V_{PENG} represents the open circuit voltage value of the PENG module.

$$N_{\text{nanowall}} \times V_{\text{nanowall}} = V_{\text{PENG}} \tag{3.4}$$

However, in this study, the maximum measured open-circuit voltage was determined to be 400 mV. These results suggest that the utilization efficiency of the nanowalls is 18%. The loss in open-circuit voltage may be attributed to the incomplete contact between ZnO nanowalls and the electrodes, as well as the metal-semiconductor contact type between the top electrode and ZnO nanowalls.

3.5. Conclusions

This research examined the effects of synthesis parameters on ZnO nanowall structures grown via hydrothermal synthesis method. It is established that the densities per unit area of ZnO nanowalls grown on the substrate and the inter-nanowall void length vary depending on the Zn^{2+} ions concentration, and the lengths of the ZnO nanowalls vary depending on both the Zn^{2+} ions concentration and the synthesis time. Furthermore, it is demonstrated that the structure of ZnO nanowalls, which varies with synthesis parameters, significantly influences output voltage values. Additionally, this study - for the first time in the literature - developed a quantitative understanding of the relationships between processing and nanowall structure and energy production in ZnO nanowall nanogenerators. The structural changes depending on the synthesis parameters were expressed quantitatively using the Image J program and their relationship with synthesis parameters were interpreted. The critical nanowall thickness (56 nm) and void length (1.7 μm) values required to achieve efficient output voltage values in nanogenerator applications energy harvesting systems were presented. Additionally, taking the critical values into account, a flexible piezoelectric module was designed using the sample that individually produced the highest output voltage. This module generated a rectified-like output voltage of approximately 400 mV under finger tapping force.

It is believed that this process-structure-property relation understanding, developed in this study, will facilitate the design of highly efficient flexible ZnO nanowall-based piezoelectric nanogenerator modules possible. Furthermore, it is anticipated that this understanding will play a significant role in the optimization studies of ZnO nanowall structures for various applications beyond nanogenerator applications. Particularly in sensor applications, where ZnO nanowalls are widely used, to determine the necessary processing parameters for an effective surface area-to-volume ratio and consequently designing superior sensor modules is regarded as crucial.

4. HYDROTHERMAL SYNTHESIS OF DOPED 2-D ZnO NANOWALL STRUCTURES

4.1. Introduction

ZnO is a direct band gap semiconductor with a wurtzite crystal structure and can exhibit piezoelectric properties due to its non-centrosymmetric structure. The wurtzite phase lacking central symmetry and the spontaneous polarization occurring between the polar planes in the c-axis, especially expressed as the [0001] direction, constitute the main source of the piezoelectric response of ZnO (Wang, 2004). ZnO is widely used in energy harvesting systems such as flexible piezoelectric nanogenerators (PENG) due to its low-temperature production capability, biocompatibility and environmental stability (Zhao et al., 2021; Song, Zhou and Wang, 2006). But, pure ZnO nanostructures have limited piezoelectric performance. In the literature, the piezoelectric charge coefficient (d_{33}) reported for bulk ZnO is around 9.9 pC/N, while for high crystallinity ZnO thin films this value is around 12.4 pC/N and for c-axis oriented ZnO nanobelts it is around 14.3 - 26.7 pC/N (Zhao, Wang and Mao, 2004). However, these theoretical values of ZnO cannot often be achieved under realistic synthesis conditions. Because the piezoelectric performance of ZnO is seriously limited by structural and electrical factors such as intracrystalline defects (e.g., oxygen vacancies, zinc interstitials), irregular crystal orientation, and excess free charge carrier density. These defects cause screening of the piezoelectric potential formed in the ZnO structure, reducing the output voltage and current that can be transferred to the external circuit. Especially in the ZnO structure, piezoelectric effects are directly dependent on the density of free carriers (electrons or holes) within the material. As a result of compressive or tensile strain applied to the ZnO structure, piezo charges are formed at the interfaces. However, these free carriers move towards these piezo-charges and neutralize them by screening them. If the carrier density of the material increases, the screening effect is strengthened and the piezoelectric response caused by the strain is weakened. In other words, the strength of the piezoelectric potential and the modulation created by these potential decreases as the carrier density increases. To increase piezoelectric performance, it is preferred that the carrier density is low in materials such as ZnO. In this way, a more efficient electrical response can be obtained from the applied mechanical strain (Pan et al., 2018).

The hydrothermal method is widely preferred for the synthesis of ZnO nanostructures, especially in nanowire and nanowall morphologies, due to its low temperature, simple equipment requirements, and solution-based controlled growth possibilities. However, the ZnO structures obtained by this method generally contain low crystallinity, random orientation, and dense structural defects, and therefore exhibit lower piezoelectric performance than ZnO structures produced by techniques such as CVD, PLD and ALD (Yang et al., 2002; Wallace et al., 2015; Bagga, Akhtar and Mishra, 2018). This crystal defects formed during the hydrothermal synthesis method prevent the piezoelectric fields from forming properly and make it difficult to obtain effective polarization under external stress. Piezoelectric polarization cannot occur effectively enough in nanowires and nanowalls whose growth direction is incompatible with the c-axis or is not axially aligned. Various strategies have been developed to overcome these limitations in hydrothermal synthesis. As mentioned in Chapter 2, the most important of these is the increase in the quality of the seed layer applied onto the substrates surface. The smooth and crystalline structure of the seed layer contributes to the increase in piezoelectric response by encouraging the orientation of the ZnO nanostructures along the c-axis. In addition, optimizing the hydrothermal synthesis parameters such as solution concentration, synthesis temperature and synthesis time also positively affects the development of the crystal structure.

However, optimization of hydrothermal synthesis conditions may not always be sufficient. At this point, especially the defects in the ZnO nanostructures, and therefore the crystal quality, are tried to be improved with additional processes. These additional processes can be listed as follows:

- Heat treatment (Annealing) applications.
- Surface modifications or passivation
- Doping of ZnO nanostructures

ZnO nanostructures synthesized by hydrothermal methods may have structural limitations that may negatively affect piezoelectric performance, such as crystal defects, low crystallinity and surface irregularities, since they are grown at low temperatures. Therefore, annealing process applied following hydrothermal synthesis is widely used to improve the quality of ZnO crystal structure and improve piezoelectric properties. Heat treatment reduces oxygen vacancies inside ZnO nanostructures, thus allowing the crystal to reorganize and thus increasing the internal electric dipole density (Narayanan,

Ganesh and Karthigeyan, 2016). For example, Ma reported in his studies that the best crystal structure was obtained in ZnO nanowires heat-treated at 400°C after hydrothermal synthesis (Ma, 2019). However, high heat treatment may deteriorate the morphology of ZnO nanostructures and lead to loss of structural integrity (Muchuweni, Sathiaraj and Nyakotyo, 2018). Therefore, heat treatment temperature and time should be carefully optimized. At the same time, the atmosphere in which the heat treatment is carried out also significantly affects the results. In the studies, it has been determined that heat treatments carried out in an oxygen-rich atmosphere instead of an inert atmosphere reduce the oxygen vacancies in the ZnO structure and reduce the free charge carrier density that causes the screening effect. Therefore, it has been observed that the piezoelectric performance of ZnO is improved as a result of heat treatment in an oxygen-rich atmosphere (Bui et al., 2021; Mahapatra, Ajimsha and Misra, 2022).

Another method followed to improve the piezoelectric properties of ZnO is surface treatments such as plasma treatments. Plasma treatments are an effective modification technique that is commonly applied to reduce defect levels in the ZnO structure, usually by using oxygen. During the oxygen plasma treatment, the produced oxygen ions and radicals diffused by targeting the oxygen vacancies of the ZnO nanostructures and fill the vacancies to balance the oxygen stoichiometry of the ZnO crystal structure. Thus, the free charge carrier concentration in the ZnO structure is also reduced and the piezoelectric potential is improved. In addition, it has been reported in the literature that oxygen plasma treatment also improves the elastic properties of ZnO nanostructures by filling the vacancies in the structure. Therefore, the improvement of both the piezoelectric potential and the elastic properties of the ZnO nanostructure by oxygen plasma treatment contributes to the production of flexible nanogenerators with high piezoelectric potential (Hussain et al, 2014; Khan et al., 2014).

Although both methods mentioned above are effective in terms of increasing the piezoelectric performance of ZnO nanostructures, they also bring some limitations depending on the application areas. For example, heat treatment applications are conducted at temperatures above 300°C, which is not suitable for ZnO nanostructures grown by hydrothermal methods, especially on polymer-based flexible substrates. Because such substrates have limited thermal stability against elevated temperatures and carry the risk of structural deformation. On the other hand, although oxygen plasma treatments are effective in terms of surface improvement, costly and technically

demanding equipment such as special vacuum systems and plasma generators are required for the application of these processes. This situation can limit the application areas, especially in large-scale production processes or low-budget laboratory environments.

In line with these limitations, doping methods applied to control electrical and structural defects within the ZnO crystal structure, which can be applied at low temperatures and are compatible with flexible substrates, also offer an effective approach to increase piezoelectric performance. By integrating appropriate doping elements into the ZnO lattice at certain ratios, control over both carrier density and crystal orientation can be achieved; thus, the piezoelectric output signal can be significantly improved. In addition, since doping processes can be integrated with the hydrothermal synthesis process, it stands out as a cost-effective solution that does not require elevated temperatures or extra special equipment for ZnO nanostructures synthesized for use in flexible electronic applications.

Different p-type and n-type doping elements can be used in doping ZnO nanostructures. In n-type doping, the dopant induces crystal lattice strain along the polar c axis of the ZnO nanostructures, thus increasing the piezoelectric coefficient. So, the output performance of piezoelectric nanogenerators has improved. However, if the ionic radius of the dopant is too large or the dopant concentration is too high, more lattice defects may be generated, which prevents the charge from flowing in the external circuit and reduces the performance of output. The choosing proper dopant ion and optimized the dopant concentration have significant importance for n-type doping. In p-type doping, the screening effect of free electrons in the ZnO nanostructures is reduced by the dopant ions. It is expected that these elements will reduce the leakage current by capturing free electrons in the crystal structure and thus increase the piezoelectric potential (Hu et al., 2019). Elements with an ionic radius similar to Zn^{2+} ion (0.74 Å) and which can replace Zn^{2+} ion are preferred in p-type doping applications.

To increase the piezoelectric performance of ZnO nanostructures, doping studies with some halogen ions such as fluoride (F^-), chloride (Cl^-), bromide (Br^-) or iodide (I^-) have been carried out. It is expected that the difference in ionic radii between oxygen and halogen ions will affect the piezoelectric performance by changing the compressive or tensile lattice strain in the ZnO crystal lattice structure. The ionic radii of O^{2-}, F^-, Cl^-, Br^- and I^- ions are given as 1.4, 1.33, 1.81, 1.93 and 2.20 Å, respectively. The strains

formed in the ZnO lattice because of the replacement of halogen ions with oxygen ions are determined as follows: −0.035% (F-doped) < 0.16% (I-doped) < 0.30% (Cl-doped) < 0.45% (Br-doped). The piezoelectric voltage values are listed as $V_{F\text{-}ZnO}<V_{ZnO}<V_{I\text{-}ZnO}<V_{Cl\text{-}ZnO}<V_{Br\text{-}ZnO}$. In F-doped ZnO nanowires, since the F^- radius is slightly smaller than the O^{2-} radius, compressive strain occurs in the crystal structure and decreases the output performance. However, the ionic radii of Cl^-, Br^- and I are all larger than O^{2-}. The expansion strain formed along the c-axis of the ZnO lattice increases the tensile strain and improves the performance of piezoelectric nanogenerators. Since the I^- radius is much larger than O^{2-}, the lattice of the ZnO crystal is defective and distorted, and the screening effect of free electrons is also increased and decreases the piezoelectric performance than expected. (Zhang et al., 2016).

Figure 4.1 shows the comparison graph of the changes in the piezoelectric coefficient (d_{33}) of the ZnO structure doped with different metal ions. ZnO nanowires doped with metal ions exhibit higher d_{33} compared to pure ZnO nanowires. The doped metal ion (M^{n+}) replaces the Zn^{2+} ion in the ZnO crystal region to form an M–O bond. When the size of the doped metal ion is small, it results in easier rotation of the nonlinear M–O bonds along the c-axis under the applied field. This produces a large piezoelectric displacement and increases the d_{33} value. On the other hand, when the size of the doped ion is large, it becomes difficult to rotate the nonlinear M–O bond, resulting in a decrease in the piezoelectric response and d_{33} value. However, when the size of the doped ion is large, the orientation of ZnO nanowires along the c-axis will be increased and the lattice constant in ZnO crystals will be decreased along the c-axis. The synergistic effect between these two effects (increase of orientation and decrease of reduced lattice constant) will enhance the piezoelectric response and d_{33} value (Hu et al., 2019). In the literature, studies, it was determined that Cu^{2+} doping (2.0% at.) increased the d_{33} value of the ZnO nanofilm structure from 12 pm/V to 14 pm/V (Wang et al., 2006). It was determined that the d_{33} value increased to 30 pC/N in ZnO nanoparticles doped with 1 mol% Ce (Sinha et al., 2014). The d_{33} value for 5 M % Eu-doped ZnO nanorods was determined as 43.38 pm/V (Yadav et al., 2016). As a result of doping the ZnO thin film with low concentrations of Mg, d_{33} was determined as 54.1 pm/V (Chen et al., 2017). In La-doped ZnO nanoparticles, the d_{33} value was measured as 101.30 pm/V. The reason for this extremely high value was stated to be that the nonlinear La-O bonds formed in the crystal structure have stronger polarity than the Zn-

O bonds (Goel et al., 2017). In the V-doped ZnO thin film structures with up to 2.5% at. doping ratio, the d_{33} value increased and the maximum d_{33} value was measured as 110 pC/N with 2.5% doping (Yang et al., 2008). Luo et al. investigated the effect of Fe doping on ZnO d_{33} values and claimed that the results changed depending on the ionic radius of the Fe ion. They synthesized Fe^{3+} (0.64 Å) and Fe^{2+} (0.76 Å) doped ZnO film layers and measured the d_{33} values as 127 pC/N and 7 pC/N, respectively. They determined that this difference was due to the rotation movements of the Fe-O bonds under the electric field. They reported that the Fe^{3+}-O bond showed stronger polarity and since its ionic radius is smaller than Zn^{2+}, it can rotate more easily under the electric field, thus exhibiting a higher d_{33} value. On the contrary, since the ionic radius of Fe^{2+} is larger than Zn^{2+}, it can rotate more difficult under the electric field, thus exhibiting a lower d_{33} value (Luo et al., 2010).

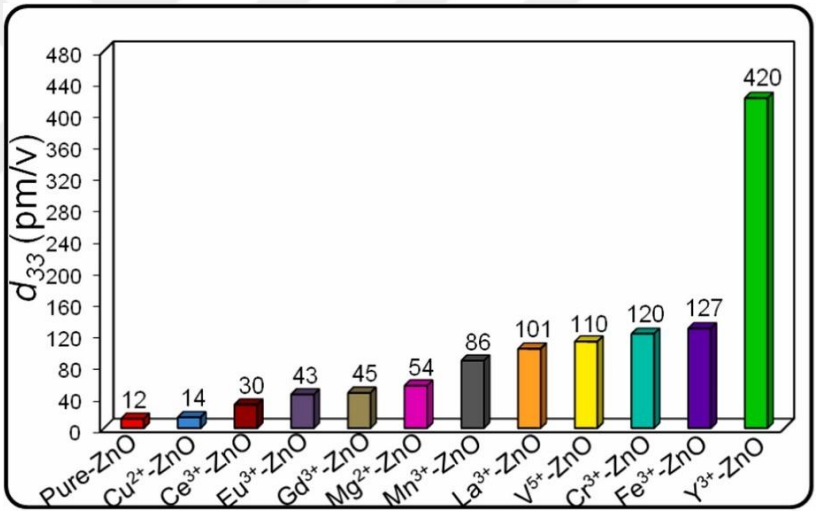

Figure 4.1. *Comparison of piezoelectric coefficient (d_{33}) of pure ZnO and M-ZnO doped with various metal ions (Hu et al., 2019)*

Ahmad et al. doped the ZnO nanorods with group I elements, the output voltage values increased by 2-3 times compared to the as-grown ZnO nanorods. They obtained the following voltage values for the 2% sodium (Na), potassium (K) and lithium (Li) doped ZnO nanorod arrays: V_{ZnO} (0.5 V) < V_K (0.85 V) < V_{Na} (1.23 V) < V_{Li} (1.87 V). Also, they reported that the piezoelectric voltage values obtained by applying oxygen surface treatment to the doped ZnO nanorods increased by approximately 30% (Ahmad et al., 2022). Shin et al. made a flexible nanogenerator by adding Li-doped ZnO nanowires into PDMS. Before the nanogenerator application they applied heat treatment

to Li-doped ZnO nanowires at 550°C in an oxygen atmosphere. Then, they produced a nanogenerator module and applied polarization process to this nanogenerator module. As a result, they obtained approximately 9 V output voltage and 3 mA output current with 10% Li-doped ZnO nanogenerator module by bending process (Shin et al., 2014). However, it is not possible to say that the high voltage obtained here is obtained completely from Li-doped ZnO nanowires. The effect of PDMS polymer in nanogenerator structure on the output voltage should be taken into consideration. Sohn et al. determined that Li doping increases the piezoelectric potential of ZnO by decreasing the free electron density in the ZnO nanowire structure. They obtained an output voltage of 2.9 V with Li-doped ZnO nanowires and reported that this value was 30 times higher than undoped ZnO nanowires (Sohn et al., 2013). It has been reported that the 10 cm^2 Ag-doped ZnO nanowire-based nanogenerator, which was developed to harvest energy from sound waves, has an output voltage of 4 V, an output current of 1 μA and a power of 0.5 μW. It has been determined that these values obtained with Ag-doped ZnO nanowires are 3 times higher than the pure ZnO nanowires (Lee et al., 2013). Rare earth elements are also used in the synthesis of p-type ZnO nanowires. Kank et al. investigated the effect of the rare earth element Lanthanum (La) on the piezoelectric properties of ZnO nanowires. They designed nanogenerator modules from ZnO nanowire arrays obtained by hydrothermal synthesis using 5% mol La. In their measurements, they obtained approximately 40% higher (3 V) output voltage of nanogenerators produced with La-doped ZnO nanowires compared to undoped ZnO nanowires (Kang et al., 2019).

Shin et al. designed a V-doped ZnO nanosheet/PDMS composite nanogenerator to obtain maximum output voltage and tried to determine both the optimum vanadium doping ratio in the ZnO nanosheet structure and the most suitable doped ZnO nanosheet amount in the PDMS matrix. They determined that the output voltage value was 32 V and the output current was 6.2 μA when the vanadium doping in the ZnO nanosheet structure was at. 13% and the doped ZnO nanosheet amount in the PDMS matrix was wt. 10% (Shin et al., 2016). Sinha et al. synthesized undoped 1-D ZnO nanowires and Y-doped 2-D ZnO nanosheets. The d_{33} value for Y-doped ZnO nanosheets was measured as 420 pm/V. The main reason for the high electromechanical response was shown to be that the nonlinear Y-O bonds exhibit stronger polarity than the Zn-O bonds and rotate more easily along the c-axis under electric field. In the nanogenerators they

produced by dispersing undoped ZnO nanowires and Y-doped ZnO nanosheets in PDMS, an output voltage value of 2 V was observed for undoped ZnO nanowires and 20 V for Y-doped ZnO nanosheets (Sinha et al., 2018).

As mentioned before, there are many doping studies aimed at increasing the piezoelectric properties of ZnO nanoparticles and ZnO nanowires, especially the d_{33} piezoelectric coefficient. In contrast, studies on improving the piezoelectric performance of ZnO nanowalls are quite limited. The main reason for this situation is that nanowall structures are generally preferred in sensor applications due to their high surface area. However, in recent years, with the understanding that ZnO nanowalls can be used as active piezoelectric layers in piezoelectric nanogenerators, the necessity of piezoelectric performance enhancement studies for these structures has emerged. Accordingly, the research objective of this study is to obtain ZnO nanowalls doped with different elemental ions in a controlled manner by hydrothermal synthesis method to increase the piezoelectric performance of ZnO nanowall structures. Thus, it is aimed to develop higher performance active layers for piezoelectric nanogenerator applications by taking advantage of the high surface area provided by the nanowall morphology and the synergistic effect of the doping elements.

4.2. Experimental

4.2.1 Hydrothermal synthesis of doped ZnO nanowalls

An aluminum foil (5 cm × 5 cm) was used as the substrate, which acts as the bottom electrode. Before the hydrothermal synthesis, the substrates were cleaned with acetone for 10 minutes and then left to dry. Table 4.1 shows the experimental conditions used in this study. Throughout the text, the ZnO-X-Y designation system where X and Y refer to doping element and the amount of the doping element in at. % respectively, is used for describing the samples developed in this study.

Hydrothermal synthesis was performed as described in the literature (Kaur and Singh, 2020). Equal molar (1:1) zinc nitrate hexahydrate ($Zn(NO_3)_2$, Sigma Aldrich, MW: 297.49 $g.mol^{-1}$) and hexamethylenetetramine (HMTA, $C_6H_{12}N_4$, MERCK, MW: 140.19 $g.mol^{-1}$) aqueous solutions at 25 mM concentration were prepared. Mg, Fe, Al, Li, and Mn were used as dopants in the study. Since hydrothermal synthesis will be carried out, the salt forms of these dopants, $Mg(NO_3)_2 \cdot 6H_2O$ (MERCK, MW: 256.41 $g.mol^{-1}$), $Fe(NO_3)_3 \cdot 9H_2O$ (MERCK, MW: 404.00 $g.mol^{-1}$), $Al(NO_3)_3 \cdot 9H_2O$ (MERCK,

MW: 375.13 g.mol^{-1}), LiCl (Fluka, MW: 42.39 g.mol^{-1}), and $Mn(NO_3)_2 \cdot 4H_2O$ (MERCK, MW: 251.01 g.mol^{-1}), were used. The hydrothermal synthesis steps are shown in Figure 4.2. The 25 mM zinc nitrate hexahydrate, HMTA and determined amount of dopants (Table 4.1) were added into distilled water (200 ml) and mixed with magnetic stirrer at room temperature for 20 minutes. At the end of the process, a clear solution was obtained. The cleaned aluminum foil substrates were placed on the solution. Because of the surface tension, aluminum foil was floating over the solution meniscus. The beaker was covered then placed in a hot water bath previously set at 95° kept for 6 h. At the end of the synthesis, the beakers were removed from the hot water bath and allowed to cool to room temperature. After cooling the samples were removed from the beakers and washed several times with distilled water then left to dry at room conditions.

Table 4.1. *Hydrothermal synthesis condition of doped ZnO nanowalls on Al-foil substrates*

Sample Code	Element	*Concentration of Doping Element (at. %)*
ZnO-Mg-0.5	Mg	0.5
ZnO-Mg-1.0	Mg	1.0
ZnO-Mg-2.0	Mg	2.0
ZnO-Fe-0.5	Fe	0.5
ZnO-Fe-1.0	Fe	1.0
ZnO-Fe-2.0	Fe	2.0
ZnO-Al-0.5	Al	0.5
ZnO-Al-1.0	Al	1.0
ZnO-Al-2.0	Al	2.0
ZnO-Li-0.5	Li	0.5
ZnO-Li-1.0	Li	1.0
ZnO-Li-2.0	Li	2.0
ZnO-Mn-0.5	Mn	0.5
ZnO-Mn-1.0	Mn	1.0
ZnO-Mn-2.0	Mn	2.0

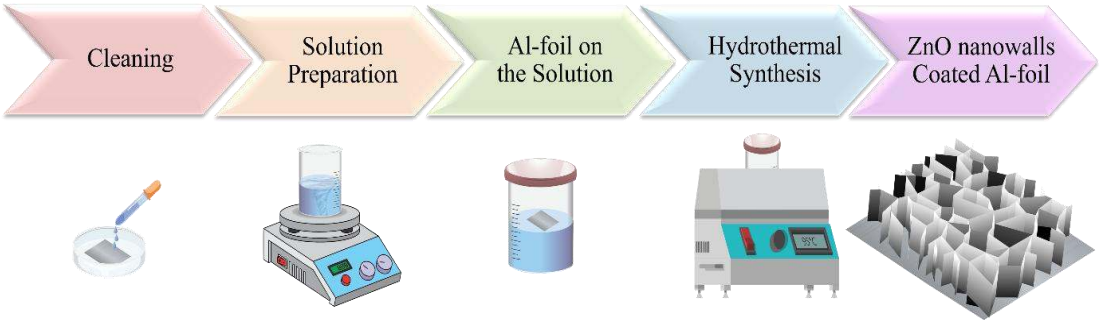

Figure 4.2. *Schematic illustration of hydrothermal synthesis of doped ZnO nanowall arrays on Al-foil*

4.2.2. Characterization

X-ray diffraction (XRD, Bruker D2 Phaser, Cu anode kα1 = 1.54 Å) analysis was performed to examine the crystal structure of doped ZnO nanowall arrays grown on the surface of aluminum foils and to determine the planes in which the crystals are oriented. Scanning electron microscopy (SEM, Zeiss Supra, secondary electron mode and 15 kV acceleration voltage) analysis was performed for morphological examinations. In addition, the inter-nanowall void lengths of doped ZnO nanowalls grown on aluminum foil substrates were also measured using the Image J program (http-2, 2024).

4.3. Results and Discussions

ZnO nanowall doping processes were carried out via hydrothermal synthesis method at 95°C for 6 hours with the element and additive ratios given in Table 4.1. XRD graphs of ZnO nanowalls obtained as a result of hydrothermal synthesis with Mg are given in Figure 4.3. In the graphs, the diffraction peaks at 2θ= 44.8°, 65.2° and 78.3° belong to the (200), (220) and (311) planes of aluminum in the cubic crystal structure, respectively. The diffraction peaks of the (006), (012) and (110) planes belong to ZnAl:LDH layer were obtained at angles of 2θ = 21.3°, 34.0° and 60.4°. The XRD pattern obtained for all samples is consistent with the studies of Kim et al (Kim et al., 2013). They observed three peaks at 22.7°, 33.6° and 60.1° corresponding to ZnAl:LDH planes in their study, which was confirmed from standard powder diffraction peaks of ZnAl:LDH (JCPDS card No. 85-1327). It was observed that the only diffraction peak belongs to the ZnO structure obtained at 2θ = 34.6° indicate the plane (002) for pure ZnO nanowalls. Since only the diffraction peak belonging to the plane (002) was obtained, it is possible to say that the ZnO structures grown on the substrate have a

preferred growth orientation along the c-axis. No diffraction peaks were observed for Mg and its compounds. This proves that no second phase formation occurred in the structure after hydrothermal synthesis and that the only structure formed was ZnO nanowalls. However, as seen in the graphs, the intensity of the ZnO diffraction peak in the (002) plane decreased with increasing Mg content and shifted slightly to the right. This shift is due to the radius of the Mg^{2+} ion (0.72Å) being smaller than the radius of the Zn^{2+} ion (0.74Å). During doping, Mg^{2+} ions replace Zn^{2+} ions in the ZnO crystal structure. The smaller ionic radius causes shrinkage in the crystal lattice structure, leading to a decrease in the interplanar distance (d). Consequently, the diffraction peaks of the ZnO plane shift to larger angles as a result of the decreased interplanar distance.

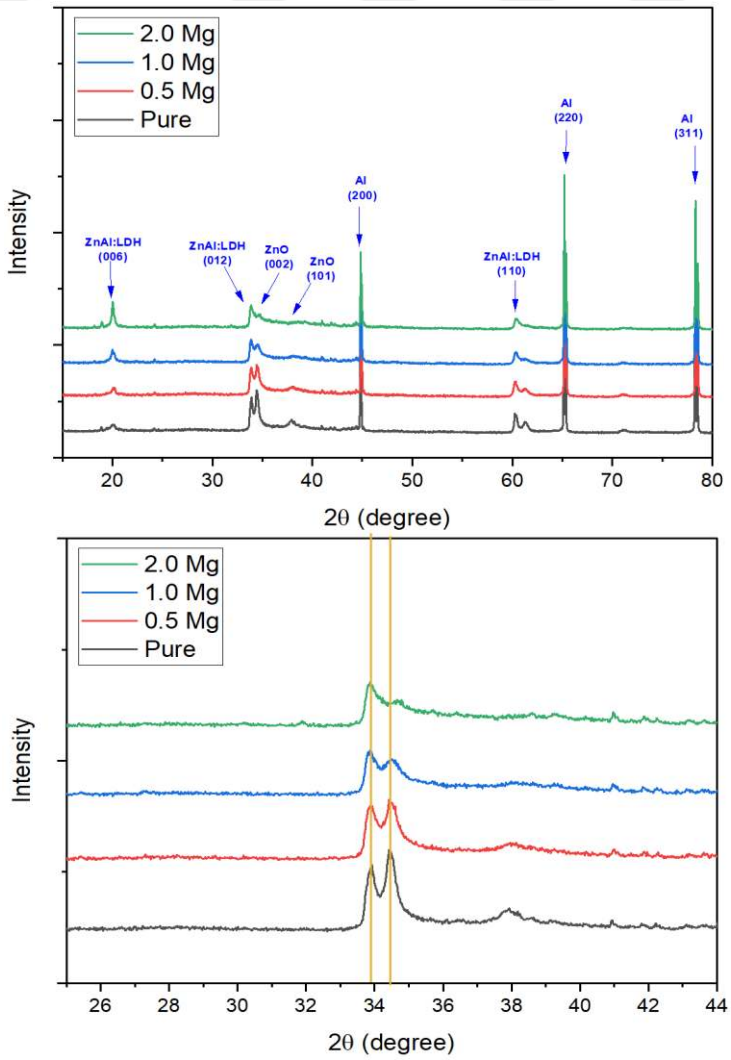

Figure 4.3. *XRD graphs of pure ZnO nanowall, ZnO-Mg-0.5, ZnO-Mg-1.0 and ZnO-Mg-2.0*

Figure 4.4 shows top-view SEM micrographs and void lengths of ZnO nanowall structures doped with Mg. At all three concentrations, ZnO nanowalls with an interconnected network structure were observed on the aluminum foil surface. However, with increasing Mg concentration, the nanowall density per unit area increased and the inter-nanowall void length decreased. The inter-nanowall void lengths of ZnO-Mg-0.5, ZnO-Mg-1.0, and ZnO-Mg-2.0 were measured as 2.083 ± 1.039 µm, 1.758 ± 0.785 µm, and 1.179 ± 0.514 µm, respectively. Even in the 2% doped sample, the nanowall structures began to agglomerate, thus disrupting the network-like nanowall structure.

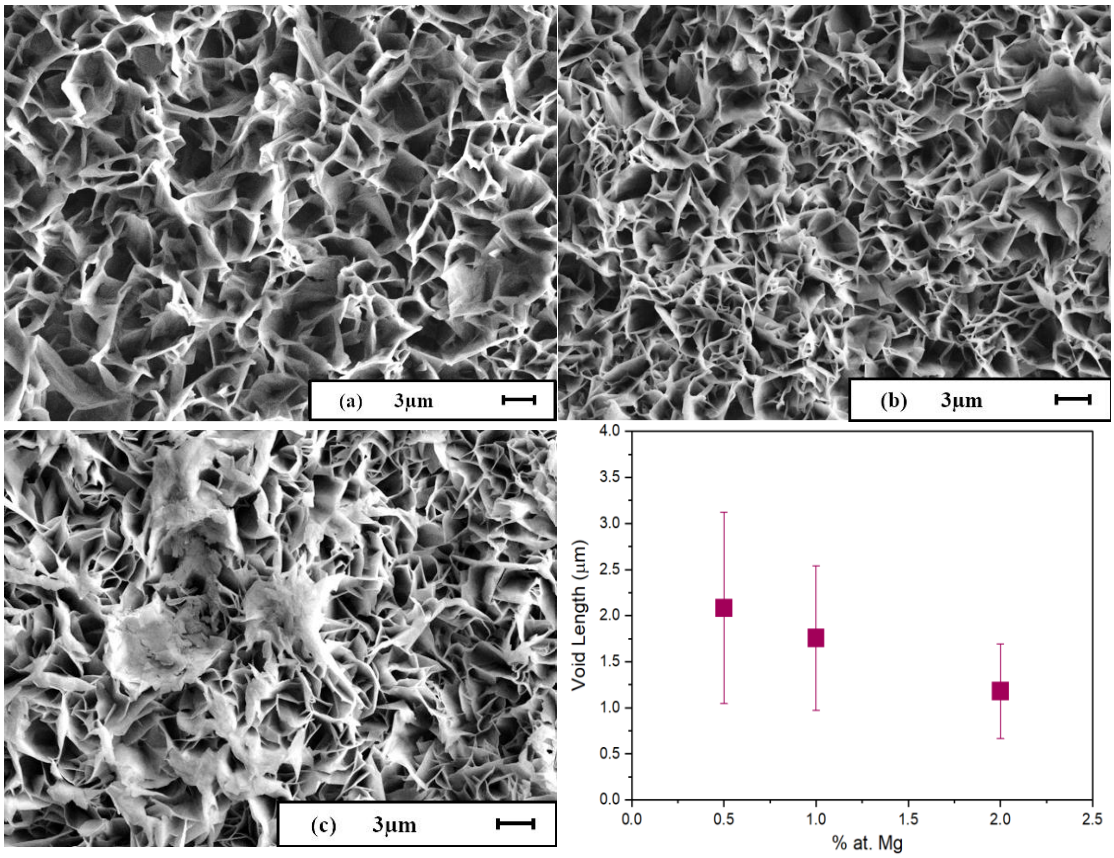

Figure 4.4. *Top-view SEM micrographs of a) ZnO-Mg-0.5, b) ZnO-Mg-1.0, c) ZnO-Mg-2.0 and graph of void length variation as a function of dopant concentration*

XRD graphs of ZnO nanowalls obtained as a result of hydrothermal synthesis with Fe are given in Figure 4.5. In the graphs, the diffraction peaks at 2θ= 44.8°, 65.2° and 78.3° belong to the (200), (220) and (311) planes of aluminum in the cubic crystal structure, respectively. The diffraction peaks of the (006), (012) and (110) planes belong to ZnAl:LDH layer were obtained at angles of 2θ = 21.3°, 34.0° and 60.4°. The XRD pattern obtained for all samples is consistent with the studies of Kim et al (Kim et al.,

2013). They observed three peaks at 22.7°, 33.6° and 60.1° corresponding to ZnAl:LDH planes in their study, which was confirmed from standard powder diffraction peaks of ZnAl:LDH (JCPDS card No. 85-1327). It was observed that the only diffraction peak belongs to the ZnO structure obtained at $2\theta = 34.6°$ indicate the plane (002) for pure ZnO nanowalls. Since only the diffraction peak belonging to the plane (002) was obtained, it is possible to say that the ZnO structures grown on the substrate have a preferred growth orientation along the c-axis. No diffraction peaks were observed for Fe and its compounds. This proves that no second phase formation occurred in the structure after hydrothermal synthesis and that the only structure formed was ZnO nanowalls. However, as seen in the graphs, ZnO diffraction peak in the (002) plane shifted slightly to the right with an increase in Fe content. This shift is due to the radius of the Fe^{3+} ion (0.65 Å) being smaller than the radius of the Zn^{2+} ion (0.74Å). During doping, Fe^{3+} ions replace Zn^{2+} ions in the ZnO crystal structure. The smaller ionic radius causes shrinkage in the crystal lattice structure, leading to a decrease in the interplanar distance (d). Consequently, the diffraction peaks of the ZnO plane shift to larger angles as a result of the decreased interplanar distance. Unlike the Mg doping, there was no significant decrease in peak intensities in Fe doped ZnO nanowall structures.

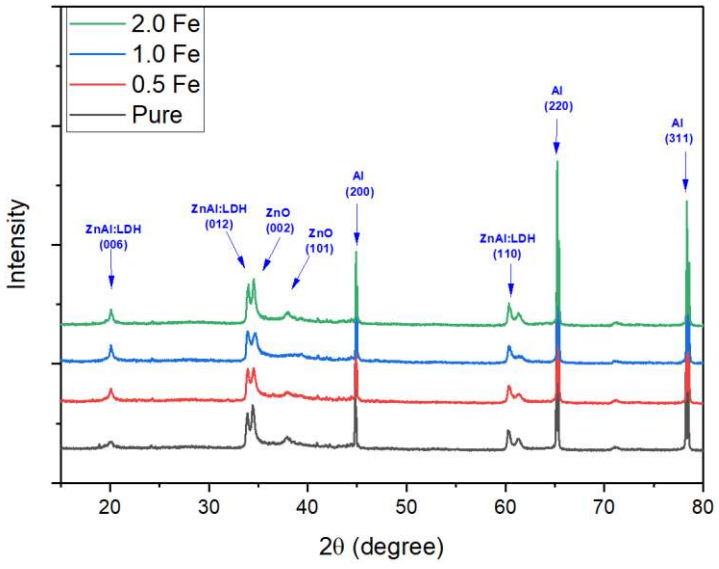

Figure 4.5. *XRD graphs of pure ZnO nanowall, ZnO-Fe-0.5, ZnO-Fe-1.0 and ZnO-Fe-2.0*

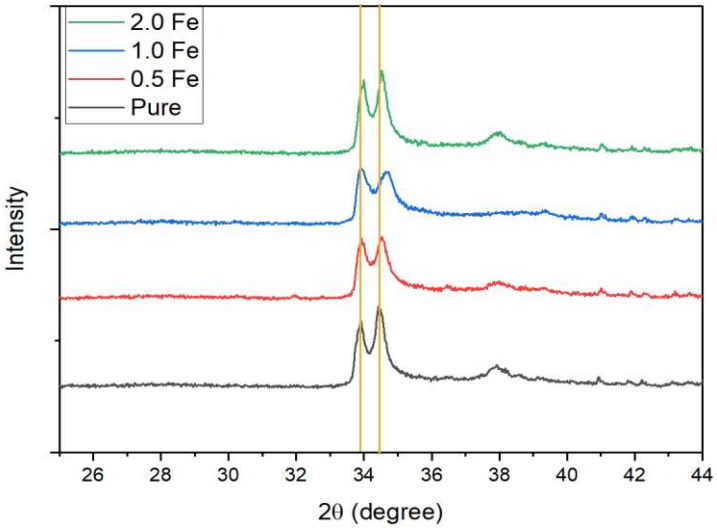

Figure 4.5. (Continued) *XRD graphs of pure ZnO nanowall, ZnO-Fe-0.5, ZnO-Fe-1.0 and ZnO-Fe-2.0*

Figure 4.6 shows top-view SEM micrographs and void-lengths of ZnO nanowall structures doped with Fe. At all three concentrations, ZnO nanowalls with an interconnected network structure were observed on the aluminum foil surface. No significant change in ZnO nanowall morphology was observed with varying Fe concentrations, but the nanowall density per unit area increased with increasing concentration, and the inter-nanowall void length decreased. The inter-nanowall void lengths of ZnO-Fe-0.5, ZnO-Fe-1.0, and ZnO-Fe-2.0 were measured as 1.798 ± 0.829 µm, 1.646 ± 0.815 µm, and 1.618 ± 0.692 µm, respectively.

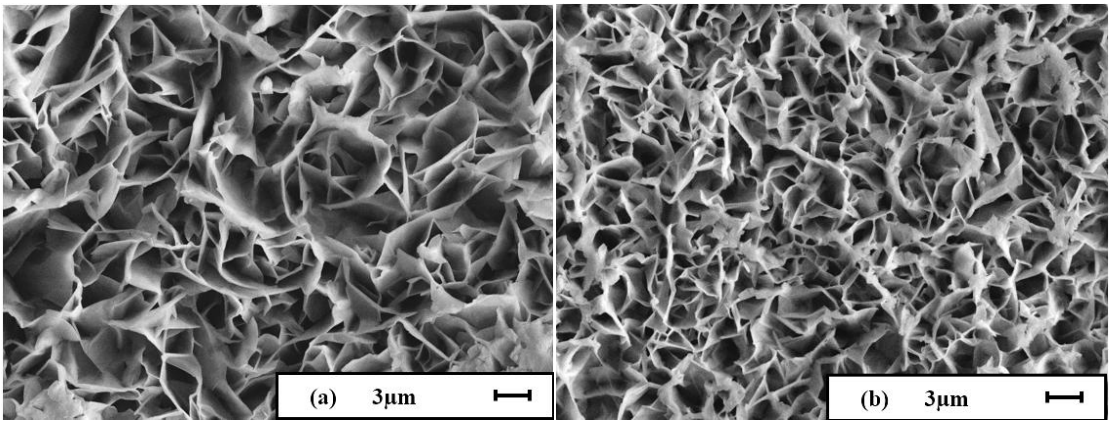

Figure 4.6. *Top-view SEM micrographs of a) ZnO-Fe-0.5, b) ZnO-Fe-1.0, c) ZnO-Fe-2.0 and graph of void length variation as a function of dopant concentration*

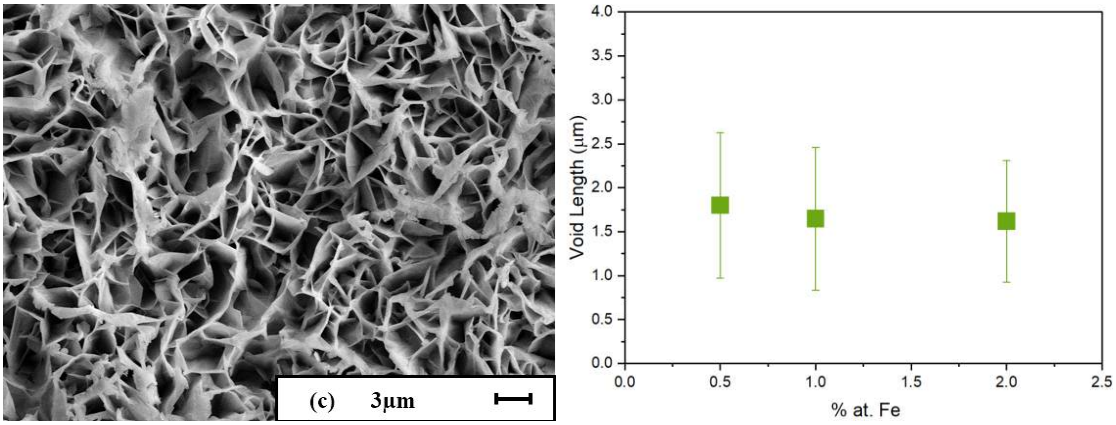

Figure 4.6. (Continued) *Top-view SEM micrographs of a) ZnO-Fe-0.5, b) ZnO-Fe-1.0, c) ZnO-Fe-2.0 and graph of void length variation as a function of dopant concentration*

XRD graphs of ZnO nanowalls obtained as a result of hydrothermal synthesis with Al are given in Figure 4.7. In the graphs, the diffraction peaks at 2θ= 44.8°, 65.2° and 78.3° belong to the (200), (220) and (311) planes of aluminum in the cubic crystal structure, respectively. The diffraction peaks of the (006), (012) and (110) planes belong to ZnAl:LDH layer were obtained at angles of 2θ = 21.3°, 34.0° and 60.4°. The XRD pattern obtained for all samples is consistent with the studies of Kim et al (Kim et al., 2013). They observed three peaks at 22.7°, 33.6° and 60.1° corresponding to ZnAl:LDH planes in their study, which was confirmed from standard powder diffraction peaks of ZnAl:LDH (JCPDS card No. 85-1327). It was observed that the only diffraction peak belongs to the ZnO structure obtained at 2θ = 34.6° indicate the plane (002) for pure ZnO nanowalls. Since only the diffraction peak belonging to the plane (002) was obtained, it is possible to say that the ZnO structures grown on the substrate have a preferred growth orientation along the c-axis. No diffraction peaks were observed for Al and its compounds. This proves that no second phase formation occurred in the structure after hydrothermal synthesis and that the only structure formed was ZnO nanowalls. However, as seen in the graphs, ZnO diffraction peak in the (002) plane shifted slightly to the right with an increase in Al content. This shift is due to the radius of the Al^{3+} ion (0.56 Å) being smaller than the radius of the Zn^{2+} ion (0.74Å). During doping, Al^{3+} ions replace Zn^{2+} ions in the ZnO crystal structure. The smaller ionic radius causes shrinkage in the crystal lattice structure, leading to a decrease in the interplanar distance (d). Consequently, the diffraction peaks of the ZnO plane shift to larger angles as a result of the decreased interplanar distance. It was also observed that the intensity of the ZnO (002) diffraction peak increased with increasing Al content.

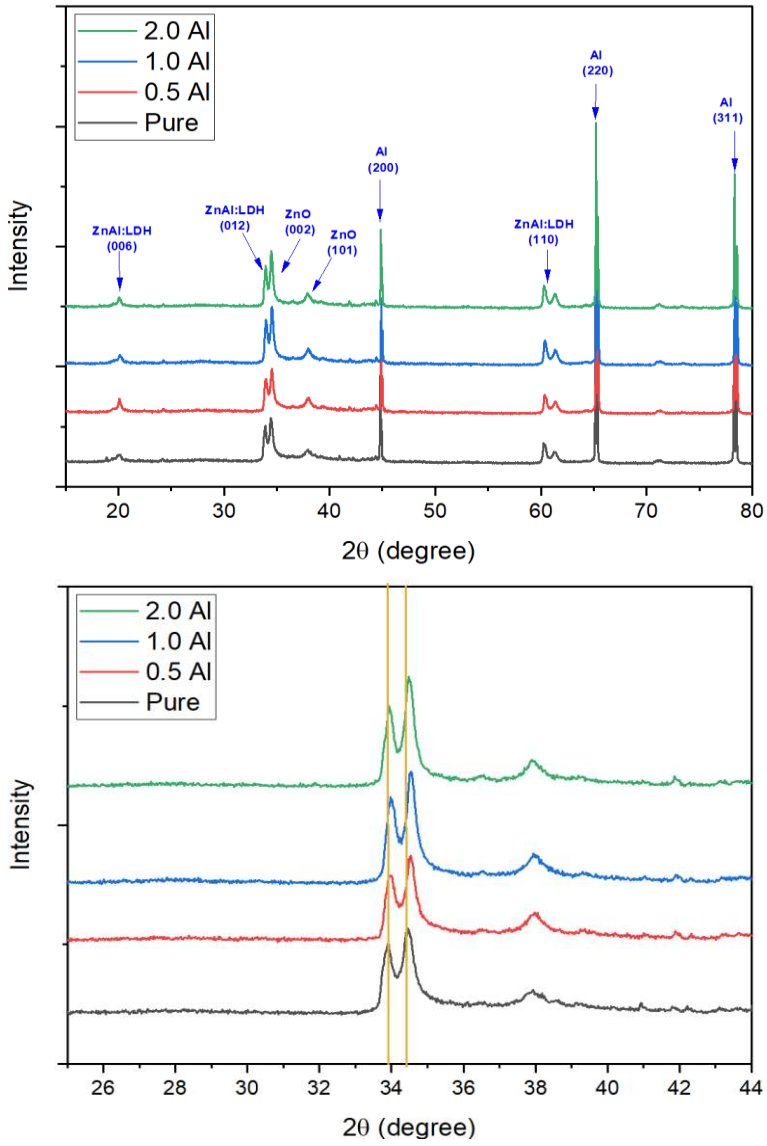

Figure 4.7. *XRD graphs of pure ZnO nanowall, ZnO-Al-0.5, ZnO-Al-1.0 and ZnO-Al-2.0*

Figure 4.8 shows top-view SEM micrographs and void lengths of ZnO nanowall structures doped with Al. At all three concentrations, ZnO nanowalls with an interconnected network structure were observed on the aluminum foil surface. It was observed that, with increasing Al concentration, the nanowalls became thinner and gained sharper lines, the nanowall density per unit area increased and the inter-nanowall void lengths decreased. The inter-nanowall void lengths of ZnO-Al-0.5, ZnO-Al-1.0, and ZnO-Al-2.0 were measured as 1.822 ± 0.886 µm, 1.452 ± 0.692 µm, and 1.226 ± 0.527 µm, respectively.

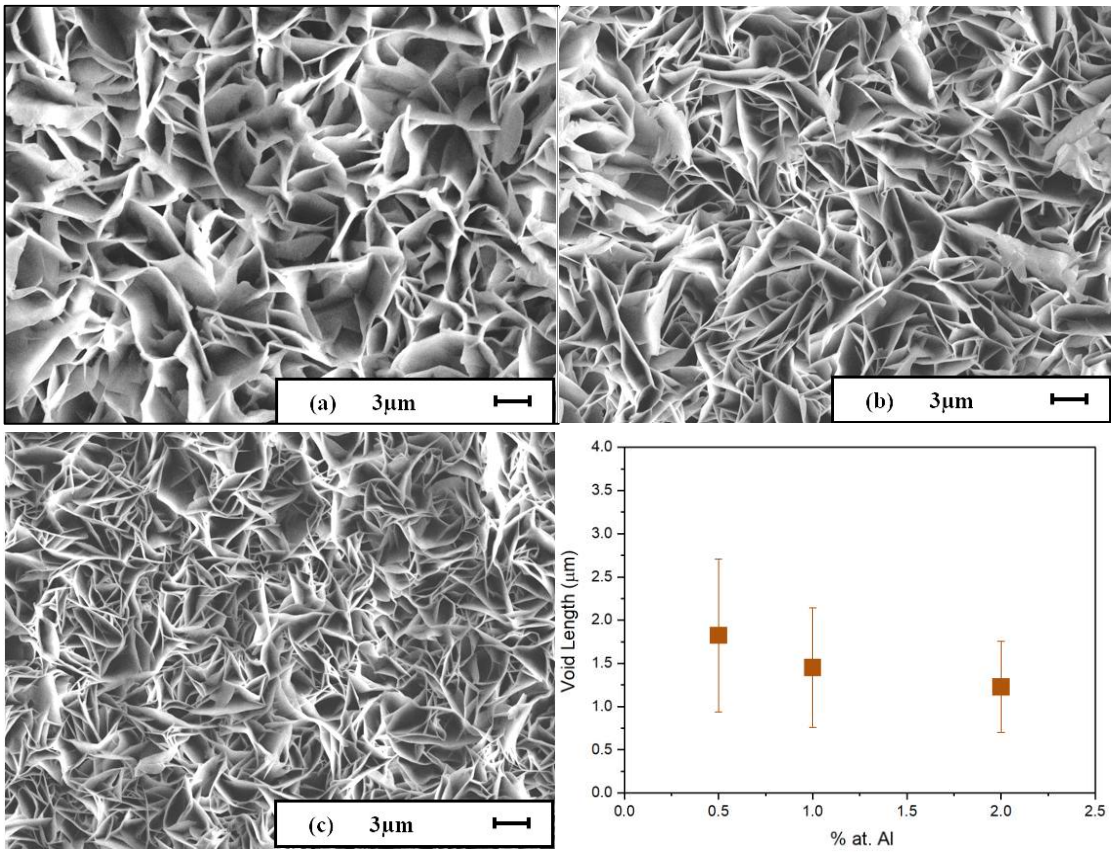

Figure 4.8. *Top-view SEM micrographs of a) ZnO-Al-0.5, b) ZnO-Al-1.0, c) ZnO-Al-2.0 and graph of void length variation as a function of dopant concentration*

XRD graphs of ZnO nanowalls obtained as a result of hydrothermal synthesis with Li are given in Figure 4.9. In the graphs, the diffraction peaks at 2θ= 44.8°, 65.2° and 78.3° belong to the (200), (220) and (311) planes of aluminum in the cubic crystal structure, respectively. The diffraction peaks of the (006), (012) and (110) planes belong to ZnAl:LDH layer were obtained at angles of 2θ = 21.3°, 34.0° and 60.4°. The XRD pattern obtained for all samples is consistent with the studies of Kim et al (Kim et al., 2013). They observed three peaks at 22.7°, 33.6° and 60.1° corresponding to ZnAl:LDH planes in their study, which was confirmed from standard powder diffraction peaks of ZnAl:LDH (JCPDS card No. 85-1327). It was observed that the only diffraction peak belongs to the ZnO structure obtained at 2θ = 34.6° indicate the plane (002) for pure ZnO nanowalls. Since only the diffraction peak belonging to the plane (002) was obtained, it is possible to say that the ZnO structures grown on the substrate have a preferred growth orientation along the c-axis. No diffraction peaks were observed for Li and its compounds. This proves that no second phase formation occurred in the structure after hydrothermal synthesis and that the only structure formed was ZnO nanowalls.

However, as seen in the graphs, ZnO diffraction peak in the (002) plane shifted slightly to the right with an increase in Li content. This shift is due to the radius of the Li^{+} ion (0.60 Å) being smaller than the radius of the Zn^{2+} ion (0.74Å). During doping, Li^{+} ions replace Zn^{2+} ions in the ZnO crystal structure. The smaller ionic radius causes shrinkage in the crystal lattice structure, leading to a decrease in the interplanar distance (d). Consequently, the diffraction peaks of the ZnO plane shift to larger angles as a result of the decreased interplanar distance. It was also observed that the intensity of the ZnO (002) diffraction peak decreased with increasing Li content up to 2%, but the peak intensity increased significantly when it increased to 2%.

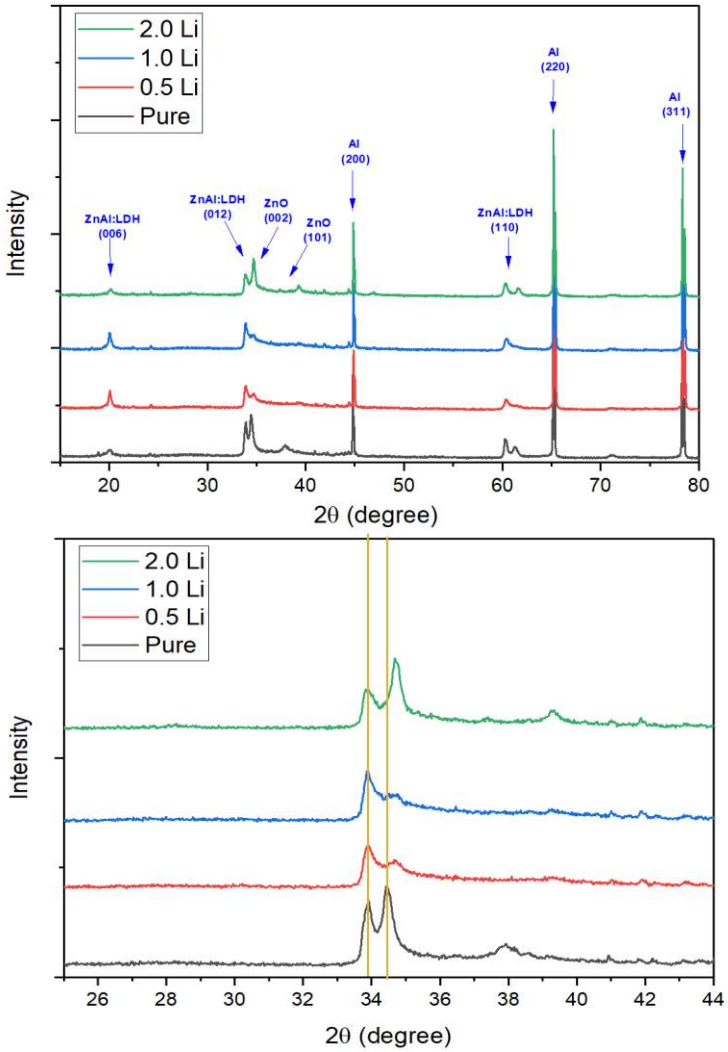

Figure 4.9. *XRD graphs of pure ZnO nanowall, ZnO-Li-0.5, ZnO-Li-1.0 and ZnO-Li-2.0*

Figure 4.10 shows top-view SEM micrographs and void lengths of ZnO nanowall structures doped with Li. At all three concentrations, ZnO nanowalls with an

interconnected network structure were observed on the aluminum foil surface. While coarse nanowall formations were observed in the 0.5% and 1% Li-doped samples, thin nanowall formations with sharp edges were observed in the 2% Li-doped sample. It was also determined that as the doping ratio reached 2%, the inter-nanowall void lengths decreased and the nanowalls began to fold onto each other. The inter-nanowall void lengths of ZnO-Li-0.5, ZnO-Li-1.0, and ZnO-Li-2.0 were measured as 1.422 ± 0.644 µm, 2.132 ± 0.792 µm, and 0.812 ± 0.402 µm, respectively. Consequently, the nanowall density per unit area increased.

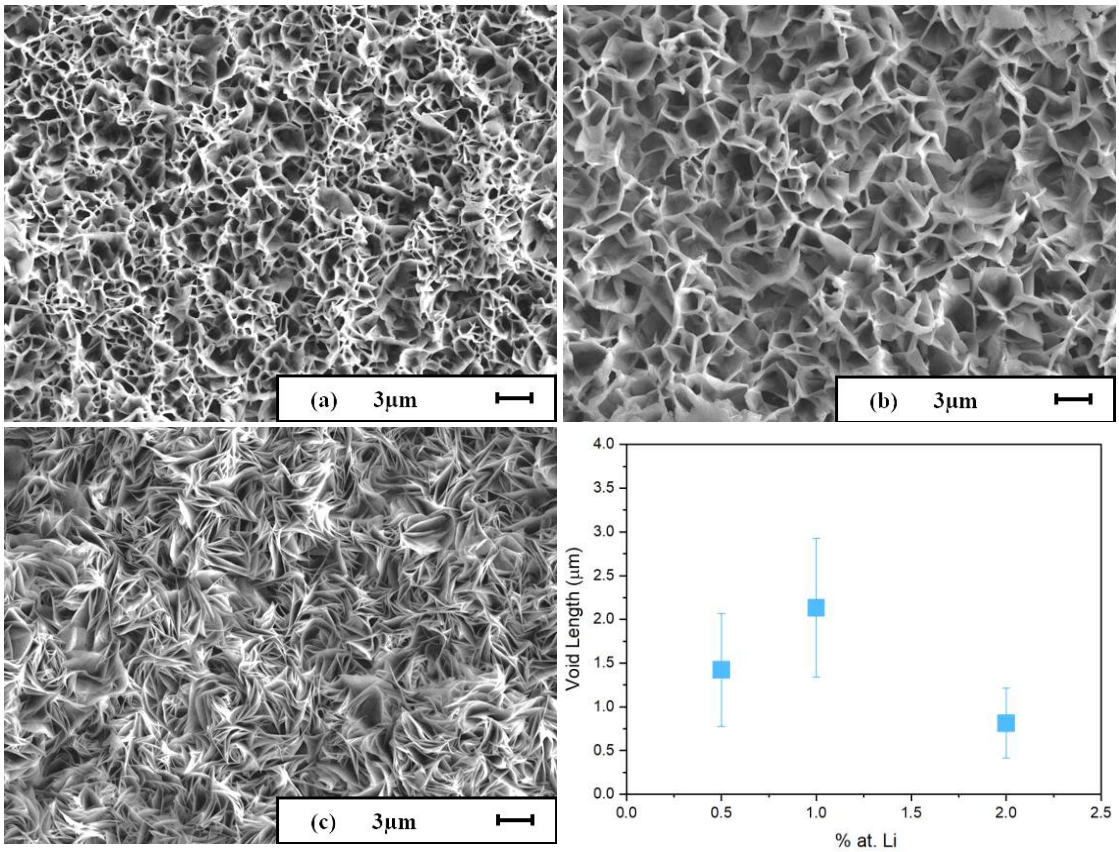

Figure 4.10. *Top-view SEM micrographs of a) ZnO-Li-0.5, b) ZnO-Li-1.0, c) ZnO-Li-2.0 and graph of void length variation as a function of dopant concentration*

XRD graphs of ZnO nanowalls obtained as a result of hydrothermal synthesis with Mn are given in Figure 4.11. In the graphs, the diffraction peaks at 2θ= 44.8°, 65.2° and 78.3° belong to the (200), (220) and (311) planes of aluminum in the cubic crystal structure, respectively. The diffraction peaks of the (006), (012) and (110) planes belong to ZnAl:LDH layer were obtained at angles of 2θ = 21.3°, 34.0° and 60.4°. The XRD pattern obtained for all samples is consistent with the studies of Kim et al (Kim et al.,

2013). They observed three peaks at 22.7°, 33.6° and 60.1° corresponding to ZnAl:LDH planes in their study, which was confirmed from standard powder diffraction peaks of ZnAl:LDH (JCPDS card No. 85-1327). It was observed that the only diffraction peak belongs to the ZnO structure obtained at $2\theta = 34.6°$ indicate the plane (002) for pure ZnO nanowalls. Since only the diffraction peak belonging to the plane (002) was obtained, it is possible to say that the ZnO structures grown on the substrate have a preferred growth orientation along the c-axis. No diffraction peaks were observed for Mn and its compounds. This proves that no second phase formation occurred in the structure after hydrothermal synthesis and that the only structure formed was ZnO nanowalls. However, as seen in the graphs, ZnO diffraction peak in the (002) plane shifted slightly to the right with an increase in Mn content. It was also observed that the intensity of the ZnO (002) diffraction peak decreased with increasing Mn content.

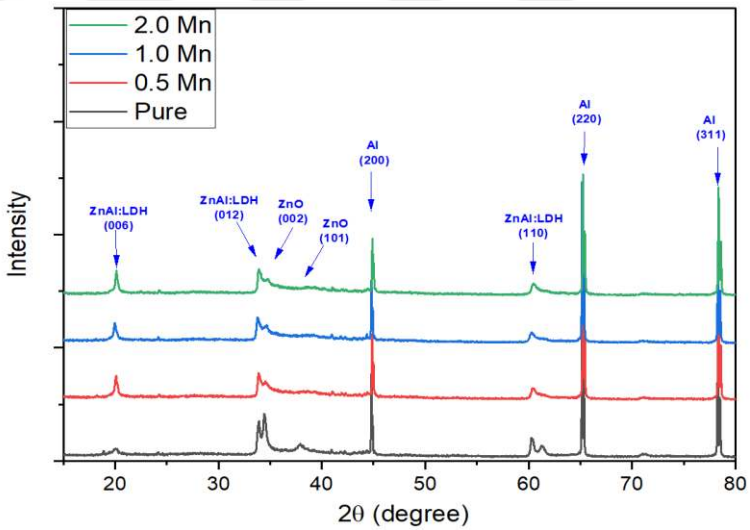

Figure 4.11. *XRD graphs of pure ZnO nanowall, ZnO-Mn-0.5, ZnO-Mn-1.0 and ZnO-Mn-2.0*

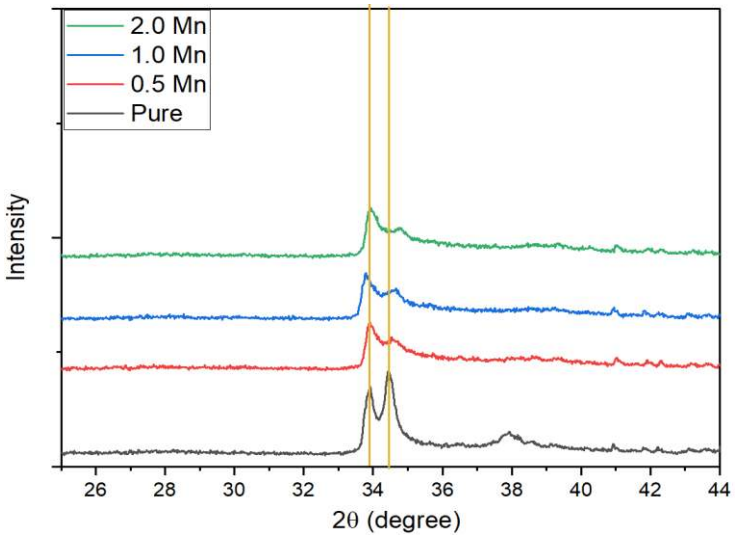

Figure 4. 11. (Continued) *XRD graphs of pure ZnO nanowall, ZnO-Mn-0.5, ZnO-Mn-1.0 and ZnO-Mn-2.0*

Figure 4.12 shows top-view SEM micrographs and void lengths of ZnO nanowall structures doped with Mn. At all three concentrations, ZnO nanowalls with an interconnected network structure were observed on the aluminum foil surface. It was determined that the ZnO nanowalls synthesized at all three doping rates had coarse edges. It was determined that the number of nanowalls per unit area increased as the doping ratio reached 2%. The inter-nanowall void lengths of ZnO-Mn-0.5, ZnO-Mn-1.0, and ZnO-Mn-2.0 were measured as 1.779 ± 0.836 µm, 1.439 ± 0.570 µm, and 1.385 ± 0.565 µm, respectively.

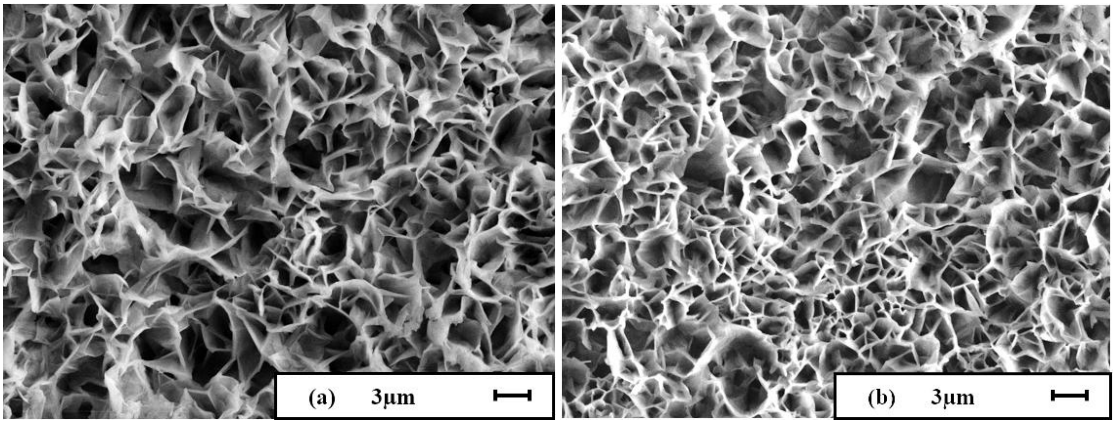

Figure 4.12. *Top-view SEM micrographs of a) ZnO-Mn-0.5, b) ZnO-Mn-1.0, c) ZnO-Mn-2.0 and graph of void length variation as a function of dopant concentration*

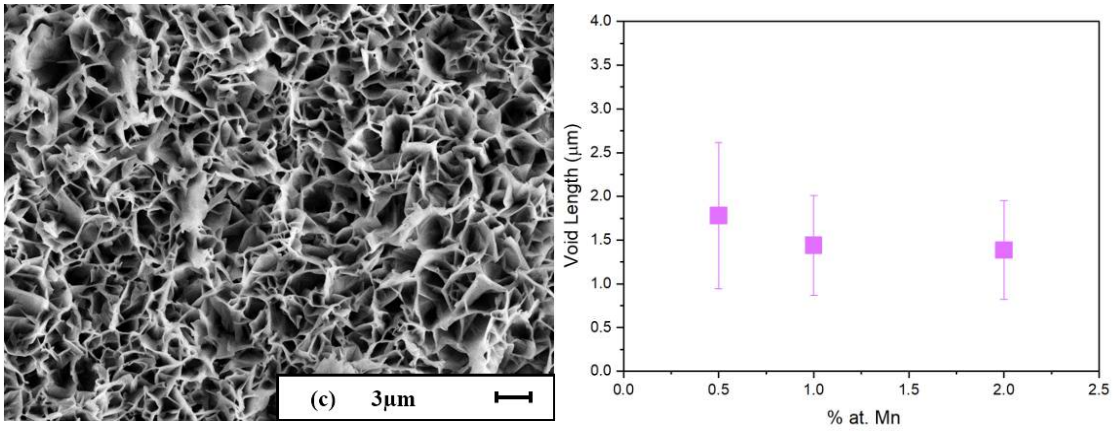

Figure 4.12. (Continued) *Top-view SEM micrographs of a) ZnO-Mn-0.5, b) ZnO-Mn-1.0, c) ZnO-Mn-2.0 and graph of void length variation as a function of dopant concentration*

4.4. Conclusions

In this study, the effect of doping on nanowall structures was systematically investigated to improve the performance of ZnO nanowall-based piezoelectric nanogenerators. In the first step, the main structural defects that limit the efficiency of ZnO nanowalls synthesized via hydrothermal methods and the approaches proposed in the literature for eliminating these defects were evaluated. The findings indicate that such defects can be reduced through doping in the ZnO crystal structure.

A literature review revealed that while doping studies on ZnO nanowire arrays are widespread, doping research on ZnO nanowall arrays remains quite limited. Therefore, it was considered that elements such as Mg, Fe, Al, Li, and Mn could be used as dopants to improve the piezoelectric performance of ZnO nanowalls. Using low concentrations of selected dopants (0.5 2% at.), ZnO nanowall arrays were successfully synthesized on the surface of aluminum foil via hydrothermal synthesis.

XRD analyses performed on the synthesized samples revealed that the dopants used entered the crystal lattice without forming a second phase in the ZnO structure. Furthermore, due to the different radii of the doping ions compared to the Zn^{2+} ions, shifts in diffraction angles were observed in the ZnO crystal structure, and this was attributed to doping-induced lattice distortions. SEM imaging showed that as the doping ratio reached 2%, the void between the nanowalls decreased and the nanowall density per unit area increased.

Although these results indicate that increasing nanowall density can positively affect piezoelectric output, it is thought that decreasing void length may limit

mechanical deformation capabilities, which in turn may negatively impact voltage generation. Therefore, it was concluded that maintaining the doping ratio at an optimum level is critical for maximizing the performance of ZnO nanowall-based nanogenerators.

5. DESIGN OF PIEZOELECTRIC, TRIBOELECTRIC AND HYBRID NANOGENERATOR MODULES AND INTEGRATION ON THE TEXTILE

5.1. Introduction

The rapidly increasing use of portable electronic devices and the increasing interest in wearable technologies have led to the need for low-power, sustainable, and flexible energy sources. In this context, nanogenerator technologies such as piezoelectric nanogenerators (PENGs) and triboelectric nanogenerators (TENGs), which can convert environmental mechanical energy into electrical energy, stand out as attractive alternatives. PENGs are based on the principle that piezoelectric materials generate an electric charge under applied mechanical stress. Furthermore, piezoelectric structures are ideal candidates for biomechanical energy harvesting applications (e.g., walking, breathing, muscle movements) due to their sensitivity to low-frequency vibrations. This technology was first introduced by Wang and Song in 2006 using ZnO nanowire structures (Wang and Song, 2006). Since then, attempts have been made to increase the energy conversion efficiency in PENG systems by using different morphologies (nanowires, nanosheets, nanorods) of piezoelectric ceramics and polymers such as ZnO, $BaTiO_3$, and PVDF. On the other hand, TENGs generate electrical energy from the electrostatic potential difference created by the transfer of surface charges resulting from the physical interaction of two different materials. This technology, introduced by Wang and his team in 2012 (Fan, 2012), has found wide application in energy harvesting and sensor technologies due to its low-cost material selection, extensive design flexibility, and high voltage output. TENG devices are particularly prominent in the evaluation of irregular mechanical energy sources such as human movements, wind, and water droplets.

Both types of nanogenerators offer significant advantages for the integration of energy harvesting systems into micro- and nano-systems. However, the performance of PENG and TENG devices varies depending on many parameters, including the selected material type, surface morphology, electrode design, mechanical strength, and flexibility. For PENG and TENG modules to operate efficiently, numerous parameters, ranging from material properties to structural design, must be carefully optimized. These parameters directly impact performance indicators such as the resulting output voltage, current density, energy conversion efficiency, and device mechanical durability. Therefore, a multidisciplinary approach is required, both in terms of materials

engineering and device architecture. The key factors affecting the performance of these modules are described in detail below.

- ***Material Selection and Crystal Structure***

The piezoelectric coefficient (d_{33}), crystal orientation, and morphology (e.g., ZnO nanowires, $BaTiO_3$ nanoparticles, or PVDF films) of the active material used in piezoelectric modules directly determine the energy conversion capacity. In wurtzite materials such as ZnO, single-crystal nanowires growing in the [0002] direction exhibit high piezoelectric response (Xiang et al., 2006). Crystal quality, defect density, and doping processes play critical roles in enhancing piezoelectric properties or promoting the desired orientation. For triboelectric modules, the material's position in the tribo-serial table, surface charge density, and electron affinity are important. Using materials with different electron acceptors and donor properties maximizes surface charge transfer, resulting in higher electrical output (Zhang and Olin, 2020).

- ***Surface Morphology and Nanostructure Design***

For both types of nanogenerators, surface morphology is a determining parameter in terms of contact area and charge density. Nanostructures with high surface area (e.g., ZnO nanowire arrays or micro/nanopatterned PDMS surfaces) can increase contact efficiency and enhance energy production. Surface roughness also contributes to surface charge accumulation for the triboelectric effect (Jantač et al., 2023).

- ***Electrode Material and Structure***

The electrode material affects energy harvesting efficiency through properties such as conductivity, flexibility, optical transmittance, and mechanical strength. Metal and semiconductor electrodes such as Ag, Au, and ITO offer high conductivity, while carbon-based or metal-coated textile substrates enable flexible device designs. Electrode thickness, interface contact quality, and material compatibility are important for output signal stability (Aazem et al., 2022).

Literature reviews have determined that module design has a significant impact on the electrical output. In this context, module designs with and without polymers have been studied. Another parameter not encountered in the literature reviews but that has an impact on module design is the variety of electrodes used. The Schottky and Ohmic contacts formed by the piezoelectric layer on the bottom and top electrodes used in the module design have a direct impact on the module's output voltage and current values. A Schottky contact is a type of contact formed between a metal with a high work

function and a semiconductor with a lower work function than the metal. The work function can be defined as the amount of energy required to remove a free electron from a molecule. In this case, a barrier forms between the semiconductor and the metal, which restricts the flow of charge carriers, resulting in lower current values. A Schottky contact generally generates high voltage because the barrier increases electrical potential differences and allows charge carriers to flow in only one direction. On the other hand, Ohmic contacts lack an energy barrier created by the work function difference between the metal and the semiconductor, allowing charge carriers to move freely. This results in increased current but limited voltage (Chen et al., 2017; Sheoran, Kumar and Singh, 2022). Table 5.1 summarizes the similarities and differences between Schottky and Ohmic contacts.

Table 5.1. *Similarities and differences between Schottky and Ohmic contact*

Features	**Ohmic Contact**	**Schottky Contact**
Energy Barrier	None or very low	High
Charge Transfer	Free, low resistance	Controlled by energy barrier
Electrical Resistance	Low	Medium – High
Piezoelectric Potential	Weak, piezoelectric charges are quickly neutralized	Piezoelectric potential is maintained
Charge Backflow	Charge flow occurs; energy is lost	Charge backflow is prevented; energy efficiency is high
Output Voltage	Low	High
Output Current	High	Medium
Applications	Low voltage applications	High voltage applications

A summary of the literature research indicates that many parameters, including active layer material selection, electrode material selection, active surface-electrode interfacial interaction, and module design, influence nanogenerator efficiency. However, the efficiency of ZnO nanowall-based nanogenerators has not been thoroughly investigated based on these variables. The research objective of this study is a systematic investigation of the effects of module designs and electrode materials on nanogenerator efficiency.

5.2. Experimental

In the ZnO nanowall-based nanogenerator designs, aluminum foils on which ZnO nanowalls were grown via hydrothermal synthesis were used in Chapter 3 and Chapter 4. The nanogenerator modules were designed in three different ways, as shown in Figure 5.1.

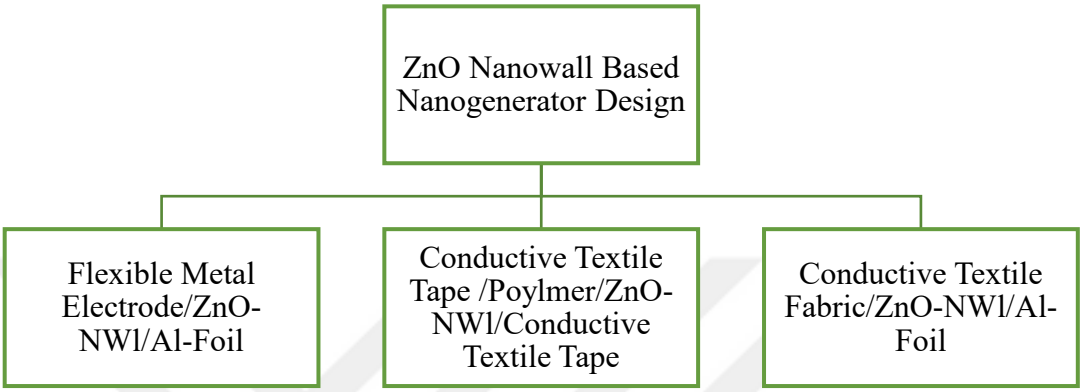

Figure 5.1. *Piezoelectric nanogenerator modules designed using ZnO nanowalls*

5.2.1. Design of flexible metal electrode/ZnO-NWl/Al-foil nanogenerator module

In the designs shown in Figure 5.2, ZnO nanowall-coated aluminum foil was used as the bottom electrode. Flexible aluminum, copper, titanium, zinc, stainless steel, nickel and copper/nickel-coated polyamide fabric, were used as the top electrode. The final structure was encapsulated with Kapton tape to ensure contact between the two electrodes. In this design, the metal foils and fabric used as the top electrode were smaller than the bottom electrode to prevent a potential short circuit between the bottom and top electrodes. The modules were manufactured as follows:

- A conductive copper wire cable was placed in the center of a Kapton tape.
- A ZnO nanowall-coated aluminum foil (with the nanowall structures facing up) was placed on the conductive wire in the center of the Kapton tape.
- Another conductive copper wire was placed in the center of a second Kapton tape.
- The top electrode, cut smaller than the ZnO nanowall-coated aluminum foil, was placed on the copper wire on the second Kapton tape.
- Finally, these two Kapton tapes were adhered to the top electrode and the ZnO nanowalls, overlapping each other.

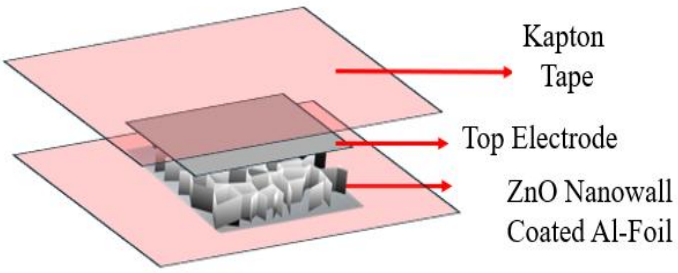

Figure 5.2. *Illustration of Flexible Metal Electrode/ZnO-NWl/Al-Foil Nanogenerator Module*

5.2.2. Design of conductive textile tape/polymer/ZnO-NWl/conductive textile tape nanogenerator module

In the design shown in Figure 5.3, Cu/Ni-coated conductive textile tape was used as the top and bottom electrodes. A module consisting of ZnO nanowall-coated aluminum foil was placed between these two Cu/Ni-coated conductive textile tapes. The remaining parts of the module were insulated with various polymers such as PDMS, Ecoflex, and PVC to prevent potential short circuits between the top and bottom electrodes. The polymer thin films used between the top and bottom electrodes were cut with a doctor blade.

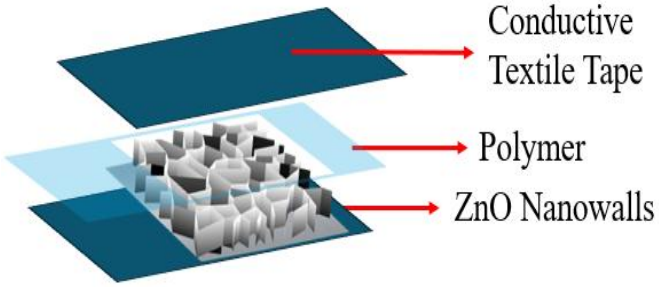

Figure 5.3. *Illustration of Conductive Textile Tape/Polymer/ZnO-NWl/Conductive Textile Tape Nanogenerator Module*

Thin film production with Ecoflex:

- Ecoflex components A and B were mechanically mixed for 2 minutes in a 1:1 volume ratio. Degassing was performed in a vacuum desiccator for 3 minutes to remove air bubbles.
- The prepared polymer mixture was cut on a glass surface with a doctor blade set to 120 µm thickness.

- It was then allowed to be cured for 2 hours at room temperature.

Thin film production with PDMS:

- PDMS components were mechanically mixed for 5 minutes in a 10:1 volume ratio. Degassing was performed in a vacuum desiccator for 30 minutes to remove air bubbles.
- The prepared polymer mixture was cut on a glass surface with a doctor blade set to 120 µm thickness.
- It was then allowed to be cured for 24 hours at room temperature.

PVC thin film production:

- A 1:4 PVC: NMP mixture by mass was prepared by stirring it in a magnetic stirrer at 60°C for 24 hours.
- The prepared polymer mixture was cut onto a glass surface with a doctor blade set at 120µm thickness.
- Then, it was immersed in room-temperature water and left for 4 hours to remove the solvent.
- Finally, it was removed from the water and placed in a 50°C oven until dry.

5.2.3. Design of conductive textile fabric/ZnO-NWl/Al-foil nanogenerator module

This design, intended as a preliminary study for the textile integration of nanogenerator modules, was produced as an alternative to the other two designs. The conductive fabric, intended to be used as the top electrode in the module, was produced before the module design step. Stainless steel wire (No. 12-28, Te 31U, Dia wN 35, N.W. 900 g., B.W. 348 g.) and wool yarns (90% wool / 10% polyester Nm 30/2) were used in conductive textile production.

- To obtain a conductive yarn, the stainless-steel wire and wool yarn were twisted in a yarn twisting machine, first in two plies (200 turns/meter) and then in three plies (200 turns/meter), as indicated in Figure 5.4.
- After the yarn twisting process, wool yarn was made conductive with stainless steel wire. Conductive (gray) and non-conductive (white) fabrics were produced using the circular knitting machine shown in Figure 5.5.

Figure 5.4. *Double and triple twisting processes of conductive yarn and wool yarns*

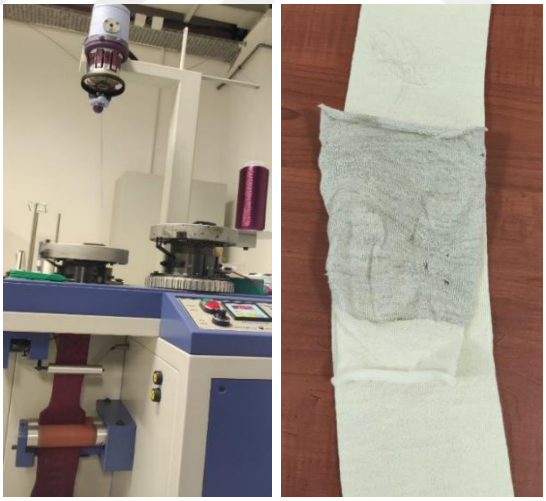

Figure 5.5. *Conductive (grey) and non-conductive (white) fabrics obtained with a circular knitting machine*

- The fabric knitted with wool yarn (white) was planned to be used as the base on which the module will be integrated. A 5 cm x 5 cm window was created in the center of the knitted wool fabric. Then, a 5 cm x 5cm Al18-25-6-95 sample (with the nanowall structures facing up) was sewn into this opening, as shown in Figure 5.6.

- The fabric knitted with conductive yarn was planned to be used as the top electrode. A 5 cm x 5 cm piece was cut from the conductive gray fabric then sewn onto the Al18-25-6-95 sample, as shown in Figure 5.6.

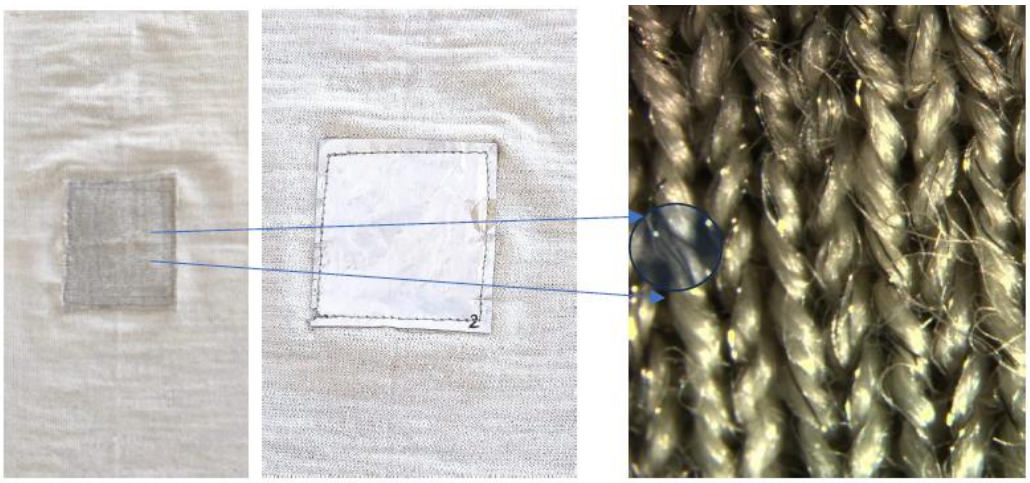

Figure 5.6. *Design of Conductive Textile Fabric/ZnO-NWl/Al-Foil Nanogenerator Module-1*

- Stainless-steel wire (No. 12-28, Te 31U, Diameter wN 35, N.W. 900 g., B.W. 348 g.) and polyester yarns (blue polyester yarn - 500/144T Denier, yellow polyester yarn - 300 denier Ne30/1) were provided. The stainless-steel wire and yellow polyester yarn were twisted on a yarn twisting machine, first in two plies (200 turns/meter), and then in three plies (200 turns/meter), to obtain a conductive yarn, as shown in Figure 5.7.

Figure 5.7. *Double and triple twisting processes of conductive yarn and yellow polyester yarns*

- After the yarn twisting process, conductive (yellow) and non-conductive (blue) fabrics were obtained with the circular knitting machine shown in Figure 5.8.

Figure 5.8. *Non-conductive (blue) and conductive (yellow) fabrics obtained with a circular knitting machine*

- A 5 cm x 5cm window was cut in the center of the knitted blue fabric. Then, a 5 cm x 5 cm Al18-25-6-95 sample (with the nanowall structures facing up) was sewn into this opening, as shown in Figure 5.9 (a).

- A 5 cm x 5 cm piece was cut from the conductive yellow fabric intended for use as the top electrode. This cut piece was then sewn onto the Al18-25-6-95 sample, as shown in Figure 5.9 (b).

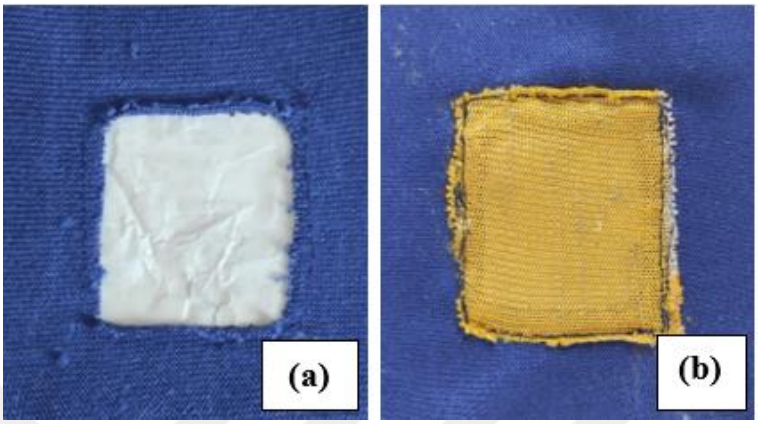

Figure 5.9. *Design of Conductive Textile Fabric/ZnO-NW/Al-Foil Nanogenerator Module - 2*

5.2.4. Integration of nanogenerator modules into textile materials and development of nanogenerator-textile composite systems

The ZnO nanowall-based modules designed for textile integration studies were planned to be integrated into different parts of the glove, as shown in Figure 5.10. For this purpose:

- Modules were prepared using Kapton tape and conductive textile tape in 1 cm x 1 cm dimensions.
- Ecoflex was prepared in a 1:1 volume ratio.
- The prepared modules were placed on the fingers of a knitted cotton glove.
- The prepared Ecoflex was then placed on the modules and fixed onto the finger.
- The prepared modules were also placed on the outside of the index finger (for bending applications) and on the palm of the glove (for clapping applications).

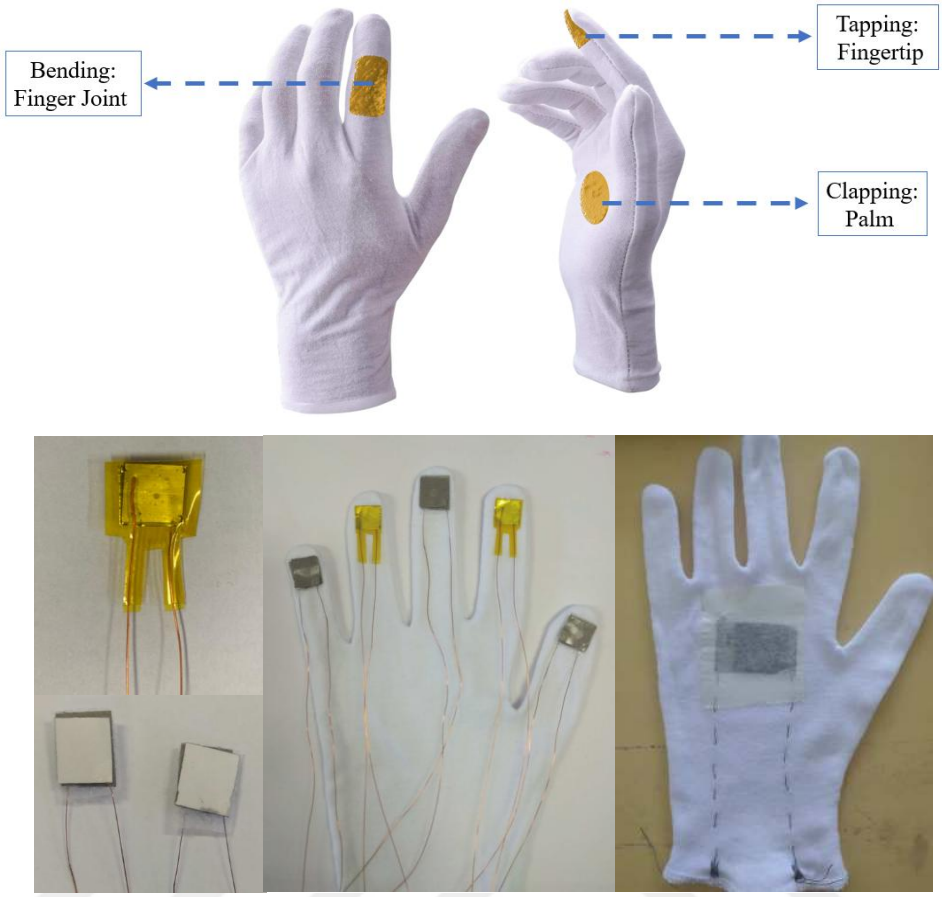

Figure 5.10. *Integration of ZnO nanowall-based nanogenerator modules into gloves*

5.2.5. Characterization

X-ray diffraction (XRD, Bruker D2 Phaser, Cu anode kα1 = 1.54 Å) analysis was performed to examine the crystal structures of electrode materials. Scanning electron microscopy (SEM, Zeiss Supra, secondary electron mode and 15 kV acceleration voltage) analysis was performed for morphological examinations of conductive fabric. To systematically perform electrical characterization tests, a mechanism capable of applying pulses at specific frequencies and forces was designed, as shown in Figure 5.11. The pulse mechanism was enclosed in a Faraday cage to prevent potential interference from the environment for precise mV and µA measurements. Open-circuit voltage and short-circuit current measurements were taken using a force applied at 60 pulses per minute (1 Hz) and a pressure of 3 bar. The open-circuit voltage generated by the modules was measured using an oscilloscope (PicoScope PC Oscilloscope Kit) and PicoScope 7 T&M software, while the short-circuit current was measured using an electrometer (Keysight b2802).

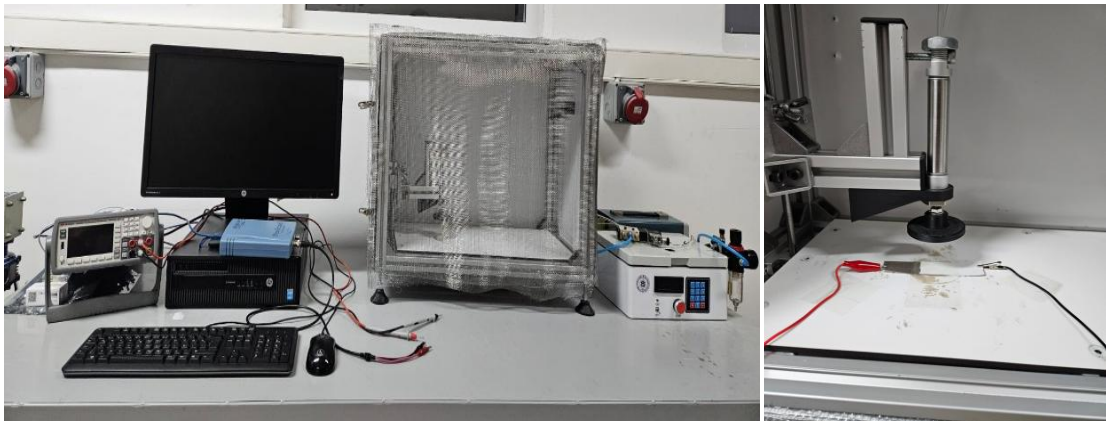

Figure 5.11. *Pneumatic system specifically designed to perform electrical measurements of modules*

Measurements were taken in four different configurations, as shown in Figure 5.12.

1. Nanowalls at the bottom and the positive electrode connected to the nanowall-coated electrode
2. Nanowalls at the bottom and the negative electrode connected to the nanowall-coated electrode
3. Nanowalls at the top and the negative electrode connected to the nanowall-coated electrode
4. Nanowalls at the top and the positive electrode connected to the nanowall-coated electrode

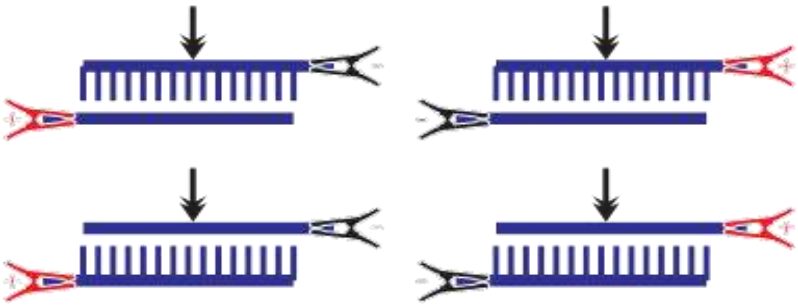

Figure 5.12. *Schematic representation of the measurement configurations of the modules*

5.3. Results and Discussions

XRD analyses of the electrodes used in the ZnO nanowall-based nanogenerator module designs were carried out. XRD graphs of the electrodes are given in Figure 5.13. For Cu-foil, the diffraction peaks of the (111), (200) and (220) planes were obtained at diffraction angles of 43.9°, 50.9° and 74°, respectively. For stainless steel foil, the diffraction peaks of the (111), (200) and (220) planes were obtained at diffraction angles

of 43.7°, 50.89° and 74.75°, respectively. For nickel foil, the diffraction peaks of the (111), (200) and (220) planes were obtained at diffraction angles of 44.63°, 52° and 76.56°, respectively. For Zn-foil, the diffraction peaks of the (002), (100), (101), (102) and (110) planes were obtained at diffraction angles of 36°, 40°, 44°, 55° and 70°, respectively. For Ti-foil, the diffraction peaks of the (100), (002), (101), (102), (110), and (103) planes were obtained at diffraction angles of 35.5°, 38°, 40°, 53°, 64°, and 71°, respectively. Also, for titanium II oxide, the diffraction peaks of the (111), (200), (220), and (311) planes were obtained at diffraction angles of 36°, 42°, 61°, and 72°, respectively. For the conductive textile fabric, the diffraction peaks of polyester were obtained at diffraction angles between 15° and 30°, the diffraction peaks of (111), (200) and (220) Cu planes were obtained at 44°, 51° and 74° diffraction angles, respectively, and the diffraction peaks of (111) and (200) Ni planes were obtained at 45° and 52° diffraction angles.

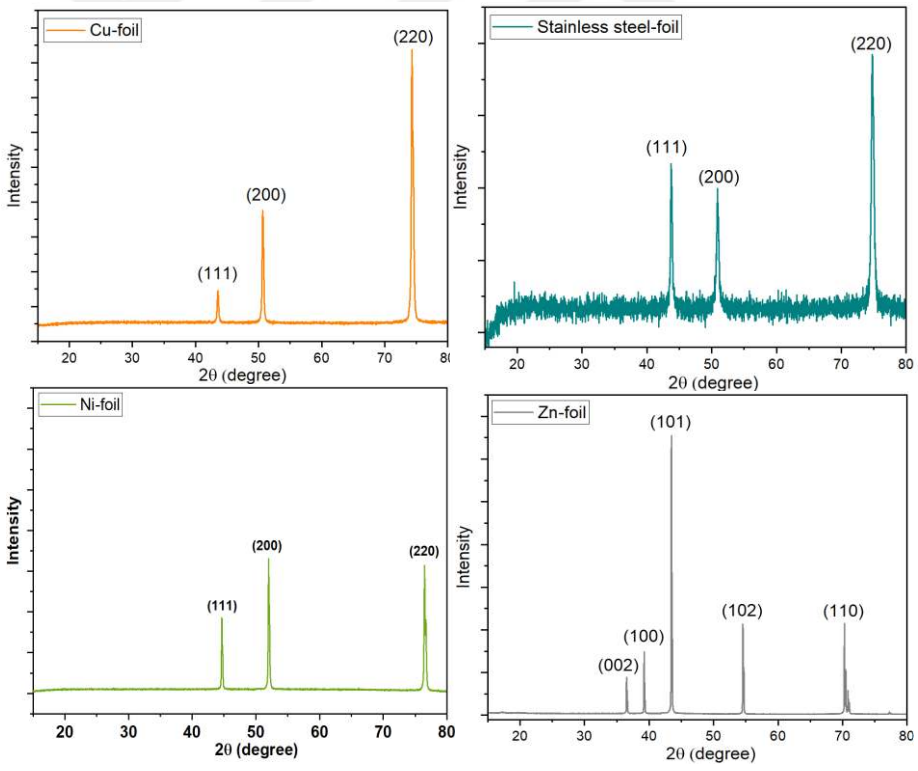

Figure 5.13. *XRD graphs of the top electrodes used in PENG module design*

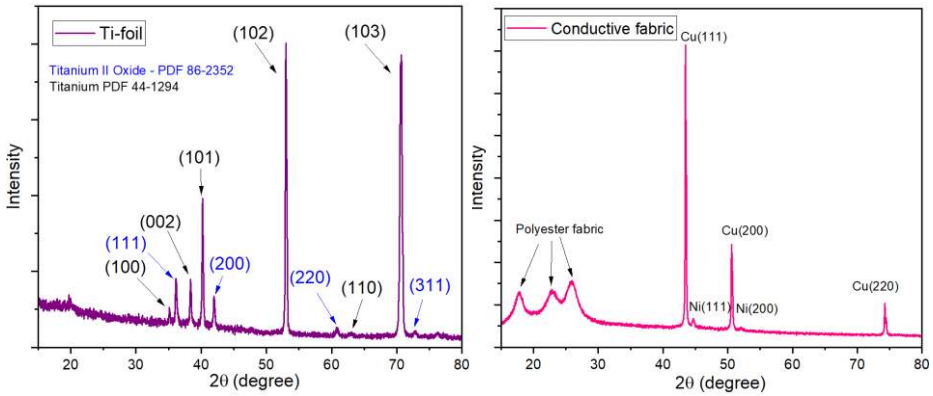

Figure 5.13. (Continued) *XRD graphs of the top electrodes used in PENG module design*

5.3.1. Flexible metal electrode/ZnO-NWl/Al-foil nanogenerator module

Open circuit voltage and short circuit current measurements for modules using Al-foil for the top electrode were carried out in the configurations shown in Figure 5.12, under 3 bar pressure and 60 pulses per minute, with the setup shown in Figure 5.11. The obtained open circuit voltage and short circuit current measurement graphs are given in Figure 5.14, and the calculated power values are given in Table 5.2. In the first configuration, where the nanowalls are at the bottom and the positive electrode is connected to the bottom electrode covered with nanowalls, the open circuit voltage is 0.9 V, the short circuit current is 3.6 µA. In the second configuration, where the nanowalls are at the bottom and the negative electrode is connected to the bottom electrode covered with nanowalls, the open circuit voltage is -0.5 V, the short circuit current is -5.6 µA. In the third configuration, where the nanowalls were on top and the positive electrode was connected to the bottom electrode covered with nanowalls, the open circuit voltage was measured as 1.3 V, the short circuit current was measured as 4.6 µA. In the fourth configuration, where the nanowalls were on top and the negative electrode was connected to the bottom electrode covered with nanowalls, the open circuit voltage was measured as -0.36 V; the short circuit current was measured as -3.8 µA. When the results were evaluated, it was determined that the highest power generation in the ZnO nanowall-based PENG modules with Al-foil as the top electrode was achieved in the configuration where the nanowalls were on top, meaning that the force was applied by the nanowall.

The power values were determined based on the Thevenin equivalent circuit model. V_{oc} denotes the open-circuit voltage, R_{in} represents the internal resistance, R_L represents the load resistance and I_{sc} refers to the short-circuit current. The internal resistance can be expressed as:

$$R_{in} = \frac{V_{OC}}{I_{SC}} \quad (5.1)$$

$$V = V_{OC} x \frac{R_L}{R_L + R_{in}} \quad (5.2)$$

$$I = \frac{V_{OC}}{R_L + R_{in}} \quad (5.3)$$

$$P = VxI = V_{OC}^2 \, x \frac{R_L}{(R_L + R_{in})^2_0} \quad (5.4)$$

The maximum power is delivered when R_L=R_{in}

$$P_{max} = \frac{V_{OC} \, x \, I_{SC}}{4} \quad (5.5)$$

Table 5.2. *Voltage, current and power values of the ZnO nanowall-based PENG module with Al-foil as the top electrode depending on the module configuration*

Module configuration	Voltage (V)	Current (mA)	Power (μW)
Nanowall at the bottom – positive pole connected to the nanowall	0.9	3.6	0.810
Nanowall at the bottom – negative pole connected to the nanowall	-0.5	-5.6	0.700
Nanowall at the top – positive pole connected to the nanowall	1.3	4.6	1.495
Nanowall at the top – negative pole connected to the nanowall	-0.36	-3.8	0.348

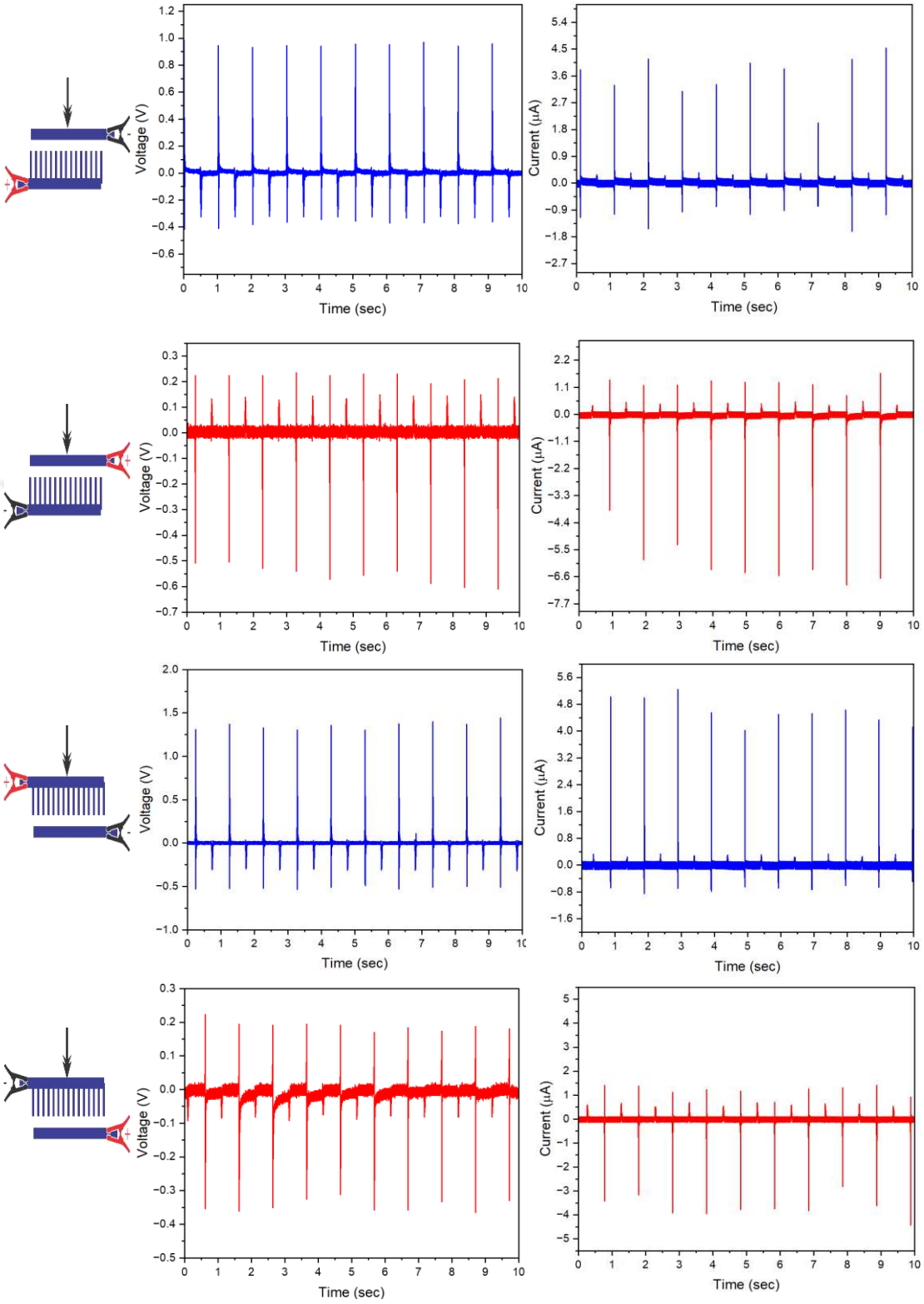

Figure 5.14. *Open circuit voltage and short circuit current graphs for ZnO nanowall-based PENG modules with Al-foil as the top electrode*

It was determined that the highest output values in ZnO nanowall-based PENG modules with Al-foil as the top electrode were obtained in the third configuration, where the nanowalls were on top and the positive pole was connected to the top electrode. It was thought that multiple modules could be connected in series and parallel to achieve higher output values with these modules. Therefore, four identical modules were placed on top of each other as shown in Figure 5.15 and first connected in parallel. The open-circuit voltage and short-circuit current measurements of the parallel-connected modules were carried out in the third configuration shown in Figure 5.12, under 3 bar pressure and 60 pulses per minute, using the setup shown in Figure 5.11. The obtained open-circuit voltage and short-circuit current measurement graphs are given in Figure 5.15. The average open-circuit voltage value for the parallel-connected modules was measured as 0.175 V, while the average short-circuit current value was measured as 13.2 µA. The power generation performance was calculated as 0.578 µW. The aim of this study was to increase power generation performance by using multiple modules. However, when the results were examined, it was determined that the power generation performance was below that obtained from single modules. This was due to the decrease in open circuit voltage despite the increase in short-circuit current.

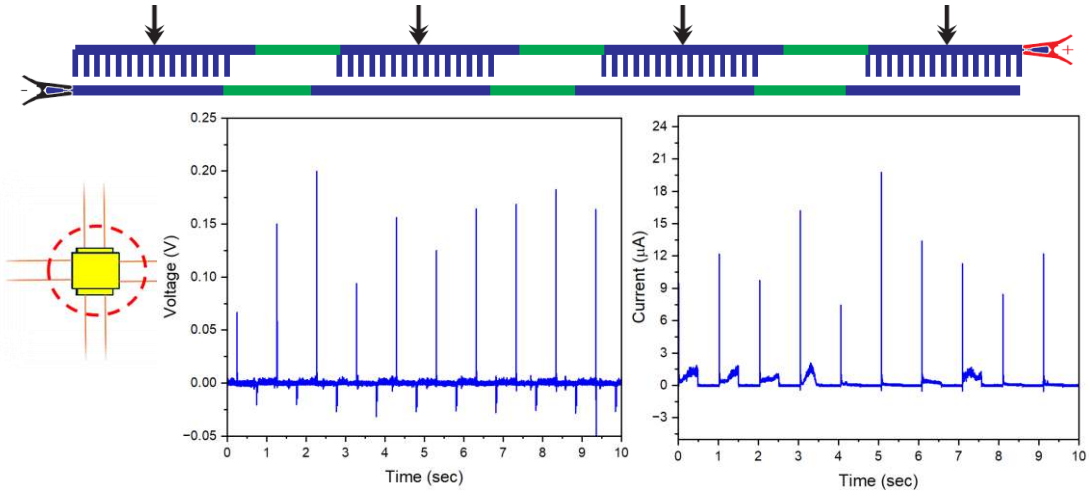

Figure 5.15. *Open circuit voltage and short circuit current graphs for parallel connected ZnO nanowall- based PENG modules*

Open-circuit voltage and short-circuit current measurements of series-connected modules were performed using the setup shown in Figure 5.11, under 3 bar pressure and 60 pulses per minute, in the third configuration shown in Figure 5.12. The resulting open-circuit voltage and short-circuit current measurement graphs are shown in Figure

5.16. The average open-circuit voltage for series-connected modules was measured as 5.2 V, while the average short-circuit current was measured as 5.9 µA. Power generation performance was calculated as 7.67 µW. The results indicate that, unlike parallel-connected modules, the power generation performance obtained with series-connected modules is approximately five times greater than that obtained with single modules. Therefore, by increasing the number of modules, series-connected nanogenerator arrays can be designed to achieve the required power output performance depending on the application area.

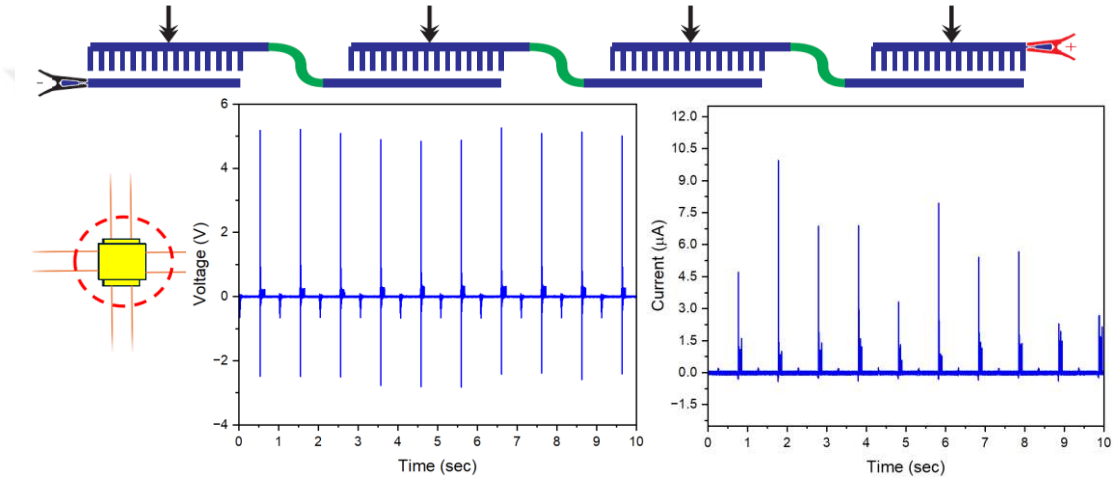

Figure 5.16. *Open circuit voltage and short circuit current graphs for series connected ZnO nanowall-based PENG modules*

For these modules, which used Al-foil for the top electrode, open-circuit voltage measurements were also performed using various force applications, such as tapping with a pen, clapping, and bending the elbow. The tapping application is shown in Figure 5.17, and the resulting measurement values are given in Table 5.3. Three measurements were taken for each of the three modules, yielding average open-circuit voltage values ranging from 0.7 V to 1.3 V. Similar results were observed with this measurement and those obtained with the pneumatic system.

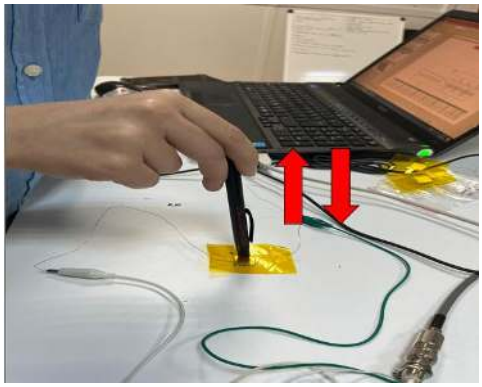

Figure 5.17. *Open-circuit voltage measurement under pen-struck force*

Table 5.3. *Open-circuit voltage values of the ZnO nanowall-based PENG module with an Al-foil top electrode under pen-struck force*

	Module 1 (V)	**Module 2 (V)**	**Module 3 (V)**
1	0.633	0.952	1.183
2	0.669	0.964	1.916
3	0.886	0.526	1.022
Mean	0.729	0.814	1.374
Standard Deviation	0.14	0.25	0.48

The clapping application is shown in Figure 5.18, and the resulting measurement values are shown in Table 5.4. Three measurements were taken for each of the three modules, yielding average open-circuit voltage values ranging from 0.03 V to 0.06 V. The low open-circuit voltage values in this measurement were attributed to the way the force was applied. It was believed that the module was not properly positioned under the applied force, and the elastic band on the module was absorbing the applied force.

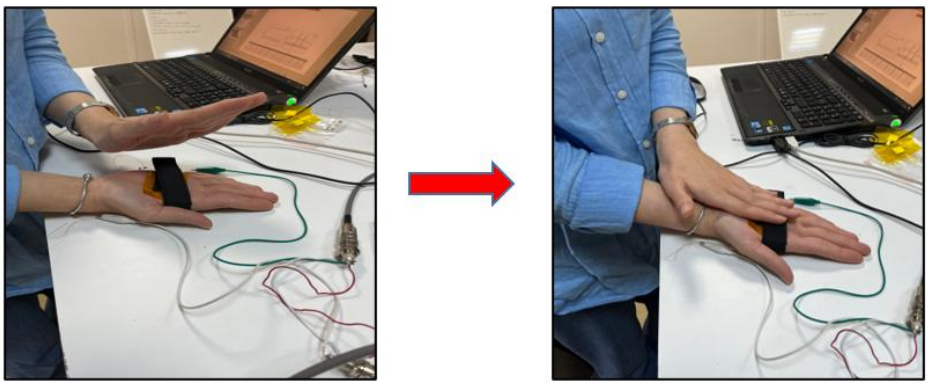

Figure 5.18. *Open-circuit voltage measurement under clapping force*

Table 5.4. *Open-circuit voltage values under clapping force of the ZnO nanowall-based PENG module with an Al-foil top electrode*

	Module 1 (V)	Module 2 (V)	Module 3 (V)
1	0.052	0.070	0.032
2	0.021	0.066	0.046
3	0.031	0.048	0.020
Mean	0.035	0.061	0.033
Standard Deviation	0.02	0.01	0.01

The elbow bending application is shown in Figure 5.19, and the resulting measurement values are presented in Table 5.5. Three measurements were taken for each of the three modules, and average open-circuit voltage values were obtained between 0.2 V and 0.4 V. In this measurement, it was determined that the open-circuit voltage values were lower than those obtained with a pen-struck force. This was again attributed to the way the force was applied. It was believed that the module was not fully inserted under the applied force, and the elastic band on the module was hindering its bending.

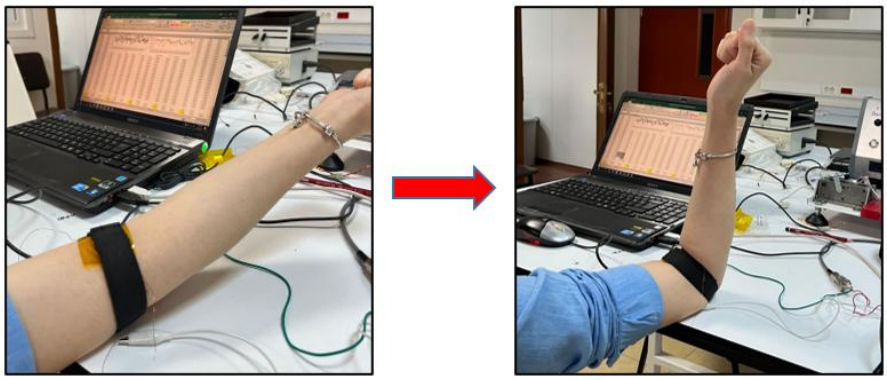

Figure 5.19. *Open-circuit voltage measurement under cantilever bending force*

Table 5.5. *Open-circuit voltage values under cantilever bending force of the ZnO nanowall-based PENG module with an Al foil top electrode*

	Module 1 (V)	Module 2 (V)	Module 3 (V)
1	0.104	0.150	0.549
2	0.172	0.340	0.179
3	0.408	0.358	0.359
Mean	0.228	0.283	0.362
Standard Deviation	0.16	0.12	0.19

To improve the electrical output efficiency, PENG modules were fabricated using doped ZnO nanowalls. The effect of doping on electrical performance was systematically investigated. Open circuit voltage and short circuit current measurements for modules were carried out in the configurations shown in Figure 5.12, under 3 bar pressure and 60 pulses per minute, with the setup shown in Figure 5.11. The open-circuit voltage, short-circuit current, and calculated power values of the PENG modules fabricated with Mg-doped ZnO nanowalls are summarized in Figure 5.20 and Table 5.6. Analysis of the results reveals that the maximum voltage output was achieved with the 0.5% Mg-doped ZnO nanowall-based PENG module, whereas the highest current output was obtained from the 2% Mg-doped ZnO nanowall-based PENG module. At very low Mg doping levels (0.5%), the concentration of intrinsic defects such as oxygen vacancies or zinc interstitials does not significantly increase. Under these conditions, the generated piezoelectric potential is not trapped by defect states, enabling a higher open-circuit voltage (Chen et al., 2017). With increasing Mg doping (2%), the free charge carrier concentration becomes more pronounced in the ZnO lattice. This increase in carrier density enhances charge transport, thereby improving the short-circuit current. However, further increase in doping concentration reduces the inter-nanowall void length, as discussed in Chapter 4. The reduction in void length limits the ability of nanowall structures to bend and polarize effectively under applied mechanical stress, which in turn decreases the voltage output despite the higher carrier density. This trade-off between voltage and current highlights the critical role of Mg doping level in optimizing the piezoelectric performance of ZnO nanowall-based PENG devices. Mg doping not only optimizes the voltage and current outputs at different concentrations, but also synergistically enhances the overall power generation. As a result, the maximum power density of Mg-doped ZnO nanowall-based PENG module reaches approximately 4.5 times higher than that of the undoped ZnO nanowall-based PENG module.

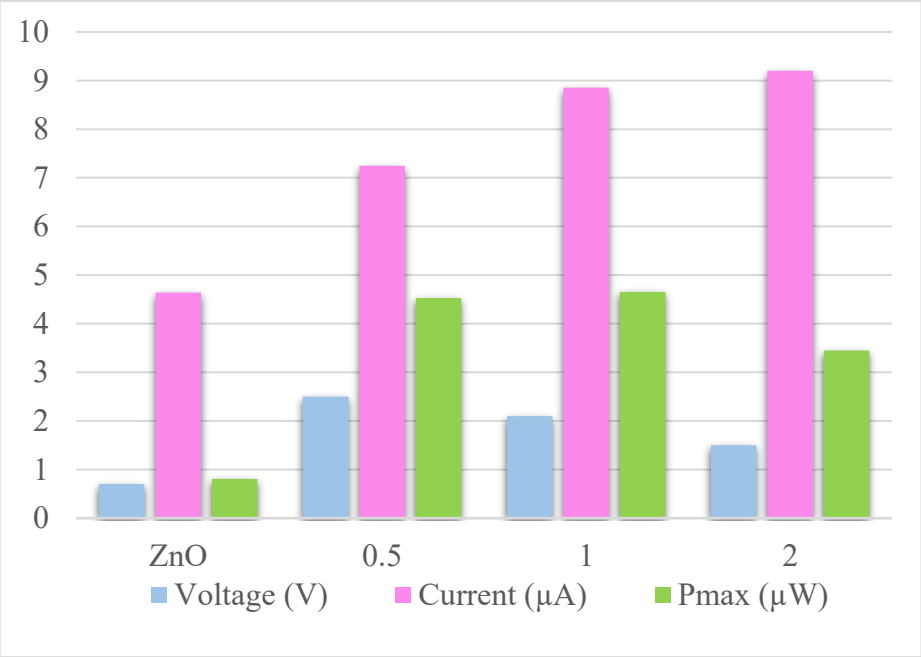

Figure 5.20. *Effect of Mg doping concentration on the electrical output of ZnO nanowall-based PENG modules*

Table 5.6. *Electrical output values of Mg doped ZnO nanowall-based PENG modules*

Sample	Concentration (at. %)	Voltage (V)	Current (µA)	Power (µW)
ZnO	-	0.9	4.6	1.03
ZnO-Mg-0.5	0.5	2.5	7.25	4.53
ZnO-Mg-1.0	1.0	2.1	8.85	4.65
ZnO-Mg-2.0	2.0	1.5	9.20	3.45

The open-circuit voltage, short-circuit current, and calculated power values of the PENG modules fabricated with Fe-doped ZnO nanowalls are summarized in Figure 5.21 and Table 5.7. Analysis of the results reveals that the maximum voltage output was achieved with the 0.5% Fe-doped ZnO nanowall-based PENG module, whereas the highest current output was obtained from the 2% Fe-doped ZnO nanowall based PENG module. The Fe doping level directly influences the Fe^{2+}/Fe^{3+} ratio in ZnO structures and, consequently, the electrical outputs. At low doping levels (e.g., 0.5%), Fe ions are incorporated substitutionally at Zn^{2+} sites, and the defect density within the crystal lattice remains limited. Under these conditions, Fe predominantly exists as Fe^{3+}, allowing the piezoelectric potential to be largely preserved, which results in higher voltage outputs. As the doping concentration increases (1 - 2%), the number of oxygen vacancies and lattice defects rises, partially reducing Fe^{3+} to Fe^{2+}. The presence of Fe^{2+}

ions increase the free carrier density, enhancing the current output, whereas the higher defect density screens the piezoelectric potential, causing a decrease in voltage. Furthermore, since the ionic radius of Fe^{2+} is larger than that of Zn^{2+}, these ions experience greater resistance to rotation under an applied electric field, leading to a reduced piezoelectric coefficient (d_{33}) (Luo et al., 2010). As a result, the maximum power output was obtained from the ZnO-based PENG module doped by 0.5% Fe. Compared to the undoped ZnO-based PENG module, an approximately 3.5-fold increase in power was achieved.

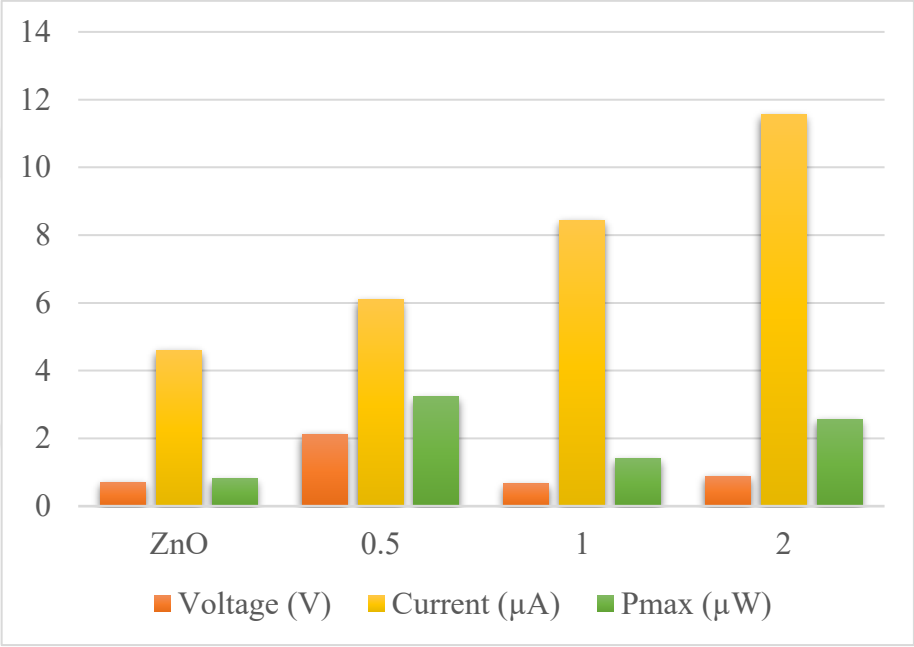

Figure 5.21. *Effect of Fe doping concentration on the electrical output of ZnO nanowall-based PENG modules*

Table 5.7. *Electrical output values of Fe doped ZnO nanowall-based PENG modules*

Sample	Concentration (at. %)	Voltage (V)	Current (µA)	Power (µW)
ZnO	-	0.9	4.6	1.03
ZnO-Fe-0.5	0.5	2.12	6.10	3.23
ZnO-Fe-1.0	1.0	0.66	8.44	1.40
ZnO-Fe-2.0	2.0	0.89	11.56	2.57

The open-circuit voltage, short-circuit current, and calculated power values of the PENG modules fabricated with Al-doped ZnO nanowalls are summarized in Figure 5.22

and Table 5.8. Analysis of the results revealed that, compared to other dopants, ZnO-based PENG samples doped with Al exhibited lower voltage values. However, the highest current output was recorded for the ZnO nanowall-based PENG module doped with 2% Al. This behavior is attributed to the fact that Al doping in ZnO structures significantly increases the free electron concentration through the substitution of Zn^{2+} by Al^{3+} ions, resulting in enhanced electrical conductivity and higher short-circuit current. However, the smaller ionic radius of Al^{3+} compared to Zn^{2+} induces local lattice distortions, which reduce the directional piezoelectric polarization and lead to a substantial decrease in the open-circuit voltage. Another reason for the decrease in open-circuit voltage is the structural changes in ZnO nanowalls caused by increasing dopant concentrations. The reduction in inter-nanowall void lengths limits the ability of the nanowalls to bend and polarize under mechanical stress, resulting in lower voltage outputs. Consequently, Al-doped ZnO demonstrates high current outputs, but considerably lower voltage values compared to Mg- or Fe-doped samples. As a result, the power output values were calculated to be lower than those of the undoped ZnO nanowall-based PENG module.

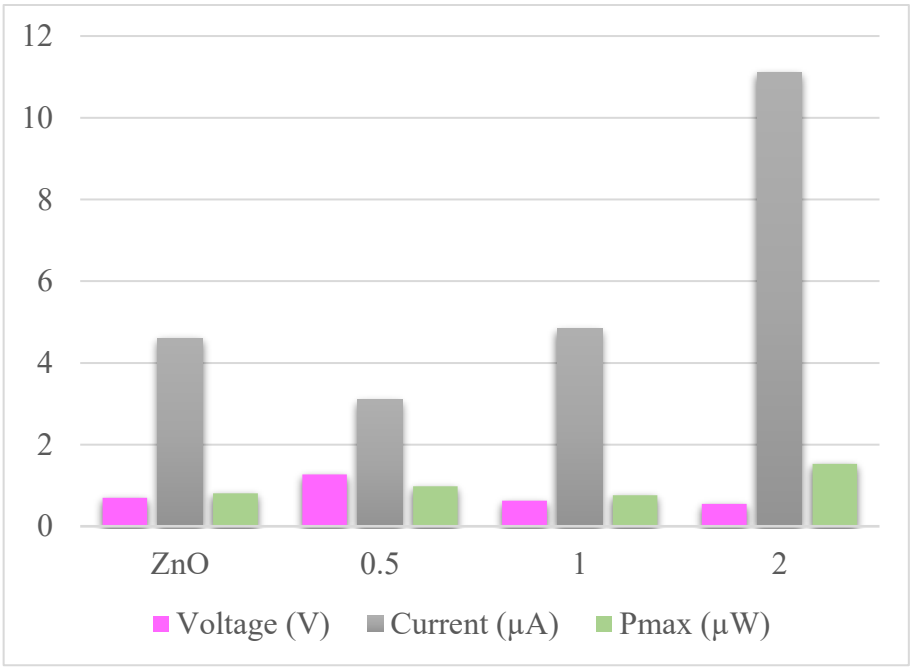

Figure 5.22. *Effect of Al doping concentration on the electrical output of ZnO nanowall-based PENG modules*

Table 5.8. *Electrical output values of Al doped ZnO nanowall-based PENG modules*

Sample	Concentration (at. %)	Voltage (V)	Current (μA)	Power (μW)
ZnO	-	0.9	4.6	1.03
ZnO-Al-0.5	0.5	1.27	3.10	0.98
ZnO-Al-1.0	1.0	0.63	4.83	0.76
ZnO-Al-2.0	2.0	0.55	11.1	1.53

The open-circuit voltage, short-circuit current, and calculated power values of the PENG modules fabricated with Li-doped ZnO nanowalls are summarized in Figure 5.23 and Table 5.9. Analysis of the results revealed that the highest voltage output was achieved with the ZnO nanowall-based PENG module doped by 1% Li. At low Li concentrations, the crystal lattice remains undistorted and the free carrier concentration decreases, resulting in enhanced voltage outputs (Sohn et al., 2013; Shin et al., 2014). When the doping level exceeds 1%, lattice distortions arise and the free carrier concentration may increase, leading to higher short-circuit current. This behavior underscores the delicate balance between crystal integrity and carrier concentration in determining the electrical performance of Li-doped ZnO nanowall-based PENGs. Another reason for the decrease in open-circuit voltage is the structural changes in ZnO nanowalls caused by increasing dopant concentrations. The reduction in inter-nanowalls void lengths limits the ability of the nanowires to bend and polarize under mechanical stress, resulting in lower voltage outputs. Calculated power outputs indicate that the module doped with 1% Li produces approximately four times higher power compared to the undoped ZnO nanowall-based PENG module.

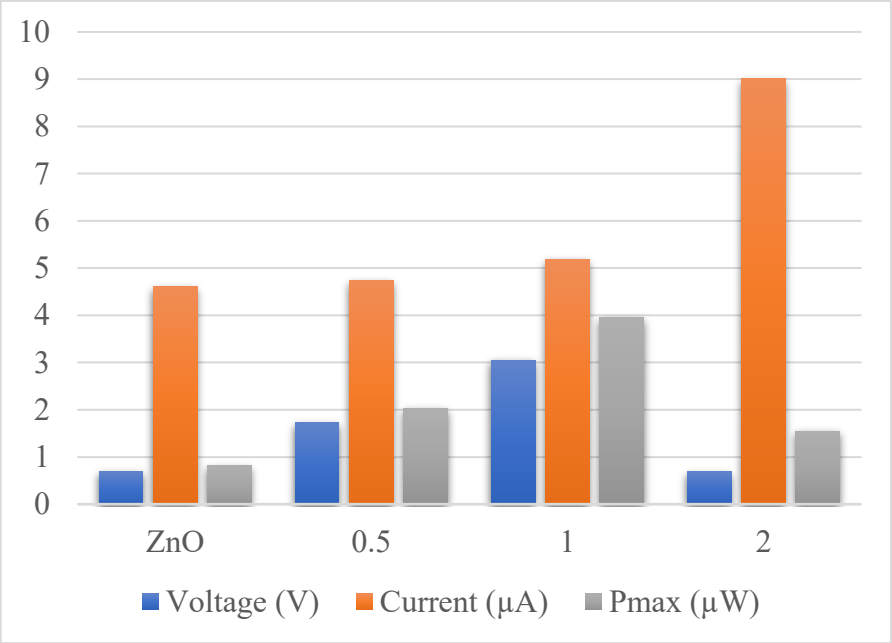

Figure 5.23. *Effect of Li doping concentration on the electrical output of ZnO nanowall-based PENG modules*

Table 5.9. *Electrical output values of Li doped ZnO nanowall-based PENG modules*

Sample	Concentration (at. %)	Voltage (V)	Current (µA)	Power (µW)
ZnO	-	0.9	4.6	1.03
ZnO-Li-0.5	0.5	1.72	4.73	2.03
ZnO-Li-1.0	1.0	3.05	5.18	3.95
ZnO-Li-2.0	2.0	0.69	9.01	1.55

The open-circuit voltage, short-circuit current, and calculated power values of the PENG modules fabricated with Mn-doped ZnO nanowalls are summarized in Figure 5.24 and Table 5.10. In Mn-doped ZnO nanowall structure, low doping levels (0.5 - 1.0 %) preserve the crystal lattice and maintain piezoelectric polarization, resulting in high open-circuit voltage and moderate short-circuit current. Increasing the Mn concentration (2.0 %) introduces higher valence Mn ions (Mn^{3+}, Mn^{4+}), which generate lattice defects and charge imbalances. These defects partially screen the piezoelectric potential, reducing open-circuit voltage, while the increase in free carrier density enhances short-circuit current. Another factor contributing to the decrease in voltage values is the reduction of inter-nanowall void lengths caused by Mn doping. When these void lengths fall below the critical value of 1.7 µm, the ability of the nanowalls to bend under mechanical stress is restricted, limiting polarization and consequently reducing the

generated voltage. However, compared to the undoped ZnO nanowall-based PENG module, the increase in current resulted in the highest power output being achieved for the ZnO nanowall-based PENG module doped with 0.5% Mn.

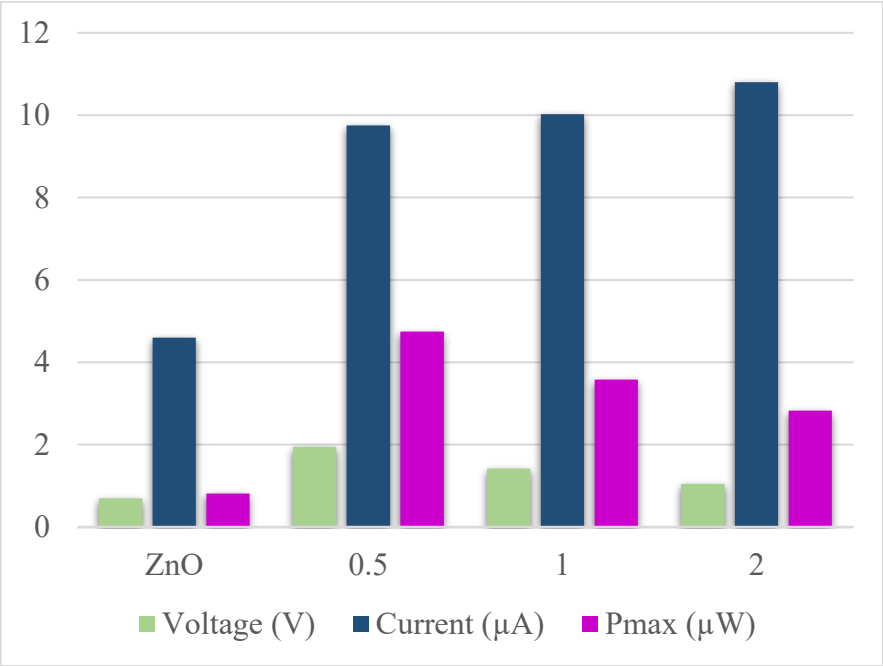

Figure 5.24. *Effect of Mn doping concentration on the electrical output of ZnO nanowall-based PENG modules*

Table 5.10. *Electrical output values of Mn doped ZnO nanowall-based PENG modules*

Sample	Concentration (at. %)	Voltage (V)	Current (µA)	Power (µW)
ZnO	-	0.9	4.6	1.03
ZnO-Mn-0.5	0.5	1.95	9.75	4.75
ZnO-Mn-1.0	1.0	1.42	10.02	3.58
ZnO-Mn-2.0	2.0	1.05	10.80	2.83

In conclusion, when comparing the calculated power outputs of doped ZnO nanowall-based PENG modules, the highest power values were obtained for modules doped with 1.0% Mg, 1.0% Li, and 0.5% Mn. Power outputs of these modules approximately 4-4.5 times higher than the undoped ZnO nanowall-based PENG module.

To investigate the influence of electrode selection on the electrical output performance of ZnO nanowall-based PENG modules, alternative electrode materials were employed in the module design. The electrode material plays a crucial role in

determining the interfacial contact type with the ZnO active layer, which directly affects charge transport and overall device efficiency. The electrical behavior at the electrode-semiconductor interface is generally classified as either Schottky contact or Ohmic contact, depending on the alignment between the electrode work function (Φm) and the electron affinity (χ) of ZnO. Table 5.11 summarizes the commonly used electrode materials, their corresponding work function values, and the theoretically expected contact type with ZnO.

Table 5.11. *Work function values of commonly used electrode materials and their theoretical contact types with ZnO*

Material	Electron Affinity (χ, eV)	Work Function (Φ, eV)	Interface Type (Φ_{Metal}-χ_{ZnO})	Cost
ZnO	4.35	4.40		
Aluminum	4.06	4.08-4.30	Ohmic	$
Titanium	4.33	4.33	Ohmic	$$$
Zinc	4.30	4.30-4.50	Ohmic/Weak Schottky	$$
Silver	1.30	4.26-4.70	Schottky	$$$$
Cupper	1.80	4.65-4.90	Schottky	$$
Stainless Steel	1.00-1.50	4.50-5.00	Schottky	$
Cupper/Nickel	-	4.80-5.10	Schottky	$$$
Nickel	1.60	5.00-5.30	Schottky	$$$
Gold	2.30	5.10-5.40	Schottky	$$$$$
Platinum	2.12	5.64-6.35	Schottky	$$$$$

When the metal work function is significantly higher than the electron affinity of ZnO ($\chi \approx 4.35$ eV), a Schottky barrier is formed at the interface, which hinders electron transport and introduces rectifying behavior. Conversely, when the metal work function is close to or lower than the ZnO electron affinity, the interface tends to behave as an Ohmic contact, allowing linear current transport with minimal barrier resistance (Sze and Ng, 2007).

In this study, aluminum (Al), zinc (Zn), titanium (Ti), copper (Cu), nickel (Ni), stainless steel (S. Steel), and Cu/Ni-coated fabric were investigated as potential electrode materials. According to theoretical considerations, electrodes such as Al, Zn, and Ti are expected to form Ohmic contacts with ZnO due to their relatively low work functions ($\Phi_{Al} \approx 4.28$ eV, $\Phi_{Zn} \approx 4.3$ eV, $\Phi_{Ti} \approx 4.33$ eV). On the other hand, Cu ($\Phi_{Cu} \approx$

4.65 eV), Ni ($\Phi_{Ni} \approx 5.15$ eV), stainless steel ($\Phi \approx 5.0$ eV), and Cu/Ni-coated fabric ($\Phi \approx 5.0$ eV), are anticipated to establish Schottky contacts, leading to rectifying behavior at the ZnO - metal interface.

The experimental determination of the contact type was performed through current - voltage (I - V) characterization. In this method, the current response is recorded as a function of the applied voltage over a defined range. The shape of the I - V curves given in the Figure 5.25 provides direct evidence of the contact behavior. A linear I - V relationship indicates Ohmic contact formation, where the resistance is constant and charge carriers can move freely across the interface. An S-shaped or nonlinear I - V curve corresponds to Schottky contact formation, suggesting the presence of a barrier to carrier transport and rectifying characteristics.

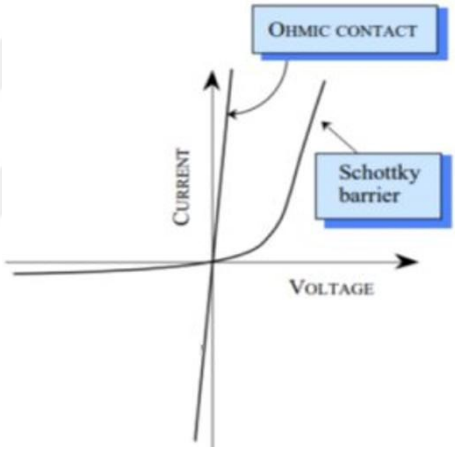

Figure 5.25. *Typical I-V characteristics of Ohmic and Schottky contacts (Ogbuehi, 2018)*

To determine the contact type formed between the ZnO layer and the electrodes used in the fabrication of the ZnO nanowall-based PENG modules, current - voltage (I - V) measurements were carried out by applying voltages in the range of –3 V to +3 V. The resulting I - V curves are presented in Figure 5.26. Theoretically, Al, Ti, and Zn electrodes are expected to form Ohmic contacts with ZnO. Therefore, linear I - V characteristics were anticipated. However, upon examining the curves, it was observed that they were not perfectly linear. This deviation may be attributed to the absence of an ideal interface between the top electrode and the ZnO surface. Possible factors include the formation of oxide layers on the electrode surfaces or the presence of air gaps at the electrode - ZnO interface, both of which can prevent the formation of a perfectly linear Ohmic contact. On the other hand, Cu, stainless steel, Ni, and Cu/Ni-coated fabric

electrodes exhibited S-shaped I - V curves. This experimental observation confirms that these electrodes form Schottky contacts with ZnO. The strength of the Schottky contact characteristics was found to follow the order: Ni > Cu/Ni > Stainless steel > Cu. This sequence is also consistent with the reported work function values of these electrodes in the literature.

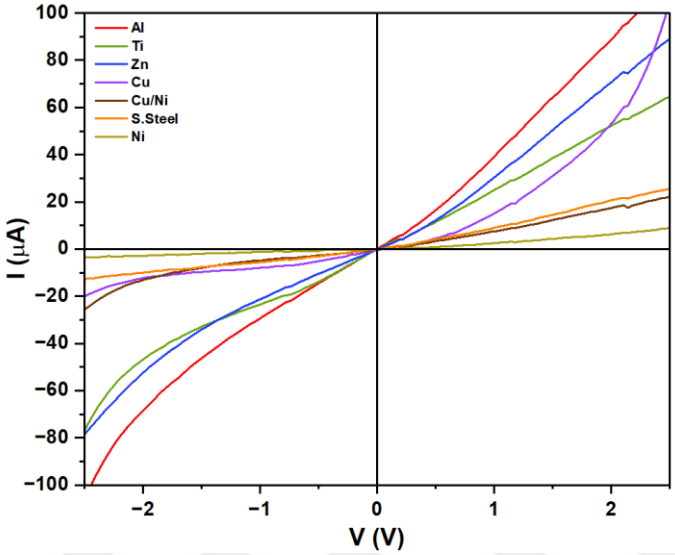

Figure 5.26. *I-V characteristics of ZnO nanowall-based PENG modules fabricated with different electrodes*

Following the determination of the contact type between the top electrode and the ZnO nanowall-based, PENG modules incorporating different electrode materials were fabricated. The electrical performance of these modules, in terms of open-circuit voltage and short-circuit current, was systematically evaluated using the configurations shown in Figure 5.12, under 3 bar pressure and 60 pulses per minute, with the setup shown in Figure 5.11. The open-circuit voltage, short-circuit current, and calculated power corresponding to PENG modules with different top electrodes are presented in Figure 5.27, with the precise values summarized in Table 5.12. Analysis of the results revealed that the highest open-circuit voltage was obtained from the ZnO nanowall-based PENG module with Ni foil as the top electrode, whereas the highest short-circuit current was measured for the ZnO nanowall-based PENG module with Al foil as the top electrode. Furthermore, it was observed that the open-circuit voltage values increased from Al foil, which exhibits ohmic contact behavior, to Ni foil, which exhibits Schottky contact behavior, while the short-circuit current exhibited the opposite trend. This correlation

between the top electrode material and the electrical output is consistent with the contact type at the electrode - ZnO interface: as the Schottky character increases, voltage rises and current decreases. However, it should be noted that the highest current or voltage alone does not necessarily indicate the best overall module performance. The selection of the optimal top electrode should be based on the maximum power output of the module. In this study, power calculations of ZnO nanowall-based PENG modules fabricated with different top electrodes indicated that the highest power output was achieved with either Cu foil or Cu/Ni-coated fabric as the top electrode.

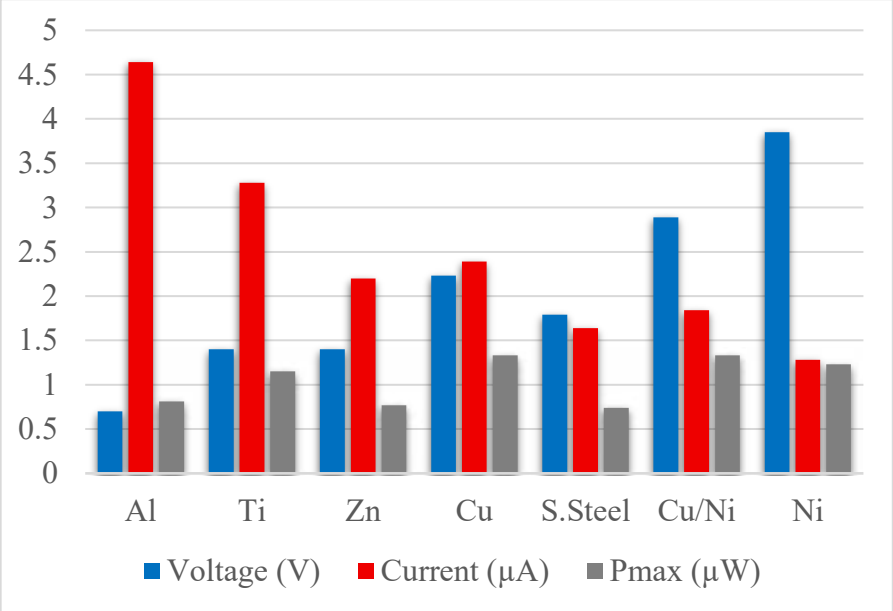

Figure 5.27. *Effect of top electrode materials on the electrical output of ZnO nanowall-based PENG modules*

Table 5.12. *Electrical output values of ZnO nanowall-based PENG modules fabricated with different top electrodes*

Top Electrode	Voltage (V)	Current (µA)	Power (µW)
Al-Foil	0.9	4.60	1.03
Ti-Foil	1.4	3.28	1.15
Zn-Foil	1.4	2.20	0.77
Cu-Foil	2.23	2.39	1.33
S. Steel-Foil	1.79	1.64	0.74
Cu/Ni Coated Fabric	2.89	1.84	1.33
Ni-Foil	3.85	1.28	1.23

5.3.2. Conductive textile tape/polymer/ZnO-NWl/conductive textile tape nanogenerator module

The relatively low power output obtained only from the piezoelectric effect in ZnO nanowall-based PENG modules highlighted the need for the development of new module designs. Accordingly, the new designs incorporated not only the ZnO nanowall layer but also polymer layers between the top and bottom electrodes. The aim was to take advantage of both the piezoelectric effect and the triboelectric effect induced by the polymers, enabling the design of flexible hybrid nanogenerator modules with enhanced power generation capability. In these new module designs, as illustrated in Figure 5.3, Cu/Ni-coated conductive fabric strips were used as the top and bottom electrodes, and layers of PDMS, Ecoflex, and PVC polymers were placed between the electrodes along with the ZnO nanowall layer. The electrical performance of these modules, in terms of open-circuit voltage and short-circuit current, was systematically evaluated using the configurations shown in Figure 5.12, under 3 bar pressure and 60 pulses per minute, with the setup shown in Figure 5.11. The open-circuit voltage, short-circuit current, and calculated power corresponding to hybrid nanogenerator modules with different polymer were presented in Figure 5.28, with the precise values summarized in Table 5.13. Analysis of the results showed that ZnO nanowall-based hybrid nanogenerator modules incorporating PDMS and Ecoflex exhibited open-circuit voltage values up to four times higher than those of conventional PENG modules, due to the additional contribution from the triboelectric effect. Furthermore, the calculated power outputs demonstrated that these polymer-enhanced hybrid nanogenerators could produce approximately 14 times more power than standard ZnO nanowall-based PENG modules.

Table 5.13. *Electrical output values of ZnO nanowall-based hybrid nanogenerator modules fabricated with different polymers*

Polymer	Voltage (V)	Current (µA)	Power (µW)
ZnO	2.89	1.84	1.33
PDMS	11.20	5.90	16.52
Ecoflex	12.20	6.10	18.61
PVC	7.40	5.10	9.44

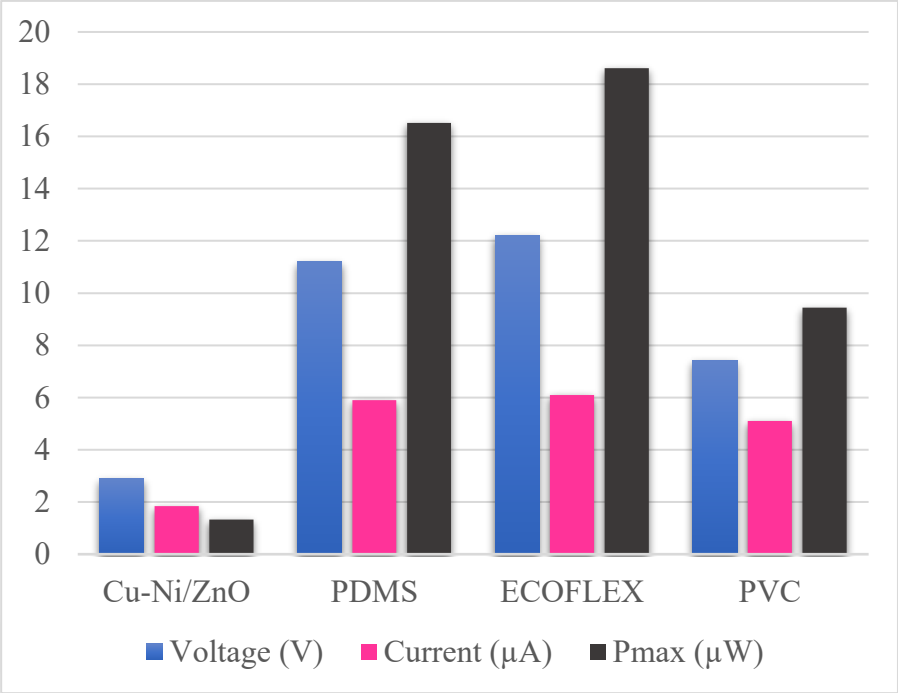

Figure 5.28. *Effect of polymers on the electrical output of ZnO nanowall-based hybrid nanogenerator modules*

To evaluate the high-power generation capacity of ZnO nanowall-based hybrid nanogenerators, a circuit design incorporating an LCD display was developed, as illustrated in Figures 5.29 and 5.30. The hybrid nanogenerator module containing an Ecoflex layer was connected to this circuit. Mechanical forces were applied in two modes: finger tapping (Figure 5.29) and bending (Figure 5.30). In both cases, the ZnO nanowall-based hybrid nanogenerator module was able to generate sufficient power to operate the LCD display, enabling the appearance of the text “EStU” on the screen.

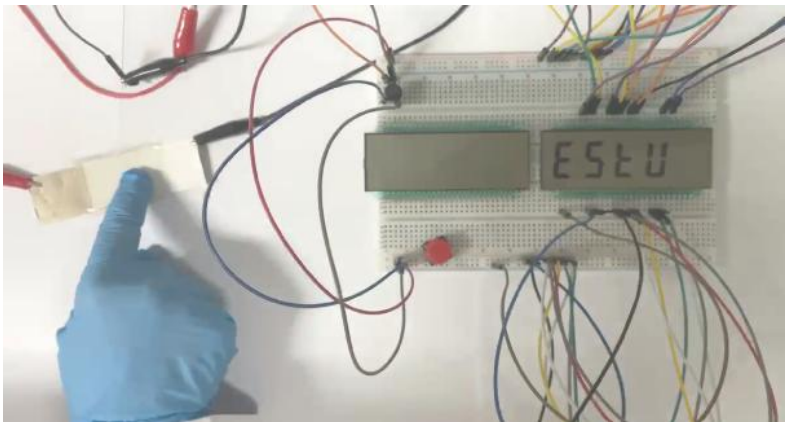

Figure 5.29. *Finger tapping test of the ZnO nanowall-based hybrid nanogenerator*

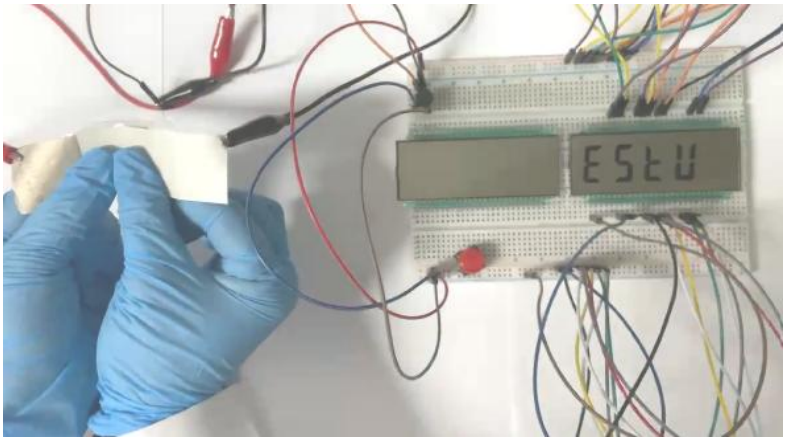

Figure 5.30. *Bending test of the ZnO nanowall-based hybrid nanogenerator*

5.3.3. Conductive textile fabric/ZnO-NWl/Al-foil nanogenerator module

The open-circuit voltage measurement graphs obtained by finger tapping for Al/ZnO/Conductive wool textile PENG module, designed as a preliminary study for the integration of nanogenerator modules into textiles, were shown in Figure 5.31. When the voltage graphs of tis module were examined, it was observed that the generated open-circuit voltage (150-350 mV) was quite similar to the results obtained for the Al-foil/ZnO/Al-foil module designs with finger tapping in Chapter 3. Therefore, it can be said that the electrical potential was generated by the piezoelectric effect.

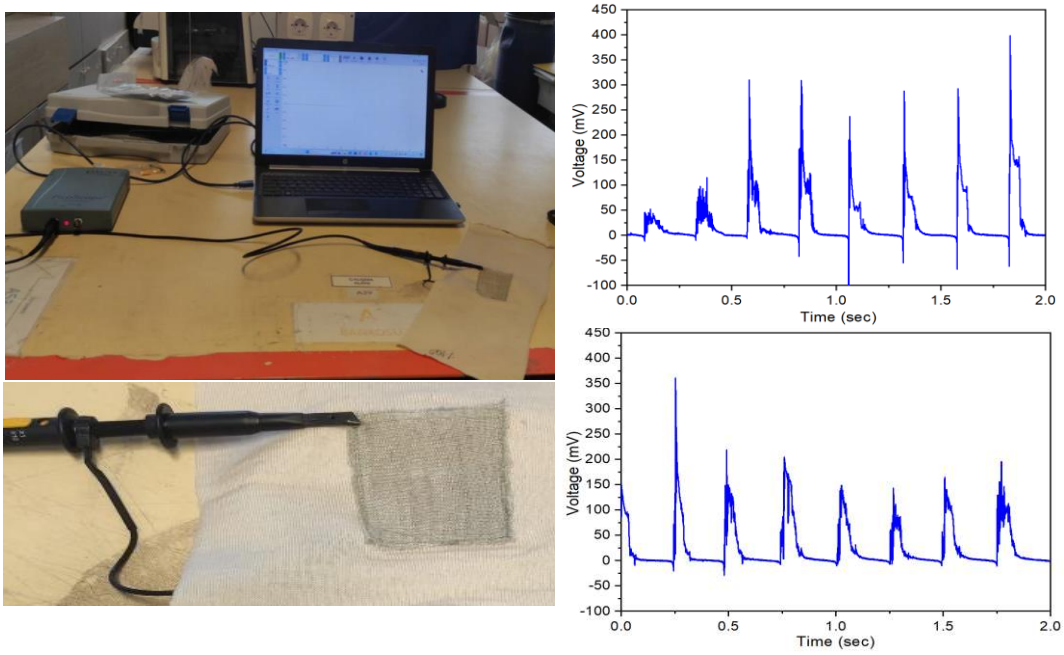

Figure 5.31. *Open circuit voltage measurement graphs taken for the Al/ZnO/Conductive Wool Textile PENG module*

The open-circuit voltage measurement graphs obtained by finger tapping for Al/ZnO/Conductive polyester textile PENG module were shown in Figure 5.32. Examining the output voltage graphs, it was observed that the generated electrical potential (150-400 mV) was quite similar to the results obtained for the Al-foil/ZnO/Al-foil module designs with finger tapping in Chapter 3. Therefore, it can be said that the generated electrical potential was achieved through the piezoelectric effect.

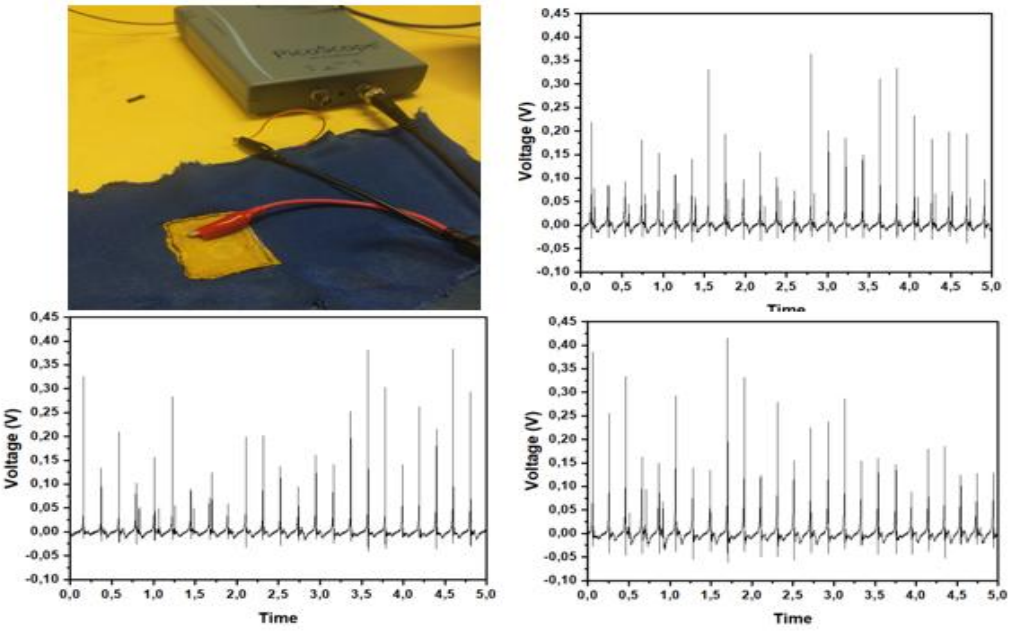

Figure 5.32. *Open circuit voltage measurement graphs taken for the Al/ZnO/Conductive Polyester Textile PENG module*

However, the instability observed in the open-circuit voltage values measured in both the module designs shown in Figure 5.31 and Figure 5.32 indicates that the use of stainless-steel wire-based conductive fabrics as electrodes is limited. The main reasons for this are the small effective contact area of the conductive fibers at the electrode interface and the tendency of stainless-steel wires to break or fracture during yarn twisting and fabric knitting processes. These issues result in low and non-uniform open-circuit voltage outputs. Therefore, it was concluded that these designs are not suitable for the scope of this study.

5.3.4. Electrical outputs of nanogenerator modules integrated into textile materials

The open circuit voltage responses of the fabricated ZnO nanowall-based PENG and hybrid nanogenerator modules were characterized using an oscilloscope under the mechanical excitation patterns illustrated in Figure 5.33, with the results summarized in Figure 5.34. The ZnO nanowall-based PENG module exhibited an average open-circuit voltage of approximately 0.45 V under finger tapping, consistent with previously reported ZnO-based piezoelectric nanogenerators demonstrating relatively low outputs in the absence of additional functional layers. In contrast, the incorporation of a polymer interlayer significantly enhanced electrical performance. The ZnO nanowall-based hybrid nanogenerator module produced an average open-circuit voltage of 2.0 V under the same tapping conditions.

Furthermore, when integrated into textile configurations, the ZnO nanowall-based hybrid nanogenerator module demonstrated reliable functionality under different types of body motions. Specifically, placement in the palm of the hand resulted in an average open-circuit voltage of 1.2 V during clapping, while placement at the finger joint generated 0.12 V under finger bending. These results clearly indicate that the synergistic contribution of piezoelectric and triboelectric mechanisms can substantially improve energy harvesting performance, in agreement with recent studies on ZnO nanowall-based hybrid nanogenerators.

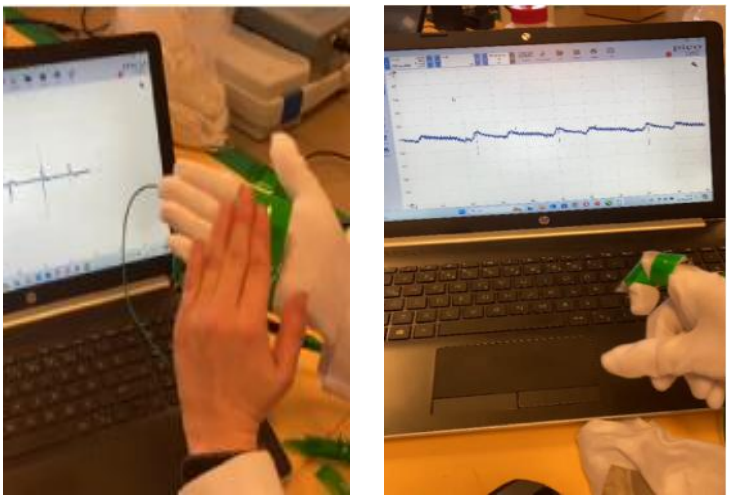

Figure 5.33. *Photos of nanogenerator modules integrated into the glove*

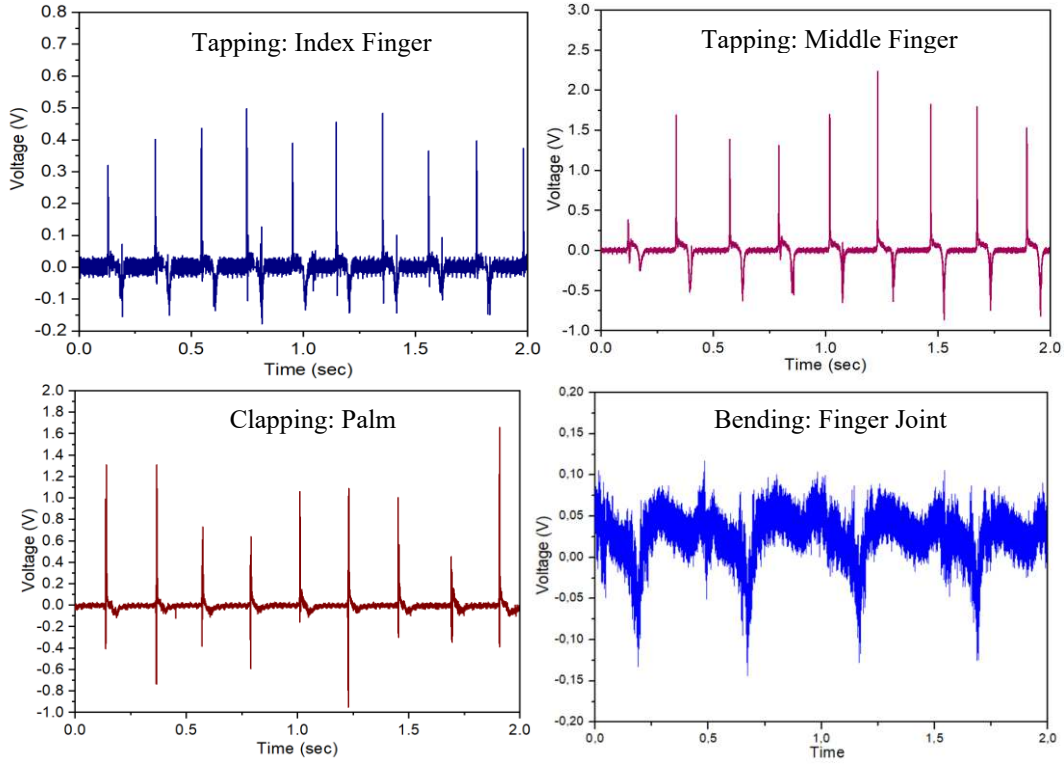

Figure 5.34. *Open-circuit voltage measurements of ZnO nanowall-based nanogenerator modules integrated into gloves*

Considering that the use of copper wires in wearable module designs may negatively affect user comfort, a market survey was conducted to explore alternative solutions. Based on this assessment, silver-coated polyamide conductive threads were identified as a suitable replacement, offering both improved user comfort and easier integration into textile structures. For this purpose, a second module design was fabricated and integrated into the palm of a knitted cotton glove, where it was stitched using silver-coated polyamide thread, as given in Figure 5.35.

Figure 5.35. *Photos of the silver-coated polyamide conductive thread and the module integrated into the palm of the glove with the silver-coated polyamide conductive thread*

The voltage generation performance of the module, along with the efficiency of the conductive thread, was evaluated using an oscilloscope. As shown in Figure 5.36, the module produced an output voltage of 1.6 V during clapping motion, which was identical to the value obtained with conventional copper wiring. These findings demonstrate that silver-coated polyamide conductive threads can effectively replace copper wires in wearable nanogenerator designs, enabling seamless integration into textile systems without compromising electrical performance.

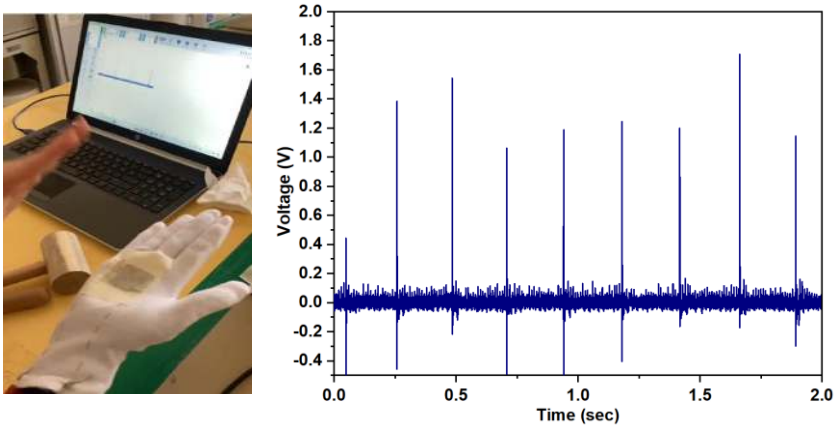

Figure 5.36. *Open-circuit voltage measurements of ZnO nanowall-based nanogenerator module integrated into the palm of the glove with the silver-coated polyamide conductive thread*

In summary, the findings confirm that ZnO nanowall-based nanogenerator modules can be successfully integrated into wearable textiles, providing stable electrical outputs from a variety of human body movements. This highlights their potential for powering low-energy wearable electronics and self-sustainable sensing systems.

5.4. Conclusions

In this study, design and material optimizations were conducted to increase the energy generation performance of ZnO nanowall-based piezoelectric and hybrid nanogenerator modules. It was determined that doping the ZnO active layer can effectively enhance the piezoelectric performance of nanogenerators. Comparative analysis of the calculated power outputs of doped ZnO nanowall-based PENG modules revealed that the highest values were achieved for modules doped by 1.0% Mg, 1.0% Li, and 0.5% Mn. Notably, the power outputs of these doped modules were approximately 4 - 4.5 times higher than that of the undoped ZnO nanowall-based PENG module, demonstrating the significant potential of elemental doping as a strategy for improving device efficiency.

Research has revealed that not only the active piezoelectric layer but also the module geometry, electrode material, and interface contact types play a key role in energy conversion efficiency. In this direction, three different ZnO nanowall-based nanogenerator modules were designed and manufactured. In the first module, aluminum foil, on which ZnO nanowalls were hydrothermally grown, was used as the bottom electrode. Foils of various metals, including Al, Cu, Ni, stainless steel, Zn, and Ti, as well as Cu/Ni-coated conductive textile alternatives, were evaluated as the top electrode. The electrodes were insulated with Kapton tape, creating a flexible and stable module structure. The piezoelectric outputs of the modules were systematically measured using a mechanical test setup operating at a fixed frequency and under controlled pressure. The measurements were repeated in different module orientations and electrode connection configurations, demonstrating that module orientation and electrode connection shape significantly affect output efficiency, particularly during textile integration.

Electrical characterization results revealed that outputs varied depending on the type of contact formed between the top electrode material and the ZnO nanowalls. Schottky contact formation generated high open-circuit voltage, while Ohmic contact resulted in high short-circuit current. These findings highlight the need to select the appropriate electrode material based on the desired output type and the application area.

In the second design, three different polymer layers were integrated in addition to the ZnO nanowall-based structure. It was determined that the high open-circuit voltages obtained from this hybrid structure were related to the triboelectric effect generated by

static charges accumulated on the polymer surfaces. Therefore, it was concluded that the second module transformed into a hybrid nanogenerator system in which piezoelectric and triboelectric effects operate synergistically.

In the third design, a flexible conductive textile was used as the top electrode instead of a metal foil. For this purpose, a conductive thread was produced by twisting steel wire with wool and polyester yarns, knitted into a fabric, and then stitched onto a ZnO nanowall-coated aluminum foil. It was observed that this module could generate electrical output upon fingertip contact. However, the mechanical strength and longevity of the upper electrode were limited due to the brittle structure of the steel wire as a result of the knitting process and mechanical stress cycles. Therefore, although electrical output was obtained in this design, it was found to be insufficient in terms of sustainability of the module.

Finally, the first and second module designs were integrated on to a glove as part of a flexible, wearable electronic system. Modules placed on the fingertips, finger joint, and palm of the glove successfully generated electrical signals through movements such as hitting the surface with the fingertip, bending the finger, and clapping. These results confirm the applicability and functionality of the developed modules in wearable energy generation systems.

6. DESIGN OF PIEZOELECTRIC NANOGENERATOR DIRECTLY ON TEXTILE SURFACE

6.1. Introduction

The growing interest in wearable electronics, smart textiles, and self-powered systems has accelerated the search for alternative energy solutions that are lightweight, sustainable, and capable of continuous operation without the need for frequent charging or large batteries. Among various energy harvesting strategies, piezoelectric nanogenerators (PENGs) have attracted significant attention due to their ability to convert small-scale environmental forces, such as human movement and body vibrations, into electrical energy. PENGs are particularly attractive for wearable technologies as they have the potential to power sensors, health monitoring devices and wireless communication modules embedded in textiles, enabling the development of next-generation autonomous and flexible electronics (Dagdeviren et al., 2014).

Zinc oxide (ZnO) is one of the most extensively studied materials for PENG applications due to its unique combination of properties: wide bandgap (3.37 eV), high exciton binding energy, chemical stability, non-toxicity, and ease of fabrication into a wide variety of 1-D nanowires, nanorods and 2-D nanowalls, nanosheets nanostructures (Özgür et al., 2005; Wang and Song, 2006) Moreover, ZnO nanostructures can be synthesized through low-temperature and solution-based techniques such as hydrothermal growth, which are compatible with flexible substrates, including textiles (Zhang, Chen and Guo, 2019).

Traditionally, PENG devices are fabricated on flexible polymer substrates (e.g., PET, PDMS, or PI) and then planned to integrate on textiles as external modules (Rong, Ren and Yu, 2019). Although such methods offer precise control over device fabrication, they introduce several disadvantages when considered for wearable applications. First, mechanical incompatibility between the textile and the integrated PENG module reduces overall flexibility and can cause discomfort to the user. Second, lamination or embedding processes can compromise the breathability and softness of the textile, which are critical for long-term wearability. Third, externally integrated modules are prone to delamination, cracking, or loss of functionality after repeated mechanical deformation or washing cycles, limiting their durability (Sheng et al., 2024). These issues not only limit device lifespan but also hinder their wide-scale adoption in practical textile-based applications.

To overcome these limitations, recent research has focused on the fabrication of ZnO-based PENGs directly onto textile surfaces. Many studies have demonstrated the successful growth of ZnO nanorods and ZnO nanowires directly onto various fabrics and yarns. For example, Rafique and et. al. demonstrated that silver-doped ZnO nanorods grown directly on cotton fabric via hydrothermal methods achieved up to three times higher power output (~1.45 mW/cm²) than undoped ZnO-nanorod PENGs (Rafique et al., 2020). Kim and et. al. reported the growth of ZnO nanorod arrays on nylon fabrics, producing wearable nanogenerators capable of biomechanical and biothermal monitoring with bending-induced currents of approximately 2.59 μA/mm (Kim et al., 2023). Similarly, Badawy et al. investigated functional piezoelectric yarns by growing ZnO nanowires on individual fibers, optimizing growth parameters for enhanced electrical performance while addressing peeling and adhesion challenges (Badawy et al., 2020). Furthermore, seedless hydrothermal growth of ZnO nanorods on wool and nylon-polypropylene fabrics has been used to fabricate flexible tactile sensors with measurable open-circuit voltages (~4.1 mV) under applied mechanical forces (Hong et al., 2020). These studies demonstrate that directly integrating ZnO nanostructures into textiles not only maintains the flexibility and breathability of the substrate but also enables functional PENGs for practical wearable applications.

As mentioned above, numerous studies have demonstrated the direct growth of ZnO nanorods or nanowires on textile substrates via hydrothermal methods for piezoelectric nanogenerator (PENG) applications. However, to the best of our knowledge, there have been no reports on the direct fabrication of ZnO nanowalls on textile surfaces specifically for PENG module design. In this study, the feasibility of growing ZnO nanowalls on textile substrates using a hydrothermal synthesis approach is systematically investigated, aiming to explore a novel morphology that could enhance the piezoelectric performance and integration of textile-based energy-harvesting devices.

6.2. Experimental

6.2.1. Hydrothermal synthesis of ZnO nanowalls

As a first step toward the direct fabrication of ZnO nanowall-based PENG modules on textile substrates, the hydrothermal synthesis of ZnO nanowall arrays directly on fabrics was considered. However, as discussed in Chapter 3, the formation

of a well-defined ZnO nanowall morphology requires the substrate surface to contain an aluminum layer of at least 100 nm in thickness. Therefore, in the initial stage of this study, commercially available aluminum-coated (Al-coated) textile products were investigated. The market survey revealed that only Al-coated fiberglass fabrics, typically used for thermal insulation, were available. To evaluate their suitability for nanogenerator applications, Al-coated fiberglass fabrics produced by two different companies were provided and examined as potential bottom electrode materials.

Hydrothermal synthesis was performed as described in the literature (Kaur and Singh, 2020). Equal molar (1:1) zinc nitrate hexahydrate ($Zn(NO_3)_2$, Sigma Aldrich, MW: 297.49 $g.mol^{-1}$) and hexamethylenetetramine (HMTA, $C_6H_{12}N_4$, MERCK, MW: 140.19 $g.mol^{-1}$) aqueous solutions at 25 mM concentration were prepared. The hydrothermal synthesis steps are shown in Figure 6.1. The proper amount of zinc nitrate hexahydrate and HMTA were added to 100 ml of distilled water separately and mixed with magnetic stirrer at room temperature for 20 minutes. Then two clear solutions mixed with each other with magnetic stirrer at room temperature for 20 minutes. At the end of the process, a clear solution was obtained. The cleaned Al-coated fiberglass fabric substrates were placed on the solution. The beaker was covered then placed in a hot water bath previously set at 95° kept for 6 h. At the end of the synthesis, the beakers were removed from the hot water bath and allowed to cool to room temperature. After cooling, the samples were removed from the beakers and washed several times with distilled water and ethanol in an ultrasonic bath then left to dry at room conditions.

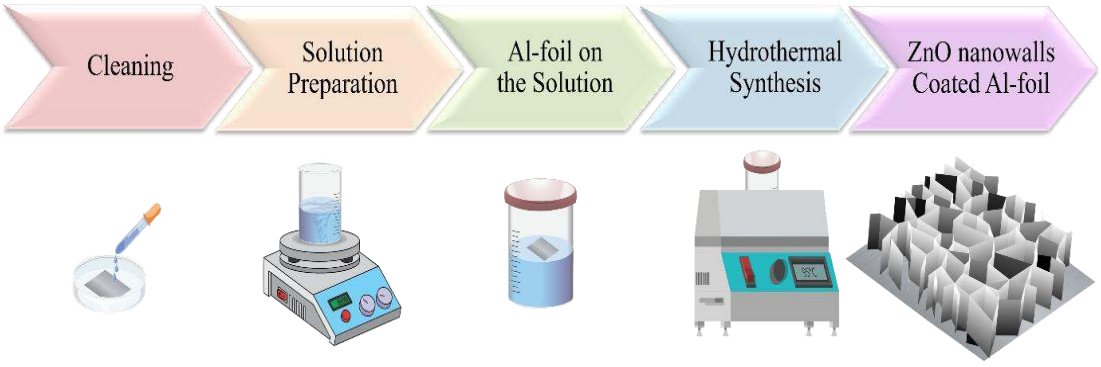

Figure 6.1. *Schematic illustration of ZnO nanowall arrays growth on Al-coated fiberglass fabrics via hydrothermal synthesis*

Commercially available Al-coated fiberglass fabrics were not included in further experiments because their rigid and abrasive nature makes them unsuitable for wearable applications. Instead, an alternative approach was adopted to ensure textile compatibility. In this method, the surface of a polyester fabric, chosen for its flexibility and wearability, was coated with aluminum powder. For this purpose, a coating solution containing aluminum powder and a binder was prepared and applied to the fabric surface using a blade coating technique. A 5 cm × 5 cm mask was employed to define the deposition area, and the solution was uniformly spread over this area with a blade to ensure controlled coating. This method provided the necessary conductivity for the fabric to serve as the bottom electrode in the nanogenerator module.

6.2.3. Characterization

X-ray diffraction (XRD, Bruker D2 Phaser, Cu anode kα1 = 1.54Å) analysis was performed to examine the crystal structure of ZnO nanowall arrays grown on the Al-coated fiberglass fabric substrates and to determine the planes in which the crystals are oriented. Scanning electron microscopy (SEM, Zeiss Supra, secondary electron mode and 15kV acceleration voltage) analysis was performed for morphological examinations.

6.3. Results and Discussions

Firstly, XRD analyses were performed on both the Al-coated and non-Al-coated surfaces of the fiberglass fabrics. Examining the XRD graphs in Figure 6.2, it was determined that: (1) Aluminum diffraction peaks in the cubic crystal structure were observed on the front surface of the first Al-coated fiberglass fabric, as well as α-Al_2O_3 diffraction peaks. (2) Only α-Al_2O_3 diffraction peaks were observed on the front surface of the second Al-coated fiberglass fabric. (3) Only amorphous peaks from glass fibers were observed on the back surfaces of both Al-coated fiberglass fabrics.

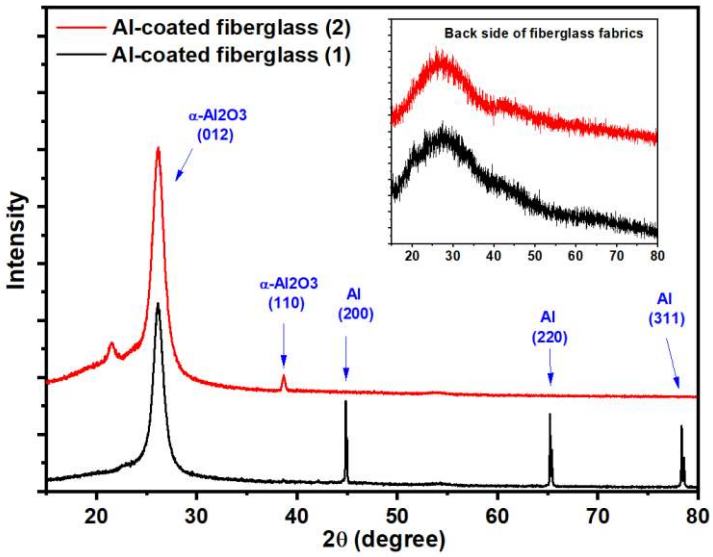

Figure 6.2. *XRD graphs of Al-coated fiberglass fabrics*

Surface morphology and elemental composition of the commercially supplied Al-coated fiberglass fabrics were examined using SEM and EDX analyses, as presented in Figure 6.3. The EDX results confirmed the presence of aluminum (Al) and oxygen (O) on the coated surfaces, verifying the successful deposition of the aluminum layer. On the uncoated glass fiber surfaces, the presence of carbon (C), oxygen (O), magnesium (Mg), aluminum (Al), silicon (Si), and calcium (Ca) were detected, consistent with the typical composition of glass fibers. These analyses provide critical insight into the surface characteristics of the fabrics, which directly influence the nucleation and growth of ZnO nanowall structures during hydrothermal synthesis.

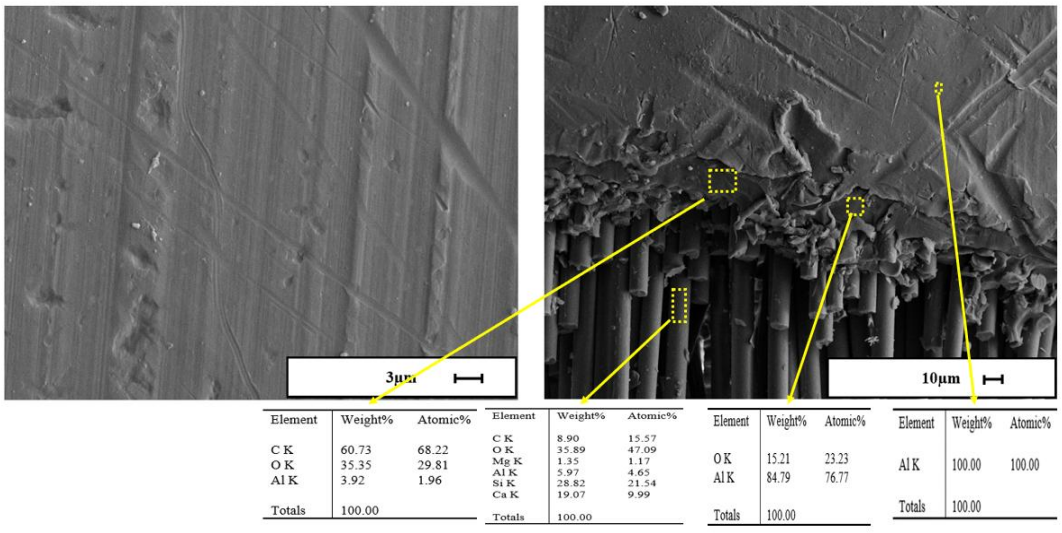

Figure 6.3. *SEM images and EDX results of first Al-coated fiberglass fabric*

The XRD patterns obtained for first Al-coated fiberglass were presented in Figure 6.4. The black diffraction pattern in bottom part of the figure corresponds to the diffraction pattern of the untreated Al-coated fiberglass fabric. The red diffraction pattern corresponds to the sample analyzed immediately after hydrothermal synthesis, prior to any washing process. This pattern exhibits diffraction peaks corresponding to the (100), (002), (101), (102), (110), (103), (112), and (201) planes of ZnO. Analysis of these peaks indicates a random distribution and the absence of a preferred orientation in the ZnO structures grown on the fabric. The blue diffraction pattern represents the sample after being washed in an ultrasonic bath with DI water and dried. A decrease in the intensity of ZnO diffraction peaks was observed after washing, which is attributed to the removal of physically deposited ZnO structures from the fabric surface. Finally, the pink diffraction pattern corresponds to the sample washed with both DI water and ethanol in an ultrasonic bath, followed by drying. At this stage, diffraction peaks corresponding to the ZnO crystal structure were observed, along with peaks associated with the (006), (012), and (110) planes of the ZnAl:LDH layer. These results indicate that the combination of ZnO nanostructures and the underlying ZnAl:LDH layer is preserved after proper washing and drying procedures.

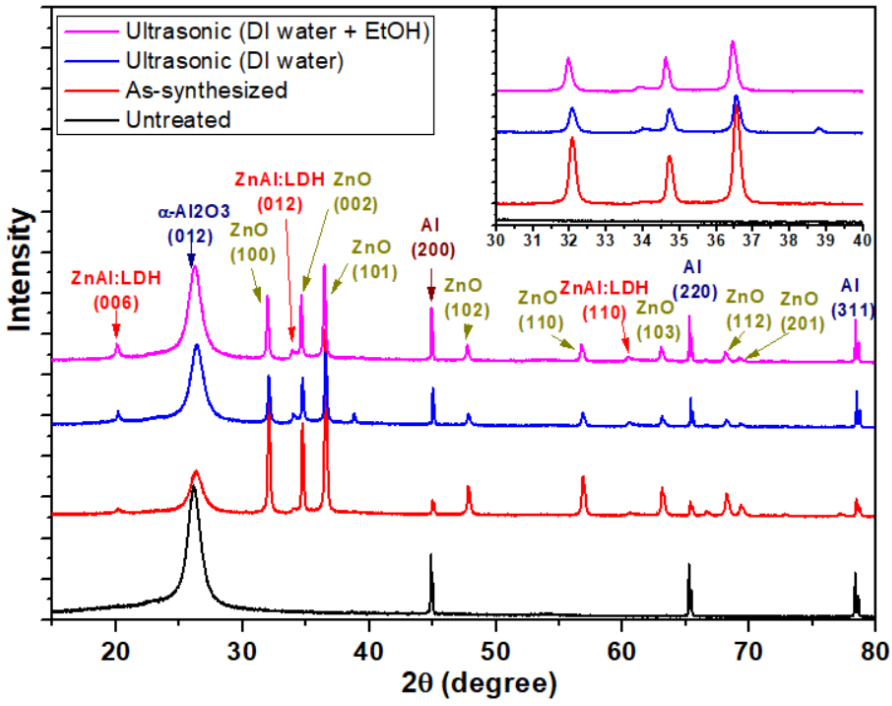

Figure 6.4. *XRD graphs of the first Al-coated fiberglass fabric after hydrothermal synthesis*

SEM images and EDX results of first Al-coated fiberglass fabric, which had not undergone any washing after hydrothermal synthesis, are presented in Figure 6.5. Examination of the SEM micrographs revealed that no well-defined ZnO nanowall structures had formed on the fabric surface; instead, randomly oriented ZnO nanorods and star-like morphologies were observed. EDX analysis confirmed that these structures consisted only Zn and O, indicating the formation of pure ZnO. Additionally, it was observed that the aluminum coating on the fabric surface had been locally removed during the 6-hour hydrothermal synthesis, leading to discontinuities in the conductive coating layer.

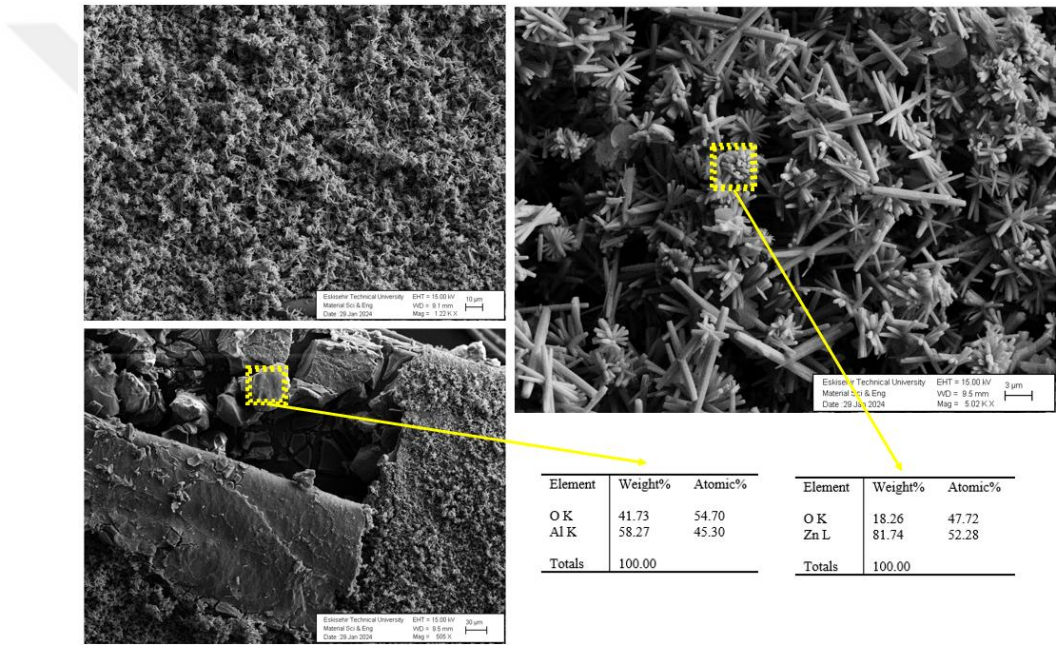

Figure 6.5. *SEM images and EDX results of the first Al-coated fiberglass fabric after hydrothermal synthesis*

SEM images and EDX results of first Al-coated fiberglass, which washed with DI water in ultrasonic bath after hydrothermal synthesis, are presented in Figure 6.6. Examination of the SEM micrographs revealed the presence of ZnO nanorods on the fabric surface, along with ZnO nanowall structures integrated into the substrate. EDX analysis of the nanowall regions confirmed that they were composed of Zn, O, and Al, indicating the formation of ZnO nanowalls. However, the ultrasonic washing process caused partial damage to the surface coating, resulting in localized ruptures and discontinuities.

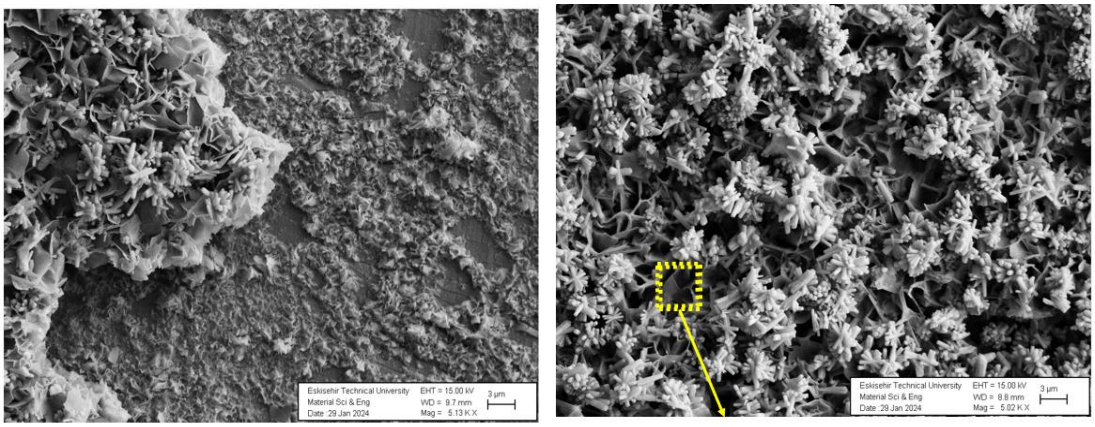

Element	Weight%	Atomic%
O K	32.05	60.88
Al K	11.39	12.83
Zn L	56.56	26.29
Totals	100.00	

Figure 6.6. *SEM images and EDX results of first Al-coated fiberglass fabric washed with DI water after hydrothermal synthesis*

SEM images and EDX results of first Al-coated fiberglass fabric, which washed with DI water and ethanol in ultrasonic bath after hydrothermal synthesis, are presented in Figure 6.7. The SEM micrographs reveal the presence of ZnO nanorods on the fabric surface as well as ZnO nanowall structures integrated into the substrate. EDX analysis of the nanowall regions confirmed that the structures were composed of Zn, O, and Al, indicating successful formation of ZnO nanowalls. However, repeated ultrasonic washing caused partial damage to the surface coating, resulting in localized ruptures and discontinuities.

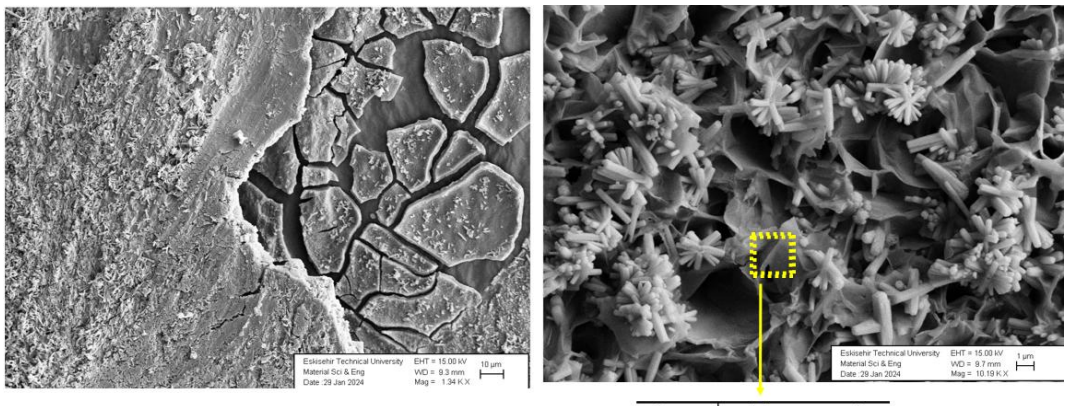

Element	Weight%	Atomic%
O K	24.46	52.64
Al K	10.12	12.91
Zn L	65.42	34.45
Totals	100.00	

Figure 6.7. *SEM images and EDX results of first Al-coated fiberglass fabric washed with DI water and ethanol after hydrothermal synthesis*

Figure 6.8 presents the XRD patterns obtained for second Al-coated fiberglass fabric. The black pattern at the bottom corresponds to the diffraction pattern of the untreated Al-coated fiberglass fabric. The red pattern represents the XRD graph recorded immediately after hydrothermal synthesis, prior to any washing process. This pattern displays diffraction peaks corresponding to the (100), (002), (101), (102), (110), (103), (112), and (201) planes of ZnO. However, comparison of the diffraction peaks indicates that their intensities are lower than those observed for the ZnO structures grown on first Al-coated fiberglass fabric. Moreover, the ZnO structures exhibit a random distribution and lack preferential orientation.

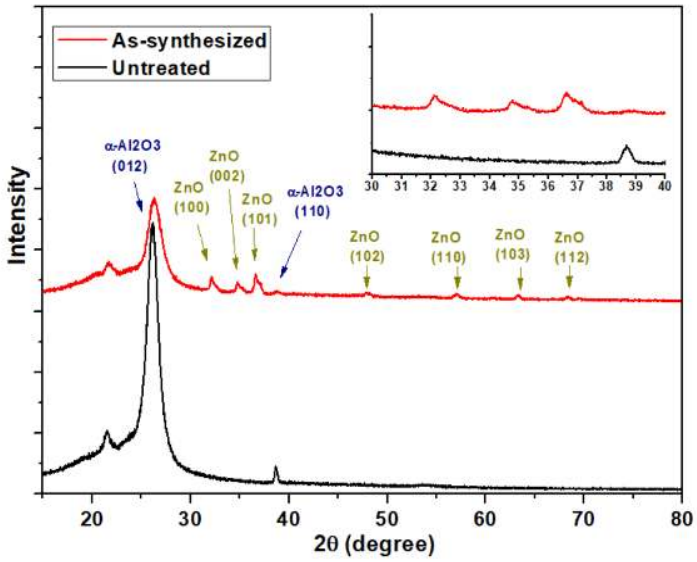

Figure 6.8. *XRD graphs of the second Al-coated fiberglass fabric after hydrothermal synthesis*

SEM images and EDX results of second Al-coated fiberglass fabric, which had not undergone any washing after hydrothermal synthesis, are presented in Figure 6.9. Examination of the images reveals that ZnO nanowall structures were formed on the fabric surface, although irregular ZnO nanoparticles were also present on the nanowalls. EDX analyses confirmed that the ZnO nanowall structures consisted of Zn, Al, and O, whereas the irregular ZnO nanoparticles were composed only of Zn and O. Additionally, it was observed that the aluminum coating on the fabric surface had partially detached from the edge regions after 6 hours of synthesis, compromising the continuity of the coating layer.

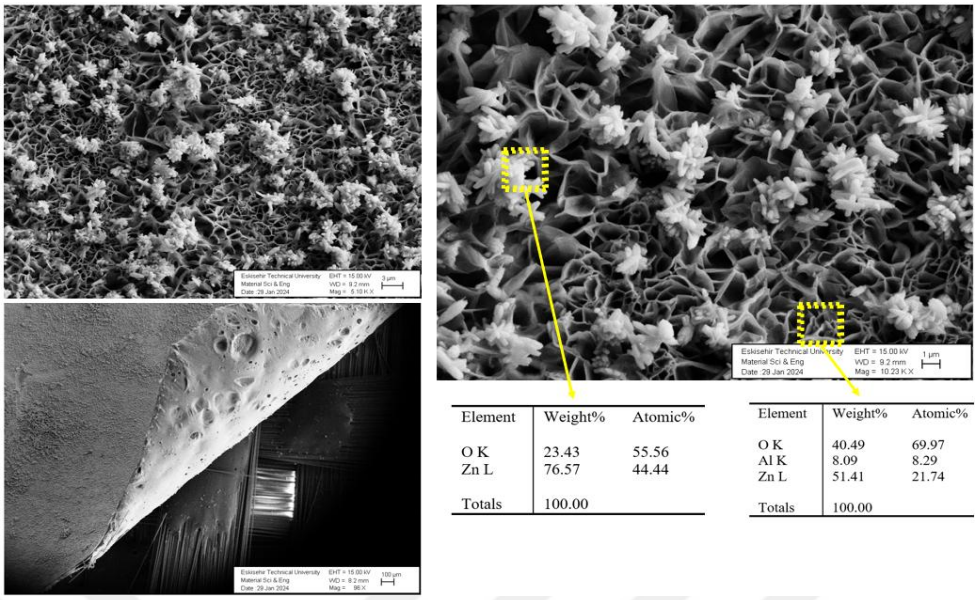

Figure 6.9. *SEM images and EDX results of the second Al-coated fiberglass fabric after hydrothermal synthesis*

Commercially available Al-coated fiberglass fabrics were considered unsuitable for further use in this study due to their poor wearability as textile materials and the inability to effectively grow ZnO nanowalls on their surfaces via hydrothermal synthesis. Therefore, an alternative approach was adopted: the surface of a wearable polyester fabric was coated with aluminum powder. For this purpose, a coating solution containing aluminum powder was prepared and uniformly applied to the fabric surface to serve as the conductive bottom electrode for the nanogenerator modules.

Figure 6.10 presents the XRD graphs of untreated polyester fabric and Al-coated polyester fabric. Examination of the graphs reveals that the untreated polyester fabric exhibits only characteristic polyester diffraction peaks in the 2θ range of 15–30°. In contrast, the Al-coated polyester fabric (red pattern) shows additional diffraction peaks corresponding to the (111), (200), (220), and (311) planes of aluminum, alongside the polyester peaks, confirming the successful deposition of the aluminum coating on the fabric surface. The blue pattern at the top of the graphs represents the XRD diffraction pattern of the Al-coated polyester fabric after hydrothermal synthesis. This pattern exhibits diffraction peaks corresponding to the (100), (002), (101), (110), and (103) planes of zinc oxide. Analysis of the diffraction peaks indicates that the ZnO structures grown on the fabric are randomly distributed, showing no preferred orientation.

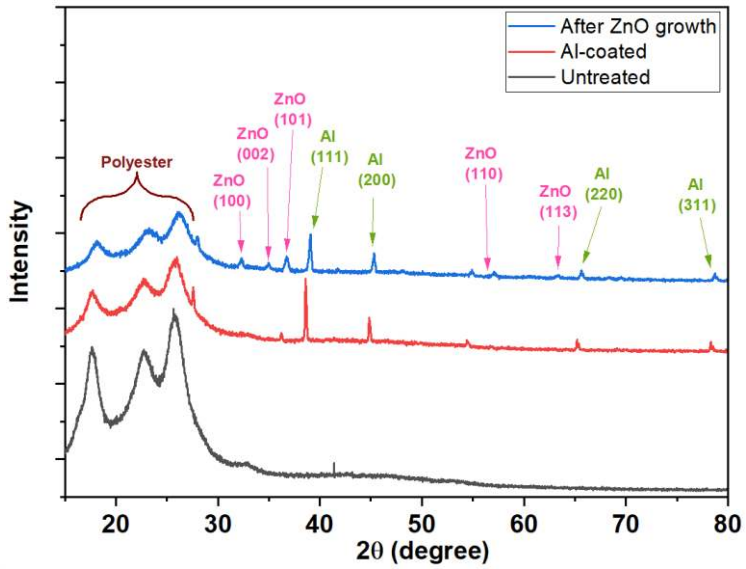

Figure 6.10. *XRD graphs of untreated polyester, Al-coated polyester, and Al-coated polyester fabrics after hydrothermal synthesis*

Surface SEM images and EDX analyses of the polyester fabric before the Al-coating process are presented in Figure 6.11. EDX analyses performed on the fiber surfaces confirmed that the polyester fibers are composed of carbon (C) and oxygen (O) elements.

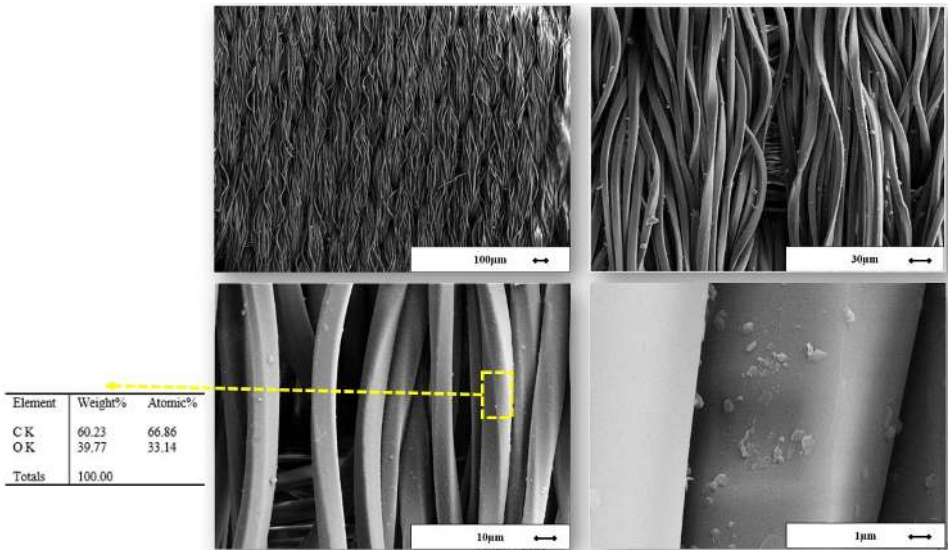

Figure 6.11. *SEM images and EDX results of polyester fabric before Al-coating process*

Surface SEM images and EDX analyses of the polyester fabric coated with aluminum powder are presented in Figure 6.12. Examination of the SEM images revealed the presence of a nanoparticle-based coating layer on the fabric surface. EDX

analyses of this coating confirmed that, in addition to aluminum (Al), the layer contained carbon (C), oxygen (O), sodium (Na), silicon (Si), and titanium (Ti).

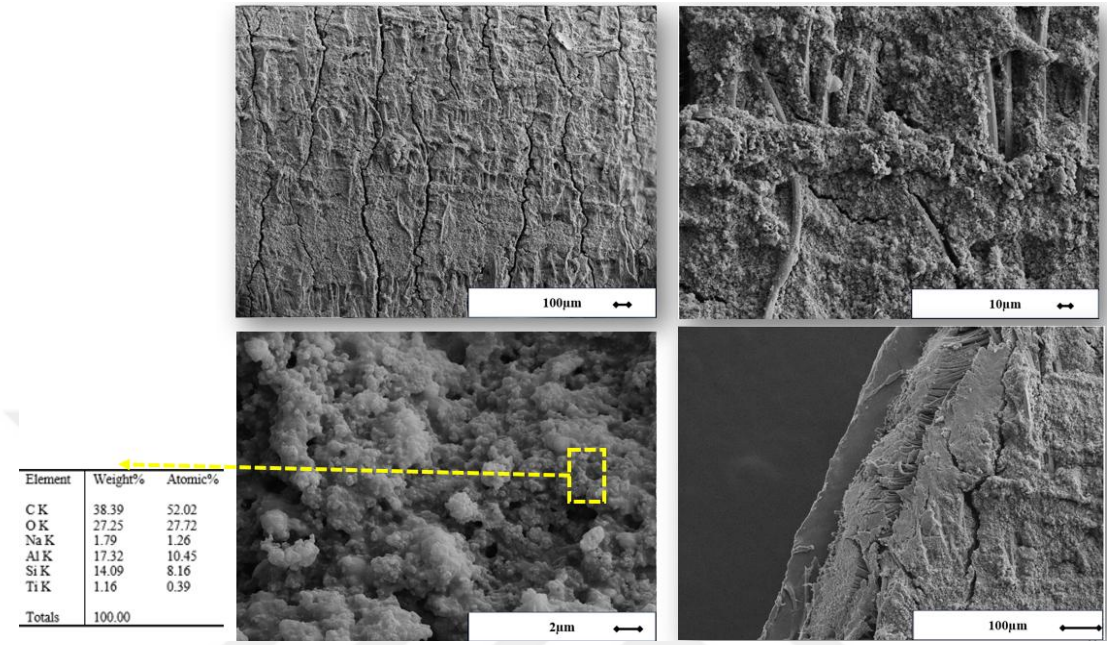

Figure 6.12. *SEM images and EDX results of polyester fabric coated with aluminum powder*

Surface SEM images and EDX analyses of the Al-coated polyester fabric, on which ZnO nanostructures were grown via hydrothermal synthesis, are presented in Figure 6.13. The SEM images revealed the formation of randomly oriented ZnO nanostructures exhibiting a nanorod and a nanocube morphology on the fabric surface; however, no ZnO nanowall structures were observed. EDX analyses indicated that these nanostructures were composed of Zn, O, C, Al, and Si. These results suggest that the surface coating was not composed of pure aluminum and that the presence of additional elements hindered the formation of the desired ZnO nanowall morphology. Additionally, it was observed that the aluminum coating on the polyester fabric surface was damaged after 6 hours of hydrothermal synthesis at 95°C, indicating that the synthesis conditions adversely affected the integrity of the coating.

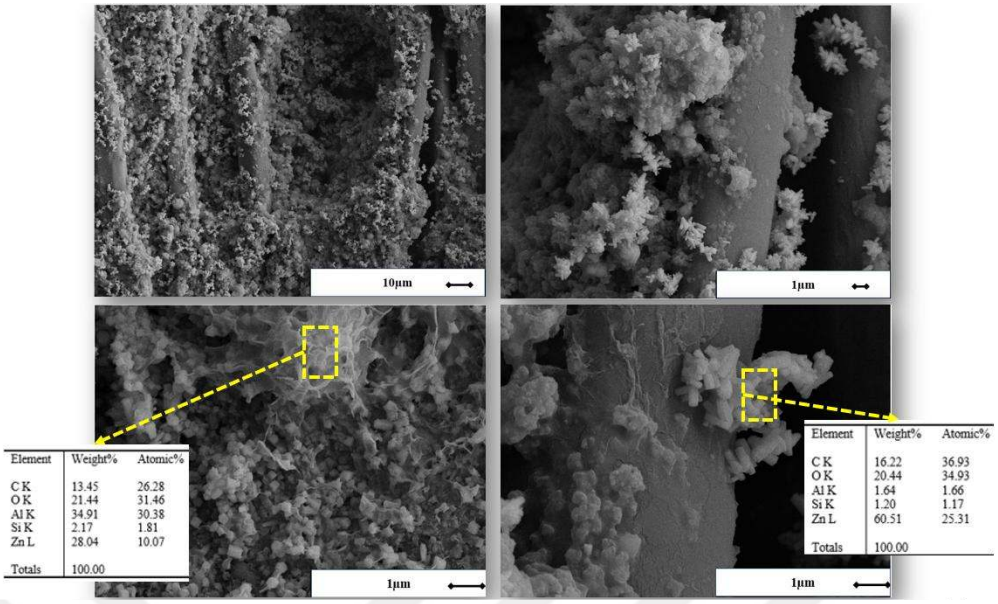

Figure 6.13. *SEM images and EDX results of Al-coated polyester fabric after hydrothermal synthesis*

Despite initial efforts to grow ZnO nanostructures directly on commercially available Al-coated fiberglass and polyester fabrics, several technical limitations were observed. The non-uniformity of the aluminum coating and the presence of additional elements in the coating layer hindered the controlled growth of ZnO nanowall structures, often resulting in randomly oriented nanorods and irregular nanoparticles. Moreover, extended hydrothermal synthesis at 95°C for 6 hours caused partial damage to the coating, further disrupting nanostructure formation. These factors collectively led to inconsistent morphology, poor alignment, and variable density of ZnO structures on the textile surfaces. Establishing continuous and reliable electrical contact between the ZnO nanostructures and the substrate was also challenging, particularly due to localized ruptures in the coating and the limited coverage of conductive layers. Consequently, achieving reproducible electrical performance while maintaining the inherent flexibility and wearability of textile substrates remains a critical challenge in the direct integration of ZnO nanostructures onto fabrics.

6.4.Conclusions

In this study, the feasibility of growing ZnO nanostructures on Al-coated textile substrates was systematically investigated. Commercial Al-coated fiberglass fabrics were initially tested; however, these materials proved unsuitable for wearable applications due to their rigidity, poor flexibility, and the non-uniform growth of ZnO

nanowalls on their surfaces. Moreover, prolonged hydrothermal synthesis led to delamination of the aluminum layer, further limiting their usability as a functional substrate.

To address these limitations, polyester fabrics were coated with aluminum powder and subsequently employed as substrates for ZnO growth. XRD and SEM analyses confirmed the presence of ZnO nanostructures with mixed nanorod and nanocube morphology. However, the desired nanowall morphology could not be obtained. EDX analyses revealed that the coating layer was not composed of pure aluminum but also contained other elements such as Na, Si, and Ti, which interfered with the oriented growth of ZnO nanowalls. In addition, the aluminum coating suffered from partial damage under hydrothermal synthesis conditions (95 °C, 6 h), raising concerns about its long-term structural stability.

Overall, the study of growing ZnO nanowall structures on textile surfaces using hydrothermal synthesis was not successful, primarily due to the inability to obtain suitable and stable aluminum coatings. The detachment of aluminum layers during the hydrothermal process not only caused a loss of conductivity but also inhibited the proper growth of ZnO nanowall structures. Consequently, due to the limitations encountered in this chapter, the electrical characterization of a piezoelectric nanogenerator module on textile substrates could not be completed.

These results indicate that although Al-coated fabrics provide a conductive platform for ZnO growth, their surface chemistry, coating homogeneity, and hydrothermal stability critically influence the resulting nanostructure morphology. Future studies should therefore focus on optimizing coating methods - such as achieving high-purity aluminum layers or exploring alternative conductive coatings - to enable controlled ZnO nanowall growth on textile substrates for reliable energy harvesting applications.

7. CONCLUSIONS

The motivation of this thesis is to develop innovative energy harvesting systems capable of meeting the energy demands of wearable electronics in a sustainable and environmentally friendly manner. In this context, it focused on flexible piezoelectric, triboelectric, and hybrid nanogenerator systems that can convert mechanical energy generated from daily body movements into electrical energy within their own ecosystem.

In the initial phase of the study, different ZnO nanostructures (nanowire and nanowall) that can be used in the active layer of nanogenerator modules were systematically compared. The hydrothermal method was identified as the most appropriate synthesis technique due to its compatibility with flexible substrates, low-temperature processing, and ability to yield oriented structures. However, ZnO nanowire arrays grown on flexible conductive substrates such as ITO/PET exhibited insufficient reproducibility, homogeneity, and c-axis alignment, making them less favorable for large-scale production and commercialization. In contrast, ZnO nanowall arrays demonstrated homogeneous growth over large areas, higher and more consistent electrical outputs, and thus were identified as promising candidates for commercialization.

Accordingly, the main focus of the study was on ZnO nanowall arrays. Structural defects that limited the efficiency of ZnO nanowalls synthesized via hydrothermal methods and their possible solutions were investigated. In this context, it was demonstrated that structural defects can be reduced by incorporating low amounts (0.5–2% at.) of doping elements into the ZnO crystal lattice. XRD analyses confirmed the incorporation of dopant ions into the ZnO lattice without forming secondary phases, and shifts in diffraction peaks revealed changes in lattice parameters depending on the ionic radius. SEM analyses showed that while higher doping levels increased nanowall density, reduced spacing between walls could limit mechanical deformation and negatively affect voltage generation. Therefore, optimizing doping levels was determined to be critical for maximizing the performance of ZnO nanowall-based modules.

Subsequently, three different ZnO nanowall-based nanogenerator module designs were systematically fabricated. In the first module, ZnO nanowalls were grown on aluminum foil serving as the bottom electrode, and various metal foils (Al, Cu, Zn, Ti,

brass) and Cu/Ni-coated conductive textiles were evaluated as top electrodes. The electrodes were encapsulated with Kapton tape to form a flexible structure. Electrical outputs were measured under different connection configurations using a mechanical test setup, revealing that module orientation and connection type directly influenced performance. Additionally, the interface contact type between the ZnO layer and the top electrode (Schottky or Ohmic) played a crucial role in determining the output characteristics. Schottky contacts produced higher open-circuit voltages, while Ohmic contacts produced higher short-circuit currents. This highlighted the importance of selecting electrode materials according to the desired application-specific output.

In the second module, a hybrid structure was developed by integrating three different polymer layers in addition to the ZnO nanowall-based piezoelectric layer. The high open-circuit voltages obtained from these measurements were attributed to the triboelectric charge accumulation capabilities of the polymer surfaces. Thus, it was concluded that this module is a hybrid nanogenerator system that utilizes both piezoelectric and triboelectric mechanisms simultaneously.

In the third design, instead of metal foil, conductive yarns formed by twisting steel wire with wool and polyester threads were knitted into a fabric and stitched onto ZnO nanowall-coated aluminum foil. Although this textile-based module could generate electrical output upon fingertip contact, its long-term durability was limited due to mechanical fatigue and potential breakage of the steel wire.

In the final stage, the first and second module designs were integrated onto a fabric glove and tested under real-use scenarios. Modules placed on fingertips, finger joint, and the palm generated significant electrical signals during tapping, bending, and clapping, movements, thus confirming the feasibility of wearable energy harvesting systems.

In conclusion, this study demonstrated that ZnO nanowall-based flexible nanogenerators, when optimized in terms of both material properties and module design, can offer practical, sustainable, and eco-friendly energy solutions for wearable electronics. The developed designs show strong potential for future applications in self-powered textiles, health monitoring sensors, and low-power IoT devices.

8. FUTURE WORKS

This thesis highlights the strong potential of ZnO-based flexible nanogenerators as promising candidates for sustainable energy harvesting in wearable electronics. The results reveal that controlling the morphology of ZnO nanostructures, applying effective doping strategies, and optimizing module designs are key to improving device performance. Future efforts should prioritize improving efficiency, lifetime, and scalability to enable successful commercialization.

ZnO nanowires represent a highly promising nanostructure for energy harvesting and flexible electronics, though their practical application still depends on precise synthesis control and the mitigation of growth-related challenges. Continued research in this field will be crucial for unlocking their full potential and enabling future commercialization. In the case of ZnO nanowalls, expanding the scope of doping strategies is vital to maximize piezoelectric performance. The low-doping approaches explored in this thesis are encouraging, but systematic studies on a wider range of dopants - including rare earth elements, transition metals, and multi-doping techniques - are needed to clarify their impact on crystal quality, defect density, morphology, and piezoelectric response. These efforts will offer deeper insight into how tailored modifications in electronic band structure and carrier density influence energy harvesting capabilities.

Advancing multilayer and three-dimensional module designs will also play a crucial role for enhancing the electrical output in future nanogenerator research. The fabrication of ZnO nanowalls in multilayer arrays on diverse substrates, combined with optimized parallel or series connection strategies, could significantly enhance power density and overcome limitations imposed by module architecture. Moreover, systematic optimization of electrode materials and deposition methods is necessary. Considering the decisive influence of electrode conductivity, work function, the type of metal-ZnO contact (Schottky vs. Ohmic), and flexibility on energy output systematic evaluation of various metals and transparent conductive oxides is recommended. In addition, employing surface engineering and coating strategies - such as thin films, printed electrodes, plasma coating, or conductive polymer coatings - can further improve module efficiency, mechanical stability, and long-term durability. In addition to advances in module design, the development of hybrid energy harvesting systems is highly recommended. Integrating multiple energy conversion mechanisms - such as

piezoelectric, triboelectric, pyroelectric, or thermoelectric effects - within a single platform could substantially enhance the ability to provide continuous power for low-power electronic devices.

Another significant direction for future research is the direct growth of ZnO nanostructures on conductive textile substrates. Hydrothermal synthesis of ZnO nanowires or nanowalls on textile surfaces allows for flexible, breathable, and wearable energy harvesting platforms. This approach not only simplifies module fabrication but also facilitates seamless integration with wearable electronic systems. Comprehensive studies on the energy generation performance of ZnO nanostructures grown on various textile types under mechanical deformation will be crucial for further progress.

Regardless of whether nanogenerators are fabricated as modules or directly on textile surfaces, their flexibility, durability, and environmental stability must be thoroughly evaluated. Assessing the performance of textile-based systems under conditions such as repeated mechanical cycling, bending, stretching, washing, and exposure to humidity or heat is essential for determining their reliability in practical, real-world applications.

Consequently, expanding the application scope of ZnO nanostructure-based flexible nanogenerators should be a key focus for future research. Potential applications include running low-power sensors, wireless communication devices, health monitoring systems, biomedical implants, and IoT-enabled wearable technologies. In particular, developing modules capable of continuously harvesting energy from user movements to monitor bio-signals - like heart rate, respiration, or step count - would strengthen the commercialization potential of this technology. The implementation of these proposed future studies will contribute to the wider use of ZnO nanowall-based flexible generators in both academic research and industrial applications.

REFERENCES

Aazem, I., Mathew, D. T., Radhakrishnan, S., Vijoy, K. V., John, H., Mulvihill, D. M., and Pillai, S. C. (2022). Electrode materials for stretchable triboelectric nanogenerator in wearable electronics. *RSC advances*, 10545-10572.

Ahmad, M., Ahmad, M. K., Mamat, M. H., Mohamed, A., Suriani, A. B., Ismail, N. M., and Nafarizal, N. (2022). Effects of group-I elements on output voltage generation of ZnO nanowires based nanogenerator; degradation of screening effects by oxidation of nanowires. *Micromachines*, 1450.

Annapureddy, V., Palneedi, H., Hwang, G. T., Peddigari, M., Jeong, D. Y., Yoon, W. H., and Ryu, J. (2017). Magnetic energy harvesting with magnetoelectrics: an emerging technology for self-powered autonomous systems. *Sustainable Energy and Fuels*, 2039-2052.

Badawy, D., Soltanian, S., Servati, P., Bahi, A., and Ko, F. (2020). Functional piezoelectric yarn: Toward optimization of zinc oxide nanowires growth. *Journal of Materials Research*, 3091-3105.

Bagga, S., Akhtar, J., and Mishra, S. (2018). Synthesis and applications of ZnO nanowire: A review. *AIP Conference*, (pp. 1989, 1).

Ballato, A. (1995). Piezoelectricity: old effect, new thrusts. *IEEE transactions on ultrasonics, ferroelectrics, and frequency control*, 916-926.

Banna, G. H., and Park, I. K. (2017). Flexible ZnO nanorod-based piezoelectric nanogenerators on carbon papers. *Nanotechnology*, 445402.

Basinova, N., Cernohorsky, O., Grym, J., Kucerova, S., Faitova, H., Yatskiv, R., and Maixner, J. (2019). Highly textured seed layers for the growth of vertically oriented ZnO nanorods. *Crystals*, 566.

Batra, K., Sinha, N., Goel, S., Yadav, H., Joseph, A. J., and Kumar, B. (2018). Enhanced dielectric, ferroelectric and piezoelectric performance of Nd-ZnO nanorods and their application in flexible piezoelectric nanogenerator. *Journal of Alloys and Compound*, 1003-1011.

Baxter, J. B., Walker, A. M., Van Ommering, K., and Aydil, E. S. (2006). Synthesis and characterization of ZnO nanowires and their integration into dye-sensitized solar cells. *Nanotechnology*, S304. .

Bell, L. E. (2008). Cooling, heating, generating power, and recovering waste heat with thermoelectric systems. *Science*, 1457-1461.

Bui, Q. C., Salem, B., Roussel, H., Mescot, X., Guerfi, Y., Jiménez, C., and Ardila, G. (2021). Effects of thermal annealing on the structural and electrical properties of ZnO thin films for boosting their piezoelectric response. *Journal of Alloys and Compounds*, 159512.

Byun, K. E., Lee, M. H., Cho, Y., Nam, S. G., Shin, H. J., and Park, S. (2017). Potential role of motion for enhancing maximum output energy of triboelectric nanogenerator. *APL Mater.*, 5 (7): 074107.

Chandra Sekhar, B., Dhanalakshmi, B., Srinivasa Rao, B., Ramesh, S., Venkata Prasad, K., Subba Rao, P. S., and Parvatheeswara Rao, B. (2021). Piezoelectricity and Its Applications. In D. R. Sahu, *Multifunctional Ferroelectric Materials* (pp. 71-88). IntechOpen.

Chang, W. Y., Fang, T. H., and Tsai, J. H. (2015). Electromechanical and photoluminescence properties of Al-doped ZnO nanorods applied in piezoelectric nanogenerators. *Journal of Low Temperature Physics*, 174-187.

Chang, Y. C., Lin, Y. R., Chen, S. W., and Chou, C. M. (2022). Density-Controlled Growth of ZnO Nanowalls for High-Performance Photocatalysts. *Materials*, 9008.

Chen, C. H., Chang, S. J., Chang, S. P., Li, M. J., Chen, I. C., Hsueh, T. J., and Hsu, C. L. (2010). Fabrication of a white-light-emitting diode by doping gallium into ZnO nanowire on a p-GaN substrate. *The Journal of Physical Chemistry C*, 12422-1242.

Chen, J., and Wang, Z. L. (2017). Reviving vibration energy harvesting and self-powered sensing by a triboelectric nanogenerator. *Joule*, 480-521.

Chen, Y. J., Brahma, S., Liu, C. P., and Huang, J. L. (2017). Enhancement of the piezoelectric coefficient in hexagonal MgxZn1-xO films at lower Mg compositions. *Journal of Alloys and Compounds*, 1248-1253.

Chen, Y., Li, Y., Wu, J., and Duan, W. (2017). General criterion to distinguish between Schottky and Ohmic contacts at the metal/two-dimensional semiconductor interface. *Nanoscale*, 2068-2073.

Cheng, J. P., Zhang, X. B., and Luo, Z. Q. (2008). Oriented growth of ZnO nanostructures on Si and Al substrates. *Surface and Coatings Technology*, 4681-4686.

Chevalier-César, C., Capochichi-Gnambodoe, M., and Leprince-Wang, Y. (2014). Growth mechanism studies of ZnO nanowire arrays via hydrothermal method. *Applied Physics A,*, 953-960.

Choi, M. Y., Choi, D., Jin, M. J., Kim, I., Kim, S. H., Choi, J. Y., and Kim, S. W. (2009). Mechanically powered transparent flexible charge-generating nanodevices with piezoelectric ZnO nanorods. *Advanced Materials*, 2185-2189.

Chu, F. H., Huang, C. W., Hsin, C. L., Wang, C. W., Yu, S. Y., Yeh, P. H., and Wu, W. W. (2012). Well-aligned ZnO nanowires with excellent field emission and photocatalytic properties. *Nanoscale*, 1471-1475.

Coban Tetik, H. S., Suvaci, E., Avci, A. M., Adem, U., Karakaya, M., (2023). Development of textured lead-free NBT-based piezoelectric materials in a matrix,

synthesized by an alternative route, via templated grain growth,. *Journal of Materials Science: Materials in Electronics*, 324.

Curie, J., and Curie, P. (1880). Développement par compression de l'électricité polaire dans les cristaux hémièdres à faces inclinées. *Bulletin de Minéralogie* , 90-93.

Dagdeviren, C., Yang, B. D., Su, Y., Tran, P. L., Joe, P., Anderson, E., and Rogers, J. A. (2014). Conformal piezoelectric energy harvesting and storage from motions of the heart, lung, and diaphragm. *Proceedings of the National Academy of Sciences*, 1927-1932.

Demes, T., Ternon, C., Riassetto, D., Roussel, H., Rapenne, L., Gélard, I., and Langlet, M. (2016). New insights in the structural and morphological properties of sol-gel deposited ZnO multilayer films. *Journal of Physics and Chemistry of Solids*, 43-55.

Desai, A. V., and Haque, M. A. (2007). Mechanical properties of ZnO nanowires. *Sensors and Actuators A: Physical*, 169-176.

Directive, E. U. (2013). Restriction of the use of certain hazardous substances in electrical and electronic equipment (RoHS). *Off. J. Eur. Communities*, 19-23.

Fan, F. R. (2012). Flexible triboelectric generator. *Nano energy*, 328-334.

Fan, F. R., Tian, Z. Q., and Wang, Z. L. (2012). Flexible triboelectric generator. *Nano Energy*, 328-334.

Fang, F., Zhao, D. X., Zhang, J. Y., Shen, D. Z., Lu, Y. M., Fan, X. W., and Wang, X. H. (2007). Growth of well-aligned ZnO nanowire arrays on Si substrate. *Nanotechnology*, 235604.

Foo, K. L., Kashif, M., . Hashim, U., and Liu, W. W. (2014). Effect of different solvents on the structural and optical properties of zinc oxide thin films for optoelectronic applications. *Ceramics International*, 753-761.

Fu, Y., Cheng, Y., Chen, C., Li, D., and Zhang, W. (2022). Study on preparation process and enhanced piezoelectric performance of pine-needle-like ZnO@ PVDF composite nanofibers. *Polymer Testing*, 107513.

Gao, P. X., Song, J., Liu, J., and Wang, Z. L. (2007). Nanowire piezoelectric nanogenerators on plastic substrates as flexible power sources for nanodevices. *Advanced Materials*, 67-72.

Ghayour, H., Nourbakhsh, A. A., Mirdamadi, S., and Rezaei, H. R. (2010). Illustration of Effective Parameters on Growth of ZnO Micro/Nano Rods, on the Borosilicate Glass via Hydrothermal Process. *Journal of nanoscience and nanotechnology*, 7455-7458.

Goel, S., Sinha, N., Yadav, H., Joseph, A. J., and Kumar, B. (2017). Experimental investigation on the structural, dielectric, ferroelectric and piezoelectric properties

of La doped ZnO nanoparticles and their application in dye-sensitized solar cells. *Physica E: Low-dimensional Systems and Nanostructures*, 72-81.

Govind, K., Pahwa, A., Aggarwal, N., and Balodhi, V. (2012). Ecosecurity energy harvesting using piezoelectric crystal. *Students Conference on Engineering and Systems*, (pp. 1-6). Allahabad.

Greene, L. E., Law, M., Goldberger, J., Kim, F., Johnson, J. C., Zhang, Y., and Yang, P. (2003). Low-temperature wafer-scale production of ZnO nanowire arrays. *Angewandte Chemie*, 3139-3142.

Guillemin, S., Appert, E., Roussel, H., Doisneau, B., Parize, R., Boudou, T., and Consonni, V. (2015). Controlling the structural properties of single step, dip coated ZnO seed layers for growing perfectly aligned nanowire arrays. *The Journal of Physical Chemistry C*, 21694-21703.

Guillemin, S., Consonni, V., Appert, E., Puyoo, E., Rapenne, L., and Roussel, H. (2012). Critical nucleation effects on the structural relationship between ZnO seed layer and nanowires. *The Journal of Physical Chemistry C*, 25106-25111.

Gullapalli, H., Vemuru, V. S., Kumar, A., Botello-Mendez, A., Vajtai, R., Terrones, M., and Ajayan, P. M. (2010). Flexible piezoelectric ZnO–paper nanocomposite strain sensor. *Small*, 1641-1646.

Guo, M., Diao, P., and Cai, S. (2005). Hydrothermal growth of well-aligned ZnO nanorod arrays: Dependence of morphology and alignment ordering upon preparing conditions. *Journal of solid state Chemistry*, 1864-1873.

Gupta, M. K., Lee, J. H., Lee, K. Y., and Kim, S. W. (2013). Two-dimensional vanadium-doped ZnO nanosheet-based flexible direct current nanogenerator. *ACS nano*, 8932-8939.

Han, Y., Guo, J., Luo, Q., and Ma, C. Q. (2023). Solution-Processable Zinc Oxide for Printed Photovoltaics: Progress, Challenges, and Prospect. *Advanced Energy and Sustainability Research*, 2200179.

He, W., Zhang, G., Zhang, X., Ji, J., Li, G., and Zhao, X. (2015). Recent development and application of thermoelectric generator and cooler. *Applied Energy*, 1-25.

Hong, G. W., Kim, J., Lee, J. S., Shin, K., Jung, D., and Kim, J. H. (2020). A flexible tactile sensor using seedless hydrothermal growth of ZnO nanorods on fabrics. *Journal of Physics Communications*, 045002.

Hosono, E., Fujihara, S., Kimura, T., and Imai, H. (2004). Non-basic solution routes to prepare ZnO nanoparticles. *Journal of Sol-Gel Science and Technology*, 71-79.

Hsueh, T. J., Hsu, C. L., Chang, S. J., and Chen, I. C. (2007). Laterally grown ZnO nanowire ethanol gas sensors. *Sensors and Actuators B: Chemical*, 473-477.

Hu, D., Yao, M., Fan, Y., Ma, C., Fan, M., and Liu, M. (2019). Strategies to achieve high performance piezoelectric nanogenerators. *Nano energy*, 288-304.

Hu, Y., Zhang, Y., Xu, C., Lin, L., Snyder, R. L., and Wang, Z. L. (2011). Self-powered system with wireless data transmission. *Nano letters*, 2572-2577.

Huang, H., Wang, H., Li, B., Mo, X., Long, H., Li, Y., and Fang, G. (2013). Seedless synthesis of layered ZnO nanowall networks on Al substrate for white light electroluminescence. *Nanotechnology*, 315203.

Hussain, M., Abbasi, M. A., Ibupoto, Z. H., Nur, O., and Willander, M. (2014). The improved piezoelectric properties of ZnO nanorods with oxygen plasma treatment on the single layer graphene coated polymer substrate. *Physica status Solidi (a)*, 455-459.

Hussain, M., Khan, A., Nur, O., Willander, M., and Broitman, E. (2014). The effect of oxygen-plasma treatment on the mechanical and piezoelectrical properties of ZnO nanorods. *Chemical Physics Letters*, 235-238.

Ibn Shamsah, S. M. (2024). Thermoelectric Materials: A Scientometric Analysis of Recent Advancements and Future Research Directions. *Energies*, 5002.

Indumathi, S., Venkatesan, S., and Manikandan, M. (2023). Influence of manganese addition in ZnO-based piezoelectric nanogenerator for mechanical energy harvesting. *J Mater Sci: Mater Electron*, 563.

Iwu, K. O., Strano, V., Di Mauro, A., Impellizzeri, G., and Mirabella, S. (2015). Enhanced quality, growth kinetics, and photocatalysis of ZnO nanowalls prepared by chemical bath deposition. *Crystal Growth and Design*, 4206-4212.

Jantač, S., Pelcová, J., Sklenářová, J., Grosshans, H., and Kosek, J. (2023). A model of surface roughness effect on triboelectric charging of particles. *arXiv preprint arXiv*, 13441.

Ji, L. W., Peng, S. M., Wu, J. S., Shih, W. S., Wu, C. Z., and Tang, I. T. (2009). Effect of seed layer on the growth of well-aligned ZnO nanowires. *Journal of Physics and Chemistry of Solids*, 1359-1362.

Jiang, B. C., and Yang, S. H. (2021). Nickel-doped ZnO nanowalls with enhanced electron transport ability for electrochemical water splitting. *Nanomaterials*, 1980.

Jie, J., Wang, G., Chen, Y., Han, X., Wang, Q., Xu, B., and Hou, J. G. (2005). Synthesis and optical properties of well-aligned ZnO nanorod array on an undoped ZnO film. *Applied Physics Letters*, 031909.

Jung, W. S., Kang, M. G., Moon, H. G., Baek, S. H., Yoon, S. J., Wang, Z. L., and Kang, C. Y. (2015). High Output Piezo/Triboelectric Hybrid Generator. *Scientific Reports*, 9309.

Kang, L., An, H., Park, J. Y., Hong, M. H., Nahm, S., and Lee, C. G. (2019). La-doped p-type ZnO nanowire with enhanced piezoelectric performance for flexible nanogenerators. *Applied Surface Science*, 969-973.

Kaur, J., and Singh, H. (2019). Synthesis and fabrication of zinc oxide nanostrands based piezoelectric nanogenerator. *Journal of Materials Science: Materials in Electronics*, 4437-4445.

Kaur, J., and Singh, H. (2020). Fabrication and analysis of piezoelectricity in 0D, 1D and 2D Zinc Oxide nanostructures. *Ceramics International*, 19401-19407.

Kenanakis, G., Vernardou, D., Koudoumas, E., and Katsarakis, N. (2009). Growth of c-axis oriented ZnO nanowires from aqueous solution: the decisive role of a seed layer for controlling the wires' diameter. *Journal of Crystal Growth*, 4799-4804.

Khan, A., Ali Abbasi, M., Hussain, M., Hussain Ibupoto, Z., Wissting, J., Nur, O., and Willander, M. (2012). Piezoelectric nanogenerator based on zinc oxide nanorods grown on textile cotton fabric. *Applied Physics Letters*, 193506.

Kim, K. H., Kumar, B., Lee, K. Y., Park, H. K., Lee, J. H., Lee, H. H., and Kim, S. W. (2013). Piezoelectric two-dimensional nanosheets/anionic layer heterojunction for efficient direct current power generation. *Scientific reports*, 1-6.

Kim, M. J., Song, Z., Yun, T. G., Kang, M. J., Son, D. H., and Pyun, J. C. (2023). Wearable fabric-based ZnO nanogenerator for biomechanical and biothermal monitoring. *Biosensors and Bioelectronics*, 115739.

Klingshirn, C. (2007). ZnO: From basics towards applications. *Physica Status Solidi (b)*, 3027-3073.

Kumar, B., Lee, K. Y., Park, H. K., Chae, S. J., Lee, Y. H., and Kim, S. W. (2011). Controlled growth of semiconducting nanowire, nanowall, and hybrid nanostructures on graphene for piezoelectric nanogenerators. *Acs Nano*, 4197-4204.

Law, M., Goldberger, J., and Yang, P. (2004). Semiconductor nanowires and nanotubes. *Annu. Rev. Mater. Res.*, 83-122.

Lee, C. Y., Tseng, T. Y., Li, S. Y., and Lin, P. (2003). Growth of zinc oxide nanowires on silicon (100). *Journal of Applied Science and Engineering*, 127-132.

Lee, S., Lee, J., Ko, W., Cha, S., Sohn, J., Kim, J., and Hong, J. (2013). Solution-processed Ag-doped ZnO nanowires grown on flexible polyester for nanogenerator applications. *Nanoscale*, 9609-9614.

Leonov, V., and Vullers, R. J. (2009). Wearable electronics self-powered by using human body heat: The state of the art and the perspective. *Journal of Renewable and Sustainable Energy*, 1(6).

Leprince-Wang, Y. (2015). *Piezoelectric ZnO nanostructure for energy harvesting.* John Wiley and Sons.

Li, C., Fang, G., Su, F., Li, G., Wu, X., and Zhao, X. (2006). Synthesis and photoluminescence properties of vertically aligned ZnO nanorod–

nanowalljunction arrays on a ZnO-coated silicon substrate. *Nanotechnology*, 3740.

Li, W. J., Shi, E. W., Zhong, W. Z., and W., Y. Z. (1999). Growth mechanism and growth habit of oxide crystals. *Journal of crystal growth*, 186-196 .

Liang, Z., Gao, R., Lan, J. L., Wiranwetchayan, O., Zhang, Q., Li, C., and Cao, G. (2013). Growth of vertically aligned ZnO nanowalls for inverted polymer solar cells. *Solar Energy Materials and Solar Cells*, 34-40.

Liu, X., Jin, Z., Liu, Z., Yu, K., and Bu, S. (2006). Nanostructured ZnO films obtained by a basic erosion method . *Applied surface science*, 8668-8672.

Look, D. C. (2001). Recent advances in ZnO materials and devices. *Materials science and engineering: B*, 383-387.

Lu, M. P., Song, J., Lu, M. Y., Chen, M. T., Gao, Y., Chen, L. J., and Wang, Z. L. (2009). Piezoelectric nanogenerator using p-type ZnO nanowire arrays. *Nano letters*, 1223-1227.

Luo, J. T., Yang, Y. C., Zhu, X. Y., Chen, G., Zeng, F., and Pan, F. (2010). Enhanced electromechanical response of Fe-doped ZnO films by modulating the chemical state and ionic size of the Fe dopant. *Physical Review B—Condensed Matter and Materials Physics*, 014116.

Lupan, O., Emelchenko, G. A., Ursaki, V. V., Chai, G., Redkin, A. N., Gruzintsev, A. N., and Yakimov, E. E. (2010). Synthesis and characterization of ZnO nanowires for nanosensor applications. *Materials Research Bulletin*, 1026-1032.

Ma, H. (2019). Influence of Heat Treatments on the Properties of ZnO Nanorods Prepared by Hydrothermal Synthesis. *Semiconductors*, 1811-1816.

Mahapatra, A., Ajimsha, R. S., and Misra, P. (2022). Oxygen annealing induced enhancement in output characteristics of ZnO based flexible piezoelectric nanogenerators. *Journal of Alloys and Compounds*, 165277.

Manikandan, M., Rajagopalan, P., Patra, N. J., Muralidharan, M., Prabu, S. M., and Singh, V. (2020). Development of Sn-doped ZnO based ecofriendly piezoelectric nanogenerator for energy harvesting application. *Nanotechnology*, 185401.

Manjula, Y., Kumar, R. R., Raju, P. M., Kumar, G. A., Rao, T. V., Akshaykranth, A., and Supraja, P. (2020). Piezoelectric flexible nanogenerator based on ZnO nanosheet networks for mechanical energy harvesting. *Chemical Physics*, 110699.

Mondal, R., Hasan, M. A., Baik, J. M., and Yang, Y. (2023). Advanced pyroelectric materials for energy harvesting and sensing applications. *Materials Today*, 273-301.

Muchuweni, E., Sathiaraj, T. S., and Nyakotyo, H. (2018). Effect of annealing on the microstructural, optical and electrical properties of ZnO nanowires by

hydrothermal synthesis for transparent electrode fabrication. *Materials Science and Engineering: B*, 68-73.

Murillo, G., Leon-Salguero, E., Martínez-Alanis, P. R., Esteve, J., Alvarado-Rivera, J., and Güell, F. (2019). Role of aluminum and HMTA in the hydrothermal synthesis of two-dimensional n-doped ZnO nanosheets. *Nano Energy*, 817-826.

Narayanan, G. N., Ganesh, R. S., and Karthigeyan, A. (2016). Effect of annealing temperature on structural, optical and electrical properties of hydrothermal assisted zinc oxide nanorods. *Thin Solid Films*, 39-45.

Nayak, A. P., Katzenmeyer, A. M., Gosho, Y., Tekin, B., and Islam, M. S. (2012). Sonochemical approach for rapid growth of zinc oxide nanowalls. *Applied Physics A*, 661-667.

Newnham, R. E. (2004). *Properties of materials: anisotropy, symmetry, structure.* OUP Oxford.

Ogbuehi, A. C. (2018, March). *Influence of contact barrier on the transport properties of micro structured ZnO thin films.* Leipzig: University of Leipzig. Retrieved from ResearchGate.

Ohyama, M., Kouzuka, H., and Yoko, T. (1997). Sol-gel preparation of ZnO films with extremely preferred orientation along (002) plane from zinc acetate solution. *Thin solid films*, 78-85.

Özgür, Ü., Alivov, Y. I., Liu, C., Teke, A., Reshchikov, M. A., Doğan, S., and Morkoç, A. H. (2005). A comprehensive review of ZnO materials and devices. *Journal of applied physics*.

Pan, Z., and Wang, Z. (2001). Nanobelts of semiconducting oxides. *Science*, 1947-1949.

Pan, Z., Peng, W., Li, F., and He, Y. (2018). Carrier concentration-dependent piezotronic and piezo-phototronic effects in ZnO thin-film transistor. *Nano Energy*, 529-537.

Pandey, R. K., Dutta, J., Brahma, S., Rao, B., and Liu, C. P. (2021). Review on ZnO-based piezotronics and piezoelectric nanogenerators: Aspects of piezopotential and screening effect. *Journal of Physics: Materials*, 044011.

Park, H. K., Lee, K. Y., Seo, J. S., Jeong, J. A., Kim, H. K., Choi, D., and Kim, S. W. (2011). Charge-generating mode control in high-performance transparent flexible piezoelectric nanogenerators. *Advanced Functional Materials,*, 1187-1193.

Park, W. I., and Yi, G. C. (2004). Electroluminescence in n-ZnO nanorod arrays vertically grown on p-GaN. *Advanced Materials*, 87-90.

Pearton, S. J., Norton, D. P., Ip, K., Heo, Y. W., and Steiner, T. (2004). Recent advances in processing of ZnO, Microelectronics and Nanometer Structures Processing, Measurement, and Phenomena. *Journal of Vacuum Science and Technology B*, 932-948.

Pellegrino, D., Franzò, G., Strano, V., M. S., and Bruno, E. (2019). Improved synthesis of ZnO nanowalls: effects of chemical bath deposition time and annealing temperature. *Chemosensors*, 18.

Pointon, A. J. (1982). Piezoelectric devices. *IEE Proceedings A: Physical Science, Measurement and Instrumentation* , 285-307.

Postels, B., Wehmann, H. H., Bakin, A., Kreye, M., Fuhrmann, D., Blaesing, J., and Waag, A. (2007). Controlled low-temperature fabrication of ZnO nanopillars with a wet-chemicalapproach. *Nanotechnology*, 195602.

Prauzek, M., Konecny, J., Borova, M., Janosova, K., Hlavica, J., and Musilek, P. (2018). Energy harvesting sources, storage devices and system topologies for environmental wireless sensor networks: A review. *Sensors*, 2446.

Qin, Y., Wang, X., and Wang, Z. (2008). Microfibre–nanowire hybrid structure for energy scavenging. *Nature*, 809-813.

Rafique, S., Kasi, A. K., Kasi, J. K., Aminullah, Bokhari, M., and Shakoor, Z. (2020). Fabrication of silver-doped zinc oxide nanorods piezoelectric nanogenerator on cotton fabric to utilize and optimize the charging system. *Nanomaterials and Nanotechnology*, 1847980419895741.

Rajagopalan, P., Jakhar, P., Palani, I. A., Singh, V., and Kim, S. J. (2020). Elucidations on the effect of lanthanum doping in ZnO towards enhanced performance nanogenerators. *International Journal of Precision Engineering and Manufacturing-Green Technology*, 77-87.

Rajagopalan, P., Singh, V., and Palani, I. A. (2018). Enhancement of ZnO-based flexible nano generators via a sol–gel technique for sensing and energy harvesting applications. *Nanotechnology*, 105406.

Rong, P., Ren, S., and Yu, Q. (2019). Fabrications and applications of ZnO nanomaterials in flexible functional devices-a review. *Critical reviews in analytical chemistry*, 336-349.

Ruhaizat, N., Ainuddin, A., and Z., K. (2021). Experimental the Influence of Growth Solution on Zinc Oxide Crystal Structures via Hydrothermal Method. *International Journal of Integrated Engineering*, 222-228.

Saravanakumar, B., and Kim, S. J. (2014). Growth of 2D ZnO nanowall for energy harvesting application. *The Journal of Physical Chemistry C*, 8831-8836.

Schmidt-Mende, L., and MacManus-Driscoll, J. L. (2007). ZnO–nanostructures, defects, and devices. *Materials Today*, 40-48.

Sheng, H., Ma, Y., Zhang, H., Yuan, J., Li, F., Li, W., and Lan, W. (2024). Integration of Supercapacitors with Sensors and Energy-Harvesting Devices: A Review. *Advanced Materials Technologies*, 2301796.

Sheoran, H., Kumar, V., and Singh, R. (2022). A comprehensive review on recent developments in ohmic and Schottky contacts on Ga2O3 for device applications. *ACS Applied Electronic Materials*, 2589-2628.

Shin, S. H., Kim, Y. H., Lee, M. H., Jung, J. Y., Seol, J. H., and Nah, J., (2014). Lithium-doped zinc oxide nanowires–polymer composite for high performance flexible piezoelectric nanogenerator. *ACS nano*, 10844 - 10850.

Shin, S. H., Kwon, Y. H., Lee, M. H., Jung, J. Y., Seol, J. H., and Nah, J. (2016). A vanadium-doped ZnO nanosheets–polymer composite for flexible piezoelectric nanogenerators. *Nanoscale*, 1314-1321.

Sinha, N., Goel, S. J., Yadav, H., Batra, K., Gupta, M. K., and Kumar, B. (2018). Y-doped ZnO nanosheets: Gigantic piezoelectric response for an ultra-sensitive flexible piezoelectric nanogenerator. *Ceramics International*, 8582-8590.

Sinha, N., Ray, G., Bhandari, S., Godara, S., and Kumar, B. (2014). Synthesis and enhanced properties of cerium doped ZnO nanorods. *Ceramics International*, 12337-12342.

Sinha, N., Ray, G., Godara, S., Gupta, M. K., and Kumar, B. (2014). Enhanced piezoelectric output voltage and Ohmic behavior in Cr-doped ZnO nanorods. *Materials Research Bulletin*, 267-271.

Skyrme, T. (2022). *Wearable technology forecasts 2023–2033.* IDTechEx.

Skyrme, T., and Howley, J. (2024). *Wearable Sensors Market 2025–2035: Technologies, Trends, Players, Forecasts.* IDTechEx.

Sohn, J. I., Cha, S. N., Song, B. G., Lee, S., Kim, S. M., Ku, J., and Kim, K. (2013). Engineering of efficiency limiting free carriers and an interfacial energy barrier for an enhancing piezoelectric generation. *Energy and Environmental Science,*, 97-104.

Song, J., Zhou, J., and Wang, Z. L. (2006). Piezoelectric and semiconducting coupled power generating process of a single ZnO belt/wire. A technology for harvesting electricity from the environment. *Nano letters*, 1656-1662.

Sreekanth, M., Ghosh, S., Mehta, S. K., Ganguli, A. K., and Jha, M., (2017). Investigation of the growth mechanism of the formation of ZnO nanorods by thermal decomposition of zinc acetate and their field emission properties. *CrystEngComm*, 2264-2270.

Sun, H., Tian, H., Yang, Y., Xie, D., Zhang, Y. C., Liu, X., and Ren, T. L. (2013). A novel flexible nanogenerator made of ZnO nanoparticles and multiwall carbon nanotube. *Nanoscale*, 6117-6123.

Sun, Y., Fuge, G. M., and Ashfold, M. N. (2006). Growth mechanisms for ZnO nanorods formed by pulsed laser deposition. *Superlattices and Microstructures*, 33-40.

Syrrokostas, G., and Govatsi, K. S. (2016). High-quality, reproducible ZnO nanowire arrays obtained by a multiparameter optimization of chemical bath deposition growth. *Crystal Growth and Design*, 2140-2150.

Sze, S. M., and Ng, K. K. (2007). Metal-Semiconductor Contacts. In *Physics of Semiconductor Devices* (pp. 134-196). Hoboken: John Wiley and Sons.

Szyszka, B. (2008). Magnetron sputtering of ZnO films. In B. Szyszka, *In Transparent Conductive Zinc Oxide: Basics and Applications in Thin Film Solar Cells* (pp. 187-233). Berlin: Springer .

Tang, J. F., Su, H. H., Lu, Y. M., and Chu, S. Y. (2015). Controlled growth of ZnO nanoflowers on nanowall and nanorod networks via a hydrothermal method. *Cryst. Eng. Comm*, 592-597.

Vayssieres, L. (2003). Growth of arrayed nanorods and nanowires of ZnO from aqueous solutions. *Advanced Materials*, 464-466.

Vayssieres, L., Keis, K., Lindquist, S. E., and Hagfeldt, A. (2001). Purpose-built anisotropic metal oxide material: 3D highly oriented microrod array of ZnO. *The Journal of Physical Chemistry B*, 3350-3352.

Verde, M., Peiteado, M., Villegas, M., Ferrari, B., and Caballero, A. C., (2013). Soft solution processing of ZnO nanoarrays by combining electrophoretic deposition and hydrothermal growth. *Materials Chemistry and Physics*, 75-80.

Vernardou, D., Kenanakis, G., Couris, S., Koudoumas, E., Kymakis, E., and Katsarakis, N. (2007). pH effect on the morphology of ZnO nanostructures grown with aqueous chemical growth. *Thin solid films*, 8764-8767.

Wallace, I., Eshu, O. V., Chukwunonso, O. B., and Okoro, U. C. (2015). Synthesis and characterization of zinc oxide (ZnO) nanowire. *J Nanomed Nanotechnol*, 6(321), 2.

Wang, L., Zhang, X., Zhao, S., Zhou, G., Zhou, Y., and Qi, J. (2005). Synthesis of well-aligned ZnO nanowires by simple physical vapor deposition on c-oriented ZnO thin films without catalysts or additives. *Applied Physics Letters*, 024108.

Wang, M., Wang, J., Chen, W., Cui, Y., and Wang, L. (2006). Effect of preheating and annealing temperatures on quality characteristics of ZnO thin film prepared by sol–gel method. *Materials Chemistry and Physics*, 219-225.

Wang, X. (2012). Piezoelectric nanogenerators-Harvesting ambient mechanical energy at the nanometer scale. *Nano Energy*, 13-24.

Wang, X. B., Song, C., Li, D. M., Geng, K. W., Zeng, F., and Pan, F. (2006). The influence of different doping elements on microstructure, piezoelectric coefficient and resistivity of sputtered ZnO film. *Applied Surface Science*, 1639-1643.

Wang, X., Song, J., Liu, J., and Wang, Z. L. (2007). Direct-current nanogenerator driven by ultrasonic waves. *Science*, 102-105.

Wang, Z. L., and Song, J. (2006). Piezoelectric nanogenerators based on zinc oxide nanowire arrays. *Science*, 242-246.

Wang, Z. L. (2004). Zinc oxide nanostructures: growth, properties and applications. *Journal of physics: condensed matter*, R829.

Wang, Z. L. (2009). ZnO nanowire and nanobelt platform for nanotechnology. *Materials Science and Engineering: R: Reports*, 33-71.

Wang, Z. L. (2012). Progress in piezotronics and piezo-phototronics. *Advanced Materials*, 4632-4646.

Wei, T. Y., Yeh, P. H., Lu, S. Y., and Wang, Z. L. (2009). Gigantic enhancement in sensitivity using Schottky contacted nanowire nanosensor. *Journal of the American Chemical Society*, 17690-17695.

Wu, J., Zheng, Y., and Li, X. (2021). Recent progress in self-powered sensors based on triboelectric nanogenerators. *Sensors*, 7129.

Xi, Y., Song, J., Xu, S., Yang, R., Gao, Z., Hu, C., and Wang, Z. L. (2009). Growth of ZnO nanotube arrays and nanotube based piezoelectric nanogenerators. *Journal of materials chemistry*, 9260-9264.

Xiang, H. J., Yang, J., Hou, J. G., and Zhu, Q. (2006). Piezoelectricity in ZnO nanowires: A first-principles study. *Applied physics letters*, 89(22).

Xue, H., Yang, Q., Wang, D., Luo, W., Wang, W., Lin, M., and Luo, Q. (2017). A wearable pyroelectric nanogenerator and self-powered breathing sensor. *Nano Energy*, 147-154.

Yadav, H., Sinha, N., Goel, S., and Kumar, B. (2016). Eu-doped ZnO nanoparticles for dielectric, ferroelectric and piezoelectric applications. *Journal of Alloys and Compounds*, 333-341.

Yang, P., Yan, H., Mao, S., Russo, R., Johnson, J., Saykally, R. and Choi, H. J. (2002). Controlled growth of ZnO nanowires and their optical properties. *Advanced functional materials*, 323-331.

Yang, Y. C., Song, C., Wang, X. H., Zeng, F., and Pan, F. (2008). Giant piezoelectric d33 coefficient in ferroelectric vanadium doped ZnO films. *Applied Physics Letters*, 92(1).

Yang, Y., Guo, W., Pradel, K. C., Zhu, G., Zhou, Y., Zhang, Y., and Hu, Y. L. (2012). Pyroelectric nanogenerators for harvesting thermoelectric energy. *Nano letters*, 2833-2838.

Yang, Y., Jung, J. H., Yun, B. K., Zhang, F., Pradel, K. C., Guo, W., and Wang, Z. L. (2012). Flexible pyroelectric nanogenerators using a composite structure of lead-free KNbO3 nanowires. *Advanced Materials*, 5357-5362.

Ye, C., Bando, Y., Shen, G., and Golberg, D. (2006). Thickness-dependent photocatalytic performance of ZnO nanoplatelets. *The Journal of Physical Chemistry B*, 15146-15151.

Zaszczyńska, A., Gradys, A., and Sajkiewicz, P. (2020). Progress in the applications of smart piezoelectric materials for medical devices. *Polymers*, 2754.

Zhang, B., Zhou, S., Liu, B., Gong, H., and Zhang, X., (2009). Fabrication and green emission of ZnO nanowire arrays. *Science in China Series E: Technological Sciences*, 883-887.

Zhang, D., Wu, H., Bowen, C. R., and Yang, Y. (2021). Recent advances in pyroelectric materials and applications. *Small*, 2103960.

Zhang, R., and Olin, H. (2020). Material choices for triboelectric nanogenerators: A critical review. *EcoMat*, e12062.

Zhang, X., Wang, W., Zhang, D., Mi, Q., and Yu, S. (2021). Self-powered ethanol gas sensor based on the piezoelectric Ag/ZnO nanowire arrays at room temperature. *Journal of Materials Science: Materials in Electronics*, 7739-7750.

Zhang, Y., Liu, C., Liu, J., Xiong, J., Liu, J., Zhang, K., and Wang, Z. L. (2016). Lattice strain induced remarkable enhancement in piezoelectric performance of ZnO-based flexible nanogenerators. *ACS applied materials and interfaces*, 1381-1387.

Zhang, Y., Russo, R. E., and Mao, S. S. (2005). Femtosecond laser assisted growth of ZnO nanowires. *Applied Physics Letters*, 133115.

Zhang, Z., Chen, Y., and Guo, J. (2019). ZnO nanorods patterned-textile using a novel hydrothermal method for sandwich structured-piezoelectric nanogenerator for human energy harvesting. *Physica E: Low-dimensional Systems and Nanostructures*, 212-218.

Zhang, Z., Lv, Y., Yan, J., Hui, D., Yun, J., Zhai, C., and Zhao, W. (2015). Uniform ZnO nanowire arrays: Hydrothermal synthesis, formation mechanism and field emission performance. *Journal of Alloys and Compounds*, 374-380.

Zhao, M. H., Wang, Z. L., and Mao, S. X. (2004). Piezoelectric characterization of individual zinc oxide nanobelt probed by piezoresponse force microscope. *Nano Letters*, 587-590.

Zhao, T., Fu, Y., Zhao, Y., Xing, L., and Xue, X. (2015). Ga-doped ZnO nanowire nanogenerator as self-powered/active humidity sensor with high sensitivity and fast response. *Journal of Alloys and Compounds*, 571-576.

Zhao, Z., Dai, Y., Dou, S. X., and Liang, J. (2021). Flexible nanogenerators for wearable electronic applications based on piezoelectric materials. *Materials Today Energy*, 100690.

Zhou, J., Gu, Y., Hu, Y., Mai, W., Yeh, P. H., Bao, G., and Wang, Z. L. (2009). Gigantic enhancement in response and reset time of ZnO UV nanosensor by utilizing Schottky contact and surface functionalization. *Applied physics letters*, 94(19).

Zhu, G., Wang, A. C., Liu, Y., Zhou, Y., and Wang, Z. L. (2012). Functional electrical stimulation by nanogenerator with 58 V output voltage. *Nano letters*, 3086-3090.

Znaidi, L. (2010). Sol–gel-deposited ZnO thin films: A review. *Materials Science and Engineering: B*, 18-30.

Znaidi, L., Illia, G. S., Guennic, R. L., Sanchez, C., and Kanaev, A. (2003). Elaboration of ZnO thin films with preferential orientation by a soft chemistry route. *Journal of Sol-Gel Science and Technology*, 817-821.

http-1: https://sdgs.un.org/goals (Access Date: 17.06.2025)

http-2: https://imagej.net/ij/(Access Date: 26.03.2024)

CURRICULUM VITAE

ORCID ID: 0000-0001-8954-8838

Name Surname **: Gamze YÜKSEL**

Foreign Language **: English**

Place and Year of Birth **:**

Email **:**

Education and Professional Background:

- 2019, Eskişehir Technical University, Institute of Graduate Schools, Advanced Technologies – Nanotechnology Department
- 2017, Anadolu University, Business Administration Faculty, Business Administration Department
- 2016, Anadolu University, Engineering Faculty, Chemical Engineering Department
- 2025, Project Research Assistant, Eskişehir Technical University, Advanced Technology Ceramics Laboratory
- 2024, Instructor, DENEYAP Technology Workshops
- 2019, Project Research Assistant, Eskişehir Technical University, Technical Textiles and Combustion Laboratory
- 2018, Graduate Research Assistant, Eskişehir Technical University, Advanced Technologies Application and Research Center

Publications and/or Scientific/Artistic Activities:

- Çetinkaya, I. C., Yuksel, G., Macit, C., Üreyen, M. E., and Eren, T., 2021, Synthesis and Characterization of Polyphosphonates and Polyurethanes Using Chalcone and DOPO-Chalcone as a Flame Retardant, ACS Applied Polymer Materials, 3(10) (2021), 5277-5290.
- Üreyen, M. E., Uraz, E., Yuksel, G., 2020, Flame Retardant Effects of Cyclic Phosphonate with HALS and Fumed Silica in Polypropylene, Journal of Applied Polymer Science, 137(4), (2020), 48308.

- Karasu, B., Yuksel, G., Uysal, N., 2020, The Recent Developments in Ceramic Glazes", Türkiye Seramik Federasyonu Dergisi, 58, 116-128 (2020).
- Koca, A., İ., Üreyen, M. E., Yuksel, G., Karaer, F., 2019, Effects of Carbon Nanotube-Phosphorus Based Flame Retardant Combinations on Flammability of Polypropylene, International Periodical of Recent Technologies in Applied Engineering, 1 (1), 37-43 (2019).
- 2025, Oral presentation, Enhancing Energy Efficiency in ZnO-Based Nanogenerators: The Role of Electrodes, XIX ECerS Conference, Dresden, Germany.
- 2025, Poster presentation, Influence of ZnO Nanowall Morphology on The Efficiency of Flexible Piezoelectric Nanogenerators, 49th International Conference and Exposition on Advanced Ceramics and Composites, Daytona Beach, Florida, USA.
- 2025, Oral presentation, ZnO Nanowall/Polymer Hybrid Nanogenerators: Efficient Energy Harvesting for Wearable Devic, 49th International Conference and Exposition on Advanced Ceramics and Composites, Daytona Beach, Florida, USA.
- 2025, Poster presentation, Enhancing Energy Output in Piezoelectric Nanodevices: A Focus on Electrode Selection, 49th International Conference and Exposition on Advanced Ceramics and Composites, Daytona Beach, Florida, USA.
- 2024, Oral presentation, Design of ZnO Nanowall-Based Flexible Piezo-Triboelectric Nanogenerators as Wearable Energy Harvesters, Fall Meeting of Korean Ceramic Society - ECerS - KCerS Joint Symposium, Seoul, South Korea.
- 2024, Poster presentation, Designing ZnO Nanowall-Based Flexible Piezoelectric Nanogenerators for High Performance Wearable Energy Harvesters, Electroceramics XIX Conference, Vilnius Lithuania.
- 2024, Oral presentation, Understanding the Structure-Property Relationship in ZnO Nanowall Arrays to Maximize energy Harvesting Performance, 22nd International Metallurgy and Materials Congress, İstanbul, Türkiye.

- 2023, Oral presentation, Critical Parameters for Growth of Oriented ZnO Nanowire Arrays during Hydrothermal Synthesis, 15th ECerS Conference for Young Scientists in Ceramics, CYSC-2023, Novi Sad, Serbia.
- 2023, Oral presentation, Hydrothermal Synthesis Parameters Effects on ZnO Nanowall Structures for Efficient Energy Harvesting, 26th National Electron Microscopy Congress, Eskişehir, Türkiye.
- 2020, Oral presentation, Synergistic Effect of Some Nanosized Additives/HALS Combinations on The Flame Retarded Polypropylene, 7th International Symposium on Fiber and Polymer Research, Bursa, Türkiye.
- 2020, Oral presentation, Effect of Expandable Graphite and Graphene Additives on Thermal Conductivity of Polyamide-6 Composite, 7th International Symposium on Fiber and Polymer Research, Bursa, Türkiye.
- 2020, Oral presentation, Effects of HALS and Nano-TiO_2 on the Flammability of Cyclic Phosphonate-based Flame Retardant/Polypropylene System, 6th International Symposium on Fiber and Polymer Research, Bursa, Türkiye.
- 2020, Oral presentation, Flame Retardant and UV Resistant Polypropylene: A Study of Phosphorus and NOR HALS Compounds, 6th International Symposium on Fiber and Polymer Research, Bursa, Türkiye.
- 2020, Oral presentation, Synthesis and Investigation of Flame-Retardant Properties of Phosphorus Functional Polyurethanes, 32nd National Chemistry Congress, İstanbul, Türkiye.
- 2018, Poster presentation, Effects of Carbon Nanotube-Phosphorus Based Flame Retardant Combinations on Flammability of Polypropylene, 8th International Istanbul Textile Conference, ETT 2018, Istanbul, Türkiye.
- 2018, Oral presentation, Effects of CNT and Nano-SiO_2 on the Flammability of Ammonium Polyphosphate-based Flame-Retardant Polypropylene System, 3rd International Symposium on Fiber and Polymer Research, Bursa, Türkiye.

Awards:

- 2019-2023, The Council of Higher Education of Türkiye (YOK) 100/2000 Priority Areas Doctoral Scholarship – Smart and Innovative Materials, Türkiye
- 2019-2023, The Scientific and Technological Research Council of Türkiye (TÜBİTAK) 2011-General Domestic Doctorate Scholarship, Türkiye

Professional Union/Association/Organization Memberships:

- 2025, Institute of Engineers and Everyone Else (IEEE), U.S.A
- 2025, IEEE Women in Engineering, U.S.A
- 2024, The American Ceramic Society (ACerS), U.S.A
- 2024, Türkiye Chapter of The American Ceramic Society, Türkiye
- 2023, Türk Seramik Derneği, Türkiye
- 2023, European Ceramic Society (ECerS), Belgium
- 2023, Türk Elektron Mikroskopi Derneği, Türkiye